

Northumbria Research Link

Citation: Roberti, Giacomo (2021) Analysis and control of rogue waves in fibre lasers and in hydrodynamics: integrable turbulence framework. Doctoral thesis, Northumbria University.

This version was downloaded from Northumbria Research Link:
<http://nrl.northumbria.ac.uk/id/eprint/48615/>

Northumbria University has developed Northumbria Research Link (NRL) to enable users to access the University's research output. Copyright © and moral rights for items on NRL are retained by the individual author(s) and/or other copyright owners. Single copies of full items can be reproduced, displayed or performed, and given to third parties in any format or medium for personal research or study, educational, or not-for-profit purposes without prior permission or charge, provided the authors, title and full bibliographic details are given, as well as a hyperlink and/or URL to the original metadata page. The content must not be changed in any way. Full items must not be sold commercially in any format or medium without formal permission of the copyright holder. The full policy is available online: <http://nrl.northumbria.ac.uk/policies.html>



**Northumbria
University**
NEWCASTLE

**ANALYSIS AND CONTROL OF
ROGUE WAVES IN FIBRE LASERS
AND IN HYDRODYNAMICS:
INTEGRABLE TURBULENCE
FRAMEWORK**

GIACOMO ROBERTI

PhD

2022

**ANALYSIS AND CONTROL OF
ROGUE WAVES IN FIBRE LASERS
AND IN HYDRODYNAMICS:
INTEGRABLE TURBULENCE
FRAMEWORK**

GIACOMO ROBERTI

A thesis submitted in partial fulfilment of
the requirements of the University of
Northumbria at Newcastle for the degree of
Doctor of Philosophy

Faculty of Engineering and Environment

March 2022

Abstract

Understanding mechanisms underlying the formation of extreme events is the problem of primary importance in various domains of study including hydrodynamics, optics, forecasting natural disasters etc. In these domains, extreme events are known as Rogue Waves (RWs). RWs are localised coherent structures of unusually large amplitude spontaneously emerging in nonlinear random wave fields, and as such, can have damaging effect on the environment (e.g. offshore engineering structures) or on the medium they propagate through (e.g. optical fibres).

Within this PhD project several problems related to the emergence, control and manipulation of RWs in fibre optics and in hydrodynamics have been investigated. The particular emphasis is on the study of RWs emerging in the propagation of the so-called partially coherent waves described by the focusing nonlinear Schrödinger equation (fNLSE), the universal model for the propagation of modulationally unstable quasi-monochromatic wavepackets in a broad range of physical media. fNLSE belongs to the class of the completely integrable equations possessing deep mathematical structure and amenable to analytical methods such as Inverse Scattering Transform and Finite-Gap Integration. We use recent mathematical discoveries related to the semi-classical, or small-dispersion, limit of fNLSE to investigate analytically, numerically and experimentally the formation of RWs within the framework of integrable turbulence—the emerging theory of random waves in integrable systems. The study of the RW formation in this project has also prompted the investigation of a closely related problem concerned with dynamics of soliton and breather gases as special types of integrable turbulence.

The project’s findings fall in five categories: (i) the analytical description of the emergence of the so-called “heavy tails” in the probability distribution for the field intensity at the early stage of the development of integrable turbulence; (ii) the development and experimental realisation in a water tank of *nonlinear spectral engineering*, the IST-based method of control and manipulation of RWs; (iii) the development of the spectral theory of bidirectional soliton gases; (iv) numerical synthesis of breather gases and the verification of the recently developed spectral kinetic theory for such gases; (v) the investigation of the RW formation in the compression of broad optical pulses in the highly nonlinear propagation regimes, when the higher order effects such as self-steepening, third order dispersion and Raman scattering need to be taken into account.

Contents

Abstract	i
Preface	ix
Acknowledgements	xi
Declaration	xii
Introduction and Overview of Concepts	1
1 Mathematical and Physical Background	11
1.1 Propagation of light in optical fibres and Nonlinear Schrödinger equation	11
1.1.1 Losses	12
1.1.2 Chromatic Dispersion	13
1.1.3 Nonlinear effects	14
1.1.4 Nonlinear Schrödinger Equation	15
1.1.5 Normalisation	16
1.1.6 Hydrodynamics	17
1.1.7 Nonlinear Schrödinger Equation: exact solutions	19
1.2 Modulational instability	23
1.3 Rogue Waves	25
1.4 Integrability and Inverse Scattering Transform	28
1.4.1 Vanishing boundary conditions	30
1.4.2 Periodic and quasi-periodic boundary conditions	33
1.4.3 Finite-gap potentials and Rogue Waves	37
1.4.4 Semi-classical theory and Bertola-Tovbis results	39
1.5 Integrable Turbulence	43
1.5.1 Noise induced Modulational Instability	44
1.5.2 Partially coherent waves	46
1.5.3 Soliton Gas	50
1.6 Numerical Methods	57

1.6.1	Fourier collocation method	57
1.6.2	Boffetta-Osborne method	59
1.6.3	Local IST	61
2	Early stage of integrable turbulence	64
2.1	Outline of the Problem	64
2.2	Summary of Results and Outlook	65
	Early stage of integrable turbulence in the one-dimensional nonlinear schrödinger equation: A semiclassical approach to statistics, Phys. Rev. E, 100:032212, 2019 . . .	68
3	Prediction and manipulation of Rogue Waves	77
3.1	Outline of the Problem	77
3.2	Summary of Results and Outlook	80
	Prediction and manipulation of hydrodynamic rogue waves via nonlinear spectral engineering, arXiv:2108.02698 (2021), submitted for publication in a peer reviewed journal	82
4	Bidirectional soliton gas in dispersive hydrodynamics	93
4.1	Outline of the Problem	93
4.2	Summary of Results and Outlook	96
	Soliton gas in bidirectional dispersive hydrodynamics, Phys. Rev. E, 103:042201, 2021	102
5	Numerical synthesis of breather gas	118
5.1	Outline of the Problem	118
5.2	Summary of Results and Outlook	123
	Numerical spectral synthesis of breather gas for the focusing nonlinear Schrödinger equation, Phys. Rev. E, 103:042205, 2021	124
6	Extreme compression of optical pulses in highly nonlinear regimes	136
6.1	Introduction	137
6.2	Mathematical model	138
6.2.1	Model equations and characteristic parameters	138
6.2.2	Chirped initial pulse	141

6.2.3	Numerical method and computational resources	143
6.3	Semi-classical approximation	143
6.3.1	Semi-classical generalised NLS model and the initial data	144
6.3.2	Validity of semi-classical approximation	146
6.4	Gradient catastrophe analysis	146
6.4.1	The nonlinear geometric optics approximation	147
6.4.2	Gradient catastrophe and rogue wave compression distance	150
6.5	Rogue wave compression	152
6.5.1	Primary rogue wave compression: peak power	152
6.5.2	Secondary rogue wave compression at high propagation powers	154
6.5.3	Energy analysis of the rogue wave pulse compression	155
6.6	Summary	158
7	Conclusion and Outlook	160
7.1	Conclusions	160
7.2	Future research	163
	Appendix A Position shift in two breather interactions	165
	Acronyms	169
	References	170

List of Figures

1	Attenuation spectrum in a silica optical fibre at infrared band (cited from [1]). . .	12
2	Examples of exact solution of the fNLSE evaluated at $t = 0$: (a) the fundamental soliton, (b) the Akhmediev breather, (c) the Kuznetsov-Ma breather and (d) the Peregrine soliton.	20
3	Examples of Tajiri-Watanabe breather solution of the fNLSE with $\lambda = 0.2 + 0.5i$: (a) spatio-temporal evolution of wave filed amplitude $ u(x, t) $ and (b) amplitude profile of the solution at $t = 0$	21

4	(a) MI gain curve $g(k)$ calculated from the linear stability analysis of (1.18). (b-d) Schematics of three initial conditions leading to the development of MI of the condensate: (b) harmonic perturbation, (c) random noise perturbation and (d) localised perturbation.	24
5	(Adapted from [2] with permission from the authors) Exceedence probability, “heavy” tailed distribution of wave height recorded in water tank experiment . . .	26
6	Schematic of the IST method to solve nonlinear PDE	28
7	Solitonic solutions of the fNLSE and their IST spectral portraits. The wave field amplitude $ u(x, t) $ (left) and the spectral portraits (right) of (a) the fundamental soliton, (b) the Akhmediev breather, (c) the Kuznetsov-Ma breather and (d) the Peregrine soliton The red lines in spectra plotted in (b–d) represent branchcuts (spectral bands). The blue points in (a–d) represent complex conjugate double points.	35
8	(adapted from [3] with permission from authors) In the notation adopted in our work $\psi \equiv u$. Example of multiphase solution $n = 4$; $\lambda_i = (-0.39271 + i, -0.21336 + i, 0.010556 + i, 0.20525 + i, 0.39027 + i)$; $\langle \psi ^2 \rangle = 1.6452$; $K_4 = 15.1959$. (a) Plot of the amplitude of the multiphase solution $ \psi(x, t) $ and (b) plot of $ \psi(x) $ for a fixed time t	38
9	Gradient catastrophe formation: (a) power ρ and (b) chirp v for the initial pulse $\rho(\tau, 0) = \text{sech}(\tau)^2, v(\tau, 0) = 0$	40
10	Numerical simulation of the semi-classical fNLSE. Absolute value $ u(\tau, \xi) $ versus (τ, ξ) coordinates where the initial condition considered is $u(\tau, 0) = \text{sech}(\tau)$ with $\varepsilon = 0.01$	42
11	(Adapted from [4] with permission from the authors) fibre optics experimental observation of the Peregrine emergence as regularisation of the gradient catastrophe. Comparison of experimental measurements (black line), of intensity (bottom) and phase (top), with simulations (red line).	42
12	Noise-induced modulation instability scenario of integrable turbulence: (a) initial random perturbation of the condensate solution $ u(x, 0) $ and (b) 2D colour plot of the temporal evolution of the amplitude of the wave field $ u(x, t) $	44

13	(Adapted from [5] with permission from the authors) Experimental observation of the evolution of the PDF of the normalised power [(a)–(e)] and the evolution of the normalised fourth-order moment κ_4 for the development of integrable turbulence in noise-induced MI.	45
14	(Adapted from [5] with permission from the authors) Experimental observation of the evolution of the two-points statistics of optical power $g^{(2)}$ for the development of integrable turbulence in noise-induced MI.	46
15	Partially coherent wave scenario of integrable turbulence: (a) initial condition $ u(x, 0) $ and (b) 2D color plot of the temporal evolution of the amplitude of the wave field $ u(x, t) $	47
16	(Adapted from [6] with permission from the authors) In the notation adopted in our work $\psi \equiv u$. Numerical simulations of a partially coherent wave propagation in the fNLSE. (a) Probability density function of $ \psi ^2$ at three different propagation distances. (b) spatio-temporal diagram of $ \Psi $. White boxes highlight the formation of the PS as regularisation mechanism of the gradient catastrophe of the initial humps. (c) Evolution of the kurtosis (black). (d) Profile of the wave field at two different propagation distances. (colours are preserved). For details of the simulation refer to [6].	49
17	(adapted from [7] with permission from authors.) Comparison for the propagation of a free soliton with the spectral parameter $\eta = \eta_1$ in a void (black dashed line) with the propagation of the test soliton with the same spectral parameter η_1 (red solid line) through a one-component rarefied soliton gas with the DOS $f = f_0\delta(\eta - \eta_0)$. One can see that the test soliton propagates faster in the gas due to the interactions.	52

18	(adapted from [8] with permission from authors.) Example of application of the numerical periodisation procedure to known solution of the fNLSE. (a) Spatial profile of a fundamental soliton . (b) Spatial profile of the fundamental soliton periodised in space. (c) Spectral portrait of the periodised soliton showing that the periodisation procedure produces a band having a small size where the point of discrete spectrum of the exact solution would be. (d) Spatial profile of the KM soliton. (e) Spatial profile of the KM soliton periodised. (f) Spectral portrait of the periodised KM soliton showing that the periodisation procedure produces a band having a small size where the point of discrete spectrum of the exact solution would be.	62
19	Universal regularisation of the gradient catastrophe via the local emergence of the Peregrine soliton for the initial condition $u(\tau, 0) = \text{sech}(\tau) \exp[-i\mu \log(\cosh(\tau))/\epsilon]$ with (a,b) $\mu = 0$ (exact 10-soliton solution) (c,d) $\mu = 0$ (solitonless solution). (a,c) spatio-temporal evolution of the amplitude of the solution and (b,d) profile of the soliton at the maximum compression point ξ_m . (b,d) Inset with the IST spectrum of the solution.	78
20	Spectral representation of a generic breather (TW) gas characterised by the branch cut (black vertical line) and a collection of points of discrete spectrum (red dots). The corresponding multicomponent DOS (5.1) has weights $\omega_j = 1 \forall j$	120
21	Comparison of the chirped Gaussian (blue) and “sech” (orange) initial profiles. . .	145
22	Schematic for the stability criterion $\Delta < 0$. Left: Δ as function of ρ ; Right: The root ρ_2 as function of the chirp u	149
23	Comparison between the numerical solutions of the gNLSE (6.20) with $\epsilon = 0.05$ (red dots) and of the reduced model (6.28) (solid line) at $Z = 0$, $Z = 0.3$ and $Z = 0.39$. The initial pulse is $\psi(T, 0) = \exp(-T^2/2)$. Upper row: the evolution of the intensity (power) $\rho = \psi ^2$ profile. The error (the absolute value of the difference between the two solutions) is shown in the bottom row.	150

24	<p>Left: the rogue wave compression distance Z^*. Solid line: formula (6.34). Orange dots: numerical simulations of the fNLSE (6.41) for “sech” pulses; blue dots: numerical simulations for Gaussian pulses. Right: the Gaussian pulse delay function (the difference between the rogue wave compression distances for the Gaussian and sech pulses</p>	152
25	<p>The local rogue wave background a_0 as function of the normalised chirp factor μ. The curve is given by the analytical expression $a_0 = \sqrt{2 + \mu}$ obtained for sech pulses; the dots show $a_0(\mu)$ obtained numerically for Gaussian pulses.</p>	153
26	<p>Gradient catastrophe in the Gaussian pulse compression. Left: fNLSE propagation; Right: gNLSE</p>	154
27	<p>Primary rogue compression due to the PS emergence. Left: fNLSE propagation; Right: gNLSE</p>	155
28	<p>Secondary compression in the propagation of a Gaussian pulse. Left: cubic fNLSE (no secondary compression); Right: gNLSE—secondary compression due to the Raman effect.</p>	156
29	<p>Schematic of the energy “stored” in the Peregrine soliton</p>	157
30	<p>Comparison of numerical solutions of the gNLSE (6.7) with known particular solutions [9] for pulse propagation. Left: Third-order dispersion: (dashed) Gaussian shape initial pulse with $T_0^2 = 1/2$, (red dots) output of the numerical simulation for the third dispersion coefficient $\beta_3' = 0.01$ and the propagation length $Z = 10$, (solid line) analytical expression of the evolved signal. Middle: Self-steepening: (dashed) Gaussian shape initial condition, (red dots) output of the numerical simulation for $C_s = 0.01$ (self-steepening coefficient) and $Z = 15$, (solid line) analytical expression of the signal at $Z = 15$. Right: Intrapulse Raman scattering: soliton fission of the two-soliton initial condition (dotted line). The evolution is shown at $Z = 6$ (dashed line) and $Z = 16$ (solid line). The results fully agree with those available in [9].</p>	159

Preface

This PhD project is primarily concerned with the analytical, numerical and experimental study of the nonlinear wave propagation in optical fibres and in hydrodynamics. It was funded by the Defence Science and Technology Laboratory (Dstl) in the framework of the UK-France PhD Programme. The project has been completed under the joint supervision of Prof. G. El (Northumbria University) and Prof. S. Randoux (University of Lille).

The original motivation for the project was the investigation of the effect of randomness, or incoherence, of the input signal, on the generation of the so-called rogue waves—the large-amplitude fluctuations of the wave field that “appear out of nowhere and disappear without a trace”. Rogue waves can have significant (and potentially harmful) effect on the medium they propagate through, e.g. cause a damage of the optical fibre. The ability to predict and manipulate/suppress rogue waves is therefore of major importance for telecommunications and signal processing in optical systems but is also of great interest for shipbuilding industry and offshore engineering since rogue waves are known to regularly occur in the ocean with potentially devastating consequences for ships and oil platforms (in fact the original studies of rogue waves were performed in the context of water waves). Since the first officially recorded measurement of a rogue wave in the North Sea in 1995 there have been a myriad of theoretical and experimental research papers and monographs on various aspects of rogue waves occurring in a broad range of physical media, particularly in optical fibres.

The canonical mathematical model for the nonlinear propagation of quasi-monochromatic light signals through optical fibres is the cubic Nonlinear Schrödinger NLS equation, which appears in two modifications: defocusing and focusing, depending on the properties of the fibre. Certain particular solutions of the focusing Nonlinear Schrödinger Equation fNLSE called breathers have been widely recognised as “analytical prototypes” for rogue waves and have been extensively studied both theoretically and experimentally. The novelty of this project is that it considers rogue waves in fibre optics and hydrodynamics within the unified theoretical framework of integrable turbulence, the recently introduced new paradigm in the nonlinear wave theory. The integrable turbulence approach to the understanding of rogue waves proved very useful because it encompasses both the dynamical and statistical aspects of the rogue wave formation. One of the main theoretical

contributions of this project is the introduction of the semi-classical NLS approximation in integrable turbulence, which has enabled an effective application of recent deep mathematical results from the integrable systems theory to the problems of practical significance, making an important step towards our ability to predict and manipulate the rogue wave formation from a given random wave field input.

The work on the rogue wave theory and applications within this project has prompted the theoretical research on a closely related aspect of integrable turbulence—the theory of soliton and breather gases—that has been included in the project. The particular contribution of this work is the construction of the theory of soliton gases in bidirectional nonlinear dispersive systems, motivated by recent experiments on the generation of soliton gas in shallow water waves. The developed theory is also applicable to the incoherent light propagation in optical fibres with normal dispersion described by the defocusing Nonlinear Schrödinger Equation dNLSE. The work on breather gases for the fNLSE has required the development of novel numerical approaches and enabled the first verification of the recently developed spectral kinetic theory of breather gases.

Finally, a highly relevant research that has been included in the project is the work on the extreme pulse compression in optical fibres, undertaken under the research contract with LumOptica Ltd. This part of the project is concerned with the deterministic aspect of the fNLSE dynamics in which the rogue wave formation from a given initial signal can be viewed as the manifestation of the extreme pulse compression. Since the peak power in the rogue wave significantly exceeds the initial maximum power of the input pulse one may need to include the higher order effects such as the intrapulse Raman scattering and the third order dispersion to fully describe the pulse compression. Importantly, the inclusion of the higher order effects destroys integrability of the NLS equation so the main objectives of this part of the project were to investigate whether the basic mechanism of the rogue wave formation introduced in the semi-classical integrable NLS framework is robust with respect to the higher order corrections, and what are the qualitative and quantitative modifications of the pulse compression that occur in highly nonlinear propagation regimes.

Acknowledgements

I would like to thank Dstl for the generous support of this project through the UK-FR PhD Scheme. This project has enabled me to work on fascinating research topics and meet incredible people. My thanks extend to our contacts at Dstl: Prof. Jitu Patel, Dr Lee Hill and Dr Robert Deas, who supported the project during these four years. Through their interest in this work, we also got in touch with Dr Craig Stacy from LumOptica Ltd and started another interesting satellite project which enhanced this Thesis. I would like to thank LumOptica for the funding that supported me in the last part of my PhD

My knowledge of the English language prevents me to properly express the deep gratitude I have for my supervisors: Prof. Gennady El and Prof. Stéphane Randoux. Their help, support, and guidance during my PhD went far beyond the academic sphere. The stimulating environment in Newcastle and Lille has been one of the best part of this experience. I am very thankful to both of them for all they taught me and for their inspiring passion for mathematics and physics.

Declaration

I declare that the work contained in this thesis has not been submitted for any other award and that it is all my own work. I also confirm that this work fully acknowledges opinions, ideas and contributions from the work of others. The work was done in collaboration with the Defence Science and Technology Laboratory through the UK-FR PhD Scheme, with LumOptica Ltd and with PhLAM laboratory at the University of Lille, Fr.

Any ethical clearance for the research presented in this thesis has been approved. Approval has been sought and granted by the Faculty Ethics Committee on the 28th January 2019.

I declare that the Word Count of this thesis is 41453 words.

Name: Giacomo Roberti

Date: 8 October 2021

Introduction and Overview of Concepts

The propagation and interaction of nonlinear dispersive waves is a fundamental area of research with multitude of physical applications. It has originated in the works of Stokes, Boussinesq, Korteweg and de Vries in the 19th century. The field experienced a major boost in the 1960s with remarkable insights such as the discovery of solitons by Zabusky and Kruskal [10] and the development of the Inverse Scattering Transform (IST) [11], applicable to completely integrable Partial Differential Equations PDE. In parallel, Whitham introduced a general asymptotic method to study modulated periodic nonlinear dispersive waves [12].

Hydrodynamics and nonlinear optics are the two major areas of physical applications of nonlinear dispersive wave theory. The reason is that both nonlinear and dispersive regimes with small (often negligible) dissipation are relatively easily accessible in both kinds of media. The prominent examples of the wave structures where nonlinearity and dispersion are in balance are solitons – the localised waves that retain their shape, amplitude and velocity during the propagation. Solitons are ubiquitous in water waves: e.g. internal solitons play important role in mixing processes in the ocean and can affect radar signals [13, 14, 15]. Solitons are also one of the main objects of study in nonlinear optics, particularly in optical fibres where they can provide robust information transferred over large distances and have potential applications in optical communication and signal processing systems,[9, 16, 17, 18]. A remarkable analogy between water waves and optical signal propagation in fibres goes beyond the qualitative similarity — in fact the 1D propagation of weakly nonlinear quasi-monochromatic wave packets on deep water and the propagation of powerful light beams along optical fibre in a broad range of propagation regimes are described

by the same equation — the celebrated cubic Nonlinear Schrödinger (NLS) equation derived in the 1960-s by several authors including Zakharov [19] and Benney [20] for water waves and by Talanov [21] and Kelly [22] for optical propagation.

In fibre optics, which is the primary application area of this project, the NLS equation appears in two modifications: defocusing and focusing, depending on the physical properties of the fibre and the wavelength of the propagating light. In the regime of normal dispersion described by the defocusing NLS equation the solitons appear as localised intensity depletions and are called *dark, or gray, solitons*. In the anomalous dispersion propagation regime described by the focusing NLS equation optical solitons appear as localised bright spots, and are called *bright solitons*. Another important difference between the wave propagation in the normal and anomalous dispersion regimes is stability of the continuous or plane wave described by the simplest exponential solution of the NLS equation. The defocusing NLS equation describes the stable propagation regime, while the focusing NLS equation describes the fundamental process of modulational instability characterised by the disintegration of the plane wave into a series of nonlinear wave packets—bright solitons or more complicated localised wave structures called breathers. The focusing NLS equation is of the main concern in this project although some results for the defocusing NLS have also been obtained.

The NLS equation belongs to the family of completely integrable nonlinear PDEs. The IST method developed for the NLS equation (both focusing and defocusing) by Zakharov and Shabat [23, 24] enables the integration of the NLS equation with decaying initial conditions, i.e. it describes the propagation of the initially localised pulses. The IST method is sometimes called the nonlinear Fourier transform due to its conceptual similarity to the famous Fourier method for solving linear PDEs. A more complicated setting of non-decaying initial data with periodic or quasiperiodic boundary conditions is addressed by the application of the so-called *finite-gap theory* [25, 26] – a highly nontrivial extension of the IST method.

Along with decaying at infinity *fundamental solitons* the focusing NLS equation supports a family of solutions called breathers, or solitons on finite background, that exhibit large peak amplitudes and can, under special restrictions, demonstrate the unique property of localisation in both space in time. Such special breather solutions, called *Peregrine Solitons* (PSs) are considered as “analytical prototypes” of *Rogue Waves* (RWs) — the localised large-amplitude fluctuations of the wave field

in modulationally unstable media [27, 28].

RWs were first observed/measured in deep water waves [29] followed by the ground breaking experiments in optical fibres [30] and the subsequent avalanche of theoretical and experimental works that have clearly demonstrated that rogue waves are ubiquitous phenomena, observable in many physical contexts [31]. What makes RWs special is not only their large amplitudes (at least twice the significant wave height) and the remarkable localisation properties but the statistics of their occurrence which has been shown to significantly deviate from the normal (Gaussian) distribution, previously used for the estimates of the wave amplitude distribution in random sea waves. This deviation (exceedance) of the Probability Density Function PDF for the wave amplitude from the Rayleigh distribution implied by the Gaussian statistics [32] is known as the “heavy tail effect” and is the definitive signature of the rogue wave presence in the wave field. The quantitative measure of the “tailedness” of the PDF is the so-called *kurtosis*, the normalised fourth moment of the PDF, denoted κ_4 . The Rayleigh PDF (Gaussian statistics) has $\kappa_4 = 2$. Until recently, the heavy tail effect $\kappa_4 > 2$ has only been observed/studied in numerical simulations and physical experiments [2, 33, 34, 35, 36] with no analytical treatment available.

Summarising, the RW formation as a physical phenomenon has two inherent aspects: dynamical and statistical. As a dynamical object RWs are characterised by certain physical mechanisms responsible for the amplitude growth and spatio-temporal localisation. As a statistical object, RWs are characterised by the deviation of the probability distribution of the random wave field from the one implied by the Gaussian statistics. The deviation from Gaussianity is measured by the value of the kurtosis.

The mathematical property of integrability of the NLS equation and the statistical nature of RWs suggest the unlikely combination of integrability and randomness that has been proposed by V. Zakharov in his paper entitled “Turbulence in integrable systems” [37]. It was proposed that the concepts of classical turbulence theory (such as probability distribution, correlation function, power spectrum etc.) can be applied to physical systems modelled by fully deterministic, integrable equations. Unlike the classical turbulence in viscous hydrodynamics [38] or the weak (wave) turbulence in non-integrable dispersive systems [39] (see also [32]), the integrable turbulence is essentially a 1D phenomenon consisting in the generation of complex, spatio-temporal statistical ensembles of nonlinear dispersive waves, e.g. solitons or breathers. The source of randomness in

integrable turbulence is typically associated with stochastic initial or boundary conditions. There are two contrasting types of initial conditions leading to integrable turbulence that are typically considered in the mathematical modelling of this phenomenon. The first type are the so-called *partially coherent waves*, that can be viewed as an infinite random sequence of smooth large-scale pulses evolving at large times into a complex incoherent ensembles of solitons, breathers and linear dispersive waves [40]. The second type of initial conditions generating integrable turbulence is given by a modulationally unstable plane wave perturbed by small random noise [41]. The numerical simulations showed that the two above contrasting classes of initial conditions generate, at large evolution time, two very different types of integrable turbulence. Namely, the long-time development of the noise-induced integrable turbulence was shown in [41] to be characterised by the Gaussian statistics (no statistically significant rogue waves present, $\kappa_4 = 2$) while the integrable turbulence resulted from the partially coherent wave demonstrated significant heavy tail effect, $\kappa_4 > 2$, at $t \gg 1$, suggesting the presence of rogue waves [40, 42]. Both types of integrable turbulence can be (and have been) realised in fibre optics and water tank experiments [5, 34, 43] but the theoretical explanation of the properties of integrable turbulence and their connection with initial conditions was missing.

As was already mentioned, the hallmark dynamical features of RWs (the large peak amplitudes and the spatio-temporal localisation) are captured by the PS solution of the focusing NLS equation. The physical relevance of PS has been confirmed in the optical fibre [44] and in the water tank [45] experiments, where the PS was created by a careful choice of initial and boundary conditions.

A breakthrough in the understanding of the fundamental nature of PSs as a persistent nonlinear wave structure (not just a particular exotic solution of the NLS equation) has been made possible owing to the rigorous mathematical study by Bertola and Tovbis [46] who showed that the *spontaneous generation* of large-amplitude spikes locally approximated by the PS solution represents a *universal mechanism* of dispersive regularisation of a gradient catastrophe (a phenomenon of the occurrence of infinite derivatives in the wave's profile due to self-focusing). The peak intensity of the PS is 3 times the value of the pulse intensity at the gradient catastrophe point. The asymptotic analysis of Bertola and Tovbis was performed in the framework of the semi-classical, small-dispersion limit of the focusing NLS equation. The universality of the PS generation in

the Bertola-Tovbis scenario is understood in the sense that this regularisation mechanism persists regardless of the particular amplitude shape or *solitonic content* (the IST discrete spectrum) of the initial condition. In particular, the gradient catastrophe regularisation via the PS formation for smooth, rapidly decaying purely solitonic initial conditions has been examined experimentally using the optical fibre platform [4], which revealed the robustness of the mechanism in a broad range of the input parameters, even outside of the applicability of the formal semi-classical NLS setting implied in the Bertola-Tovbis analysis.

One of the main premises of this PhD project, inspired by the Bertola-Tovbis results, is that the semi-classical limit of the focusing NLS equation provides a powerful mathematical framework for the dynamical and statistical analysis of the evolution of partially coherent waves. In particular, this framework can be applied for developing the methods of the prediction and manipulation of the RW formation in the propagation of narrow-band incoherent signals in optical fibres and in deep-water waves.

One of the important applied aspects of the spontaneous PS emergence is the fundamental problem of the nonlinear pulse compression, playing a major role in fibre optics [9, 18]. Indeed the PS formation point represents the point of the maximum compression, where the peak power ($9\times$ the power at the gradient catastrophe point) can achieve very high values so that the integrable, cubic NLS description of the pulse propagation is no longer applicable and one needs to take into account higher order effects such as Raman scattering, higher order dispersion etc. Is the Bertola-Tovbis PS generation scenario still applicable, at least qualitatively, in such highly nonlinear regimes? What peak powers are achievable at the maximum compression point? These pertinent questions were investigated in a satellite study “Pulse compression in extremely nonlinear regimes” within the research contract with LumOptica Ltd. In the Thesis we shall present some general theoretical results obtained in this direction, without referring to the specific propagation regimes and configurations studied in the LumOptica project.

Finally, along with RWs, another fundamental object arising within the integrable turbulence framework is the *soliton gas* — an infinite random ensemble of localised soliton pulses nonlinearly interacting with each other. It turns out that the collective, macroscopic dynamics of a soliton gas can be described using the IST mathematical tools. The central idea in this theory is the modi-

fication of the average velocity of a “trial” or “test” soliton in a gas due to the accumulation of the phase-shifts occurring in the pairwise interactions with other solitons in the gas. The resulting *spectral kinetic equation* for soliton gas describes the evolution of the distribution function of solitons with respect to their IST spectral values and the position of their centres. Such kinetic equation was originally proposed by Zakharov in 1971 for the rarefied gas of KdV solitons [47] and later generalised to the case of dense soliton gases for the KdV and focusing NLS equations in [48, 49]. Soliton gas has been recently observed in the ocean [50] but also has been generated in laboratory experiments [51, 52]. The concept of soliton gas has been recently extended to a more general case of *breather gas* in [53]. The breather gas can be viewed as *rogue wave integrable turbulence* whose properties need detailed study.

The PhD project includes three main themes under the general umbrella of integrable turbulence and rogue waves in optical fibres and hydrodynamics

1. **Dynamical and statistical aspects of rogue waves in optical fibres and hydrodynamics using the semi-classical focusing NLS framework.**
2. **Theory of soliton and breather gases.**
3. **Optical pulse compression in highly nonlinear propagation regimes.**

The structure of the Thesis is as follows.

In **Chapter 1** an overview of the mathematical and physical background of the project is provided. This includes some important aspects of the theory of the focusing NLS equation, starting from the physical contexts of nonlinear optics and hydrodynamics and proceeding to the integrability properties (inverse scattering transform and finite gap theory). The main ideas of the rogue wave theory are introduced within the framework of the focusing NLS equation, including both dynamical and statistical aspects of this phenomenon. In particular, the semi-classical theory of Bertola and Tovbis on the regularisation of the focusing gradient catastrophes by the generation of Peregrine solitons is reviewed. The Chapter is concluded with the brief exposition of the soliton and breather gas theory and the numerical methods of the integration of the NLS equation along with the methods of numerical nonlinear spectral analysis of rogue waves.

Chapter 2 is devoted to the analytical study of an early stage of the development of integrable turbulence from partially coherent initial conditions. The focus is on the short-time asymptotic evaluation of the kurtosis evolution in the semi-classical NLS equation, both focusing and defocusing. The material of this Chapter is based on the paper: G. Roberti (lead author), G. El, S. Randoux and P. Suret. “Early stage of integrable turbulence in the one-dimensional nonlinear Schrödinger equation: A semiclassical approach to statistics”, *Phys. Rev. E*, 100:032212, 2019.

Chapter 3 is concerned with the development of the method for the prediction and manipulation of rogue waves in physical systems ruled by the focusing NLS equation. The proposed method, termed *nonlinear spectral engineering*, employs the results of the semi-classical Bertola-Tovbis theory, which is adapted to enable the comparison with experimental data. The Chapter material is based on the joint paper: A. Tikan, F. Bonnefoy, G. Roberti, G. El, A. Tovbis, G. Ducrozet, A. Cazaubiel, G. Prabhudesai, G. Michel, F. Copie, E. Falcon, S. Randoux, P. Suret, “Prediction and manipulation of hydrodynamic rogue waves via nonlinear spectral engineering”, arXiv:2108.02698 (2021) (submitted to a peer reviewed journal) and includes analytical, numerical and experimental results. The experiment confirming the efficacy of the developed method was performed in a 150m water tank facility in École Centrale de Nantes, France. The originally planned follow up fibre optics experiments on the rogue wave control and manipulation were interrupted by the Covid-19 pandemic but will resume in 2021/22.

Chapter 4 develops the theory of integrable turbulence in bidirectional soliton gases described by the defocusing and resonant NLS equations, and is based on the results of the joint paper: T. Congy, G. El and G. Roberti “Soliton gas in bidirectional dispersive hydrodynamics”, *Phys. Rev. E*, 103:042201, 2021. The main areas of application of the Chapter’s results are nonlinear fibre optics (normal dispersion propagation regime) and shallow-water waves.

Chapter 5 is concerned with the numerical realisation of breather gases and the verification of the spectral kinetic theory developed in the recent paper [53] by El and Tovbis. This research has required the development of the nontrivial numerical method of the breather gas synthesis based on nonlinear spectral theory and involving high precision arithmetics. The material of the Chapter is based on the paper: G. Roberti (lead author), G. El, A. Tovbis, F. Copie, P. Suret and S. Randoux

“Numerical spectral synthesis of breather gas for the focusing nonlinear Schrödinger equation”,
Phys. Rev. E, 103:042205, 2021

Chapter 6 contains the theoretical results of the satellite research project “Pulse compression in extremely nonlinear regimes”, where the influence of higher order effects (the intrapulse Raman scattering and the third order dispersion) on the rogue wave formation in the propagation of high intensity broad optical pulses through a fibre was studied using a combination of analytical and numerical methods. The project has been completed under the Research Contract with LumOptica Ltd.

Chapter 7 presents Conclusions and the future directions of research inspired by the PhD project.

Publications and Conference presentations

The results of the project have been published in 4 research papers and reported at the UK-France PhD Scheme Conference and at UK and international conferences on Applied Mathematics.

Publications in Peer Reviewed Journals

- **G. Roberti**, G. El, A. Tovbis, F. Copie, P. Suret and S. Randoux “Numerical spectral synthesis of breather gas for the focusing nonlinear Schrödinger equation”, *Phys. Rev. E*, 103:042205, 2021
- T. Congy, G. El and **G. Roberti** “Soliton gas in bidirectional dispersive hydrodynamics”, *Phys. Rev. E*, 103:042201, 2021
- **G. Roberti**, G. El, S. Randoux and P. Suret. “Early stage of integrable turbulence in the one-dimensional nonlinear Schrödinger equation: A semiclassical approach to statistics”, *Phys. Rev. E*, 100:032212, 2019

Pre-prints

- A. Tikan, F. Bonnefoy, **G. Roberti**, G. El, A. Tovbis, G. Ducrozet, A. Cazaubiel, G. Prabhudesai, G. Michel, F. Copie, E. Falcon, S. Randoux, P. Suret, “Prediction and manipulation of hydrodynamic rogue waves via nonlinear spectral engineering”, arXiv:2108.02698 (2021), submitted for publication in a peer reviewed journal

Conference presentations

- **4th IMA on Nonlinearity and Coherent Structures:** *Nonlinear spectral synthesis of breather gas in focusing NLS equation: a numerical approach*, Contributed Talk, Loughborough, UK – Online, July 2021
- **HYDW08 : New horizons in dispersive hydrodynamics:** *Numerical spectral synthesis of breather gas for the focusing nonlinear Schrödinger equation*, Poster, Cambridge, UK – Online, June 2021
- **Nonlinear Fourier Transform Workshop:** *Nonlinear spectral synthesis of breather gas in focusing NLS equation: a numerical approach*, Talk, Delft, NE, February 2020

- **17th European Turbulence Conference, ETC 2019:** *Initial stage of the development of integrable turbulence in 1D NLS dispersive hydrodynamics*, Talk, Torino, IT, September 2019
- **3rd IMA on Nonlinearity and Coherent Structures:** *Initial stage of the development of integrable turbulence in 1D NLS dispersive hydrodynamic*, Contributed Talk, Newcastle upon Tyne, UK, July 2019
- **7th UK-France PhD Scheme Conference:** *Analysis and control of large-amplitude fluctuations of incoherent optical field in fibre lasers: integrable turbulence framework*, Poster and talk, Portsmouth, UK, June 2019
- **British Applied Mathematics Colloquium:** *Initial stage of the development of integrable turbulence in 1D NLS dispersive hydrodynamic*, Contributed Talk, Bath, UK, April 2019
- **11th: IMACS on Nonlinear Evolution Equations and Wave Phenomena** *Initial stage of the development of integrable turbulence in 1D NLS dispersive hydrodynamic*, Contributed Talk, Athens, GA, US, April 2019
- **Dynamics Days Europe 2018:** *Initial stage of the development of integrable turbulence in 1D NLS dispersive hydrodynamic*, Contributed Talk, Loughborough, UK, September 2018
- **6th UK-France PhD Scheme Conference:** *Analysis and control of large-amplitude fluctuations of incoherent optical field in fibre lasers: integrable turbulence framework*, Poster, Paris, Fr, July 2018
- **Workshop on Advances in the Theory of Nonlinear Waves:** *Phase shifts in dynamic soliton tunnelling: focusing NLS framework*, Poster and Talk, Newcastle, UK, May 2018

Chapter 1

Mathematical and Physical Background

1.1 Propagation of light in optical fibres and Nonlinear Schrödinger equation

An optical fibre is a thin rod of high-quality glass that relies on the total internal reflection phenomenon for the transmission of light signals with little losses. To achieve the internal total reflection, the fibre is built with an external cladding layer, with a slightly lower refractive index than the core. The refractive index and dimension of the core are the physical characteristics that determine the set of electromagnetic fields, *modes*, which can propagate in the fibre. If the core is sufficiently small, the fibre will support the propagation of a single mode. The fibres designed to meet this constrain are called *single-mode fibres*. In the following sections, we will discuss the main physical effects and parameters of the optical fibres of interest. We will also introduce the mathematical model describing the signal propagation in the fibre.

For the derivation reported in this Section we mainly refer to the classic books on nonlinear optics by Agrawal [9] and on nonlinear dispersive waves by Ablowitz [54]

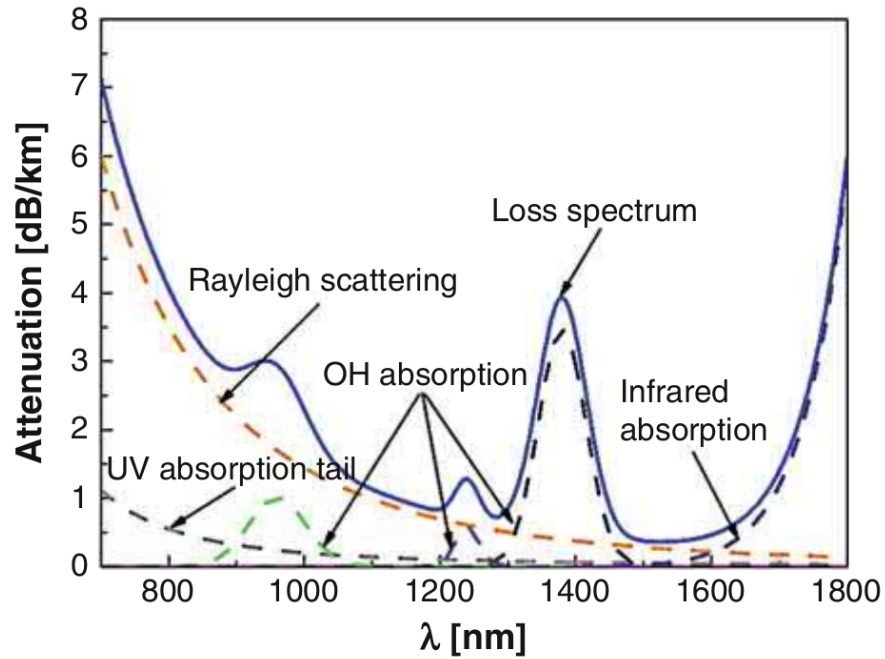


Figure 1: Attenuation spectrum in a silica optical fibre at infrared band (cited from [1]).

1.1.1 Losses

Even if the fibre is designed to maximise the transmission of the light, the interaction with the medium leads to a power loss in the signal. Given a signal of initial power P_0 injected in a fibre, the power P_T at distance z along the fibre is:

$$P_T = P_0 e^{-\alpha(\lambda)z}, \quad (1.1)$$

where the attenuation constant, $\alpha(\lambda)$, depends on the wavelength of the transmitted light signal. The fibre losses can be ascribed to different mechanisms such as material absorption, scattering and geometrical effect. The main contributing factor to the attenuation of the signal changes in relation to its wavelength, as illustrated in Fig. 1. In the short wavelength regime, the Rayleigh scattering is the main contributing mechanism. The microscopic density fluctuations formed in the silica during the manufacturing process induce local variations of the refractive index of the fibre. Given the difference of scales between the defects and the wavelength of interest, the resulting scattering can be identified as Rayleigh scattering. The magnitude of this effect is proportional to λ^{-4} , hence its role as contributing factor in the fibre losses reduces as the wavelength of the

signal increases. On the contrary, the major contributing effects to the attenuation in the far-infrared regime ($\lambda > 2\mu\text{m}$) are the vibrational resonances of the silica that induce the so-called infrared absorption peak. Besides the natural absorption of the silica, the few impurities in the material have a strong effect on the transmission attenuation of the optical fibre. In glass fibre, the OH ions created during the manufacturing process are one of the main sources of absorption. In particular, they are responsible for the dominant absorption peak located about $1.4\mu\text{m}$. However, in modern communication silica fibres, the losses exhibit a minimum in a window of 5THz around $\lambda_0 = 1.55\mu\text{m}$. In this range of frequency, the attenuation constant is considered independent from the wavelength with a value $\alpha \approx 2 \times 10^{-5}\text{cm}^{-1}$.

1.1.2 Chromatic Dispersion

One of the main effects influencing the propagation of the light in the optical fibre is the so-called *chromatic dispersion* that arises from the dependency of the medium refractive index $n(\omega)$ on the optical frequency ω . Consequently, the different spectral components associated with an optical pulse travel at different speeds $\frac{c}{n(\omega)}$, where c is the speed of light. This dependency extends to the wavenumber $\beta(\omega)$ and in the limit of a quasi-monochromatic wave it can be expanded as the Taylor series in ω about the centre of the spectrum ω_0 :

$$\beta(\omega) = n(\omega)\frac{\omega}{c} = \beta_0 + \beta_1(\omega - \omega_0) + \frac{1}{2}\beta_2(\omega - \omega_0)^2 + \dots \quad (1.2)$$

where

$$\beta_m = \left(\frac{d^m \beta}{d\omega^m} \right)_{\omega=\omega_0}. \quad (1.3)$$

In particular, $\beta_1 = \frac{1}{v_g}$ is related to the group velocity v_g at which the envelope of the signal moves. β_1 can be eliminated by choosing the frame of reference co-moving with the pulse. The broadening of the pulse is governed by the parameter β_2 , the so-called group-velocity dispersion. In fused silica, β_2 varies with the wavelength $\lambda = \frac{2\pi c}{\omega_0}$ and vanishes at the zero-dispersion wavelength $\lambda_D = 1.27\mu\text{m}$. Moreover, this value discriminates two different regimes of dispersion, the so-called normal dispersion (or defocusing) regime if $\beta_2 > 0$ and the anomalous dispersion (or focusing) regime if $\beta_2 < 0$. While the coefficient β_2 can vanish at $\lambda = \lambda_D$, the dispersion in the system does not disappear and the cubic term in the expansion (1.2) is required. This higher-

order dispersive term, characterised by β_3 , commonly called the *Third-Order-Dispersion* (TOD) parameter, plays an important role in the distortion of ultrashort optical pulses in both linear and nonlinear regimes.

1.1.3 Nonlinear effects

Optical fibres, as any dielectric material, exhibit a nonlinear response to intense electromagnetic fields. The displacement of bound electrons results in a non-linear dependency of the induced polarisation vector \mathbf{P} from the electric field \mathbf{E} . In particular the dependence of the polarisation vector on the electrical field is given by the expression:

$$\mathbf{P} = \varepsilon_0 \left(\chi^{(1)} \cdot \mathbf{E} + \chi^{(2)} : \mathbf{E}\mathbf{E} + \chi^{(3)} \vdots \mathbf{E}\mathbf{E}\mathbf{E} + \dots \right), \quad (1.4)$$

where ε_0 is the vacuum permittivity, $\chi^{(i)}$ is the i -th order susceptibility tensor of rank $j + 1$, and the symbols $:$ and \vdots denote the rank 2 and 3 tensor products. Due to the symmetry of the silica molecule (SiO_2), $\chi^{(2)}$ vanishes in silica glass optical fibres, and the lowest-order nonlinear effect can be ascribed to the third-order susceptibility. Even if $\chi^{(3)}$ is responsible for different nonlinear processes such as the third-harmonic generation and the four-wave mixing, these phenomena are negligible in optical fibres where most of the nonlinear effects arise from nonlinear refraction. In its simplest form, the dependency of the refractive index n on the light intensity $|\mathbf{E}|^2$, the so called *Kerr nonlinearity*, can be expressed as

$$n = n_0(\omega) + n_2 |\mathbf{E}|^2, \quad (1.5)$$

where n_2 , also called the nonlinear refractive index, can be expressed in term of $\chi^{(3)}$. Assuming that the electric field is linearly polarised in the x -direction, the only component of the fourth-rank tensor that contributes to n_2 is $\chi_{xxxx}^{(3)}$ such that

$$n_2 = \frac{3}{8n} \text{Re} \left(\chi_{xxxx}^{(3)} \right). \quad (1.6)$$

Moreover, under the same assumption on the optical field, it is possible to relate the real and imaginary parts of $\chi_{xx}^{(1)}$, component of the first order susceptibility tensor $\chi^{(1)}$, to the linear refractive

index $n_0(\omega)$ and to the attenuation coefficient α .

1.1.4 Nonlinear Schrödinger Equation

The first step in the study of the nonlinear phenomena in optical fibres is the introduction of an effective mathematical model to describe the light propagation in the medium embedding the physical effects described previously. Such a model is the well established Nonlinear Schrödinger (NLS) equation.

The first step in the derivation is, starting from Maxwell's equations, to write the wave equation that involves the electric field \mathbf{E} and polarisation vector \mathbf{P} :

$$\nabla \times \nabla \times \mathbf{E} = -\frac{1}{c^2} \frac{\partial^2 \mathbf{E}}{\partial t^2} - \mu_0 \frac{\partial^2 \mathbf{P}}{\partial t^2}, \quad (1.7)$$

where c is the speed of light in vacuum. Subsequently, with the introduction of a series of assumptions and approximations based on the physical characteristics of the fibre and the signal, it is possible to simplify the model and obtain the NLS equation. Considering the symmetry of the system and of the SiO_2 molecular structure, it is possible to reduce Eq. (1.7) to a scalar form. The scalar approach is valid only if the electric field maintains its direction of polarisation during the propagation; even if this is not strictly the case, this approximation holds well in practice. Moreover, since the nonlinear effect is relatively weak in silica fibre, it is possible to consider the nonlinear part of the polarisation vector \mathbf{P} as a small perturbation of the linear problem. Another key assumption is the quasi-monochromatic nature of the optical field. The spectrum of the signal, centred at ω_0 , is assumed to be narrow, with spectral width $\Delta\omega \ll \omega_0$. Using the approximations described here, the form of the electric field can be simplified in the following form:

$$\mathbf{E}(\mathbf{r}, t) = \frac{1}{2} \hat{x} \{ F(x, y) A(z, t) \exp [i(\beta_0 z - \omega_0 t)] + \text{c.c.} \}, \quad (1.8)$$

where \hat{x} is the polarisation unit vector, $A(z, t)$ is the slowly varying pulse envelope, and $F(x, y)$ is the transverse modal distribution, often approximated by a Gaussian shape. Substituting (1.8) in Eq. (1.7), it is then possible to derive the evolution of the slowly varying envelope of the electric

field $A(t, z)$ interacting with the fibre

$$i \frac{\partial A}{\partial z} = -i \frac{\alpha}{2} A + \frac{\beta_2}{2} \frac{\partial^2 A}{\partial t^2} - \gamma |A|^2 A, \quad (1.9)$$

where t identifies the time in the frame of reference moving at the group velocity $v_g = 1/\beta_1$ and z represents the distance of propagation along the fibre. This equation includes, as required, the dissipation of the fibre through the attenuation constant α , the dispersion characterised by β_2 , and the nonlinearity characterised by

$$\gamma = \frac{n_2 \omega_0}{c A_{\text{eff}}}, \quad (1.10)$$

where A_{eff} is the effective core area

$$A_{\text{eff}} = \frac{\left(\int_{-\infty}^{\infty} |F(x, y)|^2 dx dy \right)^2}{\int_{-\infty}^{\infty} |F(x, y)|^4 dx dy}, \quad (1.11)$$

measuring the area over which the energy in the electric field is distributed.

Even if Eq. (1.9) is often referred to as NLS equation, this terminology usually identifies the equation in the form without the fibre losses term in mathematics

$$i \frac{\partial A}{\partial z} = + \frac{\beta_2}{2} \frac{\partial^2 A}{\partial t^2} - \gamma |A|^2 A. \quad (1.12)$$

The NLS equation can be generalised by introducing higher order dispersive and nonlinear terms as well as a term describing stimulated scattering. These effects derive from the relaxation of some the assumptions and approximations involved in the derivation of the NLS equation.

1.1.5 Normalisation

It is standard to rescale Eq. (1.12) with the introduction of non-dimensional coordinates $T = t/T_0$, $Z = z/Z_0$ and field $u = A/\sqrt{P_0}$. There exists two main normalisations widely used:

- introducing P_0 as the power scale of the system, we define $T_0 = \sqrt{\frac{|\beta_2|}{\gamma P_0}}$ and $Z_0 = \frac{1}{\gamma P_0}$ to derive the following normalised NLS equation:

$$i \frac{\partial u}{\partial Z} + \frac{1}{2} \frac{\partial^2 u}{\partial T^2} + \sigma |u|^2 u = 0, \quad (1.13)$$

where $\sigma = \text{sgn}(\gamma\beta_2)$.

- introducing P_0 as the power scale of the system, we define $T_0 = \sqrt{\frac{|\beta_2|}{\gamma P_0}}$ and $Z_0 = \frac{2}{\gamma P_0}$ to derive the following normalised NLS equation:

$$i\frac{\partial u}{\partial Z} + \frac{\partial^2 u}{\partial T^2} + 2\sigma|u|^2u = 0, \quad (1.14)$$

where $\sigma = \text{sgn}(\gamma\beta_2)$.

Since the nature of the system is defined by the relative sign of dispersive and nonlinear term, it is standard to shift its characterisation to the nonlinear term with the introduction of the parameter σ . In the normalised equations (1.13) and (1.14), $\sigma = +1$ corresponds to the focusing (anomalous dispersion) regime and $\sigma = -1$ to the defocusing (normal dispersion) regime.

1.1.6 Hydrodynamics

The NLS equation is a universal model that arises in many physical systems: plasma physics, condense matter [55], nonlinear optics [9] and water waves [56] are some of the best known examples. It generally describes the dynamics of quasi-monochromatic, weakly nonlinear waves subject to second order dispersion and cubic nonlinear interaction. In this work the NLS equation is used in two contexts: (i) the description of nonlinear optical systems, particularly in optical fibres; (ii) the propagation of unidirectional small-amplitude gravity waves in the deep-water regime, particularly in 1-D water tank experiments. Besides the description of systems in controlled environment, this model and its two-dimensional generalisation are used to describe open ocean phenomena, such as wave packets generated by localised storm and quasi-monochromatic wavetrains generated by steady wind.

In the context of surface waves, the focusing Nonlinear Schrödinger Equation fNLSE can be de-

rived from the Euler-Bernoulli equations in the deep water and small-amplitude wave limit:

$$\phi_{xx} + \phi_{zz} = 0, \quad -\infty < z < \varepsilon\eta, \quad (1.15a)$$

$$\phi_z = 0, \quad z \rightarrow -\infty, \quad (1.15b)$$

$$\phi_t + \frac{\varepsilon}{2} (\phi_x^2 + \phi_z^2) + g\eta = 0, \quad z = \varepsilon\eta, \quad (1.15c)$$

$$\eta_t + \varepsilon\eta_x\phi_x = \phi_z, \quad z = \varepsilon\eta, \quad (1.15d)$$

where $\phi(t, x, z)$ is the velocity potential of the fluid, $\eta(x, t)$ is the height of the fluid free surface above the mean level $z = 0$, g is the gravitational constant of acceleration, and $\varepsilon \ll 1$ is the small parameter encoding the small amplitude assumption. This system of equations expresses, respectively, the ideal nature of the fluid (1.15a), the absence of flow through the bottom of the system (1.15b), Bernoulli energy conservation (1.15c), and the absence of flow transverse to the free surface (1.15d). Given the assumption of small amplitude waves, it is possible to rewrite the free-surface equations (1.15c) and (1.15d), expanding around $z = 0$ the velocity potential ϕ and its derivatives ϕ_t , ϕ_x and ϕ_z . Moreover, the wave envelope is expected to slowly vary in space and time and thus one introduces slow temporal and spatial scales $T = \varepsilon t$, $X = \varepsilon x$ and $Z = \varepsilon z$. Lastly, the presence of quadratic nonlinearity in the Euler-Bernoulli equations suggests to consider second harmonics and mean terms generation resulting in the following ansatz (Stokes' wave):

$$\begin{aligned} \phi &= (A_1 e^{i\theta + kk} + \text{c.c.}) + \varepsilon (A_2 e^{2i\theta + 2|k|z} + \text{c.c.} + \bar{\phi}), \\ \eta &= (B_1 e^{i\theta} + \text{c.c.}) + \varepsilon (B_2 e^{2i\theta} + \text{c.c.} + \bar{\eta}), \end{aligned} \quad (1.16)$$

where the complex coefficients A_1 , A_2 , B_1 , B_2 and the real coefficient $\bar{\phi}$, $\bar{\eta}$ depend on the slow scales X, Z, T . While the envelope depends on slow variables, the carrier wave depends on the rapid phase by $\theta = kx - \omega t$, where the dispersion relation is $\omega^2 = g|k|$ in the deep water regime. Following these approximations, it is possible to obtain an equation for A_1 by substituting the ansatz (1.16) in the Euler-Bernoulli system and by setting to zero the terms proportional to each power of ε . As result, one obtain at $\mathcal{O}(\varepsilon^2)$ the equation:

$$2i\omega A_\tau - \left(\frac{v_g^2}{2\omega} A_{\xi\xi} + \frac{2k^4}{\omega} |A|^2 A \right) = 0, \quad (1.17)$$

where $v_g = \frac{g}{2\omega}$ is the group velocity, $A = A_1$, $\tau = \varepsilon T$ and $\xi = X - v_g T$. In this approximation,

B_1 is proportional to A . Eq. (1.17) is the standard formulation of the fNLSE for water waves in the deep water limit. Differently from the nonlinear optic formulation (1.12), space is now the dispersive variable and time the evolution one. Nevertheless, it is possible to normalise Eq. (1.17) to obtain the forms Eq. (1.13) or (1.14).

1.1.7 Nonlinear Schrödinger Equation: exact solutions

In the previous sections, it has been shown how the NLS equation can be derived in different physical systems and admits different normalisations. For the purpose of this work, we will consider the fNLSE normalised in the form:

$$i \frac{\partial u}{\partial t} + \frac{\partial^2 u}{\partial x^2} + 2|u|^2 u = 0. \quad (1.18)$$

In this section, the main features of the fNLSE are discussed.

The fNLSE admits different families of exact solutions, the simplest being the plane wave solution, sometimes called *the condensate*, that reads:

$$u(x, t) = u_0 e^{2iu_0^2 t}, \quad (1.19)$$

where u_0 is a constant amplitude. In the focusing regime, as it will be discussed in Section 1.2, the plane wave solution is unstable with respect to long wave perturbations which initially grow exponentially with time and eventually lead to the formation of large amplitude nonlinear coherent structures.

Furthermore, together with a widespread class of nonlinear dispersive systems, the fNLSE supports a family of solitary wave solutions, called solitons in integrable systems, see Section 1.4. The balance between nonlinear and dispersive effects leads to the existence of a self-reinforcing solution that maintains its shape while it propagates at constant velocity. Moreover, the interaction between solitons is elastic, such that speed and amplitude profile remain unaltered upon the collision, while the position and phase experience well-defined shifts. The bright soliton solution

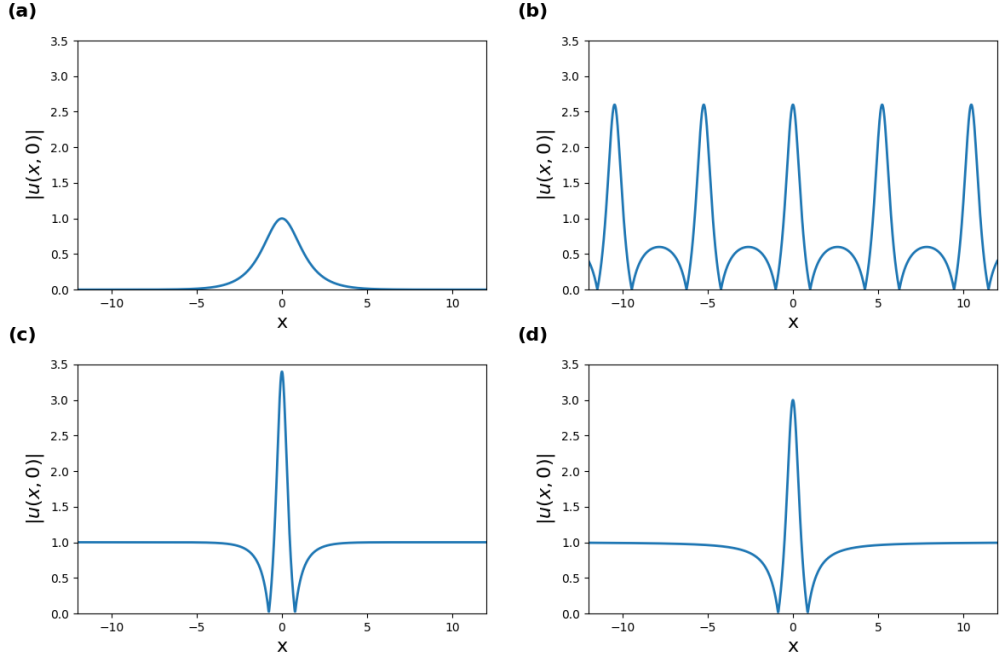


Figure 2: Examples of exact solution of the fNLSE evaluated at $t = 0$: (a) the fundamental soliton, (b) the Akhmediev breather, (c) the Kuznetsov-Ma breather and (d) the Peregrine soliton.

of the fNLSE (1.14), see Fig. 2(a), has the form:

$$u(x, t) = 2\eta \operatorname{sech} [2\eta (x + 4\xi t - x_0)] \exp [-2i\xi x - 4i (\xi^2 - \eta^2) t + i\phi_0]. \quad (1.20)$$

The structure is centred at $x_c = x_0 - 4\xi t$ with amplitude 2η and velocity -4ξ , while the parameter x_0 and ϕ_0 are the initial position and the phase of the pulse, respectively. Solitons belong to a class of localised solutions with vanishing boundary conditions at infinity, but exact solutions of the fNLSE with non-vanishing boundary conditions are also known. Breathers or Solitons on Finite Background (SFBs) represent a rich class of solutions of the fNLSE. The Peregrine soliton PS [27], Kuznetsov-Ma (KM) breather [57, 58] and Akhmediev breather (AB) [59] are well-known members of this class, and are particular cases of the generic Tajiri-Watanabe (TW) breather [60]:

$$u(x, t) = \frac{\cos(\mu) \cos(2\gamma(x - \nu t) + 2i\Psi) - \cosh(\Psi) \cosh(2\Gamma(x - V_{br}t) + 2i\mu)}{\cos(\mu) \cos(2\gamma(x - \nu t)) - \cosh(\Psi) \cosh(2\Gamma(x - V_{br}t))} e^{2it}, \quad (1.21)$$

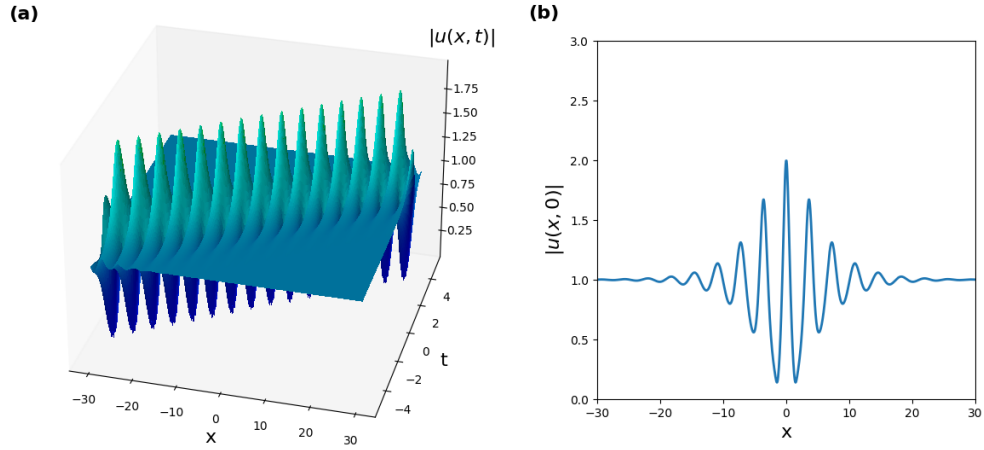


Figure 3: Examples of Tajiri-Watanabe breather solution of the fNLSE with $\lambda = 0.2 + 0.5i$: (a) spatio-temporal evolution of wave field amplitude $|u(x, t)|$ and (b) amplitude profile of the solution at $t = 0$.

where

$$\begin{aligned} \Gamma &= -\sinh(\Psi) \cos(\mu), & \gamma &= \cosh(\Psi) \sin(\mu), \\ V_{\text{br}} &= \frac{\cosh(2\Psi) \sin(2\mu)}{\Gamma}, & \nu &= \frac{\sinh(2\Psi) \cos(2\mu)}{\gamma}, \end{aligned} \quad (1.22)$$

with V_{br} and ν being respectively the group and the phase velocity of the wave packet. Without loss of generality, the background amplitude has been assumed here to be unitary ($|u(|x| \rightarrow \infty)| = 1$). An example of the TW solution of the fNLSE is illustrated in Fig. 3. The two real parameters μ and Ψ that characterise the breather structure can be recast to a single complex one $\lambda = i \cos(\mu + i\Psi)$. In particular, the amplitude u_{br} and group velocity V_{br} of the breather are given by:

$$V_{\text{br}} = -4\text{Im}(\lambda) \frac{1 + \coth^2 \Psi}{2}, \quad u_{\text{br}} = 2 \cosh(\Phi) \cos(\mu) = 2\text{Re}(\lambda). \quad (1.23)$$

The variation of the field u is constrained within the interval

$$|u_{\text{br}} - u_0| \leq |u| \leq |u_{\text{br}} + u_0|, \quad (1.24)$$

with $u_0 = 1$, the amplitude of the background. Away from the centre of the breather, the solution (1.21) reads as the plane wave background ($u(x, t) \rightarrow e^{2it}$ for $x \rightarrow \pm\infty$). The TW (1.21) breather is characterised by two oscillatory behaviours with a spacial period T_x and a temporal period T_t :

$$T_x = \frac{\pi}{\gamma}, \quad T_t = \frac{\pi}{\nu\gamma}. \quad (1.25)$$

The shape of the solution (1.21) strongly depends on the parameter λ , ranging from a pulsing disturbance to a propagating perturbation. The following is dedicated to well-known cases of TW breather with purely imaginary parameter λ . Considering the parameter in the form

$$\lambda = i \cos(\mu + i\Psi) = \sinh(\Psi) \sin(\mu) + i \cosh(\Psi) \cos(\mu), \quad (1.26)$$

the particular case $\text{Re}(\lambda) = \sinh(\Psi) \sin(\mu) = 0$ can be realised in three possible ways: $\mu = 0$, $\Psi = 0$, or $\mu = \Psi = 0$. In the first case, where $\mu \rightarrow 0$ ($\sin(\mu) = 0$), and subsequently $\text{Im}(\lambda) = \cosh(\Psi) > 1$, the solution (1.21) takes the form of the time-periodic Kuznetsov-Ma breather:

$$u_{\text{KM}}(x, t) = \frac{\cos(\omega_{\text{KM}}t - 2i\Psi) - \cosh \Psi \cosh(2\Gamma x)}{\cos(\omega_{\text{KM}}t) - \cosh \Psi \cosh(2\Gamma x)} e^{2it}, \quad (1.27)$$

where $\omega_{\text{KM}} = \frac{2\pi}{T_t}$ is the time frequency, see Fig. 2(c). Moreover, this particular solution is localised in space ($T_L \rightarrow \infty$) and does not propagate ($V_{\text{br}} = 0$). In the second case, when $\Psi \rightarrow 0$ ($\sinh(\Psi) = 0$), and subsequently $0 < \text{Im}(\lambda) = \cos(\mu) < 1$ the solution (1.21) takes the form of the space-periodic Akhmediev breather:

$$u_{\text{AB}}(x, t) = \frac{\cos(\mu) \cos(2\gamma x) - \cosh(\sigma t - 2i\mu)}{\cos(\mu) \cos(2\gamma x) - \cosh(\sigma t)} e^{2it}, \quad (1.28)$$

where $\sigma = 2 \sin(2\mu)$. The AB solution of the fNLSE is a space periodic structure with period T_x but is localised in time, see Fig. 2(b). In the last scenario, where both parameters μ and Ψ vanish and $\text{Im}(\lambda) \rightarrow 1$, the breather solution tends to the PS:

$$u_{\text{PR}}(x, t) = \left[1 - \frac{4 + 16it}{1 + 4x^2 + 16t^2} \right] e^{2it}. \quad (1.29)$$

This rational solution of the fNLSE is localised both in space and time, and, at the point of maximum compression during the evolution, the peak amplitude reaches three times the level of the continuous background, see Fig. 2(d). For this reason, it is often listed as the prototype of rogue waves, as we will discuss in section 1.3. Moreover, the fNLSE admits hierarchies of higher-order breather solutions that can be obtained using the Darboux transform technique [61]. These so-

lutions can be interpreted as nonlinear superposition of first-order breathers and can exhibit even higher maximum amplitude.

These special families of solutions of the fNLSE play a crucial role in the nonlinear dynamics of different physical phenomena. In the next section, some of these mechanisms are investigated in more detail.

1.2 Modulational instability

In many nonlinear systems, the interplay between dispersion and nonlinearity can lead to the instability of the steady state solutions: this phenomenon is known as Modulational Instability (MI) or Benjamin-Feir Instability. First reported by Benjamin and Feir in 1967 [43, 62] in the context of deep-water gravity waves, it is now known to be a ubiquitous mechanism associated to the “focusing nature” of certain nonlinear dynamics. MI has now been observed in different physical systems [63] including nonlinear optics [9], plasma waves [64], and matter waves [65]. The dynamics of MI can be roughly divided in two regimes: a linear and a nonlinear stage. While the linear (early) stage of the evolution is characterised by the exponential growth of small amplitude, long wave, perturbations, the nonlinear stage (long-time) dynamics leads to the formation of coherent structures of finite amplitude. The nonlinear evolution of the MI strongly depends on the nature of the initial perturbation.

To understand the early stage of the MI dynamics, standard tools of linear stability analysis can be employed. As was mentioned in the previous section, the plane wave solution (1.19) of the fNLSE is unstable with respect to long-wave perturbations. Considering the plane wave solution ($u(x, t) = e^{2it}$) perturbed by a harmonic wave of small amplitude ε ,

$$u(x, t) = e^{2it} + \varepsilon e^{i(kx + \Omega t)}, \quad \text{with } |\varepsilon| \ll 1, \quad (1.30)$$

and linearising (1.18) with respect to ε , one obtains the linear dispersion relation:

$$\Omega^2 = k^4 - 4k^2. \quad (1.31)$$

Thus, when $|k| < k_c = 2$, the system becomes unstable: $\Omega^2 < 0$ leads to the growth of the

perturbation in time. The growth rate of the perturbation is given as a function of its wavenumber

$$g(k) = |k| \sqrt{k_c^2 - k^2}, \quad (1.32)$$

which has a maximum at $k_{\max} = \pm\sqrt{2}$, see Fig. 4(a). Thus, in the more general case of non-harmonic excitation, the Fourier components of the perturbation with a wavenumber falling within the range $|k| < k_c$ experience an exponential growth at the early stage of the evolution. This classical (linear) mechanism, describing the early destabilisation of the condensate solution ($u = 1$) is not suitable for the description of the long-time, asymptotic stage of MI where the small amplitude assumption is no longer valid.

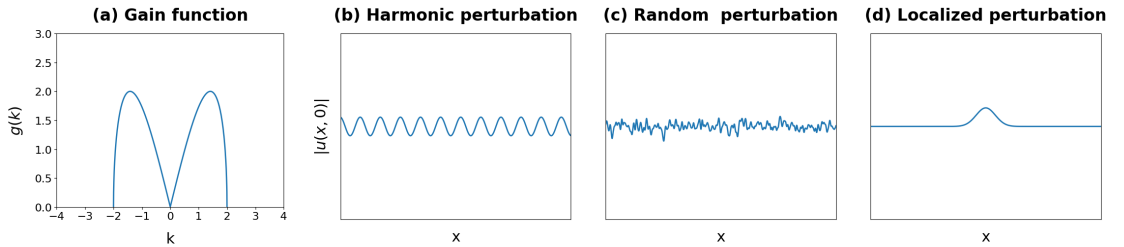


Figure 4: (a) MI gain curve $g(k)$ calculated from the linear stability analysis of (1.18). (b-d) Schematics of three initial conditions leading to the development of MI of the condensate: (b) harmonic perturbation, (c) random noise perturbation and (d) localised perturbation.

Three different scenarios arise in the nonlinear stage of MI depending on the nature of the initial perturbation, see Fig. 4(b-d).

(i) In the first scenario, the perturbation is a simple harmonic wave. After the initial linear stage of exponential growth, the dynamics is characterised by the periodic formation of AB-like structures. These structures have been observed numerically and recently described analytically [66].

(ii) Away from refined experimental controlled conditions, the perturbation of the plane wave is generally described by a small-amplitude random process leading to the concept of the noise induced MI. The stochastic nature of the initial perturbation leads to the emergence of a more complex wave field dynamics than observed in the harmonically perturbed condensate. Its description requires the introduction of a statistical approach that falls in the framework of integrable turbulence, see Section 1.5. Recently, the development of single-shot experimental techniques in fibre lasers has made possible the observation of the stochastic nature of the noise-induced MI.

Moreover, with the development of time-lens and recirculating fibre-loop system, the real-time experimental investigation of the noise-induced MI has been reported [5].

(iii) In the third scenario, the perturbation is considered to be a localised distribution. It has been shown recently that the resulting dynamic depends on the “soliton content” of the perturbation [67]. This characterisation of the perturbation can be obtained by means of the IST, a nonlinear analogue of the Fourier transform. A more detailed discussion of the IST and the connection between the IST spectrum and the physical wave field $u(x, t)$ is presented in Section 1.4. In the case where the perturbation has no soliton content (i.e. no discrete IST spectrum, see Section 1.4), the nonlinear dynamics of MI is characterised by the formation of a universal (i.e. independent from the shape of the perturbation at leading order) symmetric nonlinear wave structure expanding with time [68, 69]. This oscillatory structure is described by a modulated elliptic solution of the fNLSE, with a transition from a steady soliton at the centre to a small-amplitude dispersive wave propagating away from the initial perturbation at linear group velocity [70].

In the case of a localised perturbation with a purely solitonic content, the MI dynamics strongly differs from the non-solitonic case. The evolution is described by the so-called superregular breathers, a pair of peculiar periodic breathers with opposite velocities, whose nonlinear superposition at initial time constitutes the small perturbation of the condensate [71, 72, 73]. Furthermore, it has been shown how these two cases could coexist when the perturbation exhibits the nonlinear (IST) spectrum characterised by both discrete (solitonic) and continuous (dispersive wave) parts. In this case the nonlinear dynamics exhibit features of both scenarios with superregular breathers that lie inside or outside the wedge of the expanding nonlinear oscillatory structure [67].

1.3 Rogue Waves

The term Rogue Wave (RW) generally refers to the localised water wave phenomena of unusually large amplitude and spontaneously (unpredictably) occurring in time. Being part of the marine folklore for centuries, the existence of RWs has been accepted by the scientific community only in the past few decades. The key event leading to its recognition has been the observation of the so-called “New Year wave”, recorded on the 1st of January 1995 on the Draupner platform in the North Sea [74]. The event, with a wave height of 25.6 meters, more than twice the significant

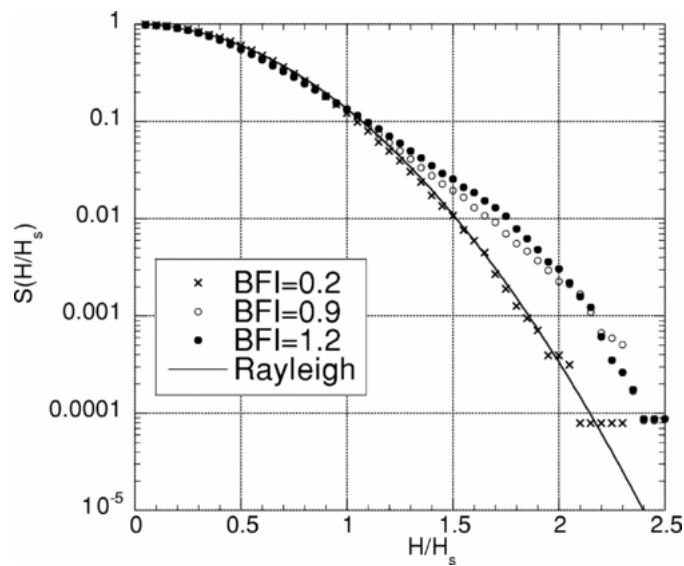


Figure 5: (Adapted from [2] with permission from the authors) Exceedence probability, “heavy” tailed distribution of wave height recorded in water tank experiment

wave height (the mean height of the highest third of the waves) of the surrounding area, was at the time considered highly improbable and outside of any known model. Nowadays, even if the physics behind the formation of RW is still being debated, their effects on offshore infrastructures is taken into account in the engineering design [42, 75].

The prescription of a large amplitude is not sufficient to adequately define a RW. The concept of RW is inherently related to the probability of such event to occur in a given ocean state. It has been shown that, when the sea surface slope is sufficiently small [76], the sea level can be assumed to be a linear superposition of many independent waves with random phases. It follows that the random sea level exhibits Gaussian statistics and the wave heights are distributed according to the Rayleigh distribution [77]. A RW is then defined as a large amplitude wave that appears with a frequency that exceeds the one predicted by the linear wave theory (i.e. more often than expected from the Gaussian statistics). The resulting Probability Density Function (PDF) of the amplitude of the field, function describing here the likelihood of a specific wave amplitude event, deviates from the Rayleigh distribution, see Fig. 5. In particular, the resulting PDF predicts more frequent high amplitude waves than the Rayleigh distribution, a feature also known as “heavy tail”, which can be observed by comparing the tails for the two distributions. This statistical feature is a key characteristic of the RW phenomenon.

At leading order, the fNLSE is often adopted to model the formation of RWs. Even if this equa-

tion may fail to describe the very steep profiles characterising the extreme event, it includes the RWs' statistical features and provides a reliable mathematical framework to investigate the phenomenon.

The formation of RWs is now understood as an ubiquitous phenomenon and it is studied in many different physical systems: light propagation in doped fibres [78], acoustic turbulence [79], nonlinear optical cavities [80] and microwave transport [81]. This work focuses, in particular, on the nonlinear optics context where, since the first experimental observation by Solli et al. [30], the study of RWs has become a rich subject of research.

Breather solutions of the fNLSE have recently attracted interest in the description of the RWs formation due to their spatio-temporal localisation properties [31]. In particular the PS [82] captures one of the main feature of RWs, it is localised both in space and time, i.e. PSs are the “waves that appear from nowhere and disappear without a trace” [83]. Moreover, the maximum amplitude of the PS is equal to three times the surrounding background, making it a particularly attractive prototype of the extreme event. However, it has been shown [84] that often the localised large amplitude fluctuations recorded in hydrodynamic and optical experiments usually classified as PSs, are rather nonlinear superpositions of breather solutions of the fNLSE.

Coherent structures such as PSs and higher-order breathers characterise the nonlinear stage dynamics of noise-induced MI. However, quite surprisingly, the numerical simulations showed that the large-amplitude fluctuations observed in this scenario at large times do not exhibit the statistical features characterising RWs events. In other words, the PDF of the amplitude of the wave field, at the asymptotic stage of the noise-driven MI, is not heavy-tailed but rather coincides with the Rayleigh distribution [41]. Another scenario characterised by the formation of PS and higher-order breathers is the evolution of partially coherent waves, which can be roughly viewed as an infinite random sequence of broad smooth pulses. Generated as linear superposition of many independent Fourier modes with random phases, this scenario is initially characterised by Gaussian statistic. The nonlinear evolution governed by the fNLSE quickly leads to a stage where the PDF exceeds the exponential tail of the Rayleigh distribution by order of magnitude, which is a strong indication of the presence of RW events [34, 85].

In the context of nonlinear optics RWs are local field fluctuations of a very large amplitude that

can be damaging for signal transmission and even for the hardware (e.g. high power lasers and amplifiers) but the possibility to control their emergence would open the way to a new generation of high power integrated fibre-based sources.

1.4 Integrability and Inverse Scattering Transform

The NLS equation belongs to the family of completely integrable nonlinear Partially Differential Equations (PDEs). The method used to solve this family of nonlinear PDEs is called the Inverse Scattering Transform (IST). Within this method a nonlinear dispersive PDE is solved by a 3-step algorithm, and each step involves solution of a linear problem.

A schematic of the IST method to solve the initial value problem for the NLS equation is shown in Fig. 6. First, the spectral representation of the initial profile is obtained by solving a linear scattering problem, the so-called *direct scattering transform*, where the initial wave field $u(x, t = 0)$ plays the role of an external potential. As result of the direct transform, scattering data at $t = 0$ are obtained. The time evolution of the scattering data is governed by a simple linear equation which is readily solved to give scattering data at any given time $t > 0$. The final step of the method is to solve the *inverse scattering problem* (a linear integral equation) to reconstruct the potential $u(x, t)$ from the scattering data. The IST procedure is also known as the Nonlinear Fourier Transform (NFT) due to the analogy with the spectral method based on the Fourier transform and used to solve linear PDEs.

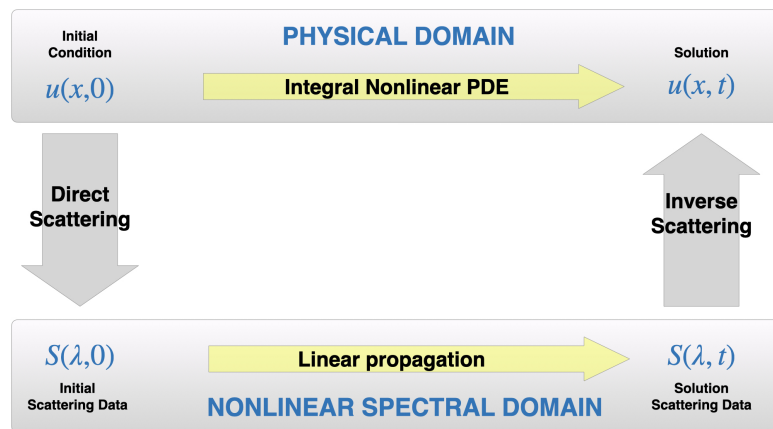


Figure 6: Schematic of the IST method to solve nonlinear PDE

The scheme was first developed in the framework of the Korteweg-de Vries (KdV) equation by Gardner, Greene, Kruskal, and Miura in 1967 [11] and soon after generalised by Lax [86]. The specific scattering problem for the fNLSE was then investigated by Zakharov and Shabat in 1972 [23] (focusing case).

The IST method relies on the possibility to represent the nonlinear PDE as the compatibility condition of two linear systems, the so-called Lax pair. In the case of the fNLSE in the form (1.18), the corresponding Lax pair (also called the Zakharov-Shabat equations) is:

$$R_x = \begin{pmatrix} -i\lambda & u \\ -u^* & i\lambda \end{pmatrix} R, \quad (1.33)$$

$$R_t = \begin{pmatrix} i(|u|^2 - 2\lambda^2) & iu_x + 2\lambda u \\ iu_x^* - 2\lambda u^* & i(2\lambda^2 - |u|^2) \end{pmatrix} R, \quad (1.34)$$

where $R(x, t)$ is a two-dimensional eigenvector and $\lambda \in \mathbb{C}$ the corresponding complex eigenvalue, called thereafter the complex spectral parameter.

The compatibility condition reads $R_{tx} = R_{xt}$. Formally, the resolution of the eigenvalue (Zakharov-Shabat scattering) problem (1.33) yields the set of eigenvalues $\lambda \in \mathcal{S} \subset \mathbb{C}$ and the corresponding eigenvectors R . The spectral set \mathcal{S} in the Zakharov-Shabat problem has the property of Schwarz symmetry, i.e. if $\lambda \in \mathcal{S}$ then also $\bar{\lambda} \in \mathcal{S}$.

However, the knowledge of the full spatio-temporal variation of the eigenvectors is not necessary to reconstruct the potential u , as we will show in the following. We call thereafter the data necessary to reconstruct such potential the scattering data. The temporal linear operator (1.34) governs the time evolution of these scattering data, and as a result, the time evolution of the potential $u(x, t)$. The complete integrability of the fNLSE and the Lax pair formalism imply the existence of an infinite hierarchy of conservation laws and conserved quantities. In particular, of primary interest for this work are the mass, momentum and energy integrals. The mass, having the meaning of the power in the optics context, is the first conserved quantity and takes the following form:

$$N = \int_{-\infty}^{\infty} |u|^2 dx. \quad (1.35)$$

The second and third conserved quantities are respectively the momentum

$$P = \int_{-\infty}^{\infty} u^* u_x dx, \quad (1.36)$$

and the total energy

$$E = E_L + E_{NL}, \quad (1.37)$$

that can be split into a linear (kinetic energy) part:

$$E_L = \int_{-\infty}^{\infty} u^* u_{xx} dx, \quad (1.38)$$

and nonlinear (potential energy) part:

$$E_{NL} = \int_{-\infty}^{\infty} |u|^4 dx. \quad (1.39)$$

Here we consider two families of initial conditions that can be solved using the IST method: rapidly decaying potentials and quasi-periodic potentials.

1.4.1 Vanishing boundary conditions

The first case considered is the rapidly decaying potential, where $u(x, t)$ decays to zero sufficiently fast as $x \rightarrow \pm\infty$ [23]. In this context, the scattering data consist of a continuous spectrum defined on $\lambda \in \mathbb{R}$, a complex discrete spectrum $\lambda_n \in \mathbb{C}$ and the asymptotic behaviour ($x \rightarrow \pm\infty$) of the eigenvector $R(x, t)$. Given the boundary conditions of the considered potential, $u \rightarrow 0$ for $x \rightarrow \pm\infty$, the Jost functions ψ and ϕ are the unique solutions of the scattering problem with the following asymptotic conditions:

$$\begin{aligned} \psi &\sim \begin{pmatrix} 0 \\ e^{i\lambda x} \end{pmatrix} \text{ as } x \rightarrow +\infty, \\ \phi &\sim \begin{pmatrix} e^{-i\lambda x} \\ 0 \end{pmatrix} \text{ as } x \rightarrow -\infty. \end{aligned} \quad (1.40)$$

Considering the solution $\psi = (\psi_1, \psi_2)^T$ of the scattering problem (1.33), (1.40), it can be shown that $\bar{\psi} = (\psi_2^*, -\psi_1^*)^T$ is solution of the same scattering problem. Moreover, the set $\{\psi, \bar{\psi}\}$ forms a complete basis of the solution space and we can thus write the solution ϕ as the linear combination:

$$\phi = a(\lambda)\bar{\psi} + b(\lambda)\psi, \quad (1.41)$$

with $a, b \in \mathbb{C}$; note that the scattering coefficient $a(\lambda)$ and $b(\lambda)$ are independent of the spacial variable x and are obtained by comparing the asymptotic behaviours of ϕ and $\psi, \bar{\psi}$. When $\lambda \in \mathbb{R}$, the Jost functions behave as plane waves for $x = \pm\infty$. Thus the direct scattering problem (1.33) reduces to the determination of the “reflected” and “transmitted” plane wave, products of the incident plane wave scattered by the potential. One can define the reflection coefficient in terms of the scattering coefficients:

$$r(\lambda) = \frac{b(\lambda)}{a(\lambda)}, \text{ with } \lambda \in \mathbb{R}. \quad (1.42)$$

The continuous spectrum is then defined as the non-vanishing reflection coefficient $r(\lambda) \neq 0$ and indicates the presence of “radiation” within the potential [56].

If λ belongs to the complex discrete spectrum λ_n , the Jost functions decay at $x \rightarrow \pm\infty$. Moreover, the points of the discrete spectrum correspond to the zeros of $a(\lambda)$ in the upper half of the complex plane. To each point of the discrete spectrum λ_n is associated a so-called norming constants c_n :

$$c_n = c(\lambda_n) = \text{Res}[r(\lambda)]|_{\lambda=\lambda_n} = \frac{b(\lambda_n)}{a'(\lambda_n)}, \quad (1.43)$$

with $a'(\lambda) = \partial a / \partial \lambda$.

If the “spectral portrait” of the potential consists of only one discrete point $\lambda \in \mathbb{C}$ (more precisely, two complex conjugate points) and no continuous spectrum part, the potential corresponds to the soliton solution of the fNLSE. Considering the soliton solution written in the form (1.20), the real and imaginary parts of the eigenvalue λ are associated to the velocity 4ξ and the amplitude 2η with the expression:

$$\lambda = \xi + i\eta. \quad (1.44)$$

Thus, the discrete part of the spectrum is often identified as the soliton content of the considered potential u . In particular, a reflectionless potential, i.e. $r(\lambda) = 0$, corresponds to the pure N-

soliton solution of the fNLSE. Moreover, if the considered potential is the single soliton solution of the fNLSE, there exists a simple relation between the norming constant and the parameters x_0 and ϕ_0 of the soliton:

$$c(\lambda, t = 0) = e^{-2\eta x_0 + i\phi_0}. \quad (1.45)$$

However, for more complex potentials with continuous and discrete spectrum, the relation between the norming constants and the soliton positions and phases is far from being simple.

As the propagation of the initial potential $u(x, 0)$ is governed by the fNLSE, its scattering representation evolves according to (1.34). The latter system is linear and determining the time-evolution of the scattering data is much simpler than solving the fNLSE.

The discrete spectrum of the potential is a constant of motion (the isospectrality property):

$$\frac{\partial \lambda_n}{\partial t} = 0 \quad \Rightarrow \quad \lambda_n(t) = \lambda_n(t = 0). \quad (1.46)$$

Given the relation between the discrete spectrum and the parameters of the soliton solution, the conservation of the discrete spectrum explains the core proprieties of the soliton solution, i.e. elastic interaction and conservation of the shape, amplitude and velocity.

On the other hand, the norming constants c_n associated to the discrete spectrum, and the reflection coefficient $r(\lambda)$ are not constants of motion. Solving the linear operator (1.34), one can determine explicitly the time evolution of the reflection coefficient

$$r(\lambda, t) = e^{+4i\lambda^2 t} r(\lambda, 0), \quad (1.47)$$

and of the norming constants

$$c_n(t) = e^{4i\lambda_n^2 t} c_n(0). \quad (1.48)$$

The last step of the IST scheme is the reconstruction of the potential $u(x, t)$ given the time evolved scattering data. The relevant inverse scattering problem can be solved via the Marchenko method [87]. For the fNLSE the corresponding Marchenko integral equation takes the form:

$$K_1(x, y, t) = F^*(x + y, t) - \int_x^\infty \int_x^\infty K_1(x, z, t) F(z + s, t) F^*(s + y, t) ds dz, \quad (1.49)$$

where the scattering data $\{r(\lambda), \lambda_n, c_n\}$ define the Marchenko kernel $F(x, t)$ of (1.49) as

$$F(x, t) = \frac{1}{2\pi} \int_{-\infty}^{\infty} d\lambda r(\lambda, t) e^{i\lambda x} - i \sum_{j=n}^N c_n(t) e^{-i\lambda_n x}. \quad (1.50)$$

Finally, the potential can be obtained from the solution $K_1(x, y, t)$ as:

$$u(x, t) = -2K_1(x, x, t). \quad (1.51)$$

If reflectionless potentials are considered, the kernel of the Marchenko equation is separable and the integral equation (1.49) turns to a system of linear algebraic equations. In this case, the potential obtained from the inverse problem is the N -soliton solution and its analytical expression can be determined explicitly.

1.4.2 Periodic and quasi-periodic boundary conditions

In the context of not-vanishing boundary conditions, the so-called Finite Gap Theory (FGT) [88, 89] is the framework adopted to extend the IST scheme to a certain class of periodic and quasi-periodic potentials. The FGT, first developed for the fNLSE in [90, 91], has proven a powerful analytical tool to investigate fundamental processes such as the modulational instability [92]. Moreover, the finite-gap solutions have been adopted both in water wave applications [26] and fibre optic communication [93, 94].

The nonlinear spectral representation of a finite-gap solution of the fNLSE is characterised by a series of Schwarz-symmetric 1D curvilinear segments called bands, or equivalently by the gaps between them. The $2(n + 1)$ fixed endpoints of the spectral bands define the main spectrum of a n -gap solution $u_n(x, t)$. Moreover, this multiphase solution can be expressed in terms of the multidimensional Riemann Theta function [26] that lives on the n -dimensional torus and whose absolute value $|u_n(x, t)|$ depends on the n real phases $\Theta = \mathbf{k}x + \boldsymbol{\omega}t + \Theta_0$ with the initial phase vector $\Theta_0 \in \mathbb{T}^n$. Thus, the finite-gap solution $u_n(x, t)$ is generally quasi-periodic, unless some additional constraints are imposed to ensure the exact periodicity of the potential. The constraints on the wavenumber vector \mathbf{k} and the frequency vector $\boldsymbol{\omega}$ that define the winding on the phase torus depend on the main spectrum λ_i of the finite-gap solution. This spectrum defines the two-sheeted

hyperelliptic Riemann surface of genus n :

$$\mathcal{R} : R(\lambda) = \prod_{i=0}^n (\lambda - \lambda_i)^{\frac{1}{2}} (\lambda - \lambda_i^*)^{\frac{1}{2}}, \quad (1.52)$$

where $\lambda \in \mathbb{C}$ is the complex spectral parameter and branchcuts made along spectral bands. The genus n , that can be calculated as the number of bands minus one, identifies the number of non-linear oscillatory modes of the finite-gap solution.

In the framework of the FGT, the well-known solutions of the fNLSE can be identified as specific limits of generic finite-gap potentials. In this context, the plane wave is the genus 0 solution and it is characterised by a single band crossing the real axis in the spectral plane, also known as the Stokes spectral band. The genus one solution is described by the elliptic functions. The soliton solution represents a special case of the genus one finite gap potential when the two Schwarz-symmetric bands in the upper and lower spectral half planes collapse in two complex conjugate points. These double points correspond to the discrete spectral points of the soliton scattering representation, see Fig. 7(a). The spectral portrait of the TW breather solution consists of a Stokes band and two symmetric collapsed bands, making it a degenerate genus two solution, see Fig. 7(b-d). These configurations can be generalised for higher-order soliton and breather solutions, considering additional collapsed bands in the finite-gap spectral representation. In particular, the recent analytical description of soliton and breather gases relies on such method where the gases correspond to a special thermodynamic limit of a multiphase finite-gap solution of the fNLSE [53].

The direct scattering problem in the FGT framework aims to recover the main spectrum and the phases of a given potential. In this discussion, we restrict the problem to the case of periodic potentials [26, 95], a key scenario for the understanding of the algorithm implemented numerically to compute the nonlinear spectrum of u , Section 1.6.2. In this context the mathematical procedure adopted for the analysis is the Floquet theory.

Considering the initial periodic potential $u(x, 0) = u(x + L, 0)$ of period L and a arbitrarily chosen base point $x = x_0$, two independent solutions, $\phi(x, x_0, \lambda) = (\phi_1, \phi_2)^T$ and $\bar{\phi}(x, x_0, \lambda) =$

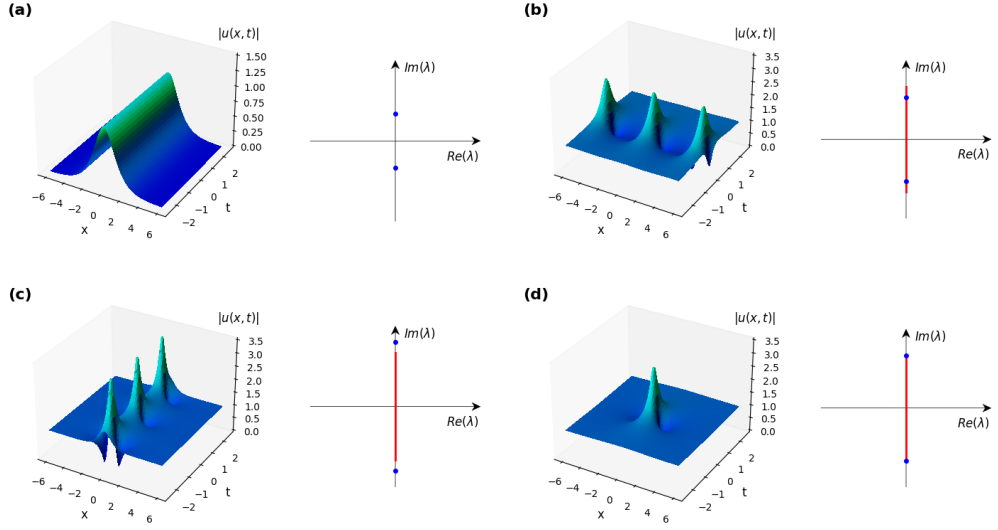


Figure 7: Solitonic solutions of the fNLSE and their IST spectral portraits. The wave field amplitude $|u(x, t)|$ (left) and the spectral portraits (right) of (a) the fundamental soliton, (b) the Akhmediev breather, (c) the Kuznetsov-Ma breather and (d) the Peregrine soliton. The red lines in spectra plotted in (b–d) represent branchcuts (spectral bands). The blue points in (a–d) represent complex conjugate double points.

$(\bar{\phi}_1, \bar{\phi}_2)^T$, of (1.33) are introduced and assumed to take the values:

$$\phi(x_0, x_0, \lambda) = \begin{pmatrix} 1 \\ 0 \end{pmatrix}, \quad \bar{\phi}(x_0, x_0, \lambda) = \begin{pmatrix} 0 \\ 1 \end{pmatrix}. \quad (1.53)$$

Then the fundamental matrix solution of (1.33) can be written as

$$\mathbf{M}(\lambda, x_0) = \mathbf{\Phi}(x, x_0, \lambda) = \begin{pmatrix} \phi_1(x, x_0, \lambda) & \bar{\phi}_1(x, x_0, \lambda) \\ \phi_2(x, x_0, \lambda) & \bar{\phi}_2(x, x_0, \lambda) \end{pmatrix}, \quad (1.54)$$

with the normalisation $\mathbf{\Phi}(x_0, x_0, \lambda) = \mathbb{I}$. The monodromy or transfer matrix is then defined as the matrix solution evaluated at $x_0 + L$

$$\mathbf{T}(\lambda, x_0) = \mathbf{\Phi}(x_0 + L, x_0, \lambda), \quad (1.55)$$

and it maps the solutions of (1.33) over the period L of the potential u . The monodromy matrices

with different basis points are related by similarity transformation [26]

$$\mathbf{T}(\lambda, x_1) = \mathbf{S}\mathbf{T}(\lambda, x_0)\mathbf{S}^{-1}. \quad (1.56)$$

The trace and the determinant of the monodromy matrix are conserved under the transformation (1.56) and are independent from the basis point x_0 . Therefore

$$\text{Tr} [\mathbf{T}(\lambda)] = \Delta(\lambda) \text{ and } \det [\mathbf{T}(\lambda)] = 1. \quad (1.57)$$

The Floquet discriminant $\Delta(\lambda)$, which plays a fundamental role in the spectral theory for periodic potential, is then function only of the spectral parameter λ . To better understand the role of the discriminant in the Floquet theory, we introduce the Bloch solution $\psi(x, \lambda)$ of (1.33). The Bloch function is defined by the condition

$$\psi(x + L, \lambda) = e^{ip(\lambda)L}\psi(x, \lambda), \quad (1.58)$$

where $p(\lambda)$ is the Floquet exponent (or quasi-momentum). The condition (1.58), evaluated at the basis point x_0 takes the form:

$$\psi(x_0 + L, \lambda) = m(\lambda)\psi(x_0, \lambda), \quad (1.59)$$

with $m(\lambda) = e^{ip(\lambda)L}$ the Floquet multiplier. Considering the fundamental solutions ϕ and $\bar{\phi}$, the Bloch function ψ can be written as:

$$\psi(x, \lambda) = A\phi(x, x_0, \lambda) + B\bar{\phi}(x, x_0, \lambda), \quad (1.60)$$

where A and B are complex coefficients. In particular, given the basis (1.53), we obtain

$$\psi(x_0, \lambda) = A\phi(x_0, x_0, \lambda) + B\bar{\phi}(x_0, x_0, \lambda) = \begin{pmatrix} A \\ B \end{pmatrix}, \quad (1.61)$$

and

$$\psi(x_0 + L, \lambda) = A\phi(x_0 + L, x_0, \lambda) + B\bar{\phi}(x_0 + L, x_0, \lambda) = \mathbf{T}(\lambda) \begin{pmatrix} A \\ B \end{pmatrix}. \quad (1.62)$$

Combining these relations with (1.59) we obtain

$$\mathbf{T}(\lambda) \begin{pmatrix} A \\ B \end{pmatrix} = m(\lambda) \begin{pmatrix} A \\ B \end{pmatrix}. \quad (1.63)$$

The nontrivial solutions of the eigenvalues problem (1.63) are obtained with

$$\det[\mathbf{T} - m\mathbb{I}] = m^2 - \text{Tr}[\mathbf{T}]m + \det[\mathbf{T}] = m^2 - \Delta(\lambda)m + 1 = 0, \quad (1.64)$$

that yields

$$m_{\pm}(\lambda) = \frac{\Delta(\lambda) \pm \sqrt{\Delta(\lambda)^2 - 4}}{2}. \quad (1.65)$$

The Bloch solution is therefore bounded and stable if

$$-2 \leq \Delta(\lambda) \leq +2. \quad (1.66)$$

The spectral bands are then identified by the values of λ for which the Floquet multiplier is complex and has modulus one:

$$\{\lambda \in \mathbb{C}, \Delta(\lambda)^2 \leq 4\}. \quad (1.67)$$

In particular, the points that satisfy the equality $\Delta(\lambda) = \pm 2$, identify the values for which the Bloch solutions are either periodic ($m(\lambda) = +1$) or antiperiodic ($m(\lambda) = -1$), and represent the main spectrum of the periodic potential.

1.4.3 Finite-gap potentials and Rogue Waves

The validity of breather solutions of the fNLSE as prototype of RWs has been already discussed in section 1.3. This model has been extended in [3] using the finite-gap (multiphase) solutions. Considering the n -gap potential defined on the n -dimensional torus \mathbb{T}^n , the conventional criterion

to determine a RW can be adapted to this new framework:

$$K_n = \frac{|u_n|_{\max}^2}{\langle |u_n|^2 \rangle} > C_r, \quad (1.68)$$

where $|u_n|_{\max}^2$ is the maximum amplitude of the finite-gap potential, $\langle |u_n|^2 \rangle$ is the mean value obtained by averaging the intensity over the spacial domain and the constant (the enhancement factor) C_r can be defined to match the agreed RW definition (e.g. one typically takes $C_r = 8$ in the context of ocean RWs [41, 77]). In this framework, the maximum amplitude of a finite-gap potential $|u_n|_{\max}$ can be computed from the spectral representation of the multiphase solution using the explicit formula derived in [96]:

$$|u_n|_{\max} = \sum_{i=0}^n \text{Im} \lambda_i, \quad (1.69)$$

where λ_i are the points of the main spectrum with $\text{Im} \lambda_i > 0$. The solution can be written in term of the Riemann Theta function and depends on the n -components phase vector $\Theta = \mathbf{k}x + \omega t + \Theta_0$, $|u_n(x, t)| = f_n(\Theta(x, t))$. An example of multiphase solution with $n = 4$ is illustrated in Fig. 8. Since the wavenumbers k_i and frequencies ω_i are generally incommensurable, ergodicity implies that the mean value $\langle |u_n|^2 \rangle$ can be evaluated in the phase domain by averaging the intensity over the torus \mathbb{T}^n .

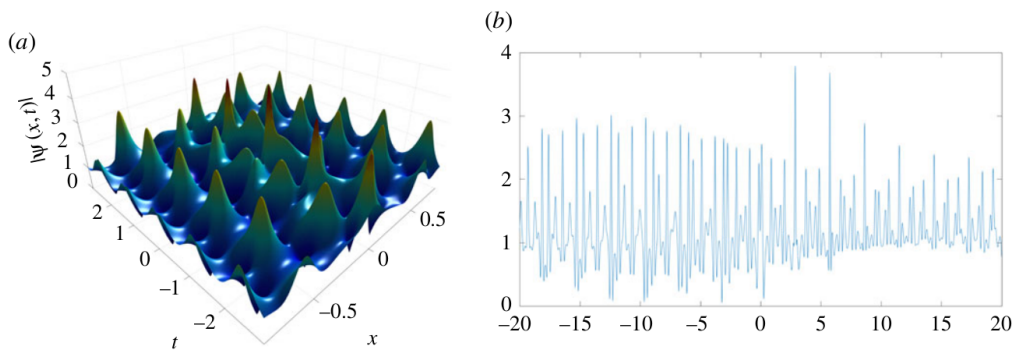


Figure 8: (adapted from [3] with permission from authors) In the notation adopted in our work $\psi \equiv u$. Example of multiphase solution $n = 4$; $\lambda_i = (-0.39271 + i, -0.21336 + i, 0.010556 + i, 0.20525 + i, 0.39027 + i)$; $\langle |\psi|^2 \rangle = 1.6452$; $K_4 = 15.1959$. (a) Plot of the amplitude of the multiphase solution $|\psi(x, t)|$ and (b) plot of $|\psi(x)|$ for a fixed time t .

Beside, given the direction of the winding around the torus parameterised by the wavenumber

vector \mathbf{k} , a particular choice of the initial phase Θ_0 selects a specific realisation of finite-gap solution. [3] shows that, by uniformly distributing the initial phase vector Θ_0 on the torus, the probability of a RW event is given by the ratio between the area of the torus confined by the level curve $|u_n|_{\max}^2 = C_r \langle |u_n|^2 \rangle$ and the total area of the torus. Thus, using the finite-gap potential as prototype for the formation of RW events naturally introduces the statistical description needed to fully characterise the phenomena.

1.4.4 Semi-classical theory and Bertola-Tovbis results

An important result obtained in the framework of the FGT is the analytical description of the PS formation as the regularisation mechanism of gradient catastrophes in the so-called semi-classical limit of the fNLSE. The semi-classical limit of the fNLSE arises in the context of strongly nonlinear initial condition and enables the study of the asymptotics space-time behaviour of the system. This formulation can be derived from (1.13) with the introduction of the small parameter $\varepsilon \ll 1$, determined by the ratio between two typical scales of the problem: the internal coherence length (equivalent to the soliton width) and the typical scale of the initial condition, or physically speaking, by the ratio of the dispersive and nonlinear lengths in the problem. Thus, rescaling the variables $\xi = \varepsilon Z$ and $\tau = \varepsilon T$, the equation assumes the form:

$$i\varepsilon \frac{\partial u}{\partial \xi} + \frac{\varepsilon^2}{2} \frac{\partial^2 u}{\partial \tau^2} + |u|^2 u = 0. \quad (1.70)$$

In this framework, a sufficiently smooth pulse undergoes a self-focusing process resulting in a gradient catastrophe, the formation of infinite derivatives in the profile of the wave field $|u(x, t)|$. The gradient catastrophe is then dispersively resolved by the generation of short-scale oscillations of finite amplitude.

The initial, self-focusing stage of the evolution of the profile is dominated by nonlinearity and the corresponding dynamics is approximately dispersionless. To describe the dynamics analytically, it is convenient to introduce the Madelung transform [97, 98]

$$u(\tau, \xi) = \sqrt{\rho(x, t)} e^{i \frac{\phi(\xi, \tau) \tau}{\varepsilon}}, \quad v(\tau, \xi) = \frac{\partial \phi(\xi, \tau)}{\partial \tau}, \quad (1.71)$$

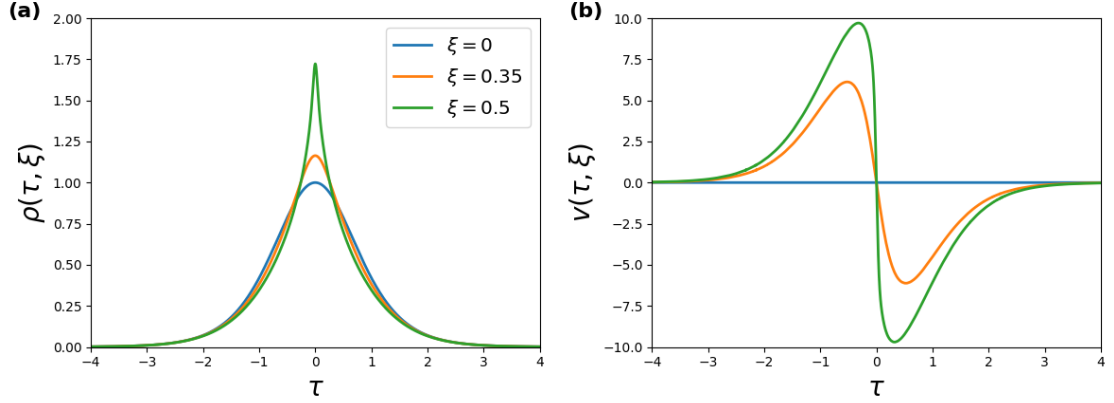


Figure 9: Gradient catastrophe formation: (a) power ρ and (b) chirp v for the initial pulse $\rho(\tau, 0) = \text{sech}(\tau)^2$, $v(\tau, 0) = 0$.

where $\sqrt{\rho} = |u|$ is the wave amplitude and v the instantaneous frequency, commonly called “chirp”. As a result equation (1.70) takes the form of the system:

$$\begin{aligned} \rho_\xi + (\rho v)_\tau &= 0, \\ v_\xi + v v_\tau - \rho_\tau + \frac{\varepsilon^2}{4} \left[\frac{\rho_\tau^2}{2\rho^2} - \frac{\rho \tau \tau}{\rho} \right] &= 0. \end{aligned} \quad (1.72)$$

The dispersionless limit is then achieved by setting $\varepsilon = 0$, and the system (1.72) assumes the form of the well-known set of nonlinear geometric optic equations [99, 100]. This approximation is valid in the early stage of the self-focusing evolution until some critical point (τ_c, ξ_c) , also called the gradient catastrophe point [101], when the solution develops infinite derivatives, see Fig. 9.

In the vicinity of the gradient catastrophe point, the contribution of the dispersive effects must be included in the dynamics and the full dispersive system (1.72) has to be considered. It was rigorously proven by M. Bertola and A. Tovbis [46] that the gradient catastrophe is *universally* regularised by dispersive effects via the local emergence of a coherent structure, which is asymptotically described by the PS solution. An example of the regularisation process is shown in Fig. 10. The universality of the PS formation is understood in the sense that this regularisation mechanism persists regardless of the particular shape ρ , chirp v or solitonic content of the initial condition $u(\tau, 0)$. More explicitly, this theory provides the following asymptotic description of

the structure that emerges at the point of maximum compression:

$$\xi_m = \xi_c + \mathcal{O}(\varepsilon^{4/5}), \quad (1.73)$$

and that coincides, at leading order $\mathcal{O}(1)$, with the PS profile (1.29):

$$u(\tau, \xi_m) = a_0 \left(1 - \frac{4}{1 + 4a_0^2(\tau/\varepsilon)^2} \right) \left[1 + \mathcal{O}(\varepsilon^{1/5}) \right], \quad (1.74)$$

where $a_0 = \sqrt{\rho(0, \xi_c)}$ is, at the leading order, the background amplitude at the point of gradient catastrophe $\xi = \xi_c$. In particular, [46] have considered the evolution of a sech-modulated plane wave,

$$u(\tau, 0) = \text{sech}(\tau)e^{i\phi/\varepsilon}, \quad v = -\mu \log(\cosh(\tau)), \quad (1.75)$$

where the chirp parameter $\mu \in \mathbb{R}$ controls the initial phase. In this case, the nonlinear spectrum of the potential can be calculated analytically [102] and it is shown to be determined by the chirp parameter μ . For $\mu = 0$ the potential is the exact N -soliton solution of the fNLSE (1.70) with $N = 1/\varepsilon$. On the other hand, if $\mu \geq 2$ the spectrum is purely continuous. The point of gradient catastrophe can be determined analytically: $\xi_c = 1/(\mu + 2)$, and the maximum compression point is asymptotically found as:

$$\xi_m = \xi_c + C\varepsilon^{4/5}, \quad (1.76)$$

where

$$C = \left(\frac{5|C_1|}{4} \right)^{1/5} (2b_0)^{-3/2} |v_p| \left(1 + \mathcal{O}(\varepsilon^{4/5}) \right), \quad (1.77)$$

with $C_1 = \frac{32\sqrt{2}i}{15(2+\mu)^{1/9}}$, $b_0 = \sqrt{\mu + 2}$ and $|v_p| \approx 2.38$ is a universal constant. Even if the regularisation mechanism exhibits a universal behaviour, the critical point and the dynamic that characterises the evolution after the formation of the PS depends on the choice of the initial chirp (i.e. the soliton content). Therefore, by properly choosing the chirp μ of the initial profile, it is possible to control the position of the emergence of the PS.

The PS formation as regularisation mechanism of the gradient catastrophe has been examined experimentally using the optical fibre platform [4, 103]. These experiments revealed the robustness of the mechanism that can be observed for a very broad range of value of ε , far from the formal semi-classical limit $\varepsilon \rightarrow 0$. The comparison between the semi-classical theory results and the

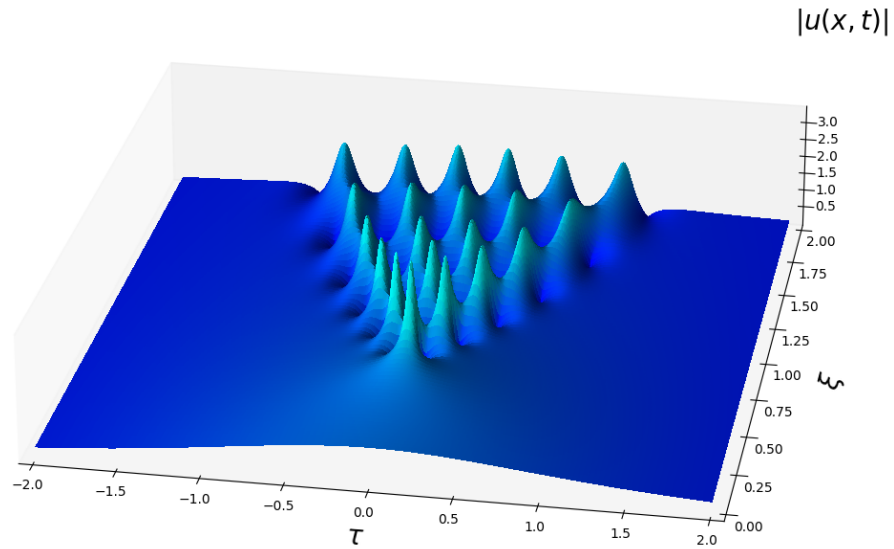


Figure 10: Numerical simulation of the semi-classical fNLSE. Absolute value $|u(\tau, \xi)|$ versus (τ, ξ) coordinates where the initial condition considered is $u(\tau, 0) = \text{sech}(\tau)$ with $\varepsilon = 0.01$.

experimental observation of the PS formation from [4] is shown in Fig. 11.

The observation of the regularisation mechanism in water tank experiment with the particular aim to control the point of the PS occurrence by spectral engineering of the initial profile has been presented in [104] and will be discussed in Chapter 3. Additionally, in Chapter 6, an in-depth study of higher-order effects on the gradient catastrophe regularisation is presented in the context of high intensity optical fibre signals.

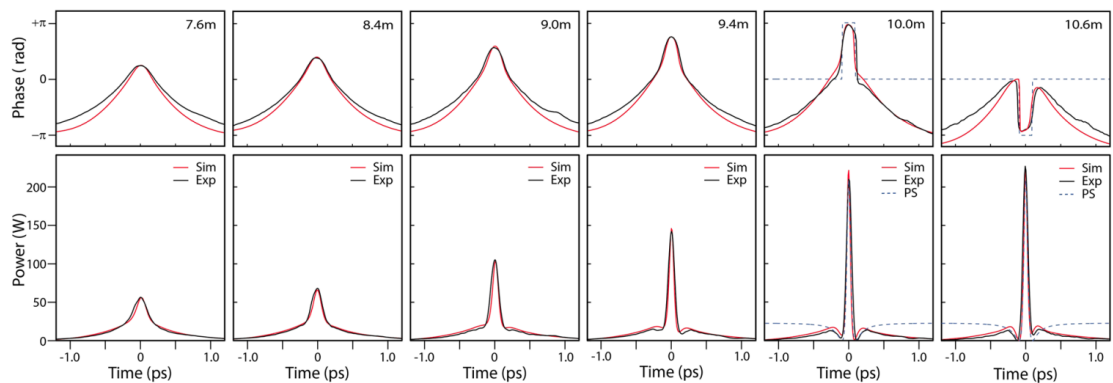


Figure 11: (Adapted from [4] with permission from the authors) fibre optics experimental observation of the Peregrine emergence as regularisation of the gradient catastrophe. Comparison of experimental measurements (black line), of intensity (bottom) and phase (top), with simulations (red line).

1.5 Integrable Turbulence

Turbulence is one of the most recognisable forms of nonlinear motion that has been, and continues to be, the subject of very active research in classical (viscous) fluid dynamics [105]. This fundamental phenomenon occurs also in dispersive media where turbulence is associated with the generation of complex, spatio-temporal statistical ensembles of interacting nonlinear waves.

The theory of weak wave turbulence in dispersive systems was developed by V. E. Zakharov in the 1960s [39]. The wave turbulence (WT) theory provides a framework for the statistical description of weak turbulence in nonintegrable wave systems dominated by resonant interactions. One of the most important results in the wave turbulence theory is the discovery by V. E. Zakharov in 1965 of a new type of solutions to a set of so-called kinetic equations, describing a constant energy flux through scales. These solutions, called Kolmogorov-Zakharov spectra by analogy with Kolmogorov energy cascade in hydrodynamics, have been observed in a variety of experiments performed in turbulent wave systems [32].

The notion of turbulence can be extended to integrable systems where it is understood as the complex, integrable, spatio-temporal dynamics of nonlinear random waves. Since many nonlinear wave systems can be described by partial differential equations having an integrable “core part”, the emerging theory of integrable turbulence, also initiated by Zakharov [37], has become an active field of research with theoretical and numerical developments supported by a number of experimental observations [35, 37, 40, 41, 71, 100, 106, 107, 108, 109]. Given the absence of resonances in integrable systems, the mechanisms underlying integrable turbulence are of profoundly different nature from those found in the standard WT [32, 39, 110] and thus require very different theoretical approaches to their study. Notably, a key feature of integrable turbulence is the establishment of an asymptotic state characterised by stationary statistical properties. This feature has been demonstrated in numerical simulations, even if Fermi-Pasta-Ulam-Tsingou (FPUT) recurrences are expected in complete integrable system [111, 112, 113, 114]. However, it is important to note that the existence of the stationary state has been observed at finite time/distance of propagation in numerical simulations and experiments, where the integrability is always broken in the long propagation limit. Even if the results obtained in numerical simulations are robust and do not depend on the scheme of integration, the rigorous mathematical proof of existence of the

stationary state of integrable turbulence is still an open question.

Given the integrable nature of the system, the choice of the random initial condition strongly affects the statistical properties of the long-time statistically stationary state [35, 40, 41, 100, 115]. Here we present an overview of the evolution of two systems widely investigated in the framework of integrable turbulence. First, we analyse the development of the asymptotic stage of the noise induced MI, already introduced in Section 1.2. Second, we consider the different stages of the evolution of partially coherent waves with Gaussian statistics, which represent the random collection of slowly varying pulses of finite amplitude.

1.5.1 Noise induced Modulational Instability

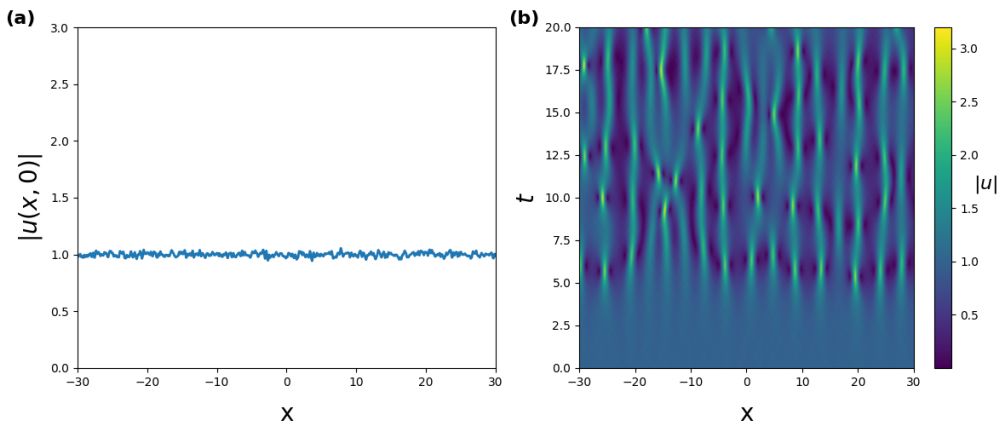


Figure 12: Noise-induced modulation instability scenario of integrable turbulence: (a) initial random perturbation of the condensate solution $|u(x, 0)|$ and (b) 2D colour plot of the temporal evolution of the amplitude of the wave field $|u(x, t)|$

The first case analysed in the framework of integrable turbulence is the nonlinear stage of evolution of the noise induced MI. The typical development of this scenario is depicted in Fig. 12. It has been numerically shown [41] that the condensate solution of the fNLSE (1.19), perturbed by a small random noise, evolves into a stationary state for which different statistical features and major characteristic of the wave field reach an asymptotic value. Of particular interest is the PDF of the wave amplitude that asymptotically approaches the Rayleigh distribution; note that the time evolution of the PDF is non trivial and oscillates, with a decaying amplitude, about the stationary Rayleigh distribution. Moreover, one can study the evolution of the PDF using a single statistical

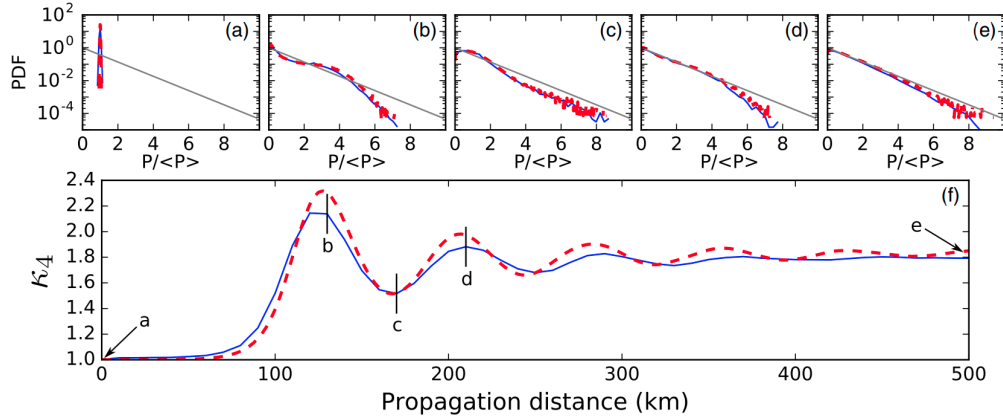


Figure 13: (Adapted from [5] with permission from the authors) Experimental observation of the evolution of the PDF of the normalised power [(a)–(e)] and the evolution of the normalised fourth-order moment κ_4 for the development of integrable turbulence in noise-induced MI.

indicator κ_4 : the normalised fourth order moment of the amplitude $|u|$ defined by:

$$\kappa_4(t) = \frac{\langle |u|^4 \rangle}{\langle |u|^2 \rangle^2}. \quad (1.78)$$

Similarly to the standard kurtosis, κ_4 quantifies the “heaviness” of the tail of the distribution (high amplitude events are more likely to happen) and the deviation from the Gaussian statistic. The nonlinear stage of MI is characterised by the oscillatory decay of κ_4 that reflects the recurring appearance of heavy-tail in the PDF during the development of the stationary state. As discussed in Section 1.3, the Rayleigh distribution and the corresponding value of the fourth order moment $\kappa_4 = 2$ are features of Gaussian processes. However, in the nonlinear stage of MI, this characterisation holds only for the single point statistics of the field. Multi-point statistics of the stationary state of the noise-induced MI are not Gaussian, effectively distinguishing this phenomenon from a purely Gaussian process. In particular, it has been shown that the two-point statistics, the autocorrelation function of the power $g^{(2)}$ defined as:

$$g^{(2)}(\tau) = \frac{\langle |u(x, t)|^2 |u(x + \tau, t)|^2 \rangle}{\langle |u(x, t)|^2 \rangle^2}, \quad (1.79)$$

oscillates around unity, whereas in the case of a purely Gaussian process is bounded from below: $g^{(2)} \geq 1$. The damped oscillatory behaviour that characterises the transient to the stationary state also manifests in other characteristics of the field: power spectrum, kinetic and potential energy of the field. In particular, the power spectrum converges to a profile characterised by a power law in

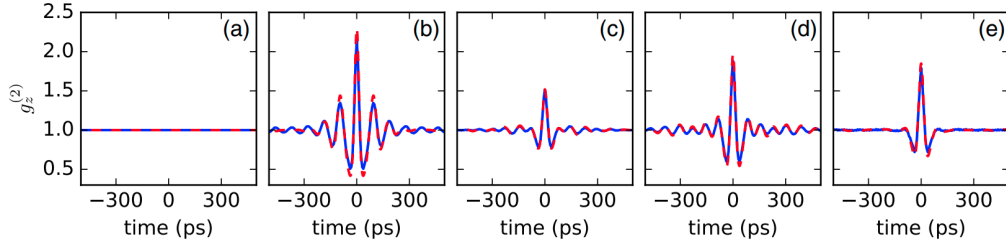


Figure 14: (Adapted from [5] with permission from the authors) Experimental observation of the evolution of the two-points statistics of optical power $g^{(2)}$ for the development of integrable turbulence in noise-induced MI.

the vicinity of the zero-th harmonic (i.e. low frequency region). The corresponding modes retain a high percentage of the initial mass of the system and have large physical scales, thus forming the so-called “quasi-condensate” [41].

Besides the detailed numerical study [41], the establishment of the stationary state and the formation of integrable turbulence from the development of MI has been recently studied and observed in fibre optic experiment [5]. This latter work has shown that the transient oscillatory behaviour, the asymptotic values and the distribution reached at the stationary state measured experimentally are in quantitative agreement with the numerical prediction, once the effective losses of the physical system are taken into account, see Fig. 13 and 14. The recirculating fibre loop system developed to measure the spatio-temporal dynamics of MI [5] plays a key role on the future study and understanding of integrable turbulence.

Furthermore, the recent result on spectral theory [53] and the connection established between the stationary state of MI and the bound-state soliton gas [109] shed new light on the theoretical framework of integrable turbulence.

1.5.2 Partially coherent waves

The evolution of initial Partially Coherent Waves (PCW) is another problem widely investigated in the framework of integrable turbulence. PCWs consist of a collection of independent smooth (i.e slowly varying) humps, and can be obtained as the linear superposition of a large number of independent Fourier modes with random phases [34, 35, 106, 108, 116]:

$$u_k(t=0) = |u_{0k}| e^{i\phi_{0k}}, \quad (1.80)$$

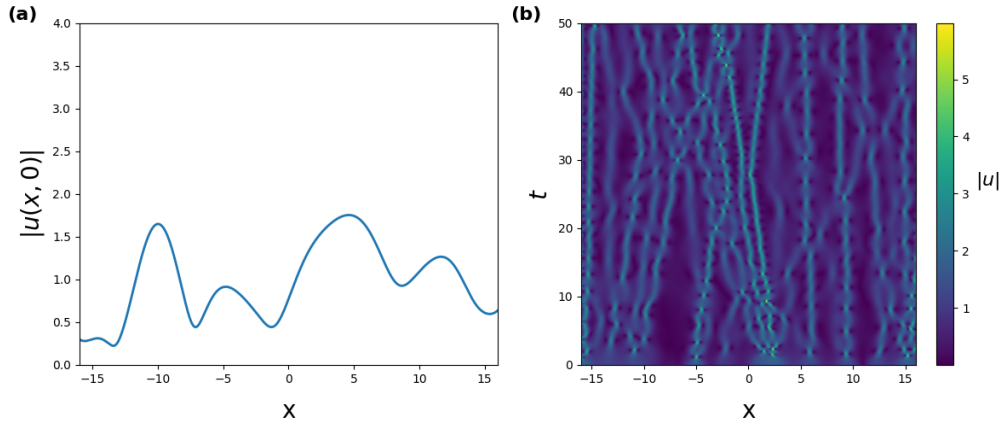


Figure 15: Partially coherent wave scenario of integrable turbulence: (a) initial condition $|u(x, 0)|$ and (b) 2D color plot of the temporal evolution of the amplitude of the wave field $|u(x, t)|$

with ϕ_{0k} the random phase uniformly distributed between 0 and 2π . A realisation of PCW evolution is illustrated in Fig. 15. According to the central limit theorem, such superposition of independent random variables generates a field with a Gaussian single point statistics [117]. In particular, the PDF for the amplitude of the initial wave field is the Rayleigh distribution, and the corresponding value of the normalised fourth-order moment is given by $\kappa_4(t=0) = 2$. PCW can be found in physical problems where the initial condition is characterised by strong nonlinearity. This type of initial condition emerges in the description of different optical phenomena: speckles [118, 119], strongly multimode lasers [40] and spontaneous light emission [106, 108].

The scale of the smooth initial fluctuations in PCW is much larger than the internal coherence length (i.e. the size of the fundamental soliton), and one can investigate the nonlinear evolution of such smooth initial conditions taking advantage of the mathematical framework of dispersive hydrodynamics by using the semi-classical theory of nonlinear dispersive waves [120]. As described in Section 1.4.4, the semi-classical formulation of the fNLSE (1.70) naturally encodes the two distinct spatio-temporal scales of the system: the long scale specified by the initial fluctuations occurring on the $\mathcal{O}(1)$ scale, and the short scale specified by the internal coherence length of $\mathcal{O}(\varepsilon)$. This scale separation enables one to analyse and describe the different stages of the evolution with different analytical methods.

As shown in [100], the scale separation in partially coherent waves allows to split the development of integrable turbulence into different distinct stages, characterised by qualitatively different dynamical and statistical features.

At the initial or “prebreaking” stage of the evolution, the nonlinear effects dominate linear dispersion and the wave fronts of the random initial field experience gradual steepening leading to the formation of gradient catastrophes. At this stage, the dynamical and statistical features of the field can be analytically described in terms of random solutions of the dispersionless (geometric optics) system:

$$\begin{aligned}\rho_\xi + (\rho v)_\tau &= 0, \\ v_\xi + vv_\tau - \sigma\rho_\tau &= 0,\end{aligned}\tag{1.81}$$

derived in the limit $\varepsilon \rightarrow 0$ from (1.72), as discussed in Section 1.4.4. Here the parameter $\sigma = \pm 1$ distinguishes, respectively, the focusing and the defocusing regimes of the NLS equation. In particular, in the defocusing regime, the dynamical and statistical features that occur at this early stage of the evolution can be interpreted in terms of evolution of random Riemann waves [100]. In Chapter 2 of this Thesis, this initial stage is studied, both in the focusing and defocusing regime, using short time asymptotics, yielding the evolution of the normalised fourth order moment κ_4 (1.78). The early evolution of κ_4 notably provides an insight into the stationary state of integrable turbulence, foreseeing the emergence of the well-known phenomena of heavy/low tails of the wave field PDF.

The initial dispersionless approximation fails when the gradient catastrophe develop, and the full dispersive system has to be considered. The gradient catastrophes have qualitatively different geometrical natures in the defocusing regime (wave-breaking singularity [121]) and the focusing regime (elliptic umbilic singularity [122]). However, both cases are regularised by dispersive effects via the generation of nonlinear short wavelength oscillations corresponding to breather structures in the focusing regime [46], and dispersive shock waves in the defocusing regime (see Ref. [98] and references therein). As discussed in Section 1.4.4, the formation of a peregrine-like structure in the focusing case universally characterises the regularisation process for a wide family of sufficiently smooth initial pulses. Considering the initial partially coherent wave field as a collection of independent humps, it has been numerically shown how the regularisation mechanism affects the development of the integrable turbulence [6]. The gradient catastrophe points of the different humps can be estimated from the width and amplitude of the initial pulses, and one can thus compute the probability to observe the formation of a PS during the development of the stationary state. The maximum of this probability has been shown to occur at the same time as the

normalised fourth-order moment reaches its maximum (also called overshoot), see in Fig. 16(b,c). Moreover, the overshoot of κ_4 corresponds to the point at which the Fourier spectral width of the field is maximal [33] and the RW events are more frequent, as the PDF of the amplitude of the wave field exhibits the “heaviest” tail.

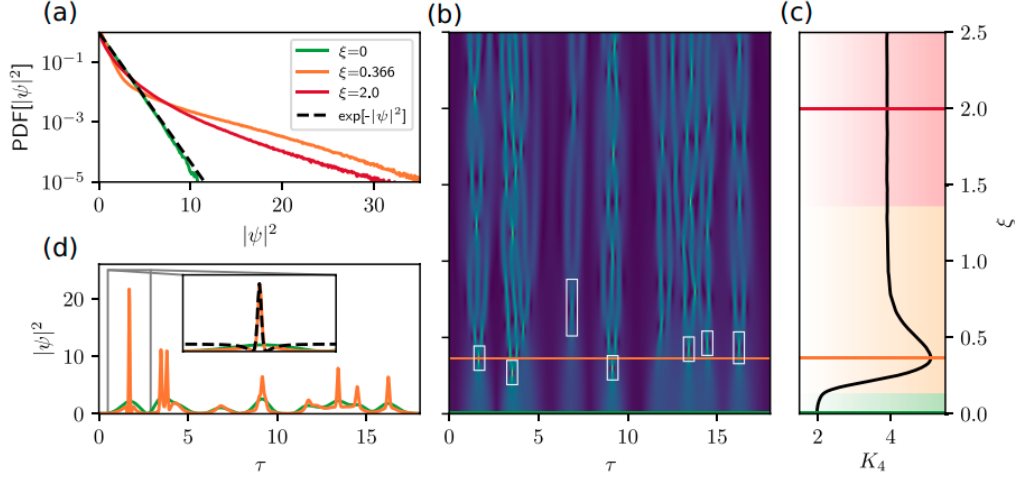


Figure 16: (Adapted from [6] with permission from the authors) In the notation adopted in our work $\psi \equiv u$. Numerical simulations of a partially coherent wave propagation in the fNLSE. (a) Probability density function of $|\psi|^2$ at three different propagation distances. (b) spatio-temporal diagram of $|\Psi|$. White boxes highlight the formation of the PS as regularisation mechanism of the gradient catastrophe of the initial humps. (c) Evolution of the kurtosis (black). (d) Profile of the wave field at two different propagation distances. (colours are preserved). For details of the simulation refer to [6].

Following the initial stages of evolution described above, the system asymptotically reaches the (statistically) stationary state. In the focusing regime, the stationary state for the partially coherent wave is characterised by the heavy tail statistic associated to the appearance of large amplitude fluctuations of the field. These fluctuations take the form of bright coherent structures localised in space and time, which is characteristic of RW events [34, 36]. The deviation from the initial Gaussian statistic is quantified by the normalised fourth-order moment of the amplitude that reaches its asymptotic value at $\kappa_4 = 4$. On the other hand, in the defocusing regime, the stationary state is characterised by the low-tail statistics of the field. In this context the deviation from the Gaussian statistic originates from the formation of dark solitons and dispersive shock waves (DSW), and is quantified by an asymptotic value of κ_4 lower than the initial Gaussian one: $\kappa_4(t = 0) = 2$ [115, 118].

1.5.3 Soliton Gas

The framework of integrable turbulence covers a broad range of turbulent wave regimes in integrable systems. In view of the fundamental nature and ubiquity of solitons in physical systems, one of the most interesting types of integrable turbulence is soliton turbulence or soliton gas, a kind of strongly nonlinear turbulent wave motion that have been observed in the ocean [50, 123] and realised in laboratory experiments [51, 52]. The spectral theory of soliton gas outlined here has been presented in the recent review [124].

The theoretical notion of soliton gas was introduced in 1971 by V. Zakharov [47], who considered an infinite ensemble of KdV solitons randomly distributed on the line. We consider the KdV equation in the form

$$u_t + 6uu_x + u_{xxx} = 0. \quad (1.82)$$

The inverse scattering theory (see Section 1.4) associates solitons of the KdV equation (1.82) with points of discrete spectrum of the Schrödinger operator $L = -\partial_{xx}^2 - u(x, t)$ in which t plays the role of a parameter. The KdV soliton solution corresponds to a discrete spectral value $\lambda_i = -\eta_i^2$, $\eta_i > 0$, and is given by the formula

$$u_s(x, t; \eta_i) = 2\eta_i^2 \operatorname{sech}^2[\eta_i(x - 4\eta_i^2 t - x_i^0)], \quad (1.83)$$

where x_i^0 is the initial position of the soliton's centre.

In a low-density, rarefied soliton gas, the solitons are well-separated and the corresponding KdV solution can be almost everywhere approximated by an infinite “stochastic soliton lattice” [7].

$$u(x, t) \sim \sum_{i=1}^{\infty} 2\eta_i^2 \operatorname{sech}^2[\eta_i(x - 4\eta_i^2 t - x_i^0)], \quad (1.84)$$

It is assumed that x_i^0 are independent random values distributed on \mathbb{R} according to the Poisson distribution with the density parameter $\beta \ll 1$, i.e. the probability of having n solitons within the interval $\Delta \subset \mathbb{R}$ is given by

$$P_{\Delta}(n, \beta) = e^{-\beta|\Delta|} \frac{(\beta|\Delta|)^n}{n!}.$$

The soliton gas is characterised by the spectral distribution function, or *density of states* (DOS)

$f(\eta, x, t)$ defined such that $f(\eta_0, x_0, t_0)d\eta dx$ is the number of solitons found at $t = t_0$ in the element $[\eta_0, \eta_0 + d\eta] \times [x_0, x_0 + dx]$ of the spectral phase space. Without loss of generality, one can assume $\eta \in [0, 1]$. The total spatial density of the soliton gas is then given by $\beta = \int_0^1 f(\eta)d\eta$. For a rarefied soliton gas described by equation (1.84), $\beta \ll 1$.

The macroscopic (large-scale, average) properties of soliton gas are determined by the “microscopic” elementary processes of pairwise soliton interactions, which are:

(i) elastic, i.e. preserving the IST spectrum values η_j , so that the solitons retain their amplitudes and speeds after the interaction;

(ii) accompanied by the phase (position) shifts [125]: namely, the collision of two solitons with spectral parameters $\eta_i > \eta_j$, $i \neq j$ results at $t \rightarrow \infty$ in the additional phase (position) shifts given by

$$\Delta_{ij} \equiv \Delta(\eta_i, \eta_j) = \frac{1}{\eta_i} \ln \left| \frac{\eta_i + \eta_j}{\eta_i - \eta_j} \right|, \quad (1.85)$$

so that the taller soliton acquires shift forward and the smaller one – shift backwards [126]. The total phase shift Δ_i of a given soliton with spectral parameter η_i after its interaction with M solitons with parameters η_j , $j = 1, \dots, M$, $j \neq i$, is equal to the sum of the individual phase shifts, $\Delta_i = \sum_{j=1}^M \Delta_{ij}$.

Consider the propagation of a “test” soliton with spectral parameter $\eta \in [0, 1]$ in a uniform (equilibrium) rarefied soliton gas with a given DOS $f(\mu)$. Due to the collisions of the “ η -soliton” with the “ μ -solitons” ($\mu \neq \eta$) in the gas, the effective (mean) velocity of this test soliton is approximately evaluated as

$$s(\eta) \approx 4\eta^2 + \frac{1}{\eta} \int_0^1 \ln \left| \frac{\eta + \mu}{\eta - \mu} \right| f(\mu) [4\eta^2 - 4\mu^2] d\mu, \quad (1.86)$$

where the leading order term represents the speed of “free” soliton $s_0(\eta) = 4\eta^2$ and the integral term gives an effective correction to the average velocity due to soliton collisions. The modification of the effective soliton velocity due to its propagation in a soliton gas is illustrated in Fig. 17.

In a weakly non-uniform gas, the DOS f becomes a slow function of x, t . The preservation of

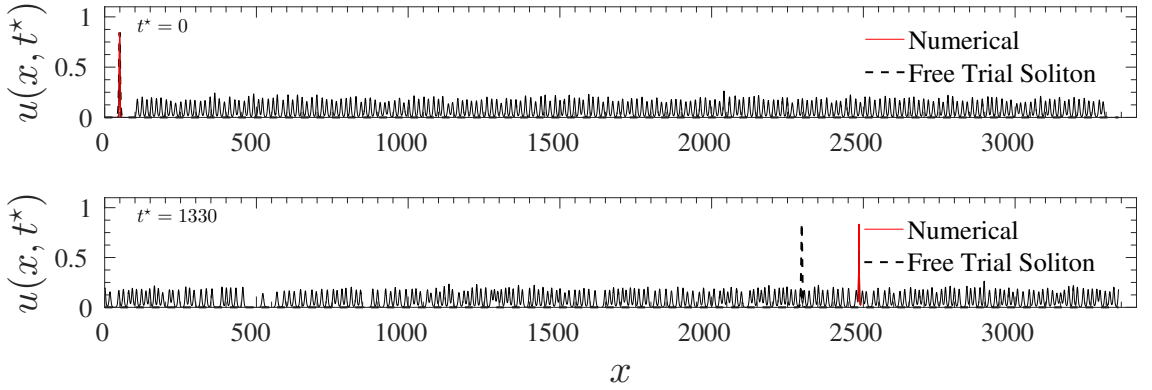


Figure 17: (adapted from [7] with permission from authors.) Comparison for the propagation of a free soliton with the spectral parameter $\eta = \eta_1$ in a void (black dashed line) with the propagation of the test soliton with the same spectral parameter η_1 (red solid line) through a one-component rarefied soliton gas with the DOS $f = f_0\delta(\eta - \eta_0)$. One can see that the test soliton propagates faster in the gas due to the interactions.

the spectral values η_i in time (isospectrality) under the KdV evolution implies the conservation equation for $f(\eta, x, t)$,

$$f_t + (sf)_x = 0, \quad (1.87)$$

which, together with the expression (1.86) for the transport velocity $s(\eta)$, constitutes the kinetic equation for rarefied soliton gas introduced by Zakharov [47].

The generalisation of Zakharov's approximate kinetic equation to the case of dense ($\beta = \mathcal{O}(1)$) soliton gas was derived in [48] using the finite-gap spectral theory and the thermodynamic limit of multiphase Whitham modulations equations. It was shown that in a dense KdV soliton gas the transport velocity $s(\eta)$ satisfies the linear integral equation

$$s(\eta) = 4\eta^2 + \frac{1}{\eta} \int_0^1 \ln \left| \frac{\eta + \mu}{\eta - \mu} \right| f(\mu) [s(\eta) - s(\mu)] d\mu. \quad (1.88)$$

Equation (1.88) can be viewed as the equation of state of the KdV soliton gas. The transport equation (1.87) complemented by the equation of state (1.88) represents the required nonlinear spectral kinetic equation for a dense soliton gas.

One can see from the comparison of the equations of state (1.88) and (1.86) that the net effect of soliton collisions in a dense KdV soliton gas can be evaluated using the elementary phenomenological principle introduced by Zakharov in [47] for a rarefied gas, one simply replaces the approx-

imate, unperturbed soliton velocities $4\eta^2$ and $4\mu^2$ in the interaction (integral) term of the equation of state (1.86) for a rarefied soliton gas with their actual, effective values $s(\eta)$ and $s(\mu)$ respectively. This observation suggests a broad generalisation of the kinetic equation for the KdV soliton gas to other integrable equations [49] as follows.

Consider a scalar (unidirectional) integrable equation of dispersive hydrodynamic type

$$u_t + F(u)_x = (D[u])_x, \quad (1.89)$$

where $F(u)$ is the nonlinear hyperbolic flux and $(D[u])_x$ is the dispersion operator. E.g. for the KdV equation (1.82) $F(u) = 3u^2$, $(D[u])_x = -u_{xxx}$. Let the soliton solution of equation (1.89) be characterised by the IST spectral parameter $\lambda \in \mathbb{R}$, so that $s_0(\lambda)$ is the soliton velocity and $\Delta(\lambda, \mu)$ is the expression for the phase (position) shift in a two-soliton interaction with $\lambda > \mu$. Introduce the DOS $f(\lambda)$, where $\lambda \in \Gamma \subset \mathbb{R}$. Then the equation of state of this soliton gas is given by

$$s(\lambda) = s_0(\lambda) + \int_{\Gamma} \Delta(\lambda, \mu)[s(\lambda) - s(\mu)]f(\mu)d\mu. \quad (1.90)$$

The system (1.87), (1.90) represents the general kinetic equation for soliton gas in unidirectional dispersive hydrodynamics.

As shown in [49, 124, 127] the kinetic equation (1.87), (1.90) admits a family of hydrodynamic reductions obtained by the multi-component ‘‘cold-gas’’ ansatz for the DOS

$$f(\lambda, x, t) = \sum_{j=1}^M w_j(x, t)\delta(\lambda - \zeta_j), \quad (1.91)$$

where $w_j(x, t) > 0$ are the components’ weights, and $\{\zeta_j\}_{j=1}^M \subset \Gamma$ ($\zeta_j \neq \zeta_k \iff j \neq k$). In practice the multicomponent delta-function distribution (1.91) is realised by placing the all discrete spectrum eigenvalues in some narrow vicinity of ξ_j ’s.

The substitution of (1.91) into the kinetic equation (1.87), (1.90) reduces it to a system of hydrodynamic conservation laws

$$(w_i)_t + (w_i s_i)_x = 0, \quad i = 1, \dots, M, \quad (1.92)$$

where the component densities $w_i(x, t)$ and the transport velocities $s_j(x, t) \equiv s(\zeta_j, x, t)$ are related algebraically:

$$s_j = s_{0j} + \sum_{m=1, m \neq j}^M \Delta_{jm} w_m (s_j - s_m), \quad j = 1, 2, \dots, M. \quad (1.93)$$

Here

$$s_{0j} \equiv s_0(\zeta_j), \quad \Delta_{jm} \equiv \Delta(\zeta_j, \zeta_m), \quad j \neq m. \quad (1.94)$$

The system (1.92), (1.93) is called the cold-gas M -component hydrodynamic reduction of the spectral kinetic equation.

Symmetrisation. Assume that the phase-shift kernel $\Delta(\eta, \mu)$ in the equation of state (1.90) can be represented as

$$\Delta(\lambda, \mu) = a(\mu)\epsilon(\lambda, \mu), \quad \text{where } \epsilon(\lambda, \mu) = \epsilon(\mu, \lambda) > 0, \quad \lambda \neq \mu, \quad (1.95)$$

for some non-singular real function $a(\mu) \neq 0$ (e.g. for the KdV equation we have $a(\mu) = \mu$, $\epsilon(\lambda, \mu) = \frac{1}{\lambda\mu} \ln \left| \frac{\lambda+\mu}{\lambda-\mu} \right|$, see (1.88)).

Then the following theorem can be proved:

Theorem [127]. *M -component cold-gas reductions (1.92), (1.93) of the generalised kinetic equation (1.87), (1.90) with the interaction kernel satisfying (1.95) are hyperbolic, linearly degenerate integrable hydrodynamic type systems for any $M \in \mathbb{N}$.*

Specifically, it was shown in [127] that the following fundamental properties are satisfied for the system (1.92), (1.93):

(i) *Riemann invariants.*

Let $u_j = a_j w_j$, where the symmetrising coefficients $a_j = a(\eta_j)$ are defined by (1.95). Then there exists the invertible point transformation $\mathbf{w} \rightarrow \mathbf{r}$ that reduces the system (1.92), (1.93) to the diagonal (Riemann invariant) form

$$\frac{\partial r_i}{\partial t} + V_i(\mathbf{r}) \frac{\partial r_i}{\partial x} = 0, \quad i = 1, 2, \dots, M, \quad (1.96)$$

where the characteristic velocities V_i are expressed in terms of the Riemann invariants r_1, r_2, \dots, r_N as

$$V_i(\mathbf{r}) = s_i(w_1(\mathbf{r}), w_2(\mathbf{r}), \dots, w_M(\mathbf{r})), \quad i = 1, 2, \dots, M. \quad (1.97)$$

Here $s_i(w_1, \dots, w_M)$ are solutions of the system (1.93),

(ii) *Linear degeneracy.*

The characteristic velocities V_j of the diagonal system (1.96) satisfy

$$\partial_j V_j = 0, \quad j = 1, 2, \dots, M, \quad \text{where} \quad \partial_j \equiv \partial/\partial r_j, \quad (1.98)$$

so that system (1.92), (1.93) is linearly degenerate in the Lax sense [128].

(iii) *Semi-Hamiltonian property.*

In addition to (1.98), the characteristic velocities $V_i(\mathbf{r})$ satisfy the overdetermined system

$$\partial_j \frac{\partial_k V_i}{V_k - V_i} = \partial_k \frac{\partial_j V_i}{V_j - V_i}, \quad i \neq j \neq k, \quad (1.99)$$

for each three distinct characteristic velocities ($\partial_k \equiv \partial/\partial r_k$). Diagonal hydrodynamic type systems satisfying (1.99) are called semi-Hamiltonian [129]. The semi-Hamiltonian property guarantees integrability of the hydrodynamic type system via the Generalised Hodograph Transform.

In the context of this PhD project we shall not be concerned with integrability of the multicomponent hydrodynamic reductions (1.92), (1.93) but will use the linear degeneracy property (1.98), which implies that the solution of the Riemann problem (the problem of the resolution of an initial discontinuity) for such systems contains only constant states separated by contact discontinuities [130].

The spectral kinetic equation can be derived for the soliton and breather gases for the 1D fNLSE. The key difference compared to the KdV theory or the general theory of unidirectional soliton gas outlined above is that for the fNLSE the discrete eigenvalues of the Zakharov-Shabat operator (1.33), corresponding to the fNLSE solitons, are complex, $\{\lambda_i, \bar{\lambda}_i\} \in \mathbb{C}$. However, since the

solitons of the fNLSE also exhibit elastic pairwise collisions characterised by the known position shifts [23] the kinetic equation for the fNLSE soliton gas can be constructed using the same phenomenological principles [49] and has the general form (1.87), (1.90), where

$$s_0(\lambda) = -4\text{Re}\lambda, \quad \Delta(\lambda, \mu) = \frac{1}{\text{Im}\lambda} \ln \left| \frac{\mu - \bar{\lambda}}{\mu - \lambda} \right|, \quad (1.100)$$

and the integration in the equation of state is performed over some 2D or 1D compact domain Γ in the complex plane. Explicitly we have [49]

$$f_t + (fs)_x = 0, \quad (1.101)$$

$$s(\lambda, x, t) = -4\text{Re}\lambda + \frac{1}{\text{Im}\lambda} \iint_{\Gamma^+} \ln \left| \frac{\mu - \bar{\lambda}}{\mu - \lambda} \right| [s(\lambda, x, t) - s(\mu, x, t)] f(\mu, x, t) d\xi d\zeta,$$

where $\mu = \xi + i\zeta$ and $\Gamma^+ \subset \mathbb{C}^+ \setminus i\mathbb{R}^+$ is a 1D or 2D compact domain. A special type of the fNLSE soliton gas with $\Gamma^+ \subset i\mathbb{R}^+$ is called the bound state (non-propagating) soliton gas and it requires a separate consideration. Kinetic equation (1.101) has been recently systematically derived in [53] using the thermodynamic limit of the fNLSE-Whitham modulation equations, an extension of the original KdV procedure developed in [48].

Breather gas is spectrally characterised by a vertical branch cut, $\lambda \in [-iq, iq]$, $q > 0$, corresponding to the plane wave background of the amplitude q , and the discrete spectrum values λ_j distributed with some density over a compact 1D or 2D Schwarz-symmetric domain in the spectral complex plane, so that one has [53]:

$$s_0(\lambda) = -2 \frac{\text{Im}[\lambda R_0(\lambda)]}{\text{Im}[R_0(\lambda)]}, \quad \Delta(\lambda, \mu) = \frac{1}{\text{Im}[R_0(\lambda)]} D(\lambda, \mu), \quad (1.102)$$

where

$$D(\lambda, \mu) = \left[\ln \left| \frac{\mu - \bar{\lambda}}{\mu - \lambda} \right| + \ln \left| \frac{R_0(\lambda)R_0(\mu) + \lambda\mu + q^2}{R_0(\bar{\lambda})R_0(\mu) + \bar{\lambda}\mu + q^2} \right| \right]. \quad (1.103)$$

Here, $R_0(z) = \sqrt{z^2 + q^2}$ (with the branch cut $[-iq, iq]$, and the branch of the radical defined by $R_0(z) \rightarrow z$ as $z \rightarrow \infty$). The Schwarz symmetry means that, if λ belongs to Γ , so does $\bar{\lambda}$. One can see that the velocity $s_0(\lambda)$ in (1.102) coincides with the group velocity of the Tajiri-Watanabe breather (cf. (1.22)) while the integral kernel $\Delta(\lambda, \mu)$ can be identified with the known expressions for the position shift in elastic two-breather interactions [131, 132]. This identification

will be performed in Chapter 5 of this Thesis.

The general configuration of a breather gas can be viewed as a dense gas of the Tajiri-Watanabe breathers, cf. (1.21). By choosing the DOS spectral support Γ in a special way, one can consider the “rogue wave gas” consisting of one of the special breathers: AB, KM or PS, see Section 1.1.7.

1.6 Numerical Methods

In Section 1.4, the IST method to solve the fNLSE has been introduced, and different families of solutions and the corresponding nonlinear spectra have been discussed. However, the analytical solutions of the direct scattering problem and the explicit evaluation of the spectrum can be obtained only for some specific potentials. Therefore, numerical methods are usually employed to calculate the IST spectra of generic potentials. We introduce here two algorithms adopted to solve numerically the direct scattering problem (1.33).

1.6.1 Fourier collocation method

The first algorithm considered here is the so-called *Fourier collocation method* [133, 134]. This method relies on the possibility to rewrite the scattering problem with periodic boundary conditions in the Fourier space and thus solve a matrix eigenvalue problem for the Fourier coefficients. One can rewrite the Zakharov–Shabat scattering problem (1.33) in the form:

$$\begin{pmatrix} -\partial_x & u \\ u^* & \partial_x \end{pmatrix} R = i\lambda R, \quad (1.104)$$

and then expand the eigenfunctions $R = (\phi_1, \phi_2)^T$ and the potential u into Fourier series. For this purpose, the spacial domain of the problem is reduced to the interval $[-\frac{L}{2}, \frac{L}{2}]$, such that the

eigenfunctions and the potential can be expand in $2N + 1$ Fourier modes:

$$\begin{aligned}\phi_{1/2}(x) &= \sum_{n=-N}^N a_{1/2,n} e^{ik_0 n x}, \\ u(x, 0) &= \sum_{n=-N}^N c_n e^{ik_0 n x},\end{aligned}\tag{1.105}$$

where $k_0 = \frac{2\pi}{L}$. Substituting these expansions in (1.33), the scattering problem takes the form of the following eigenvalue system:

$$\begin{pmatrix} -B_1 & B_2 \\ B_2^\dagger & B_1 \end{pmatrix} \begin{pmatrix} A_1 \\ A_2 \end{pmatrix} = iz \begin{pmatrix} A_1 \\ A_2 \end{pmatrix},\tag{1.106}$$

where:

$$\begin{aligned}B_1 &= ik_0 \text{diag}(-N, -N + 1, \dots, N - 1, N), \\ B_2 &= \begin{pmatrix} c_0 & c_{-1} & \cdots & c_{-N} & & & & \\ c_1 & c_0 & c_{-1} & \ddots & c_{-N} & & & \\ \vdots & c_1 & c_0 & \ddots & \ddots & \ddots & \ddots & \\ c_N & \ddots & \ddots & \ddots & \ddots & \ddots & \ddots & c_{-N} \\ & c_N & \ddots & \ddots & \ddots & \ddots & \ddots & \vdots \\ & & \ddots & \ddots & \ddots & \ddots & \ddots & c_{-1} \\ & & & c_N & \cdots & c_1 & c_0 & \end{pmatrix}, \\ A_1 &= (a_{1,-N}, a_{1,-N+1}, \dots, a_{1,N})^T, \\ A_2 &= (a_{2,-N}, a_{2,-N+1}, \dots, a_{2,N})^T,\end{aligned}$$

and B_2^\dagger is the Hermitian of B_2 . The matrix B_1 corresponds to the ∂_x operator in the Fourier space and the matrix B_2 is the convolution for the functional multiplication by $u(x, 0)$. The dimension of the matrix in Eq. (1.106) is $2(2N + 1)$. The use of Fourier expansions in the derivation of the algorithm naturally introduces a periodisation of the initial potential with a characteristic period L . Thus, one should interpret the spectrum obtained here as the FGT spectrum. In particular, the output of the algorithm is a series of ‘‘close’’ discrete points that represent the main spectrum of the periodic potential, the ends points delimiting the spectral bands, c.f. Section 1.4.2. Moreover, solving the eigenvalue problem for N even (odd), which yields periodic (anti-periodic) eigenfunc-

tions, identifies the points of the main spectrum for $\Delta(\lambda) = +2$ ($\Delta(\lambda) = -2$).

1.6.2 Boffetta-Osborne method

The second algorithm adopted in this work to solve the direct scattering problem allows us to determine if any given point on the complex spectral plain belongs to the nonlinear spectrum of the considered potential [26, 135]. Considering the periodic problem where $u(x, t) = u(x + L, t)$, the direct scattering problem (1.33) is written in the form:

$$R_x = \begin{pmatrix} -i\lambda & u \\ -u^* & i\lambda \end{pmatrix} R = Q(\lambda)R, \quad (1.107)$$

where $R = (\phi_1, \phi_2)^T$. The domain is then discretised in $N + 1$ points ($\Delta x = \frac{L}{N}$) and the potential assumes piecewise constant values $u_n = u(x_n)$ where $x_n = x_0 + n\Delta x$. The eigenfunction $R(x)$ can then be obtained integrating the eigenvalue problem on each integral Δx :

$$R(x_n + \Delta x) = U(u_n)R(x_n), \quad (1.108)$$

where $U(u; \lambda, \Delta x)$ is the exponential of the trace-vanishing matrix $Q(\lambda)$:

$$\begin{aligned} U(u) &= e^{\Delta x Q(\lambda)} \\ &= \begin{pmatrix} \cosh(k\Delta x) - \frac{iz}{k} \sinh(k\Delta x) & \frac{\psi}{k} \sinh(k\Delta x) \\ \frac{\psi^*}{k} \sinh(k\Delta x) & \cosh(k\Delta x) + \frac{iz}{k} \sinh(k\Delta x) \end{pmatrix}, \end{aligned} \quad (1.109)$$

and $k^2 = |u|^2 - \lambda^2$ is constant in the interval Δx . Then, introducing the four-component vector field:

$$\Theta(x, \lambda) = (R, R')^T, \quad (1.110)$$

where $R' = \frac{\partial R}{\partial \lambda}$, one can write the recursion relation that yields the numerical approximation of the solution (1.110) at the different nodes:

$$\Theta(x_n + \Delta x) = T(u_n)\Theta(x_n), \quad (1.111)$$

where:

$$T(u_n) = \begin{pmatrix} U(u_n) & 0 \\ U'(u_n) & U(u_n) \end{pmatrix}, \quad (1.112)$$

and $U'(u_n) = \frac{\partial U(u_n)}{\partial \lambda}$. Combining the recursion relation (1.111) evaluated at different nodes, one obtains the numerical approximation

$$\Theta(x_N) = T(u_N)T(u_{N-1}) \dots T(u_{N-2})T(u_1)T(u_0)\Theta(x_0) = \prod_{j=N-1}^0 T(u_j)\Theta(x_0). \quad (1.113)$$

In particular, one can write the scattering matrix S in the form:

$$S(\lambda) = \prod_{j=N-1}^0 T(u_j) = \begin{pmatrix} \mathbf{T}(\lambda) & 0 \\ \mathbf{T}'(\lambda) & \mathbf{T}(\lambda) \end{pmatrix}, \quad (1.114)$$

where $\mathbf{T}(x_0, \lambda) = \prod_{j=N}^0 U(u_j)$ is the monodromy matrix (1.55) and $\mathbf{T}' = \frac{\partial \mathbf{T}}{\partial z}$. The numerical approximation of the monodromy matrix enables us to determine if a given point in the spectral plane belongs to the nonlinear spectrum of the potential in exam. As discussed in Section 1.4.2, the spectral band are identified by the values of λ for which the Floquet discriminant is real and satisfies the condition:

$$\text{Tr}(\mathbf{T}) = \Delta(\lambda) \leq \pm 2. \quad (1.115)$$

In practice, given a periodic potential $u(x, t)$, one can probe the spectral plane to determine for which values of λ this condition is verified, and thus identify the spectral bands that constitute the finite-gap spectrum.

On the other hand, if vanishing boundary conditions are assumed, it is possible to identify the discrete and continuous spectrum of the potential by studying the scattering data of the problem. Considering the potential $u(x)$ defined on the domain $x \in [-L, L]$ with $u(-L) = u(L) = 0$, one can repeat the derivation presented above and obtain the scattering matrix (1.114). Formally, the scattering matrix maps the asymptotic behaviours of the scattering problem solutions from $-\infty$ to $+\infty$. However, we are constrained numerically to the finite domain $[-L, L]$. Then, considering

asymptotic solutions (1.40) (1.41), evaluated at the boundaries of the domain:

$$\begin{aligned} R(-L, z) &= \begin{pmatrix} 1 \\ 0 \end{pmatrix} e^{i\lambda L}, \\ R(L, \lambda) &= a(\lambda) \begin{pmatrix} 1 \\ 0 \end{pmatrix} e^{-i\lambda L} + b(\lambda) \begin{pmatrix} 0 \\ 1 \end{pmatrix} e^{i\lambda L}, \end{aligned} \tag{1.116}$$

the identity (1.113) can be written explicitly as:

$$\begin{pmatrix} R(L, \lambda) \\ R'(L, \lambda) \end{pmatrix} = \begin{pmatrix} \mathbf{T}(\lambda) & 0 \\ \mathbf{T}'(\lambda) & \mathbf{T}(\lambda) \end{pmatrix} \begin{pmatrix} R(-L, \lambda) \\ R'(-L, \lambda) \end{pmatrix}. \tag{1.117}$$

After few algebraic manipulations we obtain the relations between the scattering coefficients and the scattering matrix:

$$\begin{aligned} a(\lambda) &= S_{11} e^{2i\lambda L}, \\ b(\lambda) &= S_{21}, \\ \frac{\partial a(z)}{\partial \lambda} &= [S_{31} + iL(S_{11} + S_{33})] e^{2i\lambda L}, \\ \frac{\partial b(\lambda)}{\partial \lambda} &= S_{41} + iL(S_{43} - S_{21}). \end{aligned} \tag{1.118}$$

The scattering coefficients can be used to determine the discrete and continuous spectrum of the potential with vanishing boundaries condition, see Section 1.4.1. As for the periodic boundary conditions, the algorithm allows us to verify if a given point of the scattering plane λ belongs to the discrete spectrum, i.e. $a(\lambda) = 0$. Moreover, the knowledge of the analytical form of the derivatives of the scattering coefficients (1.118) allows the implementation the standard iterative Newton algorithm to determine the zeros of $a(\lambda)$ with quadratic convergence. On the other hand, the continuous spectrum (1.42) can be computed using the scattering coefficients numerically evaluated along the real axis of the spectral plane.

1.6.3 Local IST

As discussed in Section 1.4, the IST method has been developed to solve integrable nonlinear PDEs. One of the key elements of this method is the evaluation of the nonlinear spectrum, which is the spectral signature of potential that is conserved during the propagation. The IST spectrum

is a *global* characteristic of the potential and does not provide information on the local dynamic of the field. However, a *local* IST procedure has recently been successfully used to identify and classify localised coherent structures that are parts of the larger-domain wave field [8, 84].

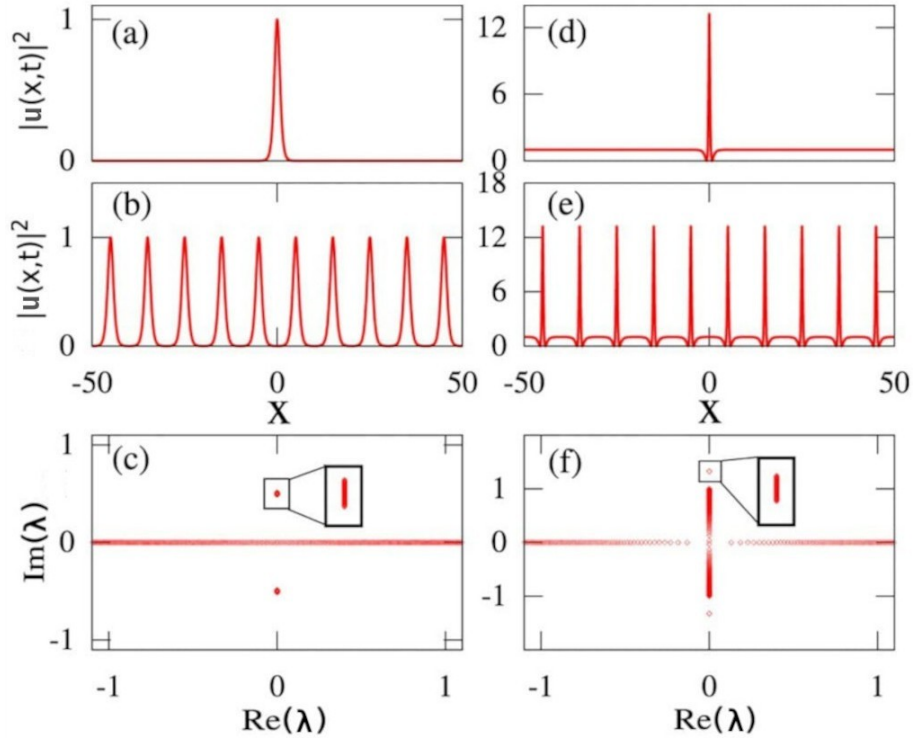


Figure 18: (adapted from [8] with permission from authors.) Example of application of the numerical periodisation procedure to known solution of the fNLSE. (a) Spatial profile of a fundamental soliton . (b) Spatial profile of the fundamental soliton periodised in space. (c) Spectral portrait of the periodised soliton showing that the periodisation procedure produces a band having a small size where the point of discrete spectrum of the exact solution would be. (d) Spatial profile of the KM soliton. (e) Spatial profile of the KM soliton periodised. (f) Spectral portrait of the periodised KM soliton showing that the periodisation procedure produces a band having a small size where the point of discrete spectrum of the exact solution would be.

The numerical methods described in the previous sections are a fundamental tool to investigate the nonlinear spectrum of complex structures and solve direct scattering problems otherwise impossible to tackle analytically. In particular, the Fourier collocation method has been shown to be a reliable and efficient algorithm to evaluate the nonlinear spectrum of decaying potentials, e.g. the solitons solutions [134]. However, to achieve the correct and accurate evaluation of the IST spectrum, a “numerical box” much larger than the typical size of the decaying structure is required. Likewise, in the context of non-decaying potentials such as the SFBs, the size of numerical box needs to be much greater than the typical width of the SFB to capture the important features of the branchcut of the spectrum [8]. Choosing a numerical box of size comparable to the typical size of

the structure, effectively neglecting the informations related to the nonlinear interaction with the surrounding field, leads to an inaccurate computation of the spectrum. As a result the analysis of localised structures emerging from the nonlinear evolution of random wave fields, e.g. PCW or MI, used to rely on fitting procedures. In this context, the localised coherent structures are compared to the well-known analytical profile of SFB solution of the fNLSE [28, 40, 106, 136, 137]. Only recently a new procedure has been developed to overcome the limitations related to the applicability of the IST analysis to localised structures. It has been shown that the spectrum can be accurately computed once the localised structure is properly periodised in space. With the periodisation process a local finite-band approximation of structure is obtained, effectively including the nonlinear interactions of the object with the surrounding wave field [8]. The period, i.e. the size of the truncated portion of wave field in exam, defines the width of the bands in the spectrum, with larger period corresponding to shorter bands, while the shape of the profile determines location and number of bands. An example of the application to the periodisation procedure on simple exact solutions of the fNLSE (soliton and PS) is reported from [8] in Fig. 18.

Thus, the periodisation procedure, providing an effective method to compute the nonlinear spectrum of localised pulses, becomes a key tool to investigate the coherent structure emerging during the nonlinear evolution of random wave fields [84]. The possibility to compute the IST spectrum of the localised pulses enables to identify the structures beyond the well-known exact SFBs solution of the fNLSE, expanding the classification of prototypes of RW event to higher genus breather solution.

Chapter 2

Early stage of integrable turbulence

2.1 Outline of the Problem

The work reviewed in this Chapter enters in the highly active field of research related to integrable turbulence. This statistical approach to the description of the complex spatio-temporal evolution of random wave fields introduced by Zakharov in [37], has produced a wide number of theoretical and experimental results [40, 41, 71, 100, 106, 108, 109]. In particular, this framework has been widely adopted to investigate two families of random systems: the noise-induced modulational instability and the partially coherent waves. Of particular interest in our work is the study of the evolution, in the framework of the NLS equation, of PCW with initial Gaussian statistics. The long time evolution of this system in the focusing regime leads to the formation of an heavy-tailed deviation from the initial Gaussian statistics in the probability density function (PDF) of the random wave field amplitude. As we discussed in Section 1.3 this statistical feature is of central importance in relation to the rogue wave events. On the other hand, in the defocusing regime, the nonlinear evolution produces a low-tailed deviation from the initial Gaussian statistical distribution. Similarly to the standard kurtosis, the normalised fourth order moment of the amplitude of the field κ_4 is used to characterise the “heaviness” of the tail of the distribution, i.e. its deviation from the initial statistical distribution:

$$\kappa_4(t) = \frac{\langle |u(x, t)|^4 \rangle}{\langle |u|^2 \rangle^2}, \quad (2.1)$$

with $\langle \dots \rangle$ denoting the ensemble average over a large number of realisations of the random process u . Since we are interested by the statistic of the extreme events in the field, we will study the time evolution of the normalised fourth moment κ_4 (we shall sometimes call it kurtosis although the standard PDF kurtosis has a different normalisation). In the weakly nonlinear regime, it has been analytically demonstrate that the kurtosis increases in the focusing case and decreases in the defocusing [33].

The aim of this work is the characterisation of the early stage of evolution of integrable turbulence in the strongly nonlinear regime. In this context we can exploit the semiclassical framework of the NLS equation:

$$i\varepsilon \frac{\partial u}{\partial t} + \frac{\varepsilon^2}{2} \frac{\partial^2 u}{\partial x^2} + \sigma |u|^2 u = 0, \quad (2.2)$$

where $\varepsilon \ll 1$ is the small parameter and $\sigma = \pm 1$ identifies the focusing and defocusing regimes, respectively. As discussed in Section 1.5.2, this formulation naturally encodes a scale separation that will enable us to asymptotically study the early stage of the evolution of the system. Moreover, introducing the Madelung transformation we can reformulate the problem as the dispersive hydrodynamic system (1.72) where $\rho(x, t)$ represents the instantaneous power (or the fluid depth) and $v(x, t)$ the chirp (or the horizontal fluid velocity). In this formalism we can derive an equation for the evolution of the normalised fourth order moment:

$$\frac{d\kappa_4}{dt} = \frac{2}{\langle N \rangle^2 L} \int_0^L \langle \rho v \rho_t \rangle dt, \quad (2.3)$$

with N the optical power; the integral over the period L here defines the average on the domain.

The purpose of this work is to derive an analytical expression for the short-time evolution of $\kappa_4(t)$ as solution of (2.3) and verify the result with the direct numerical simulation of the NLS equation.

2.2 Summary of Results and Outlook

In the context of the dispersionless limit of the semiclassical theory of the NLS equation, we derive an analytical expression for the short time evolution of the normalised fourth-order moment

of the field κ_4 . The results are then verified by comparing the analytical description to the direct numerical simulation of the NLS equation. I have been directly involved in the derivation of the analytical results and in the numerical simulation performed on the PhLAM Linux Clusters of Université de Lille, France.

The results of the project appeared in:

- **G. Roberti**, G. El, S. Randoux and P. Suret. “Early stage of integrable turbulence in the one-dimensional nonlinear schrödinger equation: A semiclassical approach to statistics”, Phys. Rev. E, 100:032212, 2019

The solution of equation (2.3) is obtained in the short-time asymptotics, when the dynamical and statistical features of the field can be modelled by the nonlinear geometric optics equations

$$\begin{aligned}\rho_t + (\rho u)_x &= 0, \\ v_t + vv_x - \sigma \rho_x &= 0,\end{aligned}\tag{2.4}$$

which is the dispersionless limit $\varepsilon \rightarrow 0$ of the hydrodynamic system (1.72). In this context the solution $\rho(x, t)$ and $v(x, t)$ of the system (2.4) are obtained as power-series expansion in time. Given the solution of the dispersionless system, the expression for $\kappa_4(t)$ in the early stage of evolution of the wave field can be computed:

$$\begin{aligned}\kappa_4(t) - \kappa_4(0) &= \frac{\sigma t^2}{\langle N \rangle^2 L} \int_0^L \langle \rho_0 \rho_{0x}^2 \rangle dx \\ &- \frac{t^4}{2 \langle N \rangle^2 L} \int_0^L \left\langle \frac{2}{3} \rho_0^2 \rho_{0x} \rho_{0xxx} + \frac{17}{6} \rho_0 \rho_{0x}^2 \rho_{0xx} + \frac{1}{2} \rho_{0x}^4 \right\rangle dx + \mathcal{O}(t^6),\end{aligned}\tag{2.5}$$

where $\rho_0 = \rho(x, t = 0)$.

From equation (2.5) one can note that the normalised fourth-order moment $\kappa_4(t)$ of the field evolves quadratically with time at leading order for $t \ll 1$. Moreover the value of $\sigma = \pm 1$, i.e. the regime of the NLS equation, defines the increase/decrease of the value of κ_4 in time giving an insight in the heavy/low tail of the PDF at the long time propagation.

The expression in (2.5) is a general result derived with the only assumption $\varepsilon \ll 1$, without any assumption on the statistic of the initial random wave field. However, this result can be further simplified assuming Gaussian statistics of the initial condition, i.e. PCW's initial condition.

Moreover, if we assume the shape of the Fourier power spectrum to be Gaussian

$$|u_0(k)|^2 = n_0 e^{\frac{-k^2}{\Delta k^2}}, \quad (2.6)$$

with $n_0 \in \mathbb{R}^+$ the normalised amplitude and Δk the width of the spectrum, we can write the short time evolution of the normalised fourth-order moment $k_4(t)$ as:

$$\kappa_4(t) - \kappa_4(0) = 2\sigma N(\Delta k)^2 t^2 + \frac{22N^2(\Delta k)^4}{3} t^4 + \mathcal{O}(t^6). \quad (2.7)$$

This formula (2.7) has been compared to direct numerical simulations of the NLS equation in the focusing and defocusing regimes showing an excellent agreement for the early stage of the evolution. We note that, while the short-time approximation may seem to have a restricted application range, it, in fact, corresponds to the quite appreciable propagation distances in the context of optical fibres.

The analytical results outlined in this work provide a convincing argument on applicability of the semiclassical approach, suggesting new lines of future theoretical research:

- Application of the methodology developed in this work to investigate the early stage of evolution of PCW in other nonlinear integrable system exhibiting RW solutions such as the modified KdV equation and integrable versions of vector NLS equations.
- Exploiting the full potential of the semiclassical approach beyond the short time asymptotics application, one could extend the description of the development of integrable turbulence at longer time.

Early stage of integrable turbulence in the one-dimensional nonlinear Schrödinger equation: A semiclassical approach to statistics

Giacomo Roberti,¹ Gennady El,¹ Stéphane Randoux,^{2,3} and Pierre Suret^{2,3,*}

¹*Department of Mathematics, Physics and Electrical Engineering, Northumbria University, Newcastle upon Tyne, NE1 8ST, United Kingdom*

²*University of Lille, CNRS, UMR 8523 - Physique des Lasers Atomes et Molécules (PHLAM), F-59000 Lille, France*

³*Centre d'Etudes et de Recherches Lasers et Applications (CERLA), Cité scientifique, 59655 Villeneuve d'Ascq Cedex, France*



(Received 8 January 2019; published 19 September 2019)

We examine statistical properties of integrable turbulence in the defocusing and focusing regimes of one-dimensional small-dispersion nonlinear Schrödinger equation (1D-NLSE). Specifically, we study the 1D-NLSE evolution of partially coherent waves having Gaussian statistics at time $t = 0$. Using short time asymptotic expansions and taking advantage of the scale separation in the semiclassical regime we obtain a simple explicit formula describing an early stage of the evolution of the fourth moment of the random wave field amplitude, a quantitative measure of the “tailedness” of the probability density function. Our results show excellent agreement with numerical simulations of the full 1D-NLSE random field dynamics and provide insight into the emergence of the well-known phenomenon of heavy (respectively, low) tails of the statistical distribution occurring in the focusing (respectively, defocusing) regime of 1D-NLSE.

DOI: [10.1103/PhysRevE.100.032212](https://doi.org/10.1103/PhysRevE.100.032212)

I. INTRODUCTION

Turbulence is one of the most recognizable forms of nonlinear motion that has been, and continues to be, the subject of very active research in classical (viscous) fluid dynamics [1]. This fundamental phenomenon occurs also in dispersive media where turbulence is associated with the generation of complex, spatiotemporal statistical ensembles of interacting nonlinear waves. The theory of weak wave turbulence in dispersive systems was developed by V. E. Zakharov in the 1960s [2]. The wave turbulence (WT) theory provides a framework for the statistical description of weak turbulence in nonintegrable wave systems dominated by resonant interactions. One of the most important results in wave turbulence theory is the discovery by V. E. Zakharov in 1965 of a new type of solutions to kinetic equations corresponding to a constant energy flux through scales. These solutions are called Kolmogorov-Zakharov spectra, and they have been observed in a variety of experiments performed in turbulent wave systems [3].

The notion of turbulence can be extended to the realm of integrable systems where it is understood as complex spatiotemporal dynamics of nonlinear random waves in physical systems whose behavior is well modeled by integrable nonlinear partial differential equations such as the Korteweg-de Vries (KdV) equation or the one-dimensional nonlinear Schrödinger equation (1D-NLSE). Since many nonlinear

wave systems can be described by partial differential equations having an integrable core part the emerging theory of *integrable turbulence*, also initiated by Zakharov [4], has become an active field of research with the theoretical (mostly numerical) developments supported by a number of experimental observations [4–14]. Given the absence of resonances in integrable systems, the mechanisms underlying integrable turbulence are of profoundly different nature from those found in the standard WT [2,3,15] and thus require very different theoretical approaches to their study.

General properties of integrable wave systems can be in principle analyzed using the inverse scattering transform (IST) method [16], which thus provides a powerful analytical framework for the description of integrable turbulence. However, only very few analytical results are available in this direction due to the high complexity of the IST with random potentials, so alternative approaches based on, e.g., asymptotic expansions could prove very valuable. In this paper, such an asymptotic approach is developed in application to integrable turbulence in the framework of 1D-NLSE which plays a fundamental role in nonlinear physics due to the unique combination of complete integrability and the ubiquity in a broad range of applications.

Depending on the relative signs of dispersion and nonlinearity the 1D-NLSE can exhibit focusing or defocusing properties which have strong effect on the evolution of the statistics of random solutions. Generally speaking, nonlinear wave propagation in media with self-focusing nonlinearity tends to produce heavy-tailed deviations from the initial Gaussian statistics, observed in the probability density function (PDF) of the random wave field amplitude. In recent years, the question of the emergence of heavy-tailed statistical distributions has been extensively studied in relation to the occurrence of extreme events such as rogue waves, mainly

*Corresponding author: Pierre.Suret@univ-lille.fr

in the physical contexts of fluid dynamics [17–20] and optics [7,8,14,21–25]. Even though statistical properties of nonlinear defocusing media have been less extensively examined, several experiments have shown that defocusing nonlinearities tend to produce low-tailed deviations from the initial Gaussian statistical distribution [26,27].

The “heaviness” of the tail in the PDF of the field amplitude distribution is characterized by the kurtosis (the fourth standardized moment of the PDF). In the WT setting, the theory based on the derivation of quasikinetiic equations for the lowest-order moments of the wave field has been developed in Refs. [15,28–30]. This theory has confirmed that the kurtosis increases in the focusing case and decreases in the defocusing case while the initial field is characterized by Gaussian statistics. However, this kind of analytical treatment is inherently *limited to the weakly nonlinear* propagation regime.

To evaluate kurtosis for certain regimes of the fully nonlinear integrable turbulence in the 1D-NLSE one can take advantage of the mathematical framework of dispersive hydrodynamics—the semiclassical theory of nonlinear dispersive waves [31]. The definitive feature of dispersive hydrodynamics is the presence of two distinct spatiotemporal scales: the long scale specified by initial conditions and the short scale by the internal coherence length (i.e., the typical size of the coherent soliton-like structures). This scale separation enables one to analyze the wave evolution asymptotically.

The semiclassical, dispersive hydrodynamic approach describes the propagation regimes of a completely opposite nature compared to the regimes considered in the framework of wave turbulence theory. This approach can be applied to the 1D-NLSE propagation if the initial scale of the fluctuations of the power of the complex field $|\psi|^2$ are much larger than the one corresponding to the balance between nonlinearity and dispersion. In most of the standard cases, this separation of scales corresponds to situations where the nonlinear part of the energy is much greater than the linear (kinetic) part of the energy at the initial time. As shown in Ref. [32], this scale separation permits one to split the development of integrable turbulence into two distinct stages characterized by qualitatively different dynamical and statistical features. At the initial (we shall call it “prebreaking”) stage of the evolution nonlinear effects dominate linear dispersion and the wave fronts of the random initial field experience gradual steepening leading to the formation of gradient catastrophes that are subsequently regularized through the generation of dispersive shock waves in the defocusing regime [33] and of Peregrine-like breather sequences in the focusing regime [34]. As shown in Ref. [32], the dynamical and statistical features that occur at the prebreaking stage of the defocusing 1D-NLSE can be interpreted in terms of the evolution of random Riemann waves.

In this paper, we extend the analysis of the previous works based on the semiclassical approach to the 1D-NLSE with random initial data by calculating the short-time evolution of the the normalized fourth moment κ_4 of the amplitude of the field. Similarly to the standard kurtosis, the quantity κ_4 describes the degree of the deviation from the initial statistical distribution which is often assumed to be Gaussian [35]. Using the

semiclassical Madelung transform and performing the zero dispersion limit, we derive a general analytical expression for the short-time evolution of the fourth moment of the random 1D-NLSE wave field in terms of hydrodynamic variables, and show that this expression can be further simplified for the wave field having Gaussian statistics at initial time. Our analytical asymptotic results are shown to be in excellent agreement with numerical simulations of the evolution of partially coherent initial data in 1D-NLSE.

The paper is organized as follows: In Sec. II, using the semiclassical approximation, we identify the initial stage of the 1D-NLSE development of partially coherent waves with the nonlinearity dominated, dispersionless regime and derive the general expression for the short-time evolution of the fourth-order moment κ_4 as a power-series expansion in time t .

In Sec. III, we apply the derived formula for κ_4 to the fundamental case of random waves characterized by Gaussian statistics at time $t = 0$. In Sec. IV we provide a comparison between our semiclassical analytical results and numerical simulations of 1D-NLSE.

II. THE DISPERSIONLESS LIMIT OF THE 1D-NLSE AND THE TIME EVOLUTION OF THE FOURTH-ORDER MOMENT OF A RANDOM WAVE FIELD

We consider the 1D-NLSE in the normalized form

$$i\varepsilon \frac{\partial \psi}{\partial t} + \frac{\varepsilon^2}{2} \frac{\partial^2 \psi}{\partial x^2} + \sigma |\psi|^2 \psi = 0, \quad (1)$$

where ψ is a complex field, ε is the dispersion parameter, $\sigma = -1$ in the defocusing regime, and $\sigma = +1$ in the focusing regime.

The 1D-NLSE (1) is considered in a periodic box of size L , $\psi(x + L, t) = \psi(x, t) \forall t$. The field ψ then can be represented as a Fourier series:

$$\psi(x, t) = \sum_k \psi_k(t) e^{\frac{2i\pi}{L} kx} \quad \text{with } k \in \mathbb{Z}, \quad (2)$$

where the Fourier coefficients are given by

$$\psi_k(t) = \frac{1}{L} \int_0^L \psi(x, t) e^{-2i\pi kx} dx. \quad (3)$$

The “density of particles” N and the momentum P represent integrals of motion and are expressed in terms of Fourier coefficients:

$$N = \frac{1}{L} \int_0^L |\psi|^2 dx = \sum_k |\psi_k|^2, \quad (4)$$

$$P = \frac{1}{L} \int_0^L \psi_x \psi^* dx = \sum_k \left(\frac{2\pi ik}{L} \right) |\psi_k|^2. \quad (5)$$

The Hamiltonian, that we represent in the form

$$H = \varepsilon^2 H_L + H_{NL} \quad (6)$$

is also integral of motion, which is naturally split into two parts: the linear (kinetic energy) part,

$$\varepsilon^2 H_L(t) = \frac{\varepsilon^2}{2L} \int_0^L |\psi_x|^2 dx = \frac{\varepsilon^2}{2} \sum_k \left(\frac{2\pi k}{L} \right)^2 |\psi_k|^2, \quad (7)$$

and the nonlinear part,

$$H_{\text{NL}}(t) = \frac{\sigma}{2L} \int_0^L |\psi|^4 dx. \quad (8)$$

We now assume that the Fourier modes at initial time $\psi_{0k} = \psi_k(t=0) = |\psi_{0k}|e^{i\phi_{0k}}$ are complex random variables. The complex field (2) is then a random periodic solution of the 1D-NLSE. No particular hypothesis about statistical properties of ψ_{0k} needs to be introduced at this step but we will show in Sec. III that the main result of our analysis can be simplified if the initial statistics of the random wave field is assumed to be Gaussian. We consider random initial conditions for which N , $H_L(t=0)$ and $H_{\text{NL}}(t=0)$ are all $\mathcal{O}(1)$. This is typically achieved by taking the initial power spectrum $n_{0k} = |\psi_{0k}|^2$ with the characteristic width $\Delta k \simeq 1$, which implies that the typical spatial size of the initial random fluctuations is also of the order of unity and much larger than the internal coherence length (that is, ε). Such random waves are often called *partially coherent*, particularly in the statistical optics context [36].

Given the 1D-NLSE evolution of individual realizations of the random field $\psi(x, t)$ the challenge is to determine the associated evolution of its statistical characteristics such as the PDF of the amplitude $|\psi|$, the power spectrum $|\psi_k|^2$, etc. The particular objective of this paper is to determine the short-time evolution of the normalized fourth moment $\kappa_4(t)$ defined as

$$\kappa_4(t) = \frac{\langle |\psi(x, t)|^4 \rangle}{\langle |\psi(x, t)|^2 \rangle^2}, \quad (9)$$

where the brackets $\langle \dots \rangle$ denote ensemble average performed over a large number of realizations of the random process $\psi(x, t)$. In what follows we shall be using the double average, $\langle \frac{1}{L} \int_0^L |\psi(x, t)|^n dx \rangle$, $n = 2, 4$, in Eq. (9) to compute $\kappa_4(t)$. This is implemented for the sake of convenience in the numerical simulations since, if the averaging procedure over space is not implemented, a very large statistical ensemble must be built, which leads to a large, unrealistic computational cost necessary to reach convergence of $\kappa_4(t)$.

The fourth moment (9) is an important characteristic of the PDF of a random process that quantifies the “heaviness” of its tail. In particular, it can be used to characterize the deviation from Gaussianity in the course of evolution, when the initial statistics is Gaussian, in which case κ_4 is known to be equal 2 [35,37]. The determination of κ_4 , while providing limited information about the PDF as a whole, is particularly relevant to the rogue wave studies as the formation of a “heavy tail” of the PDF is associated with the frequent appearance of large-amplitude events in the random process’ realizations [7,9,20,35].

Figure 1 shows a typical initial evolution of a random wave in the regime where the cubic (Kerr) nonlinearity dominates linear dispersive effects, which corresponds to the semiclassical regime described by Eq. (1) with $\varepsilon \ll 1$ (in the numerical simulations we took $\varepsilon = 0.1$). As shown in Fig. 1, the self-focusing dynamics tends to produce bright peaks while the self-defocusing dynamics leads to a decrease of the peak amplitudes but is accompanied by steepening of slopes in the random amplitude profile. While only the short-time evolution

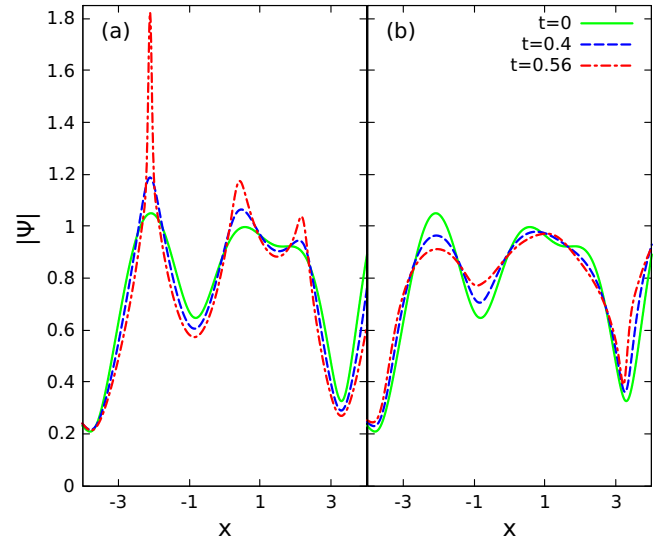


FIG. 1. Numerical simulations of Eq. (1) ($\varepsilon = 0.1$) showing the time evolution of a random field having Gaussian statistics at initial time $t = 0$ (green solid lines). (a) Focusing regime ($\sigma = +1$). At short evolution time ($t < 0.56$ in the plot) the self-focusing dynamics produces bright peaks having the amplitude that grows in time. (b) Defocusing regime ($\sigma = -1$). The self-defocusing dynamics induces the decrease in time of the amplitudes of random peaks. After some time (not reached in the plot), the random wave develops gradient catastrophes that are regularized by dispersive effects leading to the generation of breather structures in the focusing regime and of dispersive shock waves in the defocusing regime.

of the wave system is shown in Fig. 1, a longer development leads to the formation of gradient catastrophes—the explosion of the first derivatives of the wave’s profile. These gradient catastrophes have qualitatively different geometrical nature in the defocusing regime (the wave-breaking singularity [38]) and the focusing regime (the elliptic umbilic singularity [39]). In both cases the gradient catastrophes are regularized by dispersive effects via the generation of nonlinear short wavelength oscillations: breather structures in the focusing regime [40] and dispersive shock waves in the defocusing regime (see Ref. [33] and references therein). For convenience, we shall call the initial nonlinear evolution preceding the formation of gradient catastrophes, the “prebreaking stage” in both defocusing and focusing regimes. The advantage of the semiclassical, dispersive-hydrodynamic approach employed in this paper is that it enables one to asymptotically separate the prebreaking and postbreaking stages of the evolution, which exhibit qualitatively different behaviors and require very different analytical methods for their descriptions.

The starting point of our analysis is the evolution of the nonlinear part H_{NL} of the Hamiltonian. Differentiating (8) we obtain

$$\frac{dH_{\text{NL}}}{dt} = \frac{\sigma}{L} \int_0^L |\psi|^2 \left[\psi \frac{\partial \psi^*}{\partial t} + \psi^* \frac{\partial \psi}{\partial t} \right] dx. \quad (10)$$

Using Eq. (1) and integrating by parts, one readily finds

$$\frac{dH_{\text{NL}}}{dt} = \frac{\sigma \varepsilon}{L} \int_0^L \text{Im}[(\psi_x \psi^*)^2] dx. \quad (11)$$

Now, using the Madelung transformation

$$\psi = \sqrt{\rho} e^{i\phi/\varepsilon}, \quad u = \frac{\partial\phi}{\partial x}, \quad (12)$$

Eq. (11) can be rewritten as

$$\frac{dH_{\text{NL}}}{dt} = \frac{\sigma}{L} \int_0^L \rho u \rho_x dx. \quad (13)$$

Noticing from (9), (4), and (8) that

$$\kappa_4(t) = \frac{2\langle H_{\text{NL}} \rangle}{\sigma \langle N \rangle^2} \quad (14)$$

one obtains

$$\frac{d\kappa_4}{dt} = \frac{2}{\sigma \langle N \rangle^2} \frac{d\langle H_{\text{NL}} \rangle}{dt} = \frac{2}{\langle N \rangle^2 L} \int_0^L \langle \rho u \rho_x \rangle dx. \quad (15)$$

We now derive an analytical expression for $\kappa_4(t)$ for short evolution times, $t \ll 1$. If the dispersion parameter is small, $\varepsilon \ll 1$, the initial dynamics are dominated by nonlinearity. To describe these dynamics analytically, we consider the semiclassical limit of the 1D-NLSE (1) which is found by applying the Madelung transform (12) and letting $\varepsilon \rightarrow 0$. Assuming smooth evolution of $\rho(x, t)$ and $u(x, t)$ in the pre-breaking regime, we obtain in the limit $\varepsilon \rightarrow 0$ the following well-known set of nonlinear geometric optics equations [32, 41–44],

$$\begin{aligned} \rho_t + (\rho u)_x &= 0 \\ u_t + uu_x - \sigma \rho_x &= 0. \end{aligned} \quad (16)$$

If $\sigma = -1$, then Eqs. (16) are identical to the shallow-water equations for an incompressible fluid with $\rho > 0$ and u interpreted as the fluid depth and the depth-averaged horizontal fluid velocity, respectively. In the nonlinear fiber optics context, ρ represents the instantaneous optical power and u represents the instantaneous frequency (or chirp) [45].

Rigorous proofs of the pointwise convergence, as $\varepsilon \rightarrow 0$, of solutions of the 1D-NLSE (1) to the solutions of the dispersionless system (16) with the same initial data, prior to the formation of gradient catastrophe, can be found for certain classes of initial data in Ref. [46] (defocusing) and in Refs. [47,48] (focusing). Some important particular exact solutions of system (16) for the focusing case have been found as early as the 1960s and 1970s (see Refs. [49–51]). A detailed mathematical analysis of the prebreaking dynamics in the defocusing case can be found in Ref. [41] (see also Ref. [52] for the special case of the wave breaking into vacuum).

It follows from the above consideration that, to study the prebreaking dynamics of partially coherent waves in 1D-NLSE (1), we need to be able to describe *random* solutions of system (16) obtained by evolving initial data $\rho(x, 0)$, $u(x, 0)$ with given statistics (e.g., corresponding to the Gaussian statistics of ψ). The study of such solutions has been recently initiated for the defocusing case in the context of the interaction of random Riemann waves in fiber optics [32] (see also Ref. [13]). In this connection one must stress that the term “prebreaking dynamics” is understood here in the probabilistic sense, as for random initial data there is always a nonzero probability of having gradient catastrophe at any, arbitrarily small, moment of time. However, due to initial data having typical size $\Delta x = \mathcal{O}(1)$, we assume that for small ε

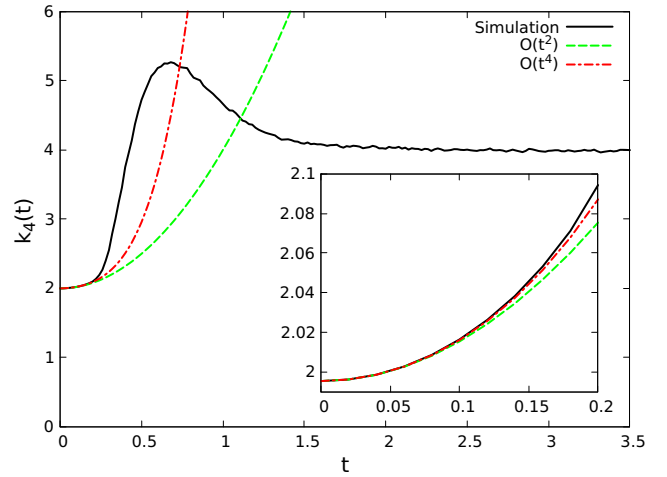


FIG. 2. Black solid line: Numerical simulations of Eq. (1) with $\varepsilon = 0.1$ in the focusing regime ($\sigma = +1$) showing the time evolution of the normalized fourth-order moment of the random field having at $t = 0$ the Gaussian statistics and the Fourier spectrum defined by Eq. (26) with $\Delta k = 1$, $N = 1$. Green dashed line: Analytical result given by Eq. (27) at leading order in t^2 . Red dashed-dotted line: Analytical result given by Eq. (27) including t^2 and t^4 evolution terms. The inset shows an enlarged view of the evolution of $\kappa_4(t)$ for $0 < t < 0.2$.

the contribution of such early gradient catastrophes to the statistics is negligibly small.

To this end, with the short-time, prebreaking evolution in mind, we look for the solutions of Eqs. (16) in the form of the time power-series expansions for the realizations $\rho(x, t)$ and $u(x, t)$:

$$\begin{aligned} \rho(x, t) &= \rho_0(x) + \rho_1(x)t + \rho_2(x)t^2 + \rho_3(x)t^3 + \mathcal{O}(t^4) \\ u(x, t) &= u_1(x)t + u_2(x)t^2 + u_3(x)t^3 + \mathcal{O}(t^4). \end{aligned} \quad (17)$$

These time power-series expansions provide the description of the evolution of ρ and of u over timescales shorter than the typical time t^* at which the gradient catastrophes occur. Rigorously speaking t^* depends on the exact shapes of the initial bell-shaped pulses found in the initial random field but for partially coherent waves with the typical amplitude and width of individual pulses equal to 1, t^* is typically around 0.5, as shown in Ref. [40]. Our theoretical analysis is therefore restricted to evolution times shorter than $t^* \approx 0.5$. This is well illustrated by Figs. 2 and 3 that show that there is a very good quantitative agreement between numerical simulations of Eq. (1) and our analytical results between $t = 0$ and $t = 0.2$.

Moreover, it is important to note that the term $\mathcal{O}(t^4)$ is the error between the Taylor expansion and the solution of the model (16). We derive here a solution of the *zero-dispersion limit of 1D-NLSE* ($\varepsilon \rightarrow 0$) for short time. The neglected term in (16) is $\mathcal{O}(\varepsilon^2)$. Thus, for example, for small but finite values of ε , the second order of the Taylor expansion in time of $\rho(t, x)$ reads $[\rho_2(x) + \mathcal{O}(\varepsilon^2)]t^2$. We show in Sec. III that the results obtained in the zero-dispersion limit are robust and are in good agreement with simulations of 1D-NLSE for $\varepsilon = 0.1$.

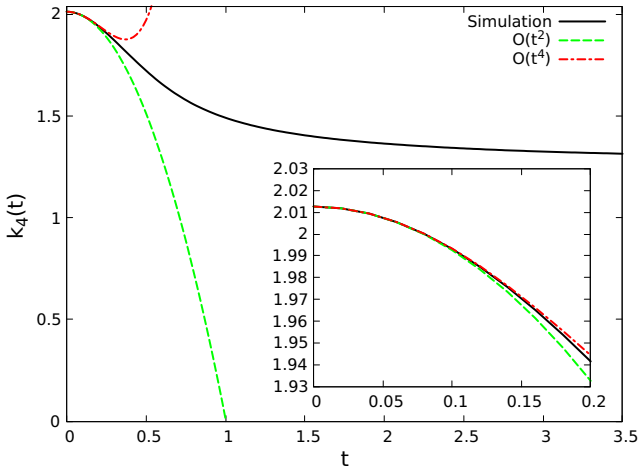


FIG. 3. Black solid line: Numerical simulations of Eq. (1) with $\varepsilon = 0.1$ in the defocusing regime ($\sigma = -1$) showing the time evolution of the normalized fourth-order moment of the random field having at $t = 0$ the Gaussian statistics and the Fourier spectrum defined by Eq. (26) with $\Delta k = 1$, $N = 1$. Green dashed line: Analytical result given by Eq. (27) at leading order in t^2 . Red dashed-dotted line: Analytical result given by Eq. (27) including t^2 and t^4 evolution terms. The inset shows an enlarged view of $\kappa_4(t)$ plot for $0 < t < 0.2$.

In (17) we assumed that initially, $u(x, 0) = u_0 = 0$, which agrees with typical physical condition $u_0 \ll \rho_0$ satisfied in standard realistic experimental conditions. Indeed timescales of amplitude and phase in partially coherent waves are generally similar [$\mathcal{O}(1)$ here]. Considering the normalizations given by the Eq. (12), this means that the derivative of the phase $\frac{\partial(\phi_0/\varepsilon)}{\partial x} = \mathcal{O}(1)$ and thus $u_0 = \frac{\partial\phi_0}{\partial x} = \mathcal{O}(\varepsilon)$, whereas $\rho_0 = \mathcal{O}(1)$. This assumption is for example satisfied in the experiments on the propagation of partially coherent light through optical fibers, see Ref. [32].

Substituting Eqs. (17) into Eqs. (16) we obtain

$$\begin{aligned} \rho(x, t) &= \rho_0 - \frac{1}{4}\sigma[\rho_0^2]_{xx}t^2 + \mathcal{O}(t^4), \\ u(x, t) &= \sigma\rho_{0x}t - \left(\frac{1}{12}[\rho_0^2]_{xxx} + \frac{1}{3}\rho_{0x}\rho_{0xx}\right)t^3 + \mathcal{O}(t^4). \end{aligned} \quad (18)$$

Next, substituting Eqs. (18) into Eq. (15) and integrating in time, we obtain the following expression for the time evolution of the normalized fourth moment of the field amplitude:

$$\begin{aligned} \kappa_4(t) - \kappa_4(0) &= \frac{\sigma t^2}{\langle N \rangle^2 L} \int_0^L \langle \rho_0 \rho_{0x}^2 \rangle dx \\ &\quad - \frac{t^4}{2\langle N \rangle^2 L} \int_0^L \left\langle \frac{2}{3}\rho_0^2 \rho_{0x} \rho_{0xxx} \right. \\ &\quad \left. + \frac{17}{6}\rho_0 \rho_{0x}^2 \rho_{0xx} + \frac{1}{2}\rho_{0x}^4 \right\rangle dx + \mathcal{O}(t^6). \end{aligned} \quad (19)$$

Equation (19) is our main general result. We note that it can also be obtained by a direct substitution of the expansion of $\rho = |\psi|^2$ in the kurtosis formula (9). We note, however, that this would require computing the terms $\mathcal{O}(t^4)$ in the expansion

(18) for ρ , which is avoided here by using in Eq. (15) the $\mathcal{O}(t^3)$ terms in the related expansion for u ensuring the necessary $\mathcal{O}(t^4)$ accuracy in Eq. (19).

One can make now two important observations. The first one is that Eq. (19) shows that the normalized fourth-order moment $\kappa_4(t)$ of the field evolves quadratically with time at leading order for $t \ll 1$. The second observation is that Eq. (19) shows that the increasing or decreasing nature of the time evolution of $\kappa_4(t)$ is determined by the value taken by σ . In the focusing regime ($\sigma = +1$), $\kappa_4(t)$ is an increasing function of time which means that the nonlinear evolution of the wave field is characterized by PDFs that exhibit heavy tailed deviations from the initial statistical distribution. On the other hand, in the defocusing regime ($\sigma = -1$) $\kappa_4(t)$ becomes a decreasing function of time which implies low-tailed deviations from the initial statistics occurring in this regime. The statistical features described by Eq. (19) are in full qualitative agreement with the results that have been recently obtained in numerical and experimental investigations of integrable turbulence [7–9,12,13,26].

Let us emphasize that the decreasing or increasing nature of the time evolution of κ_4 has also been shown to be determined by the defocusing or focusing nature of the propagation regime for *weakly* nonlinear dispersive random waves that are described by the 1D-NLSE [28]. Theoretical approaches that have been used in the weakly nonlinear regime are based on the wave turbulence theory and they consist in deriving quasikinetic equations for the lowest-order moments of the wave field [28,30]. Dispersion plays crucial role in that consideration. Our work is based on a completely different, dispersive-hydrodynamic approach, where dispersive effects are initially not of dominant but of perturbative nature.

III. INITIAL CONDITIONS WITH GAUSSIAN STATISTICS

Equation (19) represents a general result that is derived with the only assumption that $\varepsilon \ll 1$. As we already stressed, it is valid before the typical time of the gradient catastrophe occurrence, i.e., for $t \ll 1$ [for random initial conditions with typical scales for ρ and x variations at $\mathcal{O}(1)$]. Importantly, Eq. (19) is derived without any assumption on the nature of the initial statistics of the random wave field. In this section we show that Eq. (19) can be further simplified if the random wave field taken as initial condition has Gaussian statistics. To this end, we assume that the random initial field $\psi(x, 0)$ is composed of a linear superposition of a large number of *independent* random Fourier modes $\psi_k(t=0) = \psi_{0k} = |\psi_{0k}|e^{i\phi_{0k}}$, so that by the central limit theorem $\psi(x, 0)$ is a Gaussian random field [3].

In the random-phase and amplitude model, $|\psi_{0k}|$ and ϕ_{0k} are both taken as randomly distributed variables [3]. Here we will mainly use the so-called random-phase (RP) model in which only the phases ϕ_{0k} of the Fourier modes are considered as being random [3]. In this model, the phase of each Fourier mode is randomly and uniformly distributed between $-\pi$ and π . Moreover, the phases of separate Fourier modes are assumed to be uncorrelated so that $\langle e^{i\phi_{0k}} e^{i\phi_{0k'}} \rangle = \delta_k^k$. In the above expression, the brackets, as usual, represent the averaging over an ensemble of many realizations of the random process; δ_k^k is the Kronecker symbol defined by $\delta_k^k = 1$ if

$k = k'$ and $\delta_k^{k'} = 0$ if $k \neq k'$. With the assumptions of the RP model described above, the statistics of the initial field is homogeneous, which means that all statistical moments of the initial complex field $\psi(x, t = 0) = \psi_0(x)$ do not depend on x [15,53]. This RP description of the initial random field has been shown to describe in a satisfactory way many experiments performed in the field of integrable turbulence [7–9,12,13,18,19,26,54].

Given the δ correlation of the random phases, the second moment of a field composed from the linear superposition of a large number of *independent* Fourier components having Gaussian statistics is readily evaluated as

$$\langle \psi_k \psi_{k'}^* \rangle = n_k \delta_k^{k'}, \quad (20)$$

and the sixth moment can be factored into products of the second moments by using Wick's decomposition [3]

$$\begin{aligned} & \langle \psi_{k_1} \psi_{k_2} \psi_{k_3} \psi_{k_4}^* \psi_{k_5}^* \psi_{k_6}^* \rangle \\ &= n_{k_1} n_{k_2} n_{k_3} \left[\delta_{k_4}^{k_1} \delta_{k_5}^{k_2} \delta_{k_6}^{k_3} + \delta_{k_4}^{k_1} \delta_{k_5}^{k_3} \delta_{k_6}^{k_2} + \delta_{k_4}^{k_2} \delta_{k_5}^{k_1} \delta_{k_6}^{k_3} \right. \\ & \quad \left. + \delta_{k_4}^{k_2} \delta_{k_5}^{k_3} \delta_{k_6}^{k_1} + \delta_{k_4}^{k_3} \delta_{k_5}^{k_1} \delta_{k_6}^{k_2} + \delta_{k_4}^{k_3} \delta_{k_5}^{k_2} \delta_{k_6}^{k_1} \right]. \end{aligned} \quad (21)$$

Now, using Eq. (21), one can evaluate the coefficient for the $\mathcal{O}(t^2)$ term in the expansion (19):

$$\begin{aligned} & \frac{\sigma}{\langle N \rangle^2 L} \int_0^L \langle \rho_0 \rho_{0x}^2 \rangle dx \\ &= \frac{\sigma}{\langle N \rangle^2} \sum_{k_1, \dots, k_6} \left(\frac{2i\pi}{L} \right)^2 \delta_{k_4+k_5+k_6}^{k_1+k_2+k_3} \\ & \quad \times \langle \psi_{0k_1} \psi_{0k_2} \psi_{0k_3} \psi_{0k_4}^* \psi_{0k_5}^* \psi_{0k_6}^* \rangle (k_2 - k_5)(k_3 - k_6), \end{aligned} \quad (22)$$

where we have used the notation $\psi_{0k_i} = \psi_{k_i}(0)$ for the Fourier component at $t = 0$. Using Eq. (21), we obtain the following expression for the short time evolution of the fourth-order moment of a random wave field that has Gaussian statistics at initial time, i.e., $\kappa_4(0) = 2$:

$$\begin{aligned} \kappa_4(t) - \kappa_4(0) &= -\frac{\sigma}{\langle N \rangle^2} \sum_{k_1, k_2, k_3} n_{0k_1} n_{0k_2} n_{0k_3} \left(\frac{2\pi}{L} \right)^2 \\ & \quad \times [-2(k_2 - k_3)^2] t^2 + \mathcal{O}(t^4), \end{aligned} \quad (23)$$

where $n_{0k_i} = n_{k_i}(0)$ are the components of the power spectrum at $t = 0$. Using Eqs. (5), (4), and (7) and taking into account that $P = 0$ for our random Gaussian field, we can finally rewrite Eq. (23) as

$$\kappa_4(t) - \kappa_4(0) = 8\sigma \langle H_L(0) \rangle t^2 + \mathcal{O}(t^4). \quad (24)$$

[Note that $H_L = \mathcal{O}(1)$ and $H_{NL} = \mathcal{O}(1)$, whereas the linear part of the Hamiltonian (6) is $\mathcal{O}(\varepsilon^2)$].

A similar, but somewhat lengthy, calculation permits one to obtain a more accurate expression that includes $\mathcal{O}(t^4)$ correction (see Appendix):

$$\begin{aligned} \kappa_4(t) - \kappa_4(0) &= 8\sigma \langle H_L(0) \rangle t^2 + \left[\frac{208}{3} \langle H_L(0) \rangle^2 \right. \\ & \quad \left. + 4\langle N \rangle \left\langle \sum_k \left(\frac{2\pi k}{L} \right)^4 |\psi_{0k}|^2 \right\rangle \right] t^4 + \mathcal{O}(t^6). \end{aligned} \quad (25)$$

Equations (24) and (25) show that the time evolution of the fourth moment of the initially Gaussian random wave field is determined by the linear part $H_L(0)$ of the Hamiltonian computed for the initial condition.

Equation (25) can be further simplified if we assume that the shape of the Fourier power spectrum of the initial random field is described by a Gaussian,

$$|\psi_{0k}|^2 = n_0 e^{-\frac{k^2}{(\Delta k)^2}}. \quad (26)$$

The amplitude $n_0 \in \mathbb{R}^+$ has to be determined from the normalization condition provided by Eq. (4). The linear energy density determined from Eq. (7) is $\langle H_L \rangle = \frac{N(\Delta k)^2}{4}$, and we can finally rewrite Eq. (25) only in terms of the density of particles (or optical power) N and of the width Δk of the initial Fourier spectrum,

$$\kappa_4(t) - \kappa_4(0) = 2\sigma N (\Delta k)^2 t^2 + \frac{22N^2 (\Delta k)^4}{3} t^4 + \mathcal{O}(t^6). \quad (27)$$

IV. NUMERICAL SIMULATIONS

In this section, we use numerical simulations of Eq. (1) to investigate the range and the degree of validity of the semi-classical approach to the statistics of integrable turbulence presented in Secs. II and III. The initial condition used in our numerical simulations is a random complex field having Gaussian statistics. The amplitudes of the Fourier components are taken to be distributed according to Eq. (26). In our numerical simulations, the spectral phases ϕ_{0k} are random, statistically independent real numbers, uniformly distributed between $-\pi$ and $+\pi$. The width Δk of the initial spectrum profile (26) is taken to be unity ($\Delta k = 1$), and the value of ε in (1) is taken to be 0.1. The numerical simulations are performed by using a pseudospectral method with the numerical box having size $L = 256$ for the defocusing regime and $L = 128$ in the focusing regime that is discretized by using 2^{16} points.

Figure 2 shows the time evolution of the normalized fourth moment $\kappa_4(t)$ of the random wave field in the focusing regime ($\sigma = +1$). The curve plotted with black line represents the result of the numerical simulation of Eq. (1). In the large box limit ($L \rightarrow \infty$), the value assumed by κ_4 at $t = 0$ should be exactly 2. As can be seen from Fig. 2, in the numerical experiments the value taken by $\kappa_4(t)$ at $t = 0$ slightly differs from 2 [see the inset in Fig. (2)] because the conditions of the central limit theorem are not perfectly fulfilled in our numerical simulations. Indeed, because of the finite value of L , the number of Fourier modes in the spectrum given by Eq. (26) is finite, in particular, in the full width at half maximum (FWHM) we count $\frac{\sqrt{2 \ln 2} L}{\pi}$ modes. Importantly, the deviation of the initial condition from Gaussian statistics affects only the value of $\kappa_4(0)$ in Eq. (21) but not the evolution. In the initial (before the formation of a gradient catastrophe) stage of the nonlinear evolution of the random wave, $\kappa_4(t)$ is at first an increasing function of time that later reaches a maximum around $t \sim 0.6$. Then $\kappa_4(t)$ becomes a decaying function of time that reaches a stationary value around ~ 4 at long evolution time. A similar evolution of $\kappa_4(t)$ has already been evidenced in numerical simulations presented in Ref. [35].

The occurrence of the maximum of $\kappa_4(t)$ has been linked in Ref. [55] to the formation of the Peregrine breathers as the universal local structures regularizing gradient catastrophes in the semiclassical focusing 1D-NLSE [34,40].

The curves plotted with green (dashed) and red (dashed-dotted) lines in Fig. 2 show monotonic evolutions of $\kappa_4(t)$ that are obtained from Eq. (27). In particular the curves plotted in the inset of Fig. 2 clearly reveal a very good quantitative agreement between numerical and theoretical results. In particular, a better agreement between numerics and theory is obtained by including the fourth-order correction term found in the time expansion of the solution, see Eq. (27). A significant quantitative disagreement is found between our theoretical results and the numerical simulation at evolution times greater than ~ 0.2 . This arises from the fact that our approach is only valid at evolution times that are shorter than the typical wave breaking time (the prebreaking description). The significant occurrence of wave breakings at evolution times greater than ~ 0.2 has strong influence on the wave evolution and subsequently the wave statistics in a way that cannot be accounted for by using our prebreaking treatment.

Figure 3 shows the comparison between the numerical simulation of Eq. (1) and the theoretical result given by Eq. (27) in the defocusing regime ($\sigma = -1$). In the defocusing regime, $\kappa_4(t)$ is a monotonically decreasing function of time, as already evidenced in Ref. [35]. As for the focusing regime, a very good quantitative agreement is obtained between numerics and the theory at short evolution time ($t < 0.2$), i.e., before the typical occurrence of gradient catastrophes.

While the developed theory is rigorously valid in the semiclassical limit as $\varepsilon \rightarrow 0$ Fig. 2 and Fig. 3 provide the evidence of a good quantitative agreement between numerical simulations and our theory for $\varepsilon = 0.1$. To further verify the robustness of our results we have performed further numerical simulations for ε ranging between 0.08 and 0.5. In all cases a very good quantitative agreement was obtained between the numerics and the theory at short evolution time ($t < 0.2$).

V. CONCLUSION

In this paper, we have undertaken an analytical study of the problem of the evolution of a random wave field in the 1D-NLSE for both focusing and defocusing regimes. This has been done from the perspective of dispersive hydrodynamics, a semiclassical theory of nonlinear dispersive waves exhibiting two distinct spatiotemporal scales: the long scale specified by initial conditions and the short scale by the internal coherence length (i.e., the typical size ε of the coherent structures) [31]. This scale separation enabled us to split the time evolution of the nonlinear random wave system (integrable turbulence) into the initial, “prebreaking” stage, preceding the formation of gradient catastrophes, when the evolution of the 1D-NLSE wave field is almost everywhere smooth, and the “postbreaking” stage characterized by the generation of short-scale nonlinear oscillations (breathers or dispersive shock waves depending on the focusing vs. defocusing character of the 1D-NLSE).

Our work is concerned with the initial, prebreaking stage of the semiclassical integrable turbulence, when the dynamical and statistical features can be analytically described in terms of random solutions of the dispersionless (nonlinear geometric optics) system (16). As a result, we have derived a simple asymptotic formula describing the evolution of the normalized fourth moment of the random wave field. This formula, applied to the problem of the 1D-NLSE evolution of random field having initial Gaussian statistics, describes the initial stage of the formation of heavy tails of the PDF of the field amplitude in the focusing case and the formation of low tails in the defocusing case.

Recently, an exact and general identity that relates the changes in the statistical properties of the wave field to the changes of its Fourier spectrum has been derived by using the Hamiltonian structure of 1D-NLSE [35]. In other words, the knowledge of the fourth-order moment also provides the description of spectral properties. The general description of the stationary state of integrable turbulence and the theoretical prediction of the fourth-order moment is still an open fundamental question. In the weakly nonlinear regime, the wave turbulence approach provides a statistical description of the nonlinear propagation of random wave fields in 1D-NLSE systems [28–30,56]. Recently, using an approach based on the so-called large deviation theory, it has been shown that rogue waves obey a large deviation principle, i.e., the heavy tails of the PDF of the random wave field are dominated by single realizations [57,58]. This approach is very promising but does not provide a simple formula for the evolution of the statistics. In this article we have demonstrated that the semiclassical approach is an extremely powerful tool enabling one to describe in a simple way the early stage of integrable turbulence in the *strongly nonlinear (or small dispersion)* regime. The proposed methodology can be applied to the description of partially coherent random nonlinear waves described by other integrable equations, including shallow water waves described by the KdV equation and its extensions. In particular, the prebreaking statistics of bidirectional random shallow water waves is equivalent to that described by the defocusing 1D-NLSE and studied in this paper.

The semiclassical approach to the statistics of random waves in integrable systems is general and can be used beyond the short-time asymptotic regime. It is known very well that, in the semiclassical limit the evolution of nonlinear dispersive waves after the gradient catastrophe point is described by the so-called Whitham modulation equations [59] governing the behavior of the averaged integrals of motion, and replacing the dispersionless system (16) (see Refs. [33,60–62] and references therein for the application of the Whitham theory to the defocusing and focusing 1D-NLSE). Such an extension of the proposed method to longer times is very promising but also highly nontrivial.

ACKNOWLEDGMENTS

This work was supported by EPSRC Grant No. EP/R00515X/2 (G.E.) and Dstl Grant No. DSTLX-1000116851 (G.R., G.E., and S.R.). It has also been partially supported by the Agence Nationale de la Recherche through

the LABEX CEMPI project (ANR-11-LABX-0007) and by the Ministry of Higher Education and Research, Hauts-De-France Regional Council and European Regional Development Fund (ERDF) through the Contrat de Projets Etat-

Région (CPER Photonics for Society P4S). G.E. and G.R. thank the PhLAM laboratory at the University of Lille for hospitality and partial financial support (G.E.). The authors thank T. Congy for some clarifying comments.

APPENDIX: COMPUTATION OF $\mathcal{O}(t^4)$ CORRECTIONS FOR THE CASE OF GAUSSIAN STATISTICS AT $t = 0$

Here we provide the simplified expressions for the three terms that are found in the integral giving the coefficient of the $\mathcal{O}(t^4)$ term in Eq. (19). To obtain these expressions, we assume Gaussian statistics at the initial time and use Eq. (20) and Eq. (21) to obtain

$$-\frac{1}{3\langle N \rangle^2 L} \int_0^L \langle \rho_0^2 \rho_{0x} \rho_{0xx} \rangle dx = -\frac{1}{3\langle N \rangle^2} \left(\frac{2i\pi}{L} \right)^4 \sum_{k_1, \dots, k_6} \langle \psi_{0k_1} \psi_{0k_2} \psi_{0k_3} \psi_{0k_4} \psi_{0k_5}^* \psi_{0k_6}^* \psi_{0k_7}^* \psi_{0k_8}^* \rangle \times \delta_{k_5+k_6+k_7+k_8}^{k_1+k_2+k_3+k_4} (k_3 - k_7)(k_4 - k_8)^3 = 48\langle H_L \rangle^2 + 4\langle N \rangle \left\langle \sum_k \left(\frac{2\pi k}{L} \right)^4 |\psi_{0k}|^2 \right\rangle, \quad (\text{A1})$$

$$-\frac{17}{12\langle N \rangle^2 L} \int_0^L \langle \rho_0 \rho_{0x}^2 \rho_{0xx} \rangle dx = -\frac{17}{12\langle N \rangle^2} \left(\frac{2i\pi}{L} \right)^4 \sum_{k_1, \dots, k_6} \langle \psi_{0k_1} \psi_{0k_2} \psi_{0k_3} \psi_{0k_4} \psi_{0k_5}^* \psi_{0k_6}^* \psi_{0k_7}^* \psi_{0k_8}^* \rangle \delta_{k_5+k_6+k_7+k_8}^{k_1+k_2+k_3+k_4} \times (k_2 - k_6)(k_3 - k_7)(k_4 - k_8)^2 = \frac{136}{3} \langle H_L \rangle^2, \quad (\text{A2})$$

$$-\frac{1}{4\langle N \rangle^2 L} \int_0^L \langle \rho_{0x}^4 \rangle dx = -\frac{1}{4\langle N \rangle^2} \left(\frac{2i\pi}{L} \right)^4 \sum_{k_1, \dots, k_6} \langle \psi_{0k_1} \psi_{0k_2} \psi_{0k_3} \psi_{0k_4} \psi_{0k_5}^* \psi_{0k_6}^* \psi_{0k_7}^* \psi_{0k_8}^* \rangle \delta_{k_5+k_6+k_7+k_8}^{k_1+k_2+k_3+k_4} \times (k_1 - k_5)(k_2 - k_6)(k_3 - k_7)(k_4 - k_8) = -24\langle H_L \rangle^2. \quad (\text{A3})$$

-
- [1] U. Frisch, *Turbulence, the Legacy of A. N. Kolmogorov* (Cambridge University Press, Cambridge, UK, 1995).
- [2] V. Zakharov, V. L'vov, and G. Falkovich, *Kolmogorov Spectra of Turbulence I* (Springer, Berlin, 1992).
- [3] S. Nazarenko, *Wave Turbulence*, Lecture Notes in Physics (Springer, Berlin, 2011).
- [4] V. E. Zakharov, *Stud. Appl. Math.* **122**, 219 (2009).
- [5] V. E. Zakharov and A. A. Gelash, *Phys. Rev. Lett.* **111**, 054101 (2013).
- [6] D. Agafontsev and V. E. Zakharov, *Nonlinearity* **28**, 2791 (2015).
- [7] P. Walczak, S. Randoux, and P. Suret, *Phys. Rev. Lett.* **114**, 143903 (2015).
- [8] P. Suret, R. El Koussaifi, A. Tikan, C. Evain, S. Randoux, C. Szwaj, and S. Bielawski, *Nat. Commun.* **7**, 13136 (2016).
- [9] S. Randoux, P. Walczak, M. Onorato, and P. Suret, *Physica D* **333**, 323 (2016).
- [10] J. M. Soto-Crespo, N. Devine, and N. Akhmediev, *Phys. Rev. Lett.* **116**, 103901 (2016).
- [11] N. Akhmediev, J. M. Soto-Crespo, and N. Devine, *Phys. Rev. E* **94**, 022212 (2016).
- [12] S. Randoux and P. Suret, Integrable turbulence with nonlinear random optical waves, in *Rogue and Shock Waves in Nonlinear Dispersive Media* (Springer, Cham, 2016), pp. 277–307.
- [13] P. Suret, E. Gennady, M. Onorato, and S. Randoux, Rogue waves in integrable turbulence: Semi-classical theory and fast measurements, in *Nonlinear Guided Wave Optics* (IOP, Bristol, UK, 2017), pp. 12-1–12-32.
- [14] A. Tikan, S. Bielawski, C. Szwaj, S. Randoux, and P. Suret, *Nat. Photon.* **12**, 228 (2018).
- [15] A. Picozzi, J. Garnier, T. Hansson, P. Suret, S. Randoux, G. Millot, and D. Christodoulides, *Phys. Rep.* **542**, 1 (2014).
- [16] M. J. Ablowitz, M. Ablowitz, P. Clarkson, and P. A. Clarkson, *Solitons, Nonlinear Evolution Equations and Inverse Scattering*, Vol. 149 (Cambridge University Press, Cambridge, UK, 1991).
- [17] C. Kharif, E. Pelinovsky, and A. Slunyaev, *Rogue Waves in the Ocean* (Springer Verlag, Berlin, 2009).
- [18] M. Onorato, A. R. Osborne, M. Serio, L. Cavaleri, C. Brandini, and C. T. Stansberg, *Phys. Rev. E* **70**, 067302 (2004).
- [19] M. Onorato, A. Osborne, M. Serio, and L. Cavaleri, *Phys. Fluids* **17**, 078101 (2005).
- [20] M. Onorato, S. Residori, U. Bortolozzo, A. Montina, and F. Arecchi, *Phys. Rep.* **528**, 47 (2013).
- [21] D. R. Solli, C. Ropers, P. Koonath, and B. Jalali, *Nature* **450**, 1054 (2007).
- [22] A. Mussot, A. Kudlinski, M. Kolobov, E. Louvergneaux, M. Douay, and M. Taki, *Opt. Express* **17**, 17010 (2009).
- [23] D. Pierangeli, F. Di Mei, C. Conti, A. J. Agranat, and E. DelRe, *Phys. Rev. Lett.* **115**, 093901 (2015).
- [24] M. Närhi, B. Wetzel, C. Billet, S. Toenger, T. Sylvestre, J.-M. Merolla, R. Morandotti, F. Dias, G. Genty, and J. M. Dudley, *Nat. Commun.* **7**, 13675 (2016).
- [25] A. Safari, R. Fickler, M. J. Padgett, and R. W. Boyd, *Phys. Rev. Lett.* **119**, 203901 (2017).
- [26] S. Randoux, P. Walczak, M. Onorato, and P. Suret, *Phys. Rev. Lett.* **113**, 113902 (2014).
- [27] Y. Bromberg, U. Lahini, E. Small, and Y. Silberberg, *Nat. Photon.* **4**, 721 (2010).
- [28] P. A. E. M. Janssen, *J. Phys. Oceanogr.* **33**, 863 (2003).
- [29] D. B. S. Soh, J. P. Koplów, S. W. Moore, K. L. Schroder, and W. L. Hsu, *Opt. Express* **18**, 22393 (2010).

- [30] P. Suret, A. Picozzi, and S. Randoux, *Opt. Express* **19**, 17852 (2011).
- [31] G. Biondini, G. El, M. Hofer, and P. Miller, *Physica D* **333**, 1 (2016).
- [32] S. Randoux, F. Gustave, P. Suret, and G. El, *Phys. Rev. Lett.* **118**, 233901 (2017).
- [33] G. A. El and M. A. Hofer, *Physica D* **333**, 11 (2016).
- [34] A. Tikan, C. Billet, G. El, A. Tovbis, M. Bertola, T. Sylvestre, F. Gustave, S. Randoux, G. Genty, P. Suret, and J. M. Dudley, *Phys. Rev. Lett.* **119**, 033901 (2017).
- [35] M. Onorato, D. Proment, G. El, S. Randoux, and P. Suret, *Phys. Lett. A* **380**, 3173 (2016).
- [36] L. Mandel and E. Wolf, *Optical Coherence and Quantum Optics* (Cambridge University Press, Cambridge, UK, 1995).
- [37] R. El Koussaifi, A. Tikan, A. Toffoli, S. Randoux, P. Suret, and M. Onorato, *Phys. Rev. E* **97**, 012208 (2018).
- [38] Y. Pomeau, M. Le Berre, P. Guyenne, and S. Grilli, *Nonlinearity* **21**, T61 (2008).
- [39] B. Dubrovin, T. Grava, and C. Klein, *J. Non. Sci.* **19**, 57 (2008).
- [40] M. Bertola and A. Tovbis, *Commun. Pure Appl. Math.* **66**, 678 (2013).
- [41] M. G. Forest, C.-J. Rosenberg, and O. C. Wright, *Nonlinearity* **22**, 2287 (2009).
- [42] S. Wabnitz, C. Finot, J. Fatome, and G. Millot, *Phys. Lett. A* **377**, 932 (2013).
- [43] J. Fatome, C. Finot, G. Millot, A. Armaroli, and S. Trillo, *Phys. Rev. X* **4**, 021022 (2014).
- [44] Y. Kodama and S. Wabnitz, *Opt. Lett.* **20**, 2291 (1995).
- [45] B. Wetzel, D. Bongiovanni, M. Kues, Y. Hu, Z. Chen, S. Trillo, J. M. Dudley, S. Wabnitz, and R. Morandotti, *Phys. Rev. Lett.* **117**, 073902 (2016).
- [46] S. Jin, C. D. Levermore, and D. W. McLaughlin, *Commun. Pure Appl. Math.* **52**, 613 (1999).
- [47] S. Kamvissis, K. D.-R. McLaughlin, and P. D. Miller, *Semiclassical Soliton Ensembles for the Focusing Nonlinear Schrödinger Equation (AM-154)*, 154 (Princeton University Press, Princeton, NJ, 2003).
- [48] A. Tovbis, S. Venakides, and X. Zhou, *Commun. Pure Appl. Math.* **57**, 877 (2004).
- [49] V. I. Talanov, *JETP Lett.* **2**, 138 (1965).
- [50] S. A. Akhmanov, A. P. Sukhorukov, and R. V. Khokhlov, *Sov. Phys. JETP* **23**, 1025 (1966).
- [51] A. Gurevich and A. Shvartsburg, *Sov. Phys. JETP* **31**, 1084 (1970).
- [52] A. Moro and S. Trillo, *Phys. Rev. E* **89**, 023202 (2014).
- [53] A. Picozzi, *Opt. Express* **15**, 9063 (2007).
- [54] M. Onorato, A. R. Osborne, M. Serio, and S. Bertone, *Phys. Rev. Lett.* **86**, 5831 (2001).
- [55] A. Tikan, [arXiv:1905.11938](https://arxiv.org/abs/1905.11938).
- [56] N. Mori and P. A. E. M. Janssen, *J. Phys. Oceanogr.* **36**, 1471 (2006).
- [57] G. Dematteis, T. Grafke, and E. Vanden-Eijnden, *Proc. Natl. Acad. Sci. U.S.A.* **115**, 855 (2018).
- [58] G. Dematteis, T. Grafke, and E. Vanden-Eijnden, [arXiv:1808.10764](https://arxiv.org/abs/1808.10764).
- [59] G. Whitham, *Linear and Nonlinear Waves* (Wiley Interscience, New York, 1974), p. 636.
- [60] A. M. Kamchatnov, *Nonlinear Periodic Waves and Their Modulations: An Introductory Course* (World Scientific, Singapore, 2000).
- [61] G. A. El, E. G. Khamis, and A. Tovbis, *Nonlinearity* **29**, 2798 (2016).
- [62] A. Tovbis and G. A. El, *Physica D* **333**, 171 (2016).

Chapter 3

Prediction and manipulation of Rogue Waves

3.1 Outline of the Problem

The fundamental mathematical results of Bertola and Tovbis [46] on the universal nature of the PS as a localised coherent structure regularising gradient catastrophe in the semi-classical fNLSE dynamics (see Section 1.4.4) have changed the widely accepted paradigm of the solitonic nature of rogue waves by enabling the PS to emerge from a partially radiative or even completely solitonless initial data. As Bertola and Tovbis showed, the amount of the “solitonic content” (IST discrete spectrum) of the initial pulse affects only the point $\xi = \xi_m$ of the maximum compression corresponding to the PS emergence but does not change the main qualitative and quantitative features of the dispersive regularisation scenario.

For convenience of the exposition we reproduce here the main results of the semi-classical theory from Section 1.4.4 with the special emphasis on the distinction between the universal and initial data-dependent results.

The following universal asymptotic description of the structure that emerges at the point of maximum compression $\xi = \xi_m$ is valid [46]:

$$\xi_m = \xi_c + C\varepsilon^{4/5}, \quad (3.1)$$

where ε is the formal small parameter in the semi-classical approximation (defined as $\varepsilon = \sqrt{L_D/L_{NL}}$, where L_D and L_{NL} are the characteristic dispersive and nonlinear lengths in the system respectively), ξ_c is the point (physical time) of gradient catastrophe, μ is the chirp parameter and

$$C = \left(\frac{5|C_1|}{4} \right)^{1/5} (2b_0)^{-3/2} |v_p| (1 + \mathcal{O}(\varepsilon^{4/5})),$$

with $|v_p| \approx 2.38$ being the universal constant, and C_1 and b_0 the initial data-dependent coefficients.

E.g. for the initial profile

$$u(\tau, 0) = \text{sech}(\tau) e^{i\phi/\varepsilon}, \quad \phi = -\mu \log(\cosh(\tau)), \quad (3.2)$$

the exact analytical expressions for ξ_c , b_0 and C_1 are:

$$\xi_c = 1/(2 + \mu), \quad b_0 = |u(0, \xi_c)| = \sqrt{\mu + 2}, \quad C_1 = \frac{32\sqrt{2}i}{15(2 + \mu)^{9/4}}. \quad (3.3)$$

For $\mu = 0$ the initial condition (3.2) represents an exact N -soliton solution (pure discrete IST spectrum) of the fNLSE with $N = 1/\varepsilon$. For $\mu \geq 2$ the potential (3.2) is solitonless. The universality of the Bertola-Tovbis regularisation mechanism is demonstrated in in Fig. 19 where the results of the numerical simulations of the fNLSE evolution for purely solitonic and solitonless propagation regimes are shown.

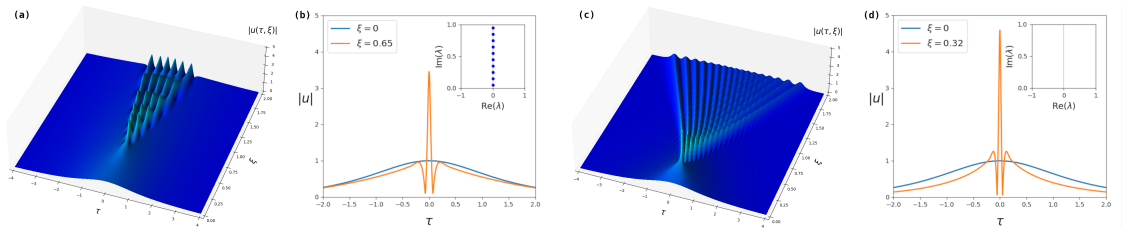


Figure 19: Universal regularisation of the gradient catastrophe via the local emergence of the Peregrine soliton for the initial condition $u(\tau, 0) = \text{sech}(\tau) \exp[-i\mu \log(\cosh(\tau))]/\varepsilon$ with (a,b) $\mu = 0$ (exact 10-soliton solution) (c,d) $\mu = 0$ (solitonless solution). (a,c) spatio-temporal evolution of the amplitude of the solution and (b,d) profile of the soliton at the maximum compression point ξ_m . (b,d) Inset with the IST spectrum of the solution.

The profile of the structure that emerges at $\xi = \xi_m$ is described by the universal asymptotic

formula:

$$u(\tau, \xi_m) = a_0 \left(1 - \frac{4}{1 + 4a_0^2(\tau/\varepsilon)^2} \right) [1 + \mathcal{O}(\varepsilon^{1/5})], \quad (3.4)$$

which coincides at leading order with the formula of the PS profile (1.29). Here the background amplitude for the case of the initial data (3.2) is given by

$$a_0 = \sqrt{2 + \mu} + \mathcal{O}(\varepsilon^{1/5}), \quad (3.5)$$

i.e. is determined at leading order by the value of $|u|$ at the gradient catastrophe point. The maximum value of $|u|$ in the local PS is then $3a_0$ and is determined up to $\mathcal{O}(\varepsilon^{1/5})$.

For other initial profiles (e.g. Gaussian) the determination of ξ_c , b_0 and C is performed numerically but often the results for sech profile (3.2) turn out to be a good approximation for other localised initial data (see Chapter 6).

The gradient catastrophe regularisation via the PS formation for smooth, rapidly decaying purely solitonic initial conditions have been examined experimentally using the optical fibre platform [4, 103] which revealed the robustness of the mechanism even when typical nonlinear and dispersive lengths are of the same order of magnitude. However, the full verification of the universality of the Bertola-Tovbis results in application to physical systems would require the investigation of the RW compression in the propagation of partially radiative, or even solitonless initial pulses, similar to the one presented in Fig. 19

The asymptotic results of Bertola and Tovbis suggest that the definitive parameters ξ_m (3.1) and a_0 (3.5) of the RW compression can be manipulated by an appropriate choice of the chirp factor μ related to the solitonic content of the pulse.

The material of this Chapter is concerned with the theoretical development and experimental realisation of the *method of nonlinear spectral engineering* for the control and manipulation of the RW emergence from single pulses using the insights from the semi-classical fNLSE theory.

3.2 Summary of Results and Outlook

The Bertola-Tovbis results (3.1)-(3.5) have been re-contextualised in the framework of deep water waves and applied to the particular conditions of the experiment performed in a 120 m long water tank with the water depth $h = 3$ m. The experiment has been performed in École Centrale de Nantes, France. I have been directly involved in the formulation of the problem, the numerical simulations and in the interpretation of the experimental results.

The results of the project appear in the pre-print

- A. Tikan, F. Bonnefoy, **G. Roberti**, G. El, A. Tovbis, G. Ducrozet, A. Cazaubiel, G. Prabhudesai, G. Michel, F. Copie, E. Falcon, S. Randoux, P. Suret, “Prediction and manipulation of hydrodynamic rogue waves via nonlinear spectral engineering”, arXiv:2108.02698 (2021), submitted for publication in a peer reviewed journal.

In this work we provide an experimental confirmation of the robustness the Bertola-Tovbis scenario of the PS emergence in the context of deep-water wave propagation modelled by the perturbed fNLSE including relevant higher order terms (the so-called Dysthe equation [138]). It is done by showing that the generation of a RW having the distinct PS signature (both amplitude and phase profiles) occurs locally, in the vicinity of the point of the gradient catastrophe and independently of the solitonic content of the initial pulse as defined by the Zakharov-Shabat scattering problem (see Section 1.4) corresponding to integrable, non-perturbed fNLSE dynamics governing the propagation at leading order. Due to the presence of higher order, nonintegrable effects in the real water tank propagation conditions, the PS type profiles observed in the experiment are slightly asymmetric, but most importantly, the point ξ_m of the maximum compression is well described by the appropriately scaled Bertola-Tovbis formula (3.1). The amount of the solitonic content in the input pulse is determined through the nonlinear Fourier (IST) analysis of the experimental data and is modified by varying the phase of the input structure. In particular, we demonstrate that, somewhat paradoxically (but in full agreement with the Bertola-Tovbis results) the PS-type RW generation is observed even in a completely solitonless case.

Further, by changing the chirp of the initial wave packet and hence, varying its solitonic content as defined by the IST, we managed to manipulate the point of the maximum compression (RW

emergence) in a controllable way. Our experimental results are in excellent agreement with the direct numerical simulations of the nonlinear wave packet propagation using the Dysthe equation. The Dysthe equation does not belong to the class of equations integrable by the IST. Nonetheless, having an integrable core in the form of the fNLSE, this model can be analysed using perturbation methods. In particular, the IST spectra of the PS-like coherent structures occurring in the Dysthe equation pulse evolution have been determined and analysed following the recently developed numerical approaches [139, 140, 141, 142]. It has been shown that the fact that the actual wave evolution in a water tank is described by a non-integrable equation results in the nontrivial slow dynamics of the locally defined IST spectra.

The outlined theoretical and experimental results on the nonlinear spectral engineering of RWs suggest two major lines of future theoretical and experimental research:

- Using nonlinear spectral engineering for the prediction and manipulation of RWs in fibre optics pulse compression.
- Application of the method to the propagation of partially coherent input signals, where the local emergence of PS's has been shown in [6] to leave a distinct trace in the evolution of the statistical properties of the signal, in particular the overshoot in kurtosis plot, see Fig. 16.

Prediction and manipulation of hydrodynamic rogue waves via nonlinear spectral engineering

Alexey Tikan,^{*} Felicien Bonnefoy,[†] Giacomo Roberti,[‡] Gennady El,[‡] Alexander Tovbis,[§] Guillaume Ducrozet,[†] Annette Cazaubiel,[¶] Gaurav Prabhudesai,^{**} Guillaume Michel,^{††} Francois Copie,^{‡‡} Eric Falcon,[¶] Stephane Randoux,^{‡‡} and Pierre Suret^{‡‡}

(Dated: August 6, 2021)

Peregrine soliton (PS) is widely regarded as a prototype nonlinear structure capturing properties of rogue waves that emerge in the nonlinear propagation of unidirectional wave trains. As an exact breather solution of the one-dimensional focusing nonlinear Schrödinger equation with nonzero boundary conditions, the PS can be viewed as a soliton on finite background, *i.e.* a nonlinear superposition of a soliton and a monochromatic wave. A recent mathematical work showed that both nonzero boundary conditions and solitonic content are not pre-requisites for the PS occurrence. Instead, it has been demonstrated that PS can emerge *locally*, as an asymptotic structure arising from the propagation of an arbitrary large decaying pulse, independently of its solitonic content. This mathematical discovery has changed the widely accepted paradigm of the solitonic nature of rogue waves by enabling the PS to emerge from a partially radiative or even completely solitonless initial data. In this work, we realize the mathematically predicted universal mechanism of the local PS emergence in a water tank experiment with a particular aim to control the point of the PS occurrence in space-time by imposing an appropriately chosen initial chirp. By employing the inverse scattering transform for the synthesis of the initial data, we are able to engineer a localized wave packet with a prescribed solitonic and radiative content. This enabled us to control the position of the emergence of the rogue wave by adjusting the inverse scattering spectrum. The proposed method of the nonlinear spectral engineering is found to be robust to higher-order nonlinear effects inevitable in realistic wave propagation conditions.

INTRODUCTION

The prediction of extreme events in various nonlinear media has been the subject of a very active research for several decades [1–6]. While the original motivation was related to the modeling of the emergence of giant water waves in the ocean, also called rogue waves (RWs) [2], the subsequent research revealed that RWs are a fundamental and ubiquitous physical phenomenon occurring, apart from classical fluids, in optical media and superfluids [3, 7].

The RW formation as a physical phenomenon has two inherent aspects: dynamical and statistical. As a dynamical object RWs are identified according to physical mechanisms responsible for the amplitude growth and spatiotemporal localization. As a statistical object, RWs are characterized by the deviation of the probability distribution of the random wave field from the one implied by the Gaussian statistics [8–11]. Among different contexts of the RW's emergence, nonlinear dynamics of unidirectional waves on the surface of the deep water has been widely studied due to *integrability* [12] of the mathematical model describing the weakly nonlinear deep-water waves at leading order. Indeed, as has been shown by V. Zakharov [13], the evolution of the narrow-band wave packets in the limit of infinite water depth is governed by the one-dimensional focusing nonlinear Schrödinger equation (1-D fNLSe), which can be integrated by means of the inverse scattering transform (IST) also known as nonlinear Fourier transform [14].

The research area that considers nonlinear evolution of random waves in integrable models has been dubbed *integrable turbulence* in [15]. There are two types of initial conditions usually considered in this framework: (i) a plane wave (condensate) perturbed by a small-amplitude noise and (ii) a partially coherent wave with large-scale finite-amplitude variations characterized by long-range incoherence. The latter can be viewed as an infinite sequence of large-scale pulses randomly distributed along the line. The variation of the statistical properties of the IST spectrum occurring in the transition between these two contrasting types of initial conditions has been examined in [16, 17]. The random nonlinear wave field (the integrable turbulence) generated in both cases exhibits deviations from the Gaussian statistics [18–23] but those deviations are manifested at different stages of the evolution. While in the development of the noise-induced modulational instability the non-Gaussian features are observed at the initial stage of the evolution and are of transient character, the nonlinear evolution of partially coherent initial conditions leads to the long-time statistically stationary non-Gaussian state [8, 21]. The non-Gaussianity of the asymptotic state in the evolution of partially coherent wave (the so-called heavy tailed distribution) is associated with the presence of RWs. Exact breather solutions of the 1-D fNLSe, also called solitons on finite background [24–27], are often considered as the main candidates for the role of RWs [28–30]. The PS [26, 31, 32] is a particular member of this family of solutions that exhibits spatiotemporal localization, thereby reflecting the main qualitative features of RWs [33].

The PS solution plays a special role in the context of the dynamics of partially coherent waves. In the strongly nonlinear regime of propagation, the individual large-scale pulses forming a partially coherent wave undergo self-focusing resulting in a gradient catastrophe, a phenomenon of the occurrence of infinite derivatives in the wave's profile. Importantly, the initial, self-focusing stage of the evolution of a partially coherent wave is dominated by nonlinearity and is approximately dispersionless. For the 1-D fNLSe, it was rigorously proved by Bertola and Tovbis (BT) [34] that the gradient catastrophe is *universally* regularized by dispersive effects via the local emergence of a coherent structure, which is asymptotically described by the PS solution in the semiclassical, small-dispersion limit. The universality of the PS generation is understood in the sense that this regularization mechanism persists regardless of the particular shape, chirp or *solitonic content* of the initial condition. In particular, the gradient catastrophe regularization via the PS formation for smooth, rapidly decaying purely solitonic initial conditions have been examined experimentally using the optical fiber platform [35, 36], which revealed the robustness of the mechanism even when typical nonlinear and dispersive lengths are of the same order of magnitude.

Recently, it has been shown that the local emergence of PSs leaves a distinct trace in the evolution of statistical properties of the partially coherent waves. Numerical simulations performed in [37] have demonstrated that the width and the position of the computed probability density function of local PS emergence positions coincides with the parameters of the *most probable distance interval for the RW observation*, which has been subsequently confirmed in water tank experiments [38]. Importantly, the above optics and hydrodynamics experimental results were obtained in the carefully chosen propagation regimes well approximated by the 1-D fNLSe

While having been confirmed experimentally for approximately integrable propagation regimes, the applicability of the universal PS regularization scenario to more physically realistic conditions remains an open question. Indeed, the presence of dissipation and the influence of the higher-order nonlinear terms can significantly modify the integrable 1-D fNLSe dynamics. Having an experimental confirmation of the robustness of the core universal PS resolution dynamics in a physically realistic context would be extremely valuable as it would open a way to a practical, quantitative prediction and manipulation of the *spontaneous emergence* of RWs via the methods of nonlinear spectral (IST) theory underlying the BT results. Of course, special care should be taken in the interpretation of the IST data in the context of perturbed integrable dynamics.

In this paper, using the BT theory as a starting point, we experimentally demonstrate the universality of the spontaneous emergence of the PS-like coherent structures in the evolution of weakly nonlinear wave packets on deep

water. As the simplest mathematical model that has an integrable core and takes into account the higher-order nonlinear effects in the propagation of weakly nonlinear wave packets on deep water, we use a version of the generalized fNLSe proposed in [39] which is usually referred to as the Dysthe equation (see Methods section).

The experiments are performed in a 120 m long water tank with a water depth $h = 3$ m. We provide an experimental confirmation of the robustness the BT scenario of the PS emergence in the context of 'non-integrable' deep-water wave propagation. It is done by showing that the generation of a RW having the structure similar to PS occurs locally, in the vicinity of the point of the gradient catastrophe and independently of the IST solitonic content of the initial pulse. In particular, we demonstrate that, somewhat paradoxically (but in full agreement with the BT results) the PS-type RW generation is observed even in a completely solitonless case.

Further, by changing the chirp of the initial wave packet and hence, varying its solitonic content as defined by the IST, we managed to manipulate the point of the PS maximum compression in a controllable way. Our experimental results are shown to be in excellent agreement with the numerical simulations of the Dysthe equation. For the analysis of the RW emergence in the wavepacket propagation modeled by the Dysthe equation we employ the recently developed IST based method [40] of the analysis of nonlinear wave dynamics applicable to the models which are not integrable but have an integrable 'core' [41–44].

RESULTS

Semi-classical limit of 1-D fNLSe. Universal formation of the Peregrine soliton

We write the 1-D fNLSe in the following form:

$$i\epsilon \frac{\partial \psi}{\partial \xi} + \frac{\epsilon^2}{2} \frac{\partial^2 \psi}{\partial \tau^2} + |\psi|^2 \psi = 0, \quad (1)$$

where ψ is the normalized complex envelope of the water waves, ξ and τ are normalized space coordinate and normalized time, $\epsilon = \sqrt{L_{NL}/L_D}$, with L_{NL} and L_D typical nonlinear and linear lengths in the system [11].

Despite the fact that 1-D fNLSe is a fully integrable equation [12], explicit analytic results are available only in some particular cases. One of the examples when an effective analytical description is possible is the so-called semi-classical limit of 1-D fNLSe. This approach is applied to the description of nonlinear dispersive waves in the case when $\epsilon \ll 1$ in Eq. (1).

We consider Equation (1) using the Madelung transformation [45, 46]:

$$\psi(\xi, \tau) = \sqrt{\rho(\xi, \tau)} e^{i\phi(\xi, \tau)/\epsilon}, \quad u(\xi, \tau) = \phi_\tau(\xi, \tau), \quad (2)$$

where $\sqrt{\rho}$ is the wave amplitude and u —the instantaneous frequency. As a result the 1-D fNLSe assumes the form of a system

$$\rho_\xi + (\rho u)_\tau = 0 \quad (3)$$

$$u_\xi + uu_\tau - \rho_\tau + \frac{\epsilon^2}{4} \left[\frac{\rho_\tau^2}{2\rho^2} - \frac{\rho_{\tau\tau}}{\rho} \right]_\tau = 0. \quad (4)$$

Equations (3), (4) are analogous to Euler's dispersive hydrodynamics for the fluid with density ρ and velocity u but characterized by negative pressure $p = -\rho^2/2$ due to the focusing effects.

The last term in Eq. (4) is proportional to ϵ^2 , therefore, assuming finite derivatives in the initial data, it can be neglected at the early stage of the propagation. The description of the evolution of smooth and decaying initial profiles by Eqs. (3) and (4) with neglected dispersive terms, i.e. with $\epsilon = 0$, is valid until the gradients of ρ or u become infinitely large at some point (τ_c, ξ_c) , termed the gradient catastrophe point. The dispersionless evolution problem is ill-posed for $\xi > \xi_c$, and the full dispersive system has to be considered in this region. To describe the solution in the vicinity of the gradient catastrophe point (τ_c, ξ_c) BT [34] employed the inverse scattering transform in the semi-classical ($\epsilon \ll 1$) approximation. It has been found that the gradient catastrophe is dispersively regularized by the *universal* appearance of a large amplitude ϵ -scaled spikes that are asymptotically described by the PS solution. Here the term ‘universal’ is used to stress that the BT scenario does not depend on the exact shape, chirp or solitonic content of the smooth (more precisely, analytic) initial condition. It is remarkable that locations of these spikes are determined by the poles of the special tritronquée solution of the Painlevé I equation, whose role in the gradient catastrophe was first recognized by B. Dubrovin et al. [47].

More explicitly, the theory developed in [34] provides the following asymptotic description of the structure that emerges at the point of maximum compression $\xi = \xi_m$:

$$\xi_m = \xi_c + C\epsilon^{4/5}, \quad (5)$$

where ξ_c is the point of gradient catastrophe, and $C = \left(\frac{5|C_1|}{4}\right)^{1/5} (2b_0)^{-3/2} |v_p| (1 + \mathcal{O}(\epsilon^{4/5}))$ with C_1 - an initial data-dependent coefficient, $b_0 = \sqrt{\rho(0, \xi_c)}$ - the wave amplitude at the point of gradient catastrophe, and $|v_p| \approx 2.38$ is a universal constant.

The amplitude profile of the spike that emerges at $\xi = \xi_m$ is described by the asymptotic formula:

$$|\psi(\tau, \xi_m)| = a_0 \left(1 - \frac{4}{1 + 4a_0^2(\tau/\epsilon)^2} \right) [1 + \mathcal{O}(\epsilon^{1/5})], \quad (6)$$

which coincides at leading order with the formula of the PS amplitude profile. Here the background amplitude $a_0 = b_0 + \mathcal{O}(\epsilon^{1/5})$, i.e. is determined at leading order by the wave amplitude at the gradient catastrophe point.

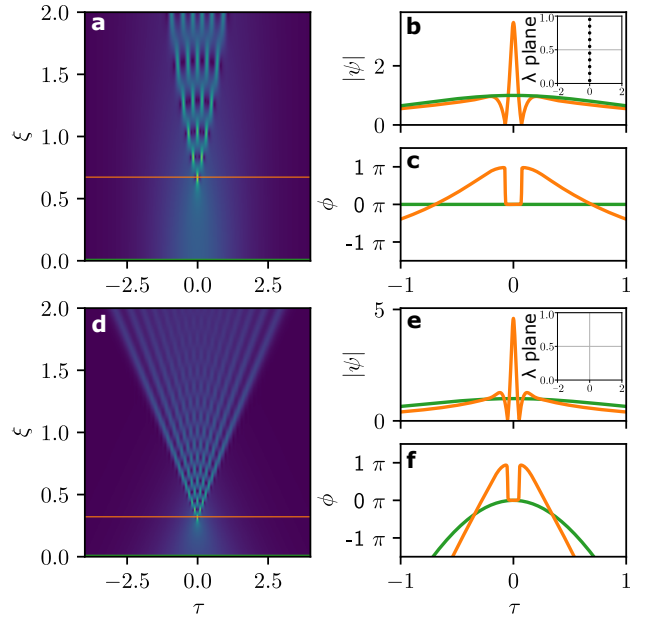


FIG. 1. **Universal regularization of the gradient catastrophe by local emergence of the Peregrine soliton.** Parameter ϵ in the simulation is equal to $1/10$. (a-c) Spatiotemporal diagram, the amplitude and phase cross-section at the maximum compression point (orange). Exact 10-soliton solution is taken as an initial condition (green). (d-f) The counterpart plots for a solitonless solution $\text{sech}(\tau) \exp[-i\mu \log(\cosh(\tau))/\epsilon]$, where $\mu = 2$. Plots in the right corner of (b) and (e) show the corresponding discrete IST spectra (λ plane). Vertical axis shows the imaginary part while the horizontal one - the real part of the discrete IST spectrum.

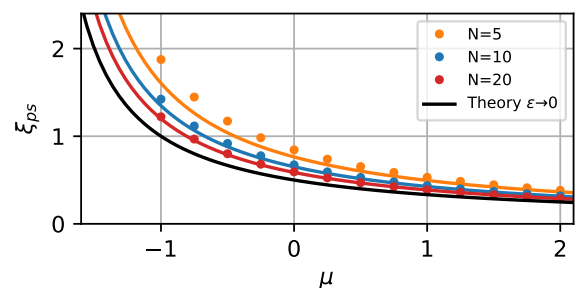


FIG. 2. **The PS emergence distance as a function of the chirp parameter μ . Comparison of the numerical simulations with the theoretical predictions.** Numerical simulations of $N = 5, 10$ and 20 solitons solutions of the 1-D fNLSe are depicted by orange, blue and red dots respectively. Theoretical prediction according to Eq. (5) are plotted with the solid line of the corresponding color. The limiting case $N \rightarrow \infty$ is plotted with the black line.

The maximum value of $|\psi|$ in the local PS is then $3a_0$ and is determined up to $\mathcal{O}(\epsilon^{1/5})$. The expression for the phase of the asymptotic solution at the maximum compression point also coincides at leading order with the PS's phase but we do not present it here. We stress that the described approximate PS solution is valid *locally*, in the ϵ -vicinity of the point $(0, \xi_m)$

The local emergence of the PS in the evolution of a decaying N -soliton pulse has been experimentally observed in [35, 36]. Importantly, the fiber optics experiments in [35] demonstrated that the BT scenario is very robust and can be observed for the values of ϵ significantly exceeding those implied by the formal asymptotic validity of the semi-classical limit of 1-D fNLSe. Specifically, the regularization of the gradient catastrophe by the emergence of a coherent structure that can be *locally* fitted by the PS was observed in [35] for $\epsilon \approx 0.45$ using high-power pulses with a Gaussian profile and a constant phase.

The universality of the described gradient catastrophe regularization mechanism can be illustrated as follows. Consider the 1-D fNLSe Eq. (1) with the initial condition

$$\psi(0, \tau) = \text{sech}(\tau)e^{i\phi/\epsilon}, \quad \phi = -\mu \log(\cosh(\tau)) \quad (7)$$

for two different values of the chirp parameter μ . In the particular case of initial data Eq. (7), coefficients found in Eq. (5) take the following form: $\xi_c = 1/(2 + \mu)$, $C_1 = \frac{32\sqrt{2i}}{15(2+\mu)^{9/4}}$, $b_0 = \sqrt{\mu + 2}$. For $\mu = 0$ the profile Eq. (7) is the exact N -soliton solution of the 1-D fNLSe (Eq. (1)) with $\epsilon = 1/N$. On the other hand, if $\mu \geq 2$ the profile Eq. (7) is *completely solitonless* [48].

The spatiotemporal diagrams and the profiles of the amplitude $|\psi|$ and phase ϕ at the maximum compression point for the evolution of the above two profiles are shown in Fig. 1. In both cases the simulations were performed with $\epsilon = 1/10$ and the value of μ in the second set of simulations was taken to be equal 2 ensuring the absence of the discrete spectrum. In order to verify the solitonic content of the initial data, the IST spectrum of the initial pulse was evaluated numerically using the Fourier collocation method [49] (see the Methods section). The discrete part of the IST spectrum of the N -soliton profile is represented by N discrete eigenvalues (and their conjugates) in the complex λ -plane, located equidistantly along the imaginary axis (Fig. 1(b) inset). The IST spectrum of the solitonless initial condition (Eq. (7) with $\mu = 2$) contains no discrete part, see Fig. 1(e) inset. We note that the IST spectra of Gaussian pulses used in the optical experiments of [35] contained both discrete and continuous spectrum parts.

One can see that, although the solitonic content of the two initial conditions is completely different, in both cases the pulse experiences the gradient catastrophe and the coherent structure that emerges at the maximum compression point has the signature amplitude and phase profiles of the PS. As predicted by Eq. (5), the maxi-

mum compression point is shifted further in the presence of the solitonic content. After the first spike we observe in Fig. 1(a) the generation of a growing chain of large-amplitude breathers. The qualitative evolution of the solitonless pulse close to the PS regularization point is similar but the long time behaviour is very different, displaying in the ξ, τ -plane an expanding cone filled with small-amplitude dispersive waves, see Fig. 1(d).

The predicted accuracy of the PS emergence position by Eq. (5) is examined by numerically simulating Eq. (1) for a series of initial conditions in the form of Eq. (7) with different values of the chirp parameter $\mu \in [-1, 2]$. The results are displayed in Fig. 2, where solid lines show the estimates of the PS emergence distance according to Eq. (5) for 5, 10 and 20 solitons at $\mu = 0$ (orange, blue and red colors, respectively) and the asymptotic case of infinite number of solitons is shown by the black curve. The points depict the position of PS emergence found in numerical simulations of Eq. (1) (color correspondence is preserved). Fig. 2 demonstrates the rapid convergence of the theoretical estimates towards the results of 1-D fNLSe simulations with increasing number of solitons in the initial condition and, importantly, their ability to provide a sufficiently accurate prediction even for low soliton numbers, i.e. way beyond the semiclassical zero-dispersion limit considered in the derivation of Eq. (5).

The above examples clearly show that, despite the widely accepted paradigm of the 'solitonic' nature of the PS, the presence of the discrete IST spectrum in the initial data is not a pre-requisite for the PS emergence. One can also conclude that the emergence of the local PS as a result of N -soliton self-compression observed in [35] is just a particular case of the general regularization mechanism described by the BT semiclassical theory.

Experimental results and comparison with numerical simulations

Experimental parameters and conditions

We investigate the influence of the soliton content on the emergence of RW in the 120 m long water tank with a water depth $h = 3$ m. To measure the surface wave elevation along the tank, 20 resistive probes have been installed equidistantly with the separation of 6 m. A schematic representation of the water tank is shown in Fig. 3. Detailed description of the experimental platform as well as the mode of operation can be found in [38, 40]. All the experiments are performed in the deep-water regime with a typical value of $kh = 15.8$, where $k = 2\pi/\lambda$ is the wavenumber. The central frequency of the wave packet is set to 1.15 Hz. Additional information can be found in the Methods section.

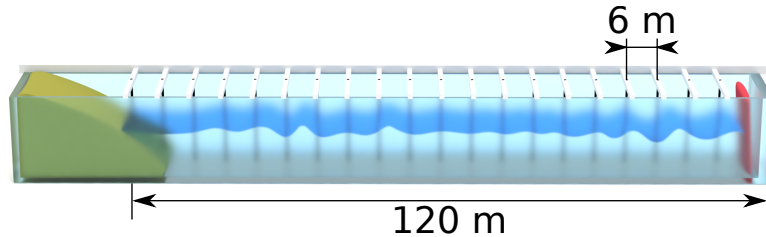


FIG. 3. **Schematic representation of the water tank.** Experimental investigations are provided in the water tank of the Hydrodynamics, Energetics, and Atmospheric Environment Lab (LHEEA) at Ecole Centrale de Nantes (France). Wave elevation is measured by a set of equidistantly-spaced probes over 120 m of the water tank length (the total length is 148 m), at every 6 m. It is equipped with a parabolic shaped absorbing beach (≈ 8 m long). With the addition of pool lanes arranged in a W pattern in front of the beach, the measured amplitude reflection coefficient is as low as 1%.

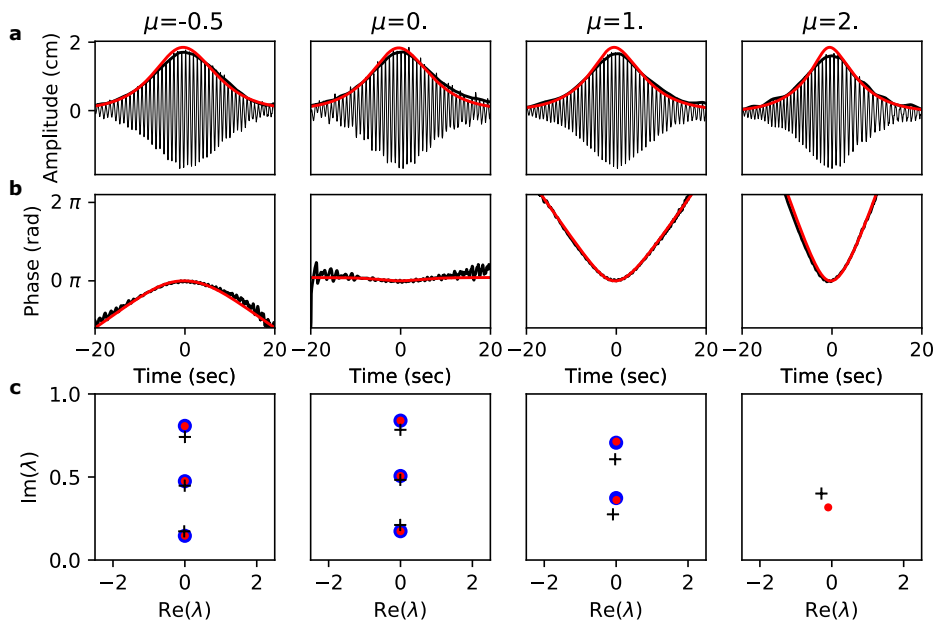


FIG. 4. **Initial conditions for experiments and simulations.** Four columns correspond to the values of $\mu = -0.5, 0, 1$ and 2 , respectively. (a) Comparison of the wave packets measured at the first probe located at 6 m from the wave maker (black line), corresponding envelope (bold black line), and simulations of Dysthe equation (red line) starting from the exact analytical expression. (b) Corresponding phase. (c) Discrete IST spectra of signals measured at the first probe (black crosses), analytical solution (blue dots) and result of simulations of Dysthe equation at 6 m of propagation (red dots).

Initial conditions

We first verify the applicability of the semi-classical theory to the conditions of our water wave experiment. We generate a sequence of wave packets having the same (3 solitons) envelope but different values of the chirp parameter μ according to Eq. (7). The parameter μ is varied from -0.8 (the value corresponding to the PS emergence point way beyond the water tank length) to 2 (completely solitonless case). Examples of the initial state measured at the 1st probe (6 m from the wave maker) are plotted in Fig. 4(a) (black line for the wave elevation). Bold black line shows the calculated envelope of the wave packet by using the Hilbert transform (see Methods section). Four columns of Fig. 4 correspond to four values of μ : $-0.5, 0$,

1 , and 2 . Red line shows the numerical simulations of the Dysthe equation at 6 m distance started from purely numerical initial conditions. Fig. 4(b) depicts corresponding phase profiles.

The precise control over the IST spectrum is essential for the experimental verification of the result of BT [34]. We analyzed the solitonic content of the initial conditions using the Fourier-collocation method [see Fig. 4 (c)]. As proposed in [41, 42], we solve here the direct scattering problem and use the discrete part of the IST spectrum for characterizing the solitonic content of the structures under investigation. The discrete IST spectra of the water waves are depicted by black crosses, the numerical data at $z = 0$ m by blue dots and at $z = 6$ m by red dots. We consider the initial conditions having exactly

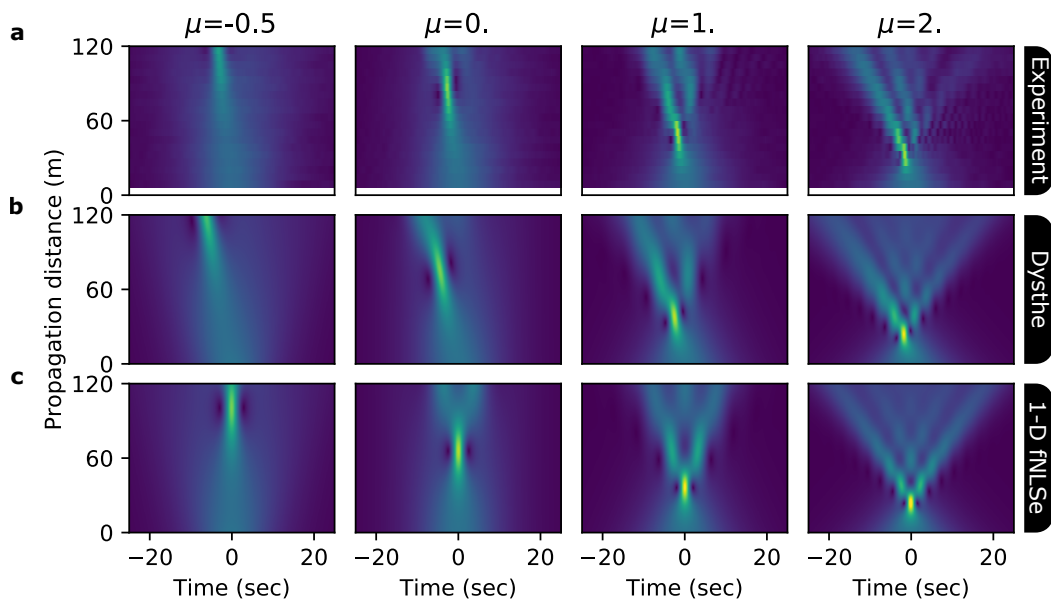


FIG. 5. **Spatiotemporal evolution. Comparison of the experimental data with numerical simulations of exact 3 soliton solution in Dysthe and NLS models.** (a) spatiotemporal diagram retrieved from the experimental measurements using the Hilbert transform. (b) Simulations of Dysthe equation starting. (c) Simulations of 1-D fNLSe. Exact analytical solution is taken as initial data for the numerical simulations.

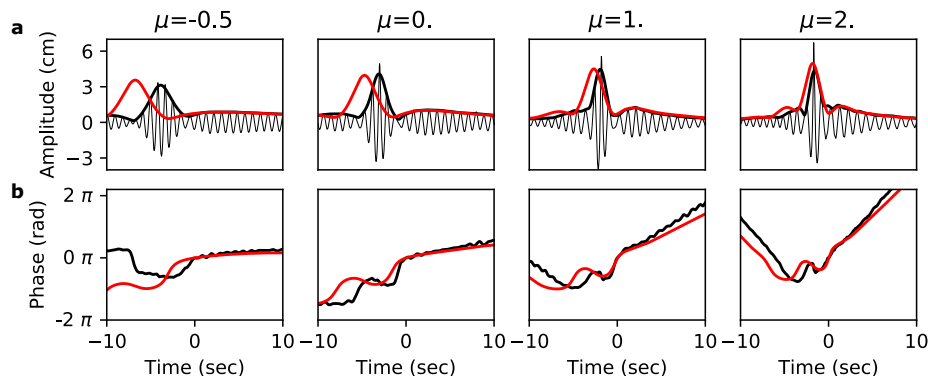


FIG. 6. **Cross-section of Fig. 5 at the maximum compression points.** (a) Measured envelope of water waves (bold black) with underlying carrying wave (black) and simulations of the Dysthe equation (red). (b) Corresponding phase. The positions of maximum compression can be different for numerical simulations and experiment. From left to right the values of μ are -0.5, 0, 1 and 2.

three solitons if the parameter μ is set to zero as can be seen from the Fig. 4(c), second column. According to the theoretical prediction [34, 48], the solitonic content of the pulse changes when the value of the chirp parameter μ is being varied. In particular, when μ increases the imaginary part of the discrete eigenvalues decreases until the point when the initial conditions become completely solitonless. This occurs for values of $\mu \geq 2$. Also, from the IST spectra shown in Fig. 4 it follows that the nonlinear propagation over $z = 6$ m does not exhibit significant deviation from the integrable case. However,

the IST spectra corresponding to $\mu = 2$ already show a deviation from isospectrality due to the presence of the higher-order nonlinear terms in the governing non-integrable (Dysthe) equation.

Nonlinear evolution

Nonlinear wave evolution from the initial conditions discussed in the previous section is shown in spatiotemporal diagrams of $|A(z, t)|$, where A is the complex wave en-

velope (see Fig. 5). We compare three cases: water tank experiments [plots (a)], simulations of the Dysthe equations [plots (b)] and simulations of the 1-D fNLSe [plots (c)] for four values of the chirp parameter $\mu = -0.5, 0, 1$ and 2. The experimental data confirms that the maximum compression point can be easily manipulated by adjusting the value of μ . The first column corresponding to $\mu = -0.5$, shows a smooth evolution of the wave packet resulting in the emergence of a localized structure near the edge of the water tank. By increasing the chirp parameter, we observe that the PS maximum compression occurs closer to the wavemaker position while the temporal profile of the local PS packet loses its initial symmetry. In the spatiotemporal diagram corresponding to $\mu = 1$, the coherent structures following the maximum compression point (propagation distance ≈ 72 m) resemble the localized spikes described in [34] despite the broken symmetry. In the solitonless case ($\mu = 2$), the compression point is found as close as 30 m from the wavemaker, and the subsequent spatiotemporal evolution is confined to an asymmetric cone.

The experimental data is found to be in an outstanding agreement with numerical simulations of the Dysthe equation [see Fig. 5(a) and (b)]. The simulations capture the entire spatiotemporal behaviour including small nuances related to the effect of the higher-order nonlinear terms. In order to take into account the effect of finite depth, we include a corresponding coefficient in the simulated model (see Methods section and Appendix in [40]). The evolution of both experimental and simulated signals exhibits the dispersive regularization of gradient catastrophe by the emergence of a ‘tilted’ local PS-like structure which follows from the similarity with the corresponding 1-D fNLS model dynamics [Fig. 5(c)] where the presence of the local PS is a verified fact [35, 50]. The asymmetric shape of the emerging PS-like structure, which has been observed in different hydrodynamic models [51], is related to the local spectral red-shift which is similar to the effect of Raman scattering in nonlinear fiber optics where the asymmetry of the local PSs has been observed as well, usually in the context of supercontinuum generation [52]. This also follows from the plots of cross-section at the maximum compression point depicted in Fig. 6. The envelopes of both experimental and simulated signals resemble an asymmetric local PS profile. By increasing the chirp parameter μ , we observed further deviation from the PS shape due to the increasing role of the amplitude-sensitive higher-order nonlinear effects. Indeed, higher values of μ correspond to the increased pulse amplitude at the gradient catastrophe point, which plays a role of the effective PS background [34, 35]. The amplitude of the PS (according to Eq. (6)) is exactly three times the background value.

We provide a systematic comparison of the dependence of the local PS-like structures emergence position on the value of the chirp parameter μ (solid line Fig. 7). A

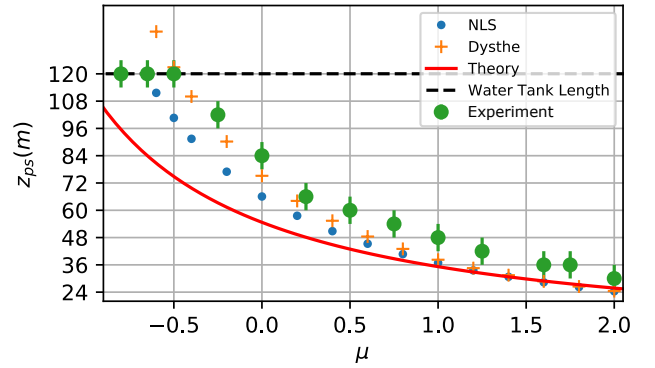


FIG. 7. **Dependence of the Peregrine soliton emergence distance on the initial chirp μ .** Each horizontal gray line represents the position of the probe in the water tank, the black dashed line shows the maximum propagation distance available in the experiments. The positions of the maximum compression point measured experimentally are shown by the green dots with the error bar which corresponds to the distance between probes. It is compared with the simulation of the exact 3 solitons solution in the 1-D fNLSe (blue dots) and the Dysthe equation (orange dots). The prediction according to Eq. (5) is plotted with the solid red line.

comparison between the data obtained in experiments, simulations of both 1-D fNLS and Dysthe equation, and prediction from the semi-classical theory for $\epsilon = 1/3$ are shown in Fig. 7. Semi-classical analysis, despite being derived in the zero-dispersion limit, predicts the result of experiments for high values of μ . Moreover, all the data presented in Fig. 7 demonstrates the same tendency. As followed from spatiotemporal diagrams (Fig. 5), numerical simulations of the Dysthe equation capture the water wave dynamics. Indeed, corresponding data depicted by orange crosses and green dots (green ticks indicate a minimum error value related to the distance between the probes) respectively, demonstrate a good agreement along all the values of μ . Experimental data at values of $\mu < -0.5$ are plotted at $z = 120$ m which indicates that the compression point occurs at distances larger than the length of the water tank.

IST spectra evolution

When the 1-D fNLSe is employed for the simulation of nonlinear wave propagation, the global IST spectrum is preserved. However, following the results of the comparison with the experimental data (Fig. 5), it becomes clear that the higher-order nonlinear effects must be taken into account in order to fully capture the complex self-focusing dynamics affected by the local spectral downshift. The Dysthe equation does not belong to the class of equations integrable by the IST technique. Nonetheless, having an integrable core in the form of 1-D fNLSe,

this model can be analysed using perturbation methods if the nonintegrable part is included with a small factor [53].

Recently, an approach which does not require the higher-order terms to be small has been introduced. In [41–43] and [44] it has been shown that IST spectra can be utilized for the characterization of coherent structures in strongly dissipative nonlinear models such as the Ginzburg-Landau equation for mode-locked lasers or the Lugiato-Lefever equation for passive microresonators. The essence of this approach relies on the fact that for each moment of time *the direct scattering problem*—the first step in the IST method [14]—can be solved for the given complex envelope of the field which has to be renormalized according to the employed convention [43]. Therefore, coherent structures that emerge in these complex models can be characterized by a discrete part of the IST spectrum and, therefore, represented by a point in the IST plane.

We use this approach for the characterization of the experimental data and simulations of the Dysthe equation presented in the previous section. For the demonstration, we choose two values of the chirp parameter $\mu = -0.8$ and 0. The resulting IST spectra evolution is shown in Fig. 8. Color gradient represents the length of the nonlinear propagation and varies from blue ($z = 6$ m) to red ($z = 120$ m). When the chirp parameter is small the discrete IST spectrum is almost conserved for both the experiments and the Dysthe model [54], which signifies that the nonlinear evolution is close to the one described by the 1-D fNLSe. Indeed, for $\mu = -0.8$ the gradient catastrophe occurs beyond the water tank length so the intensity-related higher-order nonlinear effects can be neglected. The spectral evolution corresponding to the initial condition with $\mu = 0$ —the exact three-soliton solution—demonstrates an intriguing behaviour. Namely, the two upper points of the IST spectrum make closed and open loops for simulations and experiment, respectively. The term ‘closed loop’ signifies that the discrete eigenvalues return to their initial positions while the open loop describes the situation when two eigenvalues *exchange positions* during the nonlinear evolution. The presence of a loop signifies that passing through the local PS stage, where the influence of the higher-order nonlinear effects is significant, discrete eigenvalues deviate from their initial position, however, entering the intermediate stage they return to the neighborhood of the origin, thereby, converging to the solution given by the 1-D fNLSe. Investigation of the difference between open and closed loops, as well as a possible exchange of the eigenvalues with the continuum, is beyond of the scope of this manuscript and is proposed as a novel and open problem in the nonintegrable systems evolution.

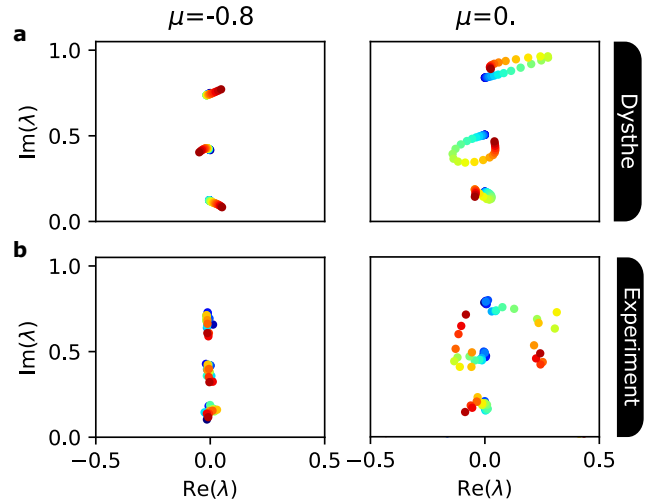


FIG. 8. **Comparison of the discrete IST spectra evolution in the Dysthe model and experiments.** (a) Simulations of the Dysthe equation. (b) Experimental data. Colors from blue to red correspond to the propagation over the full water tank length.

DISCUSSION

There are four key conclusions of this article that we would like to highlight: (i) the local emergence of the PSs as a regularization of the gradient catastrophe can occur in a completely solitonless case, which means that the soliton self-compression is a particular case of this more general process; (ii) the point of the PS emergence can be predicted and easily manipulated by adjusting the chirp parameter, i.e. by controlling the solitonic content of the initial conditions; (iii) structures similar to the local PS are observed in water tank experiments and simulations of the Dysthe model where coherent structures undergo significant red-shift in the spectral domain due to the influence of higher-order terms, which indicates another degree of universality of the gradient catastrophe regularization process; (iv) the IST spectra analysis of the non-integrable nonlinear wave evolution provides insights into the deviation and the convergence to the integrable dynamics as well as reveals unusual behaviour of the discrete points on the IST plane.

Our experimental observations also suggest that the dynamics of the N -soliton solutions rapidly deviates from the one predicted by the 1-D NLS model mainly due to the asymmetry induced by the frequency downshift. However, the local emergence of the coherent structures that can be seen as a modified analogue of the PS can be clearly observed. We, therefore, believe that further extension of the approaches used for the integrable systems to the non-integrable ones can improve our understanding of the realistic mechanisms taking place in the open sea.

METHODS

Water tank parameters and mode of operation

Experimental investigations of the gradient catastrophe regularization for solitonic and solitonless initial conditions have been performed in the water tank facility of the Hydrodynamics, Energetics, and Atmospheric Environment Lab (LHEEA) in Ecole Centrale de Nantes (France).

The water tank is 148 m long (120 m are effectively used), 5 m wide, and 3 m deep. It is equipped with a 8 m long absorbing beach having a parabolic shape. With the addition of pool lanes arranged in a “W” pattern in front of the beach the measured amplitude reflection coefficient is as low as 1%. Unidirectional waves are generated with a flap-type wave maker programmed remotely with a computer. The setup comprises of 20 equally-spaced resistive wave-gauges that are installed along the water tank at distances $z_j = 6 + (j - 1)6$ m, where $j = 1, 2, \dots, 20$ from the wave maker located at $z = 0$ m. This provides an effective measuring range of 114 m.

Models and numerical simulations

1-D fNLSe in the hydrodynamic formulation can be expressed as follows [11]:

$$\frac{\partial A}{\partial z} + \frac{i}{g} \frac{\partial^2 A}{\partial t^2} + i\alpha k_0^3 |A|^2 A = 0, \quad (8)$$

here A is the complex envelope of the water wave, g is the acceleration of gravity and k_0 - the wave number and $\alpha = 0.93$ is the finite depth correction. The general expression for α (see e.g. [55] for the details) is stated as:

$$\alpha = \frac{\cosh(4k_0 h) + 8 - 2 \tanh^2(k_0 h)}{8 \sinh^4(k_0 h)} - \frac{(2 \cosh^2(k_0 h) + 0.5)^2}{\sinh^2(2k_0 h)} \left(\frac{k_0 h}{\tanh(k_0 h)} - \frac{1}{4} \right), \quad (9)$$

where h is the water tank depth.

The Dysthe equation (a higher-order nonlinear generalized version of the 1-D fNLSe) is written in the following way [39]:

$$\frac{\partial A}{\partial z} + \frac{i}{g} \frac{\partial^2 A}{\partial t^2} + i\alpha k_0^3 |A|^2 A - \frac{k_0^3}{\omega_0} \left[6|A|^2 \frac{\partial A}{\partial t} + 2A \frac{\partial |A|^2}{\partial t} - iA \mathcal{H} \left(\frac{\partial |A|^2}{\partial t} \right) \right] = 0, \quad (10)$$

where \mathcal{H} stands for the Hilbert transform defined as follows:

$$\mathcal{F}(\mathcal{H}(f(t))) = -i \operatorname{sign}(\omega) \mathcal{F}(f(t)),$$

where \mathcal{F} represents the Fourier transform and sign is the signum function.

For the numerical simulations, we used 2048 points simulation box to avoid numerical errors appearing due to the periodicity in the Fourier space. z -axis has been discretized with 1000 point. For simulations of the nonlinear Eq. (8) and (10), we use step-adaptive Dormand-Prince Runge-Kutta method of Order 8(5,3) and approximate the dispersion operator by a pseudo-spectral scheme.

Calculation of IST spectra

Introducing the change of variables $\xi = 2\epsilon t$ and $\tau = \epsilon x$ in Eq. (1), we obtain 1-D NLSe in the following form:

$$i \frac{\partial u}{\partial \tau} + \frac{\partial^2 u}{\partial x^2} + 2|u|^2 u = 0 \quad (11)$$

We can define a so-called Lax pair for the 1-D fNLSe discovered by Zakharov and Shabat [12]:

$$Y_x = \begin{bmatrix} -i\xi & u \\ -u^* & i\xi \end{bmatrix} Y \quad (12)$$

$$Y_t = \begin{bmatrix} -i2\xi^2 + i|u|^2 & iu_x + 2\xi u \\ iu_x^* - 2\xi u^* & i2\xi^2 - i|u|^2 \end{bmatrix} Y, \quad (13)$$

where ξ is the spectral parameter and Y is a vector or matrix function. Equation (11) is a compatibility condition for Eqs. (13) and (12) (guaranties the equality of Y_{tx} and Y_{xt}).

Equation (12) can be inverted to show the spectral problem in more explicit way [49]:

$$\begin{bmatrix} -\partial_x & u \\ u^* & \partial_x \end{bmatrix} Y = i\xi Y \quad (14)$$

This problem can be numerically solved in the Fourier space with a standard routine integrated into the **SciPy package** of Python.

Numerically retrieved IST spectra are post-processed in order to eliminate points not constituting the discrete part of the spectrum, i.e. not representing the solitonic content of the analysed signal. This is realized by choosing a threshold on the imaginary axis of the IST spectrum (eigenvalues of the spectral problem represented

by Eq. (14)) and keeping only the eigenvalues that exceed the value. The threshold can be found empirically by changing the box discretization which affects non-representative part of the spectrum while keeping the actual IST spectrum unchanged within a reasonable range of parameters.

ACKNOWLEDGMENTS

This work has been partially supported by the Agence Nationale de la Recherche through the LABEX CEMPI project (ANR-11-LABX-0007) and the ANR DYSTURB Project (ANR-17-CE30-0004), the Ministry of Higher Education and Research, Hauts de France council and European Regional Development Fund (ERDF) through the Nord-Pas de Calais Regional Research Council and the European Regional Development Fund (ERDF) through the Contrat de Projets Etat-Région (CPER Photonics for Society P4S). E.F. is thankful for partial support from the Simons Foundation/MPS No. 651463. The work was also partially supported by the EPSRC (UK) grant EP/R00515X/2 (G.E.), NSF (USA) grant DMS 2009647 (A.T.) and Dstl (UK) grant DSTLX-1000116851 (G.R., G.E., S.R.).

* Univ. Lille, CNRS, UMR 8523 - PhLAM - Physique des Lasers Atomes et Molécules, F-59000 Lille, France; Present address: Institute of Physics, Swiss Federal Institute of Technology Lausanne (EPFL), CH-1015 Lausanne, Switzerland; alexey.tikan@epfl.ch

† École Centrale de Nantes, LHEEA, UMR 6598 CNRS, F-44 321 Nantes, France

‡ Department of Mathematics, Physics and Electrical Engineering, Northumbria University, Newcastle upon Tyne, NE1 8ST, United Kingdom

§ Department of Mathematics, University of Central Florida, Orlando, Florida, 32816, USA

¶ Université de Paris, MSC, UMR 7057 CNRS, F-75 013 Paris, France

** Laboratoire de Physique de l'École normale supérieure, ENS, Université PSL, CNRS, Sorbonne Université, Université Paris-Diderot, 75005 Paris, France

†† Institut Jean Le Rond d'Alembert, Sorbonne Université, CNRS, UMR 7190, F-75 005 Paris, France

‡‡ Univ. Lille, CNRS, UMR 8523 - PhLAM - Physique des Lasers Atomes et Molécules, F-59000 Lille, France

- [1] S. Annenkov and V. I. Shrira, *Physica D* **152-153**, 665 (2001).
- [2] C. Kharif, E. Pelinovsky, and A. Slunyaev, *Rogue waves in the ocean* (Springer Science & Business Media, 2008).
- [3] M. Onorato, S. Residori, U. Bortolozzo, A. Montina, and F. Arecchi, *Physics Reports* **528**, 47 (2013).
- [4] W. Cousins and T. P. Sapsis, *Physica D* **280-281**, 48 (2014).
- [5] S. Birkholz, C. Brée, A. Demircan, and G. Steinmeyer, *Phys. Rev. Lett.* **114**, 213901 (2015).
- [6] W. Cousins, M. Onorato, A. Chabchoub, and T. P. Sapsis, *Phys. Rev. E* **99**, 032201 (2019).
- [7] J. M. Dudley, G. Genty, A. Mussot, A. Chabchoub, and F. Dias, *Nature Reviews Physics* **1**, 675 (2019).
- [8] M. Onorato, A. R. Osborne, M. Serio, L. Cavaleri, C. Brandini, and C. T. Stansberg, *Phys. Rev. E* **70**, 067302 (2004).
- [9] S. Wabnitz, D. T. Reid, C. M. Heyl, R. R. Thomson, N. Akhmediev, B. Kibler, F. Baronio, and M. Beli, *J. Opt.* **18** (2016), 10.1088/2040-8978/18/6/063001.
- [10] S. Randoux, P. Walczak, M. Onorato, and P. Suret, *Physica D* **333**, 323 (2016).
- [11] R. El Koussaifi, A. Tikan, A. Toffoli, S. Randoux, P. Suret, and M. Onorato, *Phys. Rev. E* **97**, 012208 (2018).
- [12] V. E. Zakharov and A. B. Shabat, *Sov. Phys. JETP* **34**, 62 (1972).
- [13] V. E. Zakharov, *J. Appl. Mech. Tech. Phys.* **9**, 190 (1968).
- [14] S. Novikov, S. Manakov, L. Pitaevskii, and V. E. Zakharov, *Theory of solitons: the inverse scattering method* (Springer Science & Business Media, 1984).
- [15] V. E. Zakharov, *Stud. Appl. Math.* **122**, 219 (2009).
- [16] J. M. Soto-Crespo, N. Devine, and N. Akhmediev, *Phys. Rev. Lett.* **116**, 103901 (2016).
- [17] N. N. Akhmediev, J. M. Soto-Crespo, and N. Devine, *Phys. Rev. E* **94**, 022212 (2016).
- [18] D. S. Agafontsev and V. E. Zakharov, *Nonlinearity* **28**, 2791 (2015).
- [19] A. E. Kraych, D. Agafontsev, S. Randoux, and P. Suret, *Phys. Rev. Lett.* **123**, 093902 (2019).
- [20] F. Copie, S. Randoux, and P. Suret, *Reviews in Physics* , 100037 (2020).
- [21] P. Walczak, S. Randoux, and P. Suret, *Phys. Rev. Lett.* **114**, 143903 (2015).
- [22] P. Suret, R. E. Koussaifi, A. Tikan, C. Evain, S. Randoux, C. Szewaj, and S. Bielawski, *Nat. Commun.* **7**, 13136 (2016).
- [23] P. Suret, G. El, M. Onorato, and S. Randoux, "Rogue waves in integrable turbulence: semi-classical theory and fast measurements," in *Nonlinear Guided Wave Optics*, 2053-2563 (IOP Publishing, 2017) pp. 12–1 to 12–32.
- [24] E. A. Kuznetsov, *Doklady Akademii Nauk* **236**, 575 (1977).
- [25] Y. Ma, *Stud. Appl. Math.* **60**, 43 (1979).
- [26] D. H. Peregrine, *The Journal of the Australian Mathematical Society. Series B. Applied Mathematics* **25**, 16–43 (1983).
- [27] N. N. Akhmediev and V. I. Korneev, *Theor. Math. Phys.* **69**, 1089 (1986).
- [28] V. I. Shrira and V. V. Geogjaev, *J. Eng. Math.* **67**, 11 (2010).
- [29] K. B. Dysthe and K. Trulsen, *Phys. Scr.* **T82**, 48 (1999).
- [30] J. M. Dudley, F. Dias, M. Erkintalo, and G. Genty, *Nat. Photonics* **8**, 755 (2014).
- [31] B. Kibler, J. Fatome, C. Finot, G. Millot, F. Dias, G. Genty, N. N. Akhmediev, and J. M. Dudley, *Nat. Phys.* **6**, 790 (2010).
- [32] A. Chabchoub, N. P. Hoffmann, and N. N. Akhmediev, *Phys. Rev. Lett.* **106**, 204502 (2011).
- [33] N. N. Akhmediev, A. Ankiewicz, and M. Taki, *Phys. Lett. A* **373**, 675 (2009).
- [34] M. Bertola and A. Tovbis, *Commun. Pure Appl. Math.* **66**, 678 (2013).

- [35] A. Tikan, C. Billet, G. El, A. Tovbis, M. Bertola, T. Sylvestre, F. Gustave, S. Randoux, G. Genty, P. Suret, and J. M. Dudley, *Phys. Rev. Lett.* **119**, 033901 (2017).
- [36] A. Tikan, S. Randoux, G. El, A. Tovbis, F. Copie, and P. Suret, *Frontiers in Physics* **8**, 561 (2021).
- [37] A. Tikan, *Phys. Rev. E* **101**, 012209 (2020).
- [38] G. Michel, F. Bonnefoy, G. Ducrozet, G. Prabhudesai, A. Cazaubiel, F. Copie, A. Tikan, P. Suret, S. Randoux, and E. Falcon, *Phys. Rev. Fluids* **5**, 082801 (2020).
- [39] A. Goulet and W. Choi, *Physics of Fluids* **23**, 016601 (2011).
- [40] F. Bonnefoy, A. Tikan, F. Copie, P. Suret, G. Ducrozet, G. Prabhudesai, G. Michel, A. Cazaubiel, E. Falcon, G. El, and S. Randoux, *Phys. Rev. Fluids* **5**, 034802 (2020).
- [41] P. Ryczkowski, M. Närhi, C. Billet, J.-M. Merolla, G. Genty, and J. M. Dudley, *Nature Photonics* **12**, 221 (2018).
- [42] I. S. Chekhovskoy, O. V. Shtyrina, M. P. Fedoruk, S. B. Medvedev, and S. K. Turitsyn, *Phys. Rev. Lett.* **122**, 153901 (2019).
- [43] S. Sugavanam, M. K. Kopae, J. Peng, J. E. Prilepsky, and S. K. Turitsyn, *Nature communications* **10**, 1 (2019).
- [44] S. K. Turitsyn, I. S. Chekhovskoy, and M. P. Fedoruk, *Optics Letters* **45**, 3059 (2020).
- [45] E. Madelung, *Zeitschrift für Physik* **40**, 1 (1927).
- [46] G. El and M. A. Hoefer, *Physica D* **333**, 11 (2016).
- [47] B. Dubrovin, T. Grava, and C. Klein, *J. Nonlinear Sci.* **19**, 57 (2009).
- [48] A. Tovbis and S. Venakides, *Physica D: Nonlinear Phenomena* **146**, 150 (2000).
- [49] J. Yang, *Nonlinear waves in integrable and nonintegrable systems*, Vol. 16 (Siam, 2010).
- [50] A. Tikan, S. Bielawski, C. Szwaj, S. Randoux, and P. Suret, *Nat. Photonics* **12**, 228 (2018).
- [51] D. Clamond, M. Francius, J. Grue, and C. Kharif, *European Journal of Mechanics-B/Fluids* **25**, 536 (2006).
- [52] J. M. Dudley, G. Genty, and S. Coen, *Rev. Mod. Phys.* **78**, 1135 (2006).
- [53] Y. S. Kivshar and B. A. Malomed, *Rev. Mod. Phys.* **61**, 763 (1989).
- [54] P. Suret, A. Tikan, F. Bonnefoy, F. Copie, G. Ducrozet, A. Gelash, G. Prabhudesai, G. Michel, A. Cazaubiel, E. Falcon, G. El, and S. Randoux, *Phys. Rev. Lett.* **125**, 264101 (2020).
- [55] C. C. Mei, *The applied dynamics of ocean surface waves*, Vol. 1 (World scientific, 1989).

Chapter 4

Bidirectional soliton gas in dispersive hydrodynamics

4.1 Outline of the Problem

The main motivation for this work was the experimental realisation of rarefied bidirectional soliton gases in a shallow water tank [51, 143]. The bidirectional shallow water wave dynamics can be modelled by the Kaup-Boussinesq (KB) system [144]:

$$\eta_T + (\eta w)_X = -\frac{1}{3}w_{XXX}, \quad w_T + ww_X + \eta_X = 0, \quad (4.1)$$

where η is the surface wave elevation and w the depth-mean longitudinal velocity. The KB equation has two families of soliton solution that we denote in the following as: left-propagating solitons and right-propagating solitons. Note that “right” and “left” propagating solitons is not an adequate terminology to define the soliton family since a right-propagating soliton can have a negative velocity after a Galilean boost. Besides we show that the transport velocity of a soliton is affected by collisions with other solitons, and a right-propagating soliton could “effectively” propagate to the left after multiple collisions in a soliton gas. A different definition is used in the article to rigorously identify the two different families of soliton denoted $(-)$ and $(+)$: in the reference frame chosen in (4.1), the $(-)$ family coincides with left-propagating soliton solution and the $(+)$ family coincides with right-propagating soliton solution, and we will choose the phe-

nomenclological terminology for simplicity; note that this is also the case for the soliton solutions of the equation (4.3).

The nonlinear change of variables

$$\eta = \rho + \frac{1}{2} \left(u + \frac{\rho_x}{2\rho} \right)_x, \quad w = v + \frac{\rho_x}{2\rho}, \quad X = \frac{2}{\sqrt{3}} x, \quad T = \frac{2}{\sqrt{3}} t, \quad (4.2)$$

transforms the KB system into the so-called resonant NLS equation (rNLSE) :

$$\rho_t + (\rho v)_x = 0, \quad (\rho v)_t + (\rho v^2 + P(\rho))_x = a(\rho(\ln \rho)_{xx})_x, \quad (4.3)$$

where $a = -1$. The link between these two systems is surprising as the rNLSE has been originally derived in magneto-hydrodynamics of cold collisionless plasma, see for instance [145]. As a result the KB soliton gas dynamics maps to the rNLSE soliton gas dynamics. We chose to present the results using the rNLSE rather than the KB equation since they could be easily compared to another well-established bidirectional wave model: the defocusing NLS equation (dNLSE). The dNLSE can be written in the form (4.3) with $a = +1$, and can be seen as the positive dispersion counterpart ($a > 0$) of the rNLSE. Note that the rNLSE and the dNLSE (together with the fNLSE) belong to the more general family of integrable Eulerian bidirectional systems (see [12]). An essential difference with the fNLSE studied so far is the real nature of the IST spectrum for both the dNLSE and the rNLSE. In that sense these equations are rather seen as bidirectional extensions of the KdV equation which also possesses a real IST spectrum.

The aim of this work is to provide a consistent general extension of the kinetic theory initially developed for the KdV soliton gas [49] to these physically important bidirectional systems, and more generally to integrable bidirectional Eulerian systems. As presented in Section 1.5.3, we have for non spatially homogeneous KdV soliton gases $f \equiv f(\lambda, x, t)$

$$f_t + (sf)_x = 0, \quad s(\lambda, x, t) = s_0(\lambda) + \int_0^\infty \Delta(\lambda, \mu) f(\mu, x, t) |s(\lambda, x, t) - s(\mu, x, t)| d\mu, \quad (4.4)$$

where $s_0(\lambda) = 4\lambda^2$ is the velocity of an isolated single soliton of parameter λ and $\Delta(\lambda, \mu) = \frac{\text{sgn}(\lambda-\mu)}{\lambda} \ln |(\lambda - \mu)/(\lambda + \mu)|$ the expression for the phase (position) shift of a λ -soliton in a two-

soliton interaction with a μ -soliton. Contrarily to Section 1.5.3, $\Delta(\lambda, \mu)$ (and the phase-shift defined) is defined for all sign of $\lambda - \mu$. The heuristic method proposed in [49], and used in our work, relies on one important observation that the kinetic description of the gas only depends on the phase-shift relation, or phase-shift kernel, for pairwise collisions. Although this has been proven for only one additional system [53], the successful comparison between analytical predictions and numerical results for dNLSE and rNLSE soliton gases supports this conjecture.

Before introducing a similar description for bidirectional gases, one needs to discuss the different types of soliton pairwise collisions in the bidirectional systems. As written above, we suppose for simplicity that $(-)$ denotes the left-propagating solitons family and $(+)$ the right-propagating solitons family. Both dNLSE and rNLSE soliton solutions correspond to single peak pulses of the field $\rho(x, t)$, propagating on a constant background $\rho = 1$. The dNLSE soliton is commonly called dark soliton and corresponds to a depletion of the field $\rho(x, t)$, while the rNLSE soliton is called anti-dark soliton and corresponds to an augmentation of the field $\rho(x, t)$, cf. Figure 2 of the paper. We distinguish two types of the pairwise collisions occurring in bidirectional systems:

- overtaking collisions involving solitons belonging to the same family (solitons propagating in the same direction) characterised by the position shifts $\Delta_{++}(\lambda, \mu)$ and $\Delta_{--}(\lambda, \mu)$,
- head-on collisions between solitons of different kind, (solitons propagating in opposite directions), characterised by the position shifts $\Delta_{+-}(\lambda, \mu)$ and $\Delta_{-+}(\lambda, \mu)$.

For instance $\Delta_{-+}(\lambda, \mu)$ is the position shift of a soliton of parameter λ propagating to the left $(-)$ in a collision with a soliton of parameter μ propagating to the right $(+)$. We qualify the bidirectional soliton gas “isotropic” if the position shifts for the overtaking and head-on collisions between λ and μ -solitons satisfy the following sign conditions:

$$\text{sgn}[\Delta_{++}(\lambda, \mu)] = \text{sgn}[\Delta_{+-}(\lambda, \mu)], \quad \text{sgn}[\Delta_{--}(\lambda, \mu)] = \text{sgn}[\Delta_{-+}(\lambda, \mu)]. \quad (4.5)$$

i.e. the λ -soliton experiences a shift of a certain sign, say shift forward, irrespectively of the type of the collision (i.e. the family of the μ -soliton). If the conditions in (4.5) are not satisfied, the sign of the phase shift depends on the type of the collision and we call the corresponding soliton gas “anisotropic”. The phase-shift expressions for the dNLSE and the rNLSE equations are given respectively in equations (11) and (17) of the paper. Figure 1 clearly illustrates that the dNLSE

soliton gas is isotropic whereas the rNLSE soliton gas is anisotropic. Thus Eq. (4.3) provides a prototypical example to investigate bidirectional soliton gases, with an isotropic regime if $a = +1$ (dNLSE) and an anisotropic regime if $a = -1$ (rNLSE).

4.2 Summary of Results and Outlook

This work appears in the publication

- T. Congy, G. El and **G. Roberti**, “Soliton gas in bidirectional dispersive hydrodynamics”, Phys. Rev. E, 103:042201, 2021.

We can construct the kinetic description for soliton gases of dNLSE and rNLSE systems (and more generally integrable Eulerian dispersive hydrodynamic equations). We introduce two separate DOS’s: $f_-(\lambda, x, t)$ for the population of left-propagating solitons and $f_+(\lambda, x, t)$ for the population of right-propagating solitons. For the dNLSE the spectral support of f_- is $(-1, 0]$ and the spectral support of f_+ is $[0, 1)$: the two supports intersect at $\lambda = 0$ corresponding to the zero-velocity dark soliton. For the rNLSE the spectral support of f_- is $(-\infty, -1)$ and the spectral support of f_+ is $(1, \infty)$: the two supports are disjoint and there is no zero-velocity solution. The isospectrality of integrable evolution implies now two separate conservation laws:

$$(f_-)_t + (s_- f_-)_x = 0, \quad (f_+)_t + (s_+ f_+)_x = 0, \quad (4.6)$$

where $s_-(\lambda, x, t)$ and $s_+(\lambda, x, t)$ are the transport velocities associated with the motion of $(-)$ solitons and $(+)$ solitons respectively. We derive the equations of state for s_{\pm} using the direct phenomenological approach presented for the KdV soliton gas: $s_{\pm}(\lambda, x, t)$ is identified as the velocity of a trial λ -soliton of the gas. Let’s consider a tracer λ -soliton propagating to the right ($+$ family), and let’s compute its displacement in a gas over a time interval dt sufficiently large to incorporate a large number of collisions, but sufficiently small to ensure that the spatio-temporal field $f_{\pm}(\lambda, x, t)$ is stationary over dt and homogeneous on a typical spatial scale $c_{\pm}(\lambda)dt$. Having this in mind, we drop the (x, t) -dependence for convenience. The displacement is given by two distinct contributions:

- each overtaking collision with a right-propagating μ -soliton shifts the λ -soliton by the dis-

tance $\Delta_{++}(\lambda, \mu)$. $f_+(\mu)|s_+(\lambda) - s_+(\mu)|dt$ is the average number of such collisions during the time dt , and the resulting displacement of the λ -soliton is given by $\int \Delta_{++}(\lambda, \mu)f_+(\mu)|s_+(\lambda) - s_+(\mu)|d\mu$ where the integration is performed over the spectral support of $f_+(\lambda)$.

- Each head-on collision with a left-propagating μ -soliton shifts the λ -soliton by $\Delta_{+-}(\lambda, \mu)$. $f_-(\mu)|s_+(\lambda) - s_-(\mu)|dt$ is the average number of such collisions during the time dt , and the resulting displacement of the λ -soliton is given by $\int \Delta_{+-}(\lambda, \mu)f_-(\mu)|s_+(\lambda) - s_-(\mu)|d\mu$ where the integration is now performed over the spectral support of $f_-(\lambda)$.

Equating the total displacements of the right-propagating λ -solitons to $s_+(\lambda)dt$, we obtain the second component of the system:

$$\begin{aligned} s_-(\lambda) &= c_-(\lambda) + \int \Delta_{--}(\lambda, \mu)f_-(\mu)|s_-(\lambda) - s_-(\mu)|d\mu + \int \Delta_{-+}(\lambda, \mu)f_+(\mu)|s_-(\lambda) - s_+(\mu)|d\mu, \\ s_+(\lambda) &= c_+(\lambda) + \int \Delta_{++}(\lambda, \mu)f_+(\mu)|s_+(\lambda) - s_+(\mu)|d\mu + \int \Delta_{+-}(\lambda, \mu)f_-(\mu)|s_+(\lambda) - s_-(\mu)|d\mu. \end{aligned} \quad (4.7)$$

The first component of (4.7) is obtained by considering a left-propagating λ -soliton and using a similar procedure, and the equation of state (4.7) of a bidirectional gas corresponds in general to a two coupled linear system of integral equations.

Note that the supports of f_- and f_+ for the dNLSE soliton gas form a simply connected set $(-1, 0] \cup [0, 1) = (-1, 1)$, and since the gas is isotropic, the distinction between the left- and right-propagating solitons becomes unnecessary. Thus the kinetic equation (4.6),(4.7) for bidirectional dNLSE soliton gas is naturally reduced to a unidirectional gas equation similar to (4.4) for a single DOS $f(\lambda)$ defined on the set $(-1, 1)$:

$$f(\lambda) = \begin{cases} f_-(\lambda), & -1 < \lambda \leq 0 \quad (\text{left-propagating soliton}), \\ f_+(\lambda), & 0 \leq \lambda < +1 \quad (\text{right-propagating soliton}). \end{cases} \quad (4.8)$$

The dimension of the system (4.7) does not depend on the bidirectional nature of the system but rather on the anisotropic nature of their interaction and the support of their IST spectrum.

The DOS $f(\lambda)$ (or $f_{\pm}(\lambda)$ in the anisotropic case) represents a comprehensive spectral characteris-

tics that determines all statistical parameters of the nonlinear random wave field $(\rho(x, t), u(x, t))$ in a soliton gas. The most obvious set of such statistical parameters are the ensemble averages of the conserved quantities. For instance the ensemble-average $\langle \eta \rangle$ in the case of a KB soliton gas corresponds to the average surface wave elevation. We propose in this work a simple heuristic approach that enables one to link the spectral DOS of a soliton gas with the ensemble averages of conserved quantities of the integrable system (4.3). As an illustration let's consider the first conserved quantity of the dNLSE: $\rho(x, t)$.

We consider here a homogeneous soliton gas, i.e. a gas whose statistical properties, particularly the DOS, do not depend on x, t . The generalisation to a “slowly modulated” soliton gas described by $f(\lambda, x, t)$ is trivial and explained in the paper. The proposed approach is based on the natural assumption that the nonlinear wave field in a homogeneous soliton gas represents an ergodic random process, both in x and t . The ergodicity property implies that ensemble-averages in the soliton gas, such as $\langle \rho(x, t) \rangle$, can be replaced by the corresponding spatial averages:

$$\langle \rho \rangle = 1 + \lim_{L \rightarrow \infty} \frac{I}{2L}, \quad I = \int_{x-L}^{x+L} (\rho(y, t) - 1) dy, \quad (4.9)$$

for a single representative realisation of soliton gas; for computational convenience we subtract the background $\rho = 1$ from the field $\rho(y, t)$. The field $\rho(y, t)$ for $y \in (x - L, x + L)$ (and $L \gg 1$) can be approximated by a N -soliton solution of the dNLSE with $N \gg 1$. Using the conservation in time of the quantity $\int \rho dx$, we show that the integral I can be approximated by the sum:

$$I \sim \sum_i \left(\int_{-\infty}^{+\infty} (\rho_s(y; \lambda_i) - 1) dy \right) = \sum_i -2\sqrt{1 - \lambda_i^2}, \quad (4.10)$$

where λ_i are the spectral parameters of the N -soliton solution and ρ_s the single-soliton solution; the second equality is obtained by substituting the expression of the dark soliton solution in the integral. In other words, the integral of the N -soliton over the interval $(x - L, x + L)$ is equal to the sum of the integral of its constituent $\int \rho_s(y; \lambda) dy$. By definition the spectral parameters λ_i are distributed by the density $2Lf(\lambda)$. Taking the continuous limit $\sum_i \rightarrow \int_{-1}^{+1} 2Lf(\lambda) d\lambda$ we obtain:

$$\langle \rho(x, t) \rangle = 1 - \int_{-1}^{+1} 2\sqrt{1 - \lambda^2} f_-(\lambda) d\lambda. \quad (4.11)$$

The heuristic method presented here easily generalises to other conserved quantities of the dNLSE and the rNLSE, as shown in the paper. This method only requires to integrate the single-soliton solution and thus can be readily applied to any integrable dispersive hydrodynamics systems supporting the soliton resolution scenario. The formula (4.11) is then used to track the dynamics of the DOS numerically.

Our ability to solve the integral equation of state in (4.4) or (4.7) is very limited, and strongly depends on the particular form of the phase-shift integral kernel. We show in Section 1.5.3 that the integral equation of state can be solved by discretising the DOS $f(\lambda, x, t)$ or $f_{\pm}(\lambda, x, t)$ with respect to the soliton spectral parameter λ . Let's consider for instance the simpler case of the dNLSE soliton gas, and suppose that it is composed of M distinct spectral components of parameter ζ_i :

$$f(\lambda, x, t) = \sum_{i=1}^M w_i(x, t) \delta(\lambda - \zeta_i), \quad (4.12)$$

where δ is the delta-function distribution. The ansatz (4.12) transforms $f(\lambda, x, t)$ into a M -dimensional vector $\mathbf{w} = (w_1, \dots, w_n)$. As described in Section 1.5.3, (4.4) for the dNLSE soliton gas reduces to M hydrodynamic (quasi-linear) conservation laws. The expression of the moment $\langle \rho \rangle$ also simplifies and reads:

$$\langle \rho(x, t) \rangle = 1 - \sum_{i=1}^M 2\sqrt{1 - \zeta_i^2} w_i(x, t). \quad (4.13)$$

If similar expressions are known for $M - 1$ other conserved quantities q_i (using the heuristic approach presented above) one can write:

$$\langle \mathbf{q} \rangle = K(\zeta_i) \mathbf{w}, \quad \mathbf{q} = (q_1 = \rho, q_2 = u, \dots, q_M), \quad (4.14)$$

where K is a $M \times M$ matrix that only depends on ζ_i 's. Ensemble-averages \mathbf{q} can be easily computed numerically, and such a method is used in our work to determine the numerical DOS for dNLSE soliton gases $\mathbf{w} = K(\zeta_i)^{-1} \mathbf{q}$.

The validity of the kinetic description has been tested by solving, numerically and analytically,

the Riemann problem for the kinetic equation (4.4) or (4.6),(4.7). The problem describes the interaction dynamics of two soliton gases prepared in the respective uniform states $\mathbf{w}^L \in \mathbb{R}^M$ and $\mathbf{w}^R \in \mathbb{R}^M$ and initially separated:

$$\mathbf{w}(x, 0) = \begin{cases} \mathbf{w}^L, & x < 0, \\ \mathbf{w}^R, & x \geq 0. \end{cases} \quad (4.15)$$

The spectral distribution (4.15) corresponds to the soliton gas “shock tube” problem, an analogue of the standard shock tube problem of classical gas dynamics. We show that the solution of the Riemann problem is composed of $M + 1$ constant states, separated by M contact discontinuities, satisfying appropriate Rankine-Hugoniot conditions, and propagating at the transport velocities s_i . The determination of the plateaus’ value is detailed in the paper. The numerical solution of the Riemann problem is obtained by direct simulation of the dNLSE (4.3) ($a = 1$). We implement the soliton gas using the superposition method developed in [7] and summarised in Section 1.5.3. The coefficients $w_i^{L,R}$ are chosen such that the soliton gas is initially in a rarefied regime. The soliton density drastically increases in the region where the two soliton gases collide: as depicted in Figure 4 of the paper, solitons are no longer isolated in the “colliding region” (denoted region II in figure 4). Thus the theory developed in this work could be tested in the dense regime of soliton gases.

Note that we generalise the results presented in this section to the anisotropic case of the rNLSE.

The analytical predictions are in very good agreement with the numerical solution of the soliton shock tube problem, as depicted in Figures 5-9 of the paper. Although the derivation of the kinetic equation (4.6),(4.7) for a dense bidirectional soliton gas is based on the phenomenological method of [49], it could be formally justified using the thermodynamic limit of the modulation equations that has been developed for the KdV and fNLSE in [48, 53]. Besides this work highlights the importance of the anisotropic nature of a bidirectional system in the gas dynamics. This is illustrated by the Figure 6 displaying the ensemble averages $\langle \rho \rangle$ for the following rNLSE two-component gas shock tube problem: in the case (a) the soliton gas is only composed of right-propagating solitons and only overtaking collisions occur, while in the case (b) one component is right-propagating and

the other is left-propagating and only head-on collisions occur. The numerical results (solid black line) and analytical results (dash-dotted red line) are compared to a non-interacting hypothetical case (dashed blue line) where $\Delta_{\pm\pm} = \Delta_{\pm\mp} \equiv 0$: the effects of the head-on and overtaking interactions on the gas dynamics drastically differ due to the violation of the isotropy condition (4.5). Note that contact discontinuities have a finite slope in the plot of $\langle \rho \rangle$ due to the method for averaging ρ that combines both ensemble- and spatial-averaging. Besides, as noticed in the bidirectional shallow water experiment [51, 143], the impact of overtaking interactions on the gas dynamics is much stronger than the impact of head-on interactions which could be neglected in a first approximation.

This work notably proposes new extensions of the kinetic theory and averaging methods to:

- a large class of bidirectional integrable systems,
- non-integrable systems supporting solitary wave solutions that exhibit nearly elastic collisions, such as the viscous fluid conduit equation describing the dynamics of the interface between two immiscible viscous fluids with high density and viscosity contrast ratios [146].

Another important new direction of research is the description of soliton gases in a quasi-1D repulsive Bose-Einstein condensate (BEC) in a trapping potential, whose dynamics is governed by the celebrated Gross-Pitaevskii equation. The Gross-Pitaevskii equation corresponds to the dNLSE supplemented by an external potential term, and the investigation of soliton gas in BECs could shed new light on turbulence in superfluids also called “quantum turbulence”.

Soliton gas in bidirectional dispersive hydrodynamicsThibault Congy ^{*}, Gennady El , and Giacomo Roberti *Department of Mathematics, Physics and Electrical Engineering, Northumbria University, Newcastle upon Tyne, United Kingdom*

(Received 10 December 2020; accepted 5 February 2021; published 2 April 2021)

The theory of soliton gas had been previously developed for unidirectional integrable dispersive hydrodynamics in which the soliton gas properties are determined by the overtaking elastic pairwise interactions between solitons. In this paper, we extend this theory to soliton gases in bidirectional integrable Eulerian systems where both head-on and overtaking collisions of solitons take place. We distinguish between two qualitatively different types of bidirectional soliton gases: isotropic gases, in which the position shifts accompanying the head-on and overtaking soliton collisions have the same sign, and anisotropic gases, in which the position shifts for head-on and overtaking collisions have opposite signs. We construct kinetic equations for both types of bidirectional soliton gases and solve the respective shock-tube problems for the collision of two “monochromatic” soliton beams consisting of solitons of approximately the same amplitude and velocity. The corresponding weak solutions of the kinetic equations consisting of differing uniform states separated by contact discontinuities for the mean flow are constructed. Concrete examples of bidirectional Eulerian soliton gases for the defocusing nonlinear Schrödinger (NLS) equation and the resonant NLS equation are considered. The kinetic equation of the resonant NLS soliton gas is shown to be equivalent to that of the shallow-water bidirectional soliton gas described by the Kaup-Boussinesq equations. The analytical results for shock-tube Riemann problems for bidirectional soliton gases are shown to be in excellent agreement with direct numerical simulations.

DOI: [10.1103/PhysRevE.103.042201](https://doi.org/10.1103/PhysRevE.103.042201)**I. INTRODUCTION**

Dispersive hydrodynamics modeled by hyperbolic conservation laws regularized by conservative, dispersive corrections describe various nonlinear wave structures that include solitary waves (solitons), dispersive shock waves (DSWs), rarefaction waves, and their interactions [1]. A particular feature of dispersive hydrodynamics is the intrinsic scale separation, often providing a qualitatively new perspective on some classical mathematical and fluid dynamical settings (such as Riemann problems or flows past topography), but also revealing novel phenomena such as hydrodynamic soliton tunneling [2,3] and expansion shocks [4].

On a small-scale, microscopic level, dispersive hydrodynamics typically involve coherent nonlinear wave structures such as solitons and rapidly oscillating periodic waves, while the large-scale, macroscopic coherent features are represented by slow modulations of these periodic waves or soliton trains. The prominent example of a dispersive hydrodynamic structure exhibiting such two-scale coherence and persisting in integrable and nonintegrable systems is DSW, the dispersive analog of a classical, viscous shock wave [5].

There is another class of problems in dispersive hydrodynamics, which involve the wave structures exhibiting coherence at a microscopic scale, while being macroscopically incoherent, in the sense that the values of the wave field at two points separated by a distance much larger than the intrinsic dispersive length of the system (the soliton width),

are not dynamically related. These structures can be broadly viewed as dispersive-hydrodynamic analogs of turbulence, and the qualitative and quantitative properties of such a conservative turbulence strongly depend on the integrability properties of the underlying microscopic dynamics. In [6] Zakharov introduced the notion of “integrable turbulence” for random nonlinear wave fields governed by integrable equations such as the Korteweg–de Vries (KdV) or nonlinear Schrödinger (NLS) equations. The source of randomness in integrable turbulence is typically related to some sort of stochastic initial or boundary conditions, although one can envisage dynamical mechanisms of the effective randomization of the wave field [7,8]. The theoretical perspective of integrable turbulence has turned out to be very fruitful, providing new insights into some long-standing problems of nonlinear physics related, e.g., to modulational instability and the formation of rogue waves [9–11]. Indeed, integrable turbulence proved a promising theoretical framework for the interpretation of experimental and observational data in fiber optics and fluid dynamics [12].

Solitons, viewed as stable “wave particles” of macroscopic dispersive-hydrodynamic structures, can form large disordered, statistical ensembles, strikingly different from the macroscopically coherent DSWs, and calling for the analogy with gases of classical or quantum particles. Such statistical soliton ensembles, or “soliton gases,” can be naturally generated from both nonvanishing deterministic (e.g., periodic or quasiperiodic) and random initial conditions due to the processes of soliton fissioning [13,14] or modulation instability [15]. The ubiquity of solitons in applications and the integrable nature of the underlying wave dynamics makes

*Corresponding author: thibault.congy@northumbria.ac.uk

soliton gases a particularly attractive object for modeling the complex nonlinear wave phenomena occurring in the ocean and in high-intensity incoherent light propagation through optical materials (see [16], and references therein). The random nonlinear wave field in a soliton gas represents a particular case of integrable turbulence [6].

Within the inverse scattering transform (IST) formalism, each soliton is characterized by a discrete eigenvalue λ_j of the spectrum of the linear operator associated with the integrable nonlinear evolution equation. There are two basic aspects of the microscopic, soliton dynamics that determine the macroscopic, statistical properties of integrable soliton gases and turbulence: (i) isospectrality of integrable evolution resulting in the preservation of soliton eigenvalues; and (ii) pairwise elastic collisions accompanied by phase shifts (or position shifts) expressed in terms of the respective spectral parameters of the interacting solitons.

The macroscopic properties of a soliton gas are determined by the spectral characteristics called the density of states (DOS) $f(\lambda) > 0$, defined such that the number of solitons found at the moment of time t in the element $[\lambda, \lambda + d\lambda] \times [x, x + dx]$ of the phase space is $f(\lambda)d\lambda dx$ (assuming $\lambda \in \mathbb{R}$, the generalization to complex spectrum being straightforward [17]). DOS represents the definitive statistical characteristics of soliton gas distinguishing it from an arbitrary random collection of solitons. The first controlled generation of soliton gas characterized by a measurable DOS has been recently reported in [18].

For uniform, statistically homogeneous soliton gases the DOS depends on the spectral parameter only. For spatially nonhomogeneous soliton gases one has $f \equiv f(\lambda, x, t)$, and the isospectrality of integrable evolution implies the conservation equation

$$f_t + (sf)_x = 0, \quad (1)$$

where the transport velocity (the mean velocity of a “tracer” soliton in a gas) $s(\lambda, x, t)$ is found from the integral equation of state [17]

$$s(\lambda, x, t) = c(\lambda) + \int_{\Omega} \Delta(\lambda, \mu) f(\mu, x, t) \times |s(\lambda, x, t) - s(\mu, x, t)| d\mu. \quad (2)$$

Here $c(\lambda)$ is the velocity of an isolated single soliton with the spectral parameter $\lambda \in \Omega$, and the integral term describes its modification due to collisions with other “ μ solitons” in a gas, each collision being accompanied by the position shift $\Delta(\lambda, \mu)$, often called the phase shift. The integration in (2) is performed over the spectral support $\Omega \subset \mathbb{R}$ of the DOS $f(\lambda, x, t)$. If one assumes that (i) $\text{sgn}[\Delta(\lambda, \mu)] = \pm \text{sgn}(\lambda - \mu)$ and (ii) $s'(\lambda) \neq 0$, the modulus sign in (2) can be removed by introducing $\Delta(\lambda, \mu) = \text{sgn}(\lambda - \mu)G(\lambda, \mu)$ so that one arrives at the conventional form of the equation of state as in [17,19], involving $G(\lambda, \mu)$ rather than $\Delta(\lambda, \mu)$ as the integral kernel. For example, for the KdV solitons one has $c(\lambda) = 4\lambda^2$, $\text{sgn}[\Delta(\lambda, \mu)] = +\text{sgn}(\lambda - \mu)$, $s'(\lambda) > 0$, and $G(\lambda, \mu) = \lambda^{-1} \ln |(\lambda + \mu)/(\lambda - \mu)|$ (see, e.g., [20]).

The transport equation (1) for the DOS complemented by the integral equation of state (2) comprise the kinetic equation for soliton gas. A kinetic equation of the type (1), (2) was first

introduced in [21] for the case of rarefied, or dilute, gas of KdV solitons, when the interaction term in the equation state (2) represents a small correction and the soliton velocity in a gas is found from the expression $s \approx 4\lambda^2 + \lambda^{-1} \int_0^{\lambda_{\max}} \ln |(\lambda + \mu)/(\lambda - \mu)| f(\lambda, x, t) [4\lambda^2 - 4\mu^2] d\mu$, which is an approximate solution of the equation of state (2) for the KdV soliton gas. The full kinetic equation (1), (2) for a dense soliton gas was derived and analyzed in the context of the KdV equation in [22,23] and the focusing NLS equation in [16,17] (in the latter case $\lambda \in \mathbb{C}$). A general mathematical analysis of the kinetic equation (1), (2) has been undertaken in [19], which showed that it possesses an infinite series of integrable linearly degenerate hyperbolic reductions. Very recently the kinetic equation (1), (2) has attracted much attention in the context of generalized hydrodynamics, a hydrodynamic theory of quantum many-body integrable systems (see [24–26], and references therein).

In the context of dispersive hydrodynamics the kinetic equation (1), (2) describes “unidirectional” soliton gases supported by scalar integrable equations of the form

$$u_t + F(u)_x = (D[u])_x, \quad (3)$$

where $F(u)$ is the nonlinear hyperbolic flux and $D[u]$ is a differential (generally integrodifferential) operator, possibly nonlinear, that gives rise to a real-valued linear dispersion relation. The spectral single-soliton solutions to Eq. (3) are characterized by the soliton velocity $c(\lambda)$ and the phase-shift kernel $\Delta(\lambda, \mu)$ characterizing the “overtaking” two-soliton interactions. However, the scalar integrable dispersive hydrodynamics of the form (3), such as the KdV, modified KdV, Camassa-Holm, or Benjamin-Ono equations typically arise as small-amplitude, “unidirectional” approximations of more general Eulerian bidirectional systems (see [27])

$$\begin{aligned} \rho_t + (\rho u)_x &= (D_1[\rho, u])_x, \\ (\rho u)_t + [\rho u^2 + P(\rho)]_x &= (D_2[\rho, u])_x, \end{aligned} \quad (4)$$

where $D_{1,2}[\rho, u]$ are conservative, dispersive operators, $P(\rho) > 0$ is the monotonically increasing pressure law, and ρ and u are interpreted as a mass density and fluid velocity, respectively. This class of equations generalizes the shallow-water and isentropic gas dynamics equations while encompassing many of the integrable dispersive hydrodynamic models such as the Kaup-Boussinesq (KB) system [28], the hydrodynamic form of the defocusing NLS equation [29], or the Calogero-Sutherland system describing the dispersive hydrodynamics of quantum many-body systems [30]. Due to the bidirectional nature, the Eulerian dispersive hydrodynamics (4) supports solitons that experience both overtaking and head-on elastic collisions which are generally characterized by two different phase-shift kernels $\Delta_1(\lambda, \mu) \neq \Delta_2(\lambda, \mu)$. Indeed, the rarefied bidirectional shallow-water soliton gas realized in the water tank experiments [31,32] was modeled by the KB system [28], which exhibits qualitatively different properties for head-on and overtaking position shifts in the pairwise soliton collisions [33] so that the overtaking interactions can be characterized as “strong” and the head-on interactions as “weak.” We shall term such collisions and the associated soliton gases “anisotropic.” On the other hand, some bidirectional dispersive hydrodynamic systems support

soliton solutions that exhibit “isotropic” collisions characterized by the same phase-shift kernel $\Delta(\eta, \mu)$ for the head-on and overtaking interactions (e.g., the defocusing NLS equation [34]).

Despite the significant recent advances of the kinetic theory of unidirectional soliton gases, a consistent general extension of this theory to the physically important bidirectional case has not been available so far, and this paper is devoted to the development of such an extension. The paper is organized as follows. In Sec. II we present the general construction of the kinetic equation for bidirectional soliton gas and realize it for the cases of the defocusing nonlinear Schrödinger (DNLS) equation and its “stable” negative dispersion counterpart, the so-called resonant NLS (RNLS) equation, having applications in magnetohydrodynamics of cold collisionless plasma [35], and reducible to the KB system for shallow-water waves by a simple change of variables. It turns out that, due to the pairwise collisions of dark DNLS solitons being isotropic, the bidirectional kinetic equation for the dark (gray) solitons of the DNLS equation reduces to the unidirectional kinetic equation of the form (1), (2). Contrastingly, the soliton collisions of antidark RNLS solitons are anisotropic, and the kinetic equation for this case represents a pair of the kinetic equations of the type (1), (2) with some nonlinear coupling through the equation of state. In Sec. III we derive expressions for the mean field in both soliton gases in terms of the spectral DOS. To demonstrate the efficacy of the developed theory we consider in Sec. IV the “shock-tube” Riemann problem describing the collision of “monochromatic” soliton beams for both types of bidirectional gases. The collisions are described by weak solutions to the bidirectional kinetic equations, consisting of a number differing constant states for the DOS, separated by contact discontinuities for the component densities, satisfying appropriate Rankine-Hugoniot conditions. The analytical results are shown to be in excellent agreement with direct numerical simulations of the soliton gas shock-tube problem for DNLS and RNLS equations.

II. KINETIC EQUATION FOR BIDIRECTIONAL SOLITON GAS

In this section we derive the kinetic equation for integrable Eulerian dispersive hydrodynamics (4) using the general physical construction proposed in [17] for a unidirectional case. The construction uses an extension of the original Zakharov’s phase-shift reasoning [21], which, strictly speaking, is applicable only in a rarefied gas case. However, the resulting kinetic equation (1), (2) turns out to provide the correct description for a dense gas, which has been mathematically justified by the thermodynamic limit of the finite-gap Whitham modulation systems for the cases of the KdV [22] and the focusing NLS [16] equations. Our results for bidirectional gas will be later supported by comparisons with direct numerical simulations of the relevant soliton gases, justifying the validity of the phenomenological derivation.

A. Isotropic and anisotropic bidirectional soliton gases

Suppose that the system (4) supports a family of bidirectional soliton solutions that bifurcate from the two branches of

the linear wave spectrum $\omega = \omega_{\pm}(k)$ of (4) so that $\omega_{-}(k)/k < \omega_{+}(k)/k$ in the long-wavelength limit $k \rightarrow 0$. We denote the corresponding soliton families (ρ_s^-, u_s^-) and (ρ_s^+, u_s^+) . Let these soliton solutions be parametrized by a real-valued spectral (IST) parameter λ so that $\lambda \in \Omega_+$ for the “fast” branch and $\lambda \in \Omega_-$ for the “slow” branch, where Ω_{\pm} are simply connected subsets of \mathbb{R} with one intersection point at most. Let the respective soliton velocities be $c_{\pm}(\lambda)$. For convenience we assume that $c'_{\pm}(\lambda) > 0$, and $c_{-}(\lambda_1) < c_{+}(\lambda_2)$ if $\lambda_1 \in \Omega_-$ and $\lambda_2 \in \Omega_+$, $\lambda_1 \neq \lambda_2$. If $\Omega_- \cap \Omega_+ = \{\lambda_*\}$ we assume $c_{-}(\lambda_*) = c_{+}(\lambda_*)$. The above assumptions are consistent with all concrete examples of integrable dispersive hydrodynamics we consider in this paper.

One can distinguish between two types of the pairwise collisions in a bidirectional soliton gas: the overtaking collisions between solitons belonging to the same spectral branch and characterized by the position shifts Δ_{++} and Δ_{--} , respectively, and the “head-on” collisions between solitons of different branches, characterized by the position shifts Δ_{+-} and Δ_{-+} . Let $\lambda \neq \mu$, and $\Delta_{\pm\pm}(\lambda, \mu)$ and $\Delta_{\pm\mp}(\lambda, \mu)$ denote the position shifts of a λ soliton due to its collision with a μ soliton, with the first and second signs \pm in the subscript indicating the branch correspondence of the λ soliton and the μ soliton, respectively, e.g., $\Delta_{-+}(\lambda, \mu)$ is the position shift of a λ soliton with $\lambda \in \Omega_-$ in a collision with a μ soliton with $\mu \in \Omega_+$.

We call the bidirectional soliton gas “isotropic” if the position shifts for the overtaking and head-on collisions between λ and μ solitons satisfy the following sign conditions:

$$\text{sgn}[\Delta_{++}] = \text{sgn}[\Delta_{+-}], \quad \text{sgn}[\Delta_{--}] = \text{sgn}[\Delta_{-+}], \quad (5)$$

i.e., the λ soliton experiences a shift of a certain sign, say shift forward (and the μ soliton—the shift of an opposite sign), irrespectively of the type of the collision—overtaking or head-on. If conditions (5) are not satisfied, i.e., the sign of the phase shift depends on the type of the collision, we shall call the corresponding soliton gas “anisotropic.” The difference between isotropic and anisotropic collisions is illustrated in Fig. 1 using concrete examples.

B. Kinetic equation for bidirectional soliton gas: General construction

Following the construction of kinetic equation for unidirectional soliton gas outlined in the Introduction, we now consider bidirectional soliton gases for integrable Eulerian equations (4). We introduce two separate DOSs $f_{-}(\lambda, x, t)$ and $f_{+}(\lambda, x, t)$ for the populations of solitons whose spectral parameters belong to the slow (Ω_-) and fast (Ω_+) branches of the spectral set Ω , respectively. The isospectrality of integrable evolution implies now two separate conservation laws:

$$(f_{-})_t + (s_{-}f_{-})_x = 0, \quad (f_{+})_t + (s_{+}f_{+})_x = 0, \quad (6)$$

where $s_{-}(\lambda, x, t)$ and $s_{+}(\lambda, x, t)$ are the transport velocities associated with the motion of slow solitons and fast solitons associated with Ω_- and Ω_+ branches, respectively. We derive the equations of state for s_{\pm} using the direct phenomenological approach proposed [17]: we identify $s_{\pm}(\lambda, x, t)$ as the velocity of a tracer λ soliton in the gas. Consider, for instance, a tracer λ soliton from the slow branch, $\lambda \in \Omega_-$, and compute its displacement in a gas over the “mesoscopic” time interval

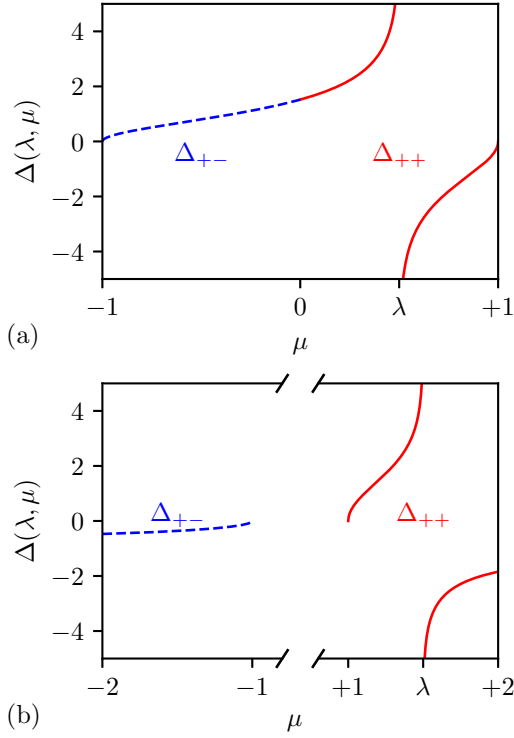


FIG. 1. Variation of the phase shifts in the isotropic (a) and anisotropic (b) interactions of solitons with spectral parameters λ and μ . The λ soliton belongs to the “+” branch with $\lambda = 1/2$ (a) and $\lambda = 3/2$ (b). Solid lines represent the variation of Δ_{++} and dashed lines the variation of Δ_{+-} .

dt , sufficiently large to incorporate a large number of collisions, but sufficiently small to ensure that the spatiotemporal field $f_{\pm}(\lambda, x, t)$ is stationary over dt and homogeneous on a typical spatial scale $c_{\pm}(\lambda)dt$. Having this in mind, we drop the (x, t) dependence for convenience. Each overtaking collision with a soliton of the same branch $\mu \in \Omega_{-}$ shifts the λ soliton by the distance $\Delta_{--}(\lambda, \mu)$. Thus the displacement of the λ soliton over the time dt due to the overtaking collisions is given by $\int_{\Omega_{-}} \Delta_{--}(\lambda, \mu) f_{-}(\mu) |s_{-}(\lambda) - s_{-}(\mu)| dt d\mu$ where $f_{-}(\mu) |s_{-}(\lambda) - s_{-}(\mu)| dt$ is the average number of collisions with encountered μ solitons (cf. [17]). Additionally, each head-on collision with a fast soliton $\mu \in \Omega_{+}$ shifts the slow λ soliton with $\lambda \in \Omega_{-}$ by $\Delta_{-+}(\lambda, \mu)$, and the resulting displacement after a time dt is $\int_{\Omega_{+}} \Delta_{-+}(\lambda, \mu) f_{+}(\mu) |s_{-}(\lambda) - s_{+}(\mu)| dt d\mu$. A similar consideration is applied to the fast soliton branch, $\lambda \in \Omega_{+}$, in the gas. Equating the total displacements of the slow and fast λ solitons to $s_{-}(\lambda)dt$ and $s_{+}(\lambda)dt$, respectively, we obtain the equation of state of a bidirectional gas in the form of two coupled linear integral equations:

$$\begin{aligned} s_{-}(\lambda) &= c_{-}(\lambda) + \int_{\Omega_{-}} \Delta_{--}(\lambda, \mu) f_{-}(\mu) |s_{-}(\lambda) - s_{-}(\mu)| d\mu \\ &\quad + \int_{\Omega_{+}} \Delta_{-+}(\lambda, \mu) f_{+}(\mu) |s_{-}(\lambda) - s_{+}(\mu)| d\mu, \\ s_{+}(\lambda) &= c_{+}(\lambda) + \int_{\Omega_{+}} \Delta_{++}(\lambda, \mu) f_{+}(\mu) |s_{+}(\lambda) - s_{+}(\mu)| d\mu \\ &\quad + \int_{\Omega_{-}} \Delta_{+-}(\lambda, \mu) f_{-}(\mu) |s_{+}(\lambda) - s_{-}(\mu)| d\mu, \end{aligned} \quad (7)$$

where $\lambda \in \Omega_{-}$ for the first equation and $\lambda \in \Omega_{+}$ for the second equation. If the spectral support $\Omega = \Omega_{-} \cup \Omega_{+} \subset \mathbb{R}$ is a simply connected set and the gas is isotropic, the distinction between the fast and slow branches becomes unnecessary and the kinetic equation (6), (7) for bidirectional soliton gas is naturally reduced to the unidirectional gas equation (1), (2) for a single DOS $f(\lambda)$ defined on the entire set Ω . We will show in Sec. IV, using concrete examples, that the dynamics governed by the kinetic equations (1), (2) and (6), (7) is in very good agreement with the results of direct numerical simulations of isotropic and anisotropic bidirectional soliton gases, respectively.

C. Kinetic equation for bidirectional soliton gas: Examples

As a representative (and physically relevant) example, we consider the integrable Eulerian dispersive hydrodynamics

$$\begin{aligned} \rho_t + (\rho u)_x &= 0, \\ (\rho u)_t + \left(\rho u^2 + \frac{\rho^2}{2} \right)_x &= \frac{\sigma}{4} [\rho (\ln \rho)_{xx}]_x, \\ \sigma &= \pm 1. \end{aligned} \quad (8)$$

For $\sigma = 1$, system (8) is equivalent to the DNLS equation:

$$i\psi_t + \frac{1}{2}\psi_{xx} - |\psi|^2\psi = 0, \quad \psi = \sqrt{\rho} \exp\left(i \int u dx\right). \quad (9)$$

The DNLS equation has a number of physical applications. In particular, it describes the propagation of light beams through optical fibers in the regime of normal dispersion, as well as nonlinear matter waves in quasi-one-dimensional (quasi-1D) repulsive Bose-Einstein condensates (BECs) (see, for instance, [36]). Pertinent to the present context, rarefied gas of dark solitons in quasi-1D BEC has been investigated in [37,38].

The DNLS equation has a family of dark (or gray) spectral soliton solutions [34]

$$\begin{aligned} \rho_s^{\pm} &= 1 - (1 - \lambda^2) \text{sech}^2[\sqrt{1 - \lambda^2}(x - c_{\pm}t)], \\ u_s^{\pm} &= \lambda \left(1 - \frac{1}{\rho_s^{\pm}(x, t)} \right), \quad c_{\pm} = \lambda \in \Omega_{\pm}, \end{aligned} \quad (10)$$

where $\Omega_{-} = (-1, 0]$ for the slow solitons branch and $\Omega_{+} = [0, +1)$ for the fast solitons branch; note that solutions (ρ_s^{+}, u_s^{+}) and (ρ_s^{-}, u_s^{-}) have the same analytical expression.

Without loss of generality we assumed in (10) the unit density background. Typical dark soliton solutions are displayed in Fig. 2. The position shifts in the DNLS overtaking and head-on soliton collisions are given by the same analytical expression $\Delta_{\pm\pm}(\lambda, \mu) = \Delta_{\pm\mp}(\lambda, \mu) \equiv \Delta(\lambda, \mu)$, where

$$\begin{aligned} \Delta(\lambda, \mu) &= \text{sgn}(\lambda - \mu) G_1(\lambda, \mu), \\ G_1(\lambda, \mu) &\equiv \frac{1}{2\sqrt{1 - \lambda^2}} \ln \frac{(\lambda - \mu)^2 + (\sqrt{1 - \lambda^2} + \sqrt{1 - \mu^2})^2}{(\lambda - \mu)^2 + (\sqrt{1 - \lambda^2} - \sqrt{1 - \mu^2})^2}, \end{aligned} \quad (11)$$

for all $\lambda, \mu \in (-1, 1)$. One can verify that the soliton position shifts given by (11) satisfy the isotropy conditions (5). The variation of $\Delta(\lambda, \mu)$ with respect to μ for a fixed λ is displayed in Fig. 1. One can see that the position shifts for the

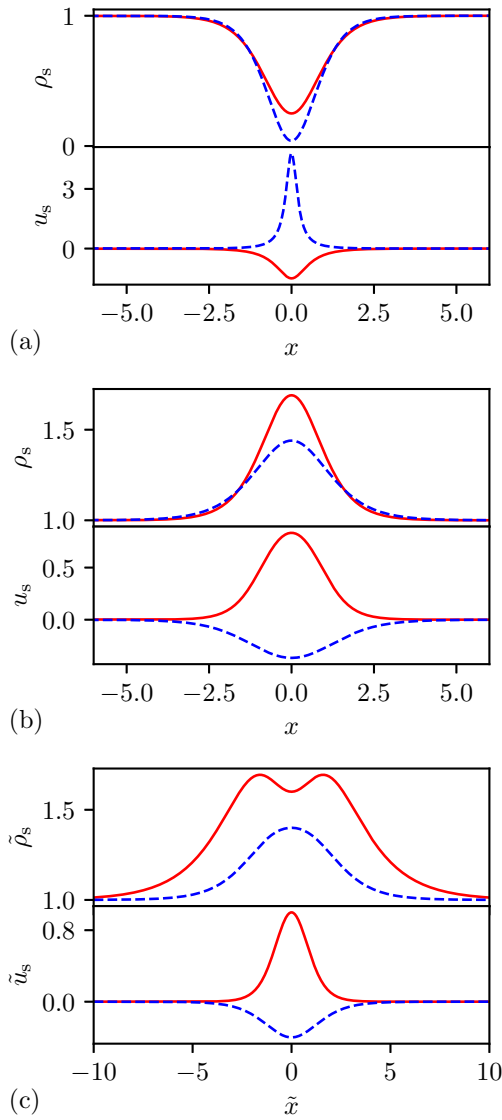


FIG. 2. Soliton solutions: solid lines represent fast branch solutions (ρ_s^+ , u_s^+) and dashed lines slow branch solutions (ρ_s^- , u_s^-). (a) Dark soliton solutions of the DNLS equation (10) with $\lambda = +0.5, -0.2$. (b) Antidark soliton solutions of the RNLS equation (16) with $\lambda = +1.3, -1.2$. (c) Antidark soliton solutions of the KB system (A3) with $\lambda = +1.3, -1.2$.

head-on and overtaking collisions lie on the same curve with $\Delta(\lambda, \mu)$ being continuous at $\lambda = 0$, the point of intersection of Ω_- and Ω_+ . Due to the isotropic nature of the DNLS soliton interactions the coupled kinetic equation (6), (7) for the bidirectional DNLS gas reduces to the single kinetic equation (1) with the equation of state

$$s(\lambda, x, t) = \lambda + \int_{-1}^{+1} G_1(\lambda, \mu) f(\mu, x, t) \times [s(\lambda, x, t) - s(\mu, x, t)] d\mu, \quad (12)$$

where $\lambda \in (-1, 1)$ and with the assumption that $s'(\lambda) > 0$; the latter assumption is verified by comparison to numerics in Sec. IV B. This reduction to the unidirectional case is similar

to the kinetic equation derived in [16] for the bidirectional soliton and breather gases of the focusing NLS equation which also exhibits isotropic soliton and breather collisions, with the essential difference that the integration in the focusing NLS case occurs over a compact domain in a complex plane of the spectral parameter.

For $\sigma = -1$ the system (8) is equivalent to the so-called RNLS equation (see, e.g., [39])

$$i\psi_t + \frac{1}{2}\psi_{xx} - |\psi|^2\psi = \frac{|\psi|_{xx}}{|\psi|}\psi, \quad \psi = \sqrt{\rho} \exp\left(i \int u dx\right). \quad (13)$$

This equation, in particular, describes long magnetoacoustic waves in a cold plasma propagating across the magnetic field [40]. The change of variables

$$\begin{aligned} \tilde{\rho} &= \rho + \frac{1}{2}\left(u + \frac{\rho_x}{2\rho}\right)_x, & \tilde{u} &= u + \frac{\rho_x}{2\rho}, \\ \tilde{x} &= \frac{2}{\sqrt{3}}x, & \tilde{t} &= \frac{2}{\sqrt{3}}t, \end{aligned} \quad (14)$$

transforms the RNLS equation into the KB system [28]:

$$\tilde{\rho}_{\tilde{t}} + (\tilde{\rho}\tilde{u})_{\tilde{x}} = -\frac{1}{3}\tilde{u}_{\tilde{x}\tilde{x}\tilde{x}}, \quad \tilde{u}_{\tilde{t}} + \tilde{u}\tilde{u}_{\tilde{x}} + \tilde{\rho}_{\tilde{x}} = 0, \quad (15)$$

describing bidirectional shallow-water waves. The KB system has a family of antidark spectral soliton solutions, cf. [63], which transforms into a family of antidark spectral soliton solutions for the RNLS equation:

$$\begin{aligned} \rho_s^\pm &= 1 + (\lambda^2 - 1)\text{sech}^2[\sqrt{\lambda^2 - 1}(x - c_\pm t)], \\ u_s^\pm &= \lambda\left(1 - \frac{1}{\rho_s^\pm(x, t)}\right), \quad c_\pm = \lambda \in \Omega_\pm. \end{aligned} \quad (16)$$

using the change of variables (14) (cf. Appendix A). Solutions (ρ_s^+ , u_s^+) and (ρ_s^- , u_s^-) have the same analytical expression. These solutions have also been obtained in [39]. Typical antidark soliton solutions are displayed in Fig. 2. One can notice in Fig. 2 that the bimodal soliton of the KB system transforms into a unimodal soliton of the RNLS equation with the change of variables (14).

In contrast with the DNLS system, the spectral set of the RNLS soliton is spanned by two disconnected subsets: $\Omega_- = (-\infty, -1)$ for slow solitons and $\Omega_+ = (+1, +\infty)$. Similar to the DNLS equation, the position shifts in head-on and overtaking collisions are given by the same analytical expression $\Delta_{\pm\pm}(\lambda, \mu) = \Delta_{\mp\mp}(\lambda, \mu) \equiv \Delta(\lambda, \mu)$, where

$$\begin{aligned} \Delta(\lambda, \mu) &= \text{sgn}(\lambda - \mu) G_2(\lambda, \mu), \\ G_2(\lambda, \mu) &\equiv \frac{1}{2\sqrt{\lambda^2 - 1}} \ln \frac{(\lambda - \mu)^2 - (\sqrt{\lambda^2 - 1} + \sqrt{\mu^2 - 1})^2}{(\lambda - \mu)^2 - (\sqrt{\lambda^2 - 1} - \sqrt{\mu^2 - 1})^2}. \end{aligned} \quad (17)$$

which is derived from the phase shift formula for KB solitons using the change of variables (14). However, one can verify that, unlike in the DNLS case, the isotropy condition (5) is not satisfied. Indeed, it follows from (17) that $\text{sgn}[\Delta_{\pm\pm}(\lambda, \mu)] = \text{sgn}(\lambda - \mu)$, whereas $\text{sgn}[\Delta_{\mp\mp}(\lambda, \mu)] = -\text{sgn}(\lambda - \mu)$, that is in a head-on collision between a λ soliton and a μ soliton with $\lambda > \mu$, the λ soliton's position is now shifted backward. The

variation of $\Delta_{\pm\pm}(\lambda, \mu)$ for the RNLS equation is shown in Fig. 1. One can see that it is qualitatively different from the variation of $\Delta_{\pm\mp}(\lambda, \mu)$ for the DNLS equation.

The kinetic equation for the anisotropic RNLS soliton gas has then the form of two continuity equations (6) complemented by the coupled equations of state

$$\begin{aligned} s_-(\lambda) &= \lambda + \int_{-\infty}^{-1} G_2(\lambda, \mu) f_-(\mu) [s_-(\lambda) - s_-(\mu)] d\mu \\ &\quad + \int_{+1}^{\infty} G_2(\lambda, \mu) f_+(\mu) [s_-(\lambda) - s_+(\mu)] d\mu, \\ s_+(\lambda) &= \lambda + \int_{+1}^{+\infty} G_2(\lambda, \mu) f_+(\mu) [s_+(\lambda) - s_+(\mu)] d\mu \\ &\quad + \int_{-\infty}^{-1} G_2(\lambda, \mu) f_-(\mu) [s_+(\lambda) - s_-(\mu)] d\mu, \end{aligned} \quad (18)$$

with the assumptions that $s'_\pm(\lambda) > 0$ and $s_+ > s_-$; the latter assumption is verified by direct comparison with numerics in Sec. IV B.

Note that for the KB system, the phase of a λ soliton after colliding with a μ soliton is: $2/\sqrt{3} \times \text{sgn}(\lambda - \mu) G_2(\lambda, \mu)$. Thus the RNLS and the KB soliton gas share the same anisotropic kinetic description. In the numerical examples presented in the next section we will mostly focus on the anisotropic RNLS soliton gas for a direct comparison with the isotropic DNLS soliton gas.

III. ENSEMBLE AVERAGES OF THE WAVE FIELD IN BIDIRECTIONAL SOLITON GASES

The DOS $f(\lambda)$ [$f_\pm(\lambda)$ in the anisotropic case] represents a comprehensive spectral characteristic, that, in principle, determines all statistical parameters of the nonlinear random wave field $[\rho(x, t), u(x, t)]$ in a soliton gas. The most obvious set of such statistical parameters are the ensemble averages of the conserved quantities. We note that for the KdV soliton gas the averages $\langle u \rangle$, $\langle u^2 \rangle$ were determined in terms of the DOS in [23,41] using the machinery of the finite-gap integration method. In this section we propose a simple heuristic approach that enables one to link the spectral DOS $f(\lambda)$ [or $f_\pm(\lambda)$] of a soliton gas with the ensemble averages of conserved quantities of the integrable system (4). As an illustration we consider the three first conserved densities of the Euler system (4): ρ , u , and ρu .

We first consider a homogeneous soliton gas, i.e., a gas whose statistical properties, particularly the DOS, do not depend on x, t . The proposed approach is based on the natural assumption that the nonlinear wave field in a homogeneous soliton gas represents an ergodic random process, both in x and t (we note in passing that ergodicity is inherent in the model of soliton gas based on the finite-gap theory; see, e.g., [42–44]). The ergodicity property implies that ensemble averages $\langle \rho(x, t) \rangle$, $\langle u(x, t) \rangle$, and $\langle \rho(x, t) u(x, t) \rangle$ in the soliton gas can be replaced by the corresponding spatial averages. Generally, for any functional $H[\rho(x, t), u(x, t)]$ we have

$$\langle H[\rho, u] \rangle = \lim_{L \rightarrow \infty} \frac{1}{2L} \int_{x-L}^{x+L} H[\rho(y, t), u(y, t)] dy, \quad (19)$$

for a single representative realization of soliton gas. We detail below the derivation of $\langle \rho \rangle$, the generalization to $\langle u \rangle$, and $\langle \rho u \rangle$ being straightforward.

Let the soliton gas propagate on a constant background $(\rho, u) = (\rho_0, u_0)$ [without loss generality one can assume $(\rho_0, u_0) = (1, 0)$]. Let $\langle \rho \rangle = \rho_0 + \langle \eta \rangle$ where $\eta = \rho - \rho_0$. We consider the general, anisotropic case for which the soliton gas is characterized by two DOSs $f_-(\lambda)$ and $f_+(\lambda)$. Define

$$I = \int_{x-L}^{x+L} \eta(y, t) dy, \quad (20)$$

where $L \gg 1$. Then $\langle \rho \rangle = \rho_0 + I/(2L) + O(L^{-1})$.

Let $[\rho(y, t), u(y, t)]$ be a realization of a soliton gas solution to the dispersive hydrodynamics (4) and let $[\tilde{\rho}(y, t), \tilde{u}(y, t)]$ be defined in such a way that for some $t = t_*$ one has $[\tilde{\rho}(y, t_*), \tilde{u}(y, t_*)] = [\rho(y, t_*), u(y, t_*)]$ for $y \in (x-L, x+L)$ and $[\tilde{\rho}(y, t_*), \tilde{u}(y, t_*)] = [\rho_0, 0]$ outside of this interval. To avoid complications we assume that the transition between the two behaviors is smooth but sufficiently rapid so that such a “windowed” portion of a soliton gas (see Fig. 3) can be approximated by the N -soliton solution of (4) for some $N \gg 1$, with the discrete IST spectrum being distributed on Ω_- and Ω_+ with densities $2L f_-(\lambda)$ and $2L f_+(\lambda)$, respectively (recall the definition of DOS in Sec. I). Equation (20) rewrites

$$I = \int_{-\infty}^{+\infty} \tilde{\eta}(y, t) dy, \quad \tilde{\eta}(y, t) = \tilde{\rho}(y, t) - \rho_0. \quad (21)$$

We note the integral (21) does not depend on time because I is a conserved quantity, in particular, for $t = \tau \gg t_*$ where the solution $[\tilde{\rho}(y, \tau), \tilde{u}(y, \tau)]$ asymptotically represents the train of spatially well-separated solitons ρ_s^\pm, u_s^\pm propagating on the background $(\rho_0, 0)$ (see Fig. 3). In this case, I can be evaluated as

$$\begin{aligned} I &= \sum_i \int_{-\infty}^{+\infty} [\rho_s^-(y - \lambda_i \tau - y_i; \lambda_i) - \rho_0] dy \\ &\quad + \sum_j \int_{-\infty}^{+\infty} [\rho_s^+(y - \lambda_j \tau - y_j; \lambda_j) - \rho_0] dy, \end{aligned} \quad (22)$$

where $\lambda_{i,j}$ are the spectral parameters and $y_{i,j}$ the initial phases of the \pm solitons. Since the spectrum is preserved by the integrable dynamics (4), $\lambda_{i,j}$ remain to be distributed on Ω_\pm with the respective densities $2L f_\pm(\lambda)$ for all t . Let $\bar{\eta}_\pm$ be the “mass” of the spectral soliton solution $\rho_s^\pm(x - \lambda t; \lambda) - \rho_0$,

$$\bar{\eta}_\pm(\lambda) = \int_{-\infty}^{+\infty} [\rho_s^\pm(y; \lambda) - \rho_0] dy, \quad (23)$$

which only depends on λ . Note that the integral in (23) converges for the example considered in Sec. II C since ρ_s^\pm decays exponentially to ρ_0 . We have with this new notation, $I = \sum_i \bar{\eta}_-(\lambda_i) + \sum_j \bar{\eta}_+(\lambda_j)$. Taking the continuous limit, $\sum_i \rightarrow \int_{\Omega_-} d\lambda 2L f_-(\lambda)$ and $\sum_j \rightarrow \int_{\Omega_+} d\lambda 2L f_+(\lambda)$, we obtain

$$\frac{I}{2L} = \int_{\Omega_-} \bar{\eta}_-(\lambda) f_-(\lambda) d\lambda + \int_{\Omega_+} \bar{\eta}_+(\lambda) f_+(\lambda) d\lambda, \quad (24)$$

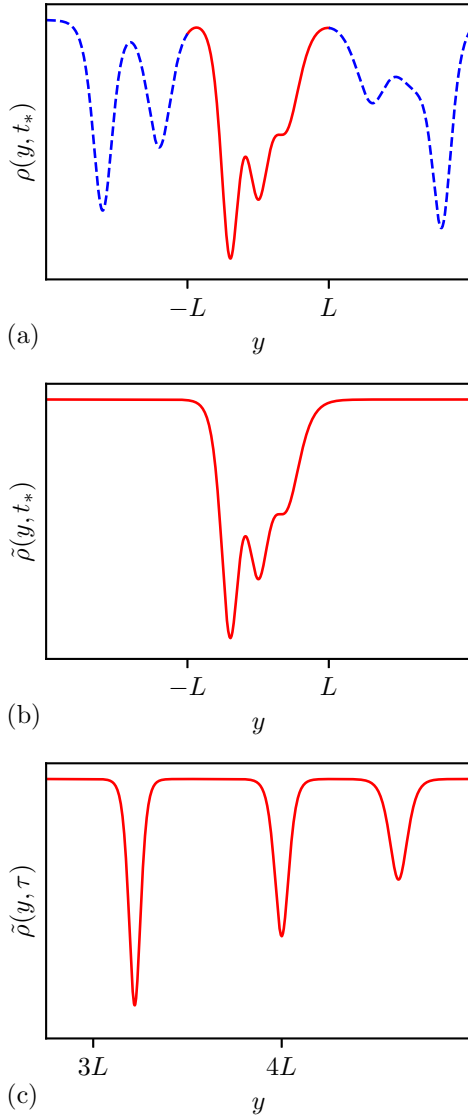


FIG. 3. Schematic for the evaluation of the integral (20) in soliton gas using the truncation procedure. (a) Typical distribution $\rho(y, t_*)$ for a DNLS dark soliton gas. (b) Truncation of the distribution $\rho(y, t_*)$ for $y \in (-L, L)$. (c) Variation of the truncated distribution $\tilde{\rho}(y, \tau)$ at time $\tau \gg t_*$.

yielding the expression for the moment $\langle \rho \rangle$:

$$\langle \rho(x, t) \rangle = \rho_0 + \int_{\Omega_-} \bar{\eta}_-(\lambda) f_-(\lambda) d\lambda + \int_{\Omega_+} \bar{\eta}_+(\lambda) f_+(\lambda) d\lambda. \quad (25)$$

Similarly, we obtain for the two other moments (recall that we assume $u \rightarrow 0$ as $x \pm \infty$)

$$\langle u(x, t) \rangle = \int_{\Omega_-} \bar{u}_-(\lambda) f_-(\lambda) d\lambda + \int_{\Omega_+} \bar{u}_+(\lambda) f_+(\lambda) d\lambda, \quad (26)$$

$$\langle \rho(x, t) u(x, t) \rangle = \int_{\Omega_-} \bar{\rho u}_-(\lambda) f_-(\lambda) d\lambda + \int_{\Omega_+} \bar{\rho u}_+(\lambda) f_+(\lambda) d\lambda, \quad (27)$$

where $\bar{u}_\pm(\lambda) = \int u_s^\pm(y; \lambda) dy$ and $\bar{\rho u}_\pm(\lambda) = \int \rho_s^\pm(y; \lambda) u_s^\pm(y; \lambda) dy$. The expressions (25), (26), and (27) rewrite in the isotropic case

$$\begin{aligned} \langle \rho(x, t) \rangle &= \rho_0 + \int_{\Omega} \bar{\eta}(\lambda) f(\lambda) d\lambda, \\ \langle u(x, t) \rangle &= \int_{\Omega} \bar{u}(\lambda) f(\lambda) d\lambda, \\ \langle \rho(x, t) u(x, t) \rangle &= \int_{\Omega} \bar{\rho u}(\lambda) f(\lambda) d\lambda. \end{aligned} \quad (28)$$

We present in Table I the expressions of $\bar{\eta}_\pm(\lambda)$, $\bar{u}_\pm(\lambda)$, and $\bar{\rho u}_\pm(\lambda)$ for the examples introduced in Sec. II C.

The method presented here only requires one to integrate the single-soliton solution and thus can be readily applied to any integrable dispersive hydrodynamic system supporting the soliton resolution scenario. Formulas (25)–(28) will be used in the next section to track the evolution of the DOS numerically. In conclusion we note that the above simple method, applied to the KdV equation, gives exactly the same results for the mean and mean square of the random field as the finite-gap theory consideration of [22,23]. It also explains why the corresponding analytical expressions for the moments in a dense gas of KdV solitons derived in [23] coincide with the corresponding expressions obtained in [45] for a rarefied gas (see also [44] for the similar modified KdV equation result).

In the above consideration of homogeneous soliton gases the ensemble averages (19) are constant. For a nonhomogeneous gas the DOS is a slowly varying function of x, t and so are the ensemble averages that now need to be interpreted as “local averages” in the spirit of modulation theory [27]. Essentially, one introduces a mesoscopic scale ℓ , much larger than the typical soliton width and much smaller than the spatial scale of the DOS variations so that the DOS is approximately constant on any interval $(x - \ell, x + \ell)$. Then the constant ensemble averages (19) are replaced by slowly varying quantities:

$$\langle H[\rho, u] \rangle_\ell(x, t) = \frac{1}{2\ell} \int_{x-\ell}^{x+\ell} H[\rho(y, t), u(y, t)] dy. \quad (29)$$

The local averages $\langle H[\rho, u] \rangle_\ell$ do not depend on ℓ at leading order, and their spatiotemporal variations occur on x and t scales that correspond to the scales associated with variations of $f(\lambda)$ and are much larger than those of ρ, u . The modulations of $\langle \rho \rangle$, $\langle u \rangle$, and $\langle \rho u \rangle$ in a nonhomogeneous soliton gas are then defined by Eqs. (25), (26), and (27), respectively, in which the DOS $f_\pm(\lambda)$ is replaced by the solution $f_\pm(\lambda, x, t)$ of the kinetic equation (6), (7). This strategy will be used in the next section where we study the dynamics of nonhomogeneous soliton gases generated in the solutions of Riemann problems for kinetic equations.

TABLE I. Expressions of the integral $\bar{\eta}_{\pm}(\lambda)$, $\bar{u}_{\pm}(\lambda)$, and $\bar{\rho u}_{\pm}(\lambda)$ for NLS solitons ($\rho_0 = 1$). For both examples we have $\rho_s^- = \rho_s^+$ and $u_s^- = u_s^+$ such that $\bar{\eta}_- = \bar{\eta}_+$, $\bar{u}_- = \bar{u}_+$, and $\bar{\rho u}_- = \bar{\rho u}_+$.

Equations	$\bar{\eta}(\lambda)$	$\bar{u}(\lambda)$	$\bar{\rho u}(\lambda)$
DNLS ($\sigma = +1$)	$-2\sqrt{1 - \lambda^2}$	$2 \sin^{-1}(\lambda) - \pi \operatorname{sgn}(\lambda)$	$-2\lambda\sqrt{1 - \lambda^2}$
RNLS ($\sigma = -1$)	$+2\sqrt{\lambda^2 - 1}$	$2 \operatorname{sgn}(\lambda) \cosh^{-1} \lambda $	$+2\lambda\sqrt{\lambda^2 - 1}$

IV. MULTICOMPONENT BIDIRECTIONAL SOLITON GASES: RIEMANN PROBLEM

A. Hydrodynamics reductions

Generally, our ability to solve the integral equation of state (2) is very limited, and strongly depends on the particular form of the interaction kernel. Some particular analytical solutions have been found [16] for special cases of soliton gases for the focusing NLS equation. At the same time, it was shown in [17,19,46] that this problem greatly simplifies if discretization of the DOS $f(\lambda, x, t)$ or $f_{\pm}(\lambda, x, t)$ with respect to the soliton spectral parameter λ is admissible. We adopt this simplification in the following, and we consider the soliton gases that are composed of a finite number of distinct spectral components, termed monochromatic, or cold, components. We consider in the following the general anisotropic description; the derivation also readily applies to the isotropic case. Suppose that the bidirectional soliton gas is spectrally composed of n_- distinct components of the “−” soliton branch, and n_+ distinct components of the “+” soliton branch:

$$\begin{aligned} f_-(\lambda, x, t) &= \sum_{i=1}^{n_-} F_i(x, t) \delta(\lambda - \Lambda_i), \\ f_+(\lambda, x, t) &= \sum_{i=n_-+1}^{n_-+n_+} F_i(x, t) \delta(\lambda - \Lambda_i), \end{aligned} \quad (30)$$

with $c_{\pm}(\Lambda_i) < c_{\pm}(\Lambda_{i+1})$ and where Λ_i are the soliton parameters of the different components and δ the Dirac delta distribution. We do not indicate in the following the branch-belonging of the component F_i for readability reasons. Additionally, we do not indicate explicitly the (x, t) dependence of the fields F_i when it is clear. As pointed out in [16,47], the multicomponent ansatz (30) is a mathematical idealization; physically one would replace the δ functions by narrow distributions around the spectral points Λ_i .

The ansatz (30) transforms the pair of distributions $[f_-(\lambda), f_+(\lambda)]$ into a $n = (n_- + n_+)$ -dimensional vector $\mathbf{F} = (F_1, \dots, F_n)$. Thus (6) reduces to n hydrodynamic (quasilinear) conservation laws:

$$(F_i)_t + (S_i F_i)_x = 0, \quad i = 1 \dots n, \quad (31)$$

where $S_i(x, t) = s_{\pm_i}(\Lambda_i, x, t)$ with \pm_i indicating the branch-belonging of the soliton Λ_i . The coupled equations of states (7) simplify into an n th-order linear algebraic system for the S_i 's:

$$S_i = C_i + \sum_{j \neq i} \Delta(\Lambda_i, \Lambda_j) F_j |S_i - S_j|, \quad C_i = c_{\pm_i}(\Lambda_i). \quad (32)$$

The system (32) simplifies for the examples considered in Sec. II C, where we assumed that $S_i < S_{i+1}$ and where the phase-shift formula has the form $\Delta_{\pm\pm}(\lambda, \mu) = \Delta_{\pm\mp}(\lambda, \mu) =$

$\operatorname{sgn}(\lambda - \mu)G(\lambda, \mu)$; the expression of G is given by (11) for the DNLS and (17) for the RNLS equation. For the NLS examples we obtain the linear system:

$$S_i = C_i + \sum_{j \neq i} G_{ij} F_j (S_i - S_j), \quad G_{ij} = G(\Lambda_i, \Lambda_j). \quad (33)$$

In order to simplify the discussion, we will focus on the latter system. Both anisotropic and isotropic soliton gases are described by the same system (31), (33): for the isotropic DNLS-soliton gas we have $G_{ij} = G_1(\Lambda_i, \Lambda_j) > 0$, and for the anisotropic RNLS-soliton gas $G_{ij} = G_2(\Lambda_i, \Lambda_j) \in \mathbb{R}$.

The resolution of the linear system (33) yields a solution $S_i(\mathbf{F})$ such that the system (31) becomes quasilinear:

$$(F_i)_t + [S_i(\mathbf{F}) F_i]_x = 0. \quad (34)$$

It was shown in [19,46] that the system (34) is a linearly degenerate integrable system [48] and its general solutions can be obtained using the generalized hodograph method [49]. In particular, the characteristic velocities of this hydrodynamic system coincide with the mean velocities S_i .

Finally, the expressions of the moments $\langle \rho \rangle$, $\langle u \rangle$, and $\langle \rho u \rangle$ are given by

$$\begin{aligned} \langle \rho(x, t) \rangle &= \rho_0 + \sum_{i=1}^n \bar{\eta}(\Lambda_i) F_i(x, t), \\ \langle u(x, t) \rangle &= \sum_{i=1}^n \bar{u}(\Lambda_i) F_i(x, t), \\ \langle \rho(x, t) u(x, t) \rangle &= \sum_{i=1}^n \bar{\rho u}(\Lambda_i) F_i(x, t), \end{aligned} \quad (35)$$

with the coefficients $\bar{\eta}$, \bar{u} , and $\bar{\rho u}$ given in Table I for the NLS equation (8). The relations in (35) can be used to obtain the DOS components F_i from the moments $\langle \rho \rangle$, $\langle u \rangle$, and $\langle \rho u \rangle$ if $n \leq 3$.

B. Shock-tube problem

We now focus on the physically relevant Riemann problem for the hydrodynamic system (33), (34) describing the interaction dynamics of two soliton gases prepared in the respective uniform states $\mathbf{F}^L \in \mathbb{R}^n$ and $\mathbf{F}^R \in \mathbb{R}^n$, that are initially separated:

$$\mathbf{F}(x, 0) = \begin{cases} \mathbf{F}^L, & \text{if } x < 0 \\ \mathbf{F}^R, & \text{if } x \geq 0. \end{cases} \quad (36)$$

The spectral distribution (36) corresponds to the soliton gas shock-tube problem, an analog of the standard shock-tube problem of classical gas dynamics. The shock-tube problem represents a good benchmark for our kinetic theory where we can investigate both overtaking and head-on collisions by

choosing the appropriate number of components. We emphasize here that the initial condition (36) constitutes a Riemann problem for the kinetic equation (34) but not for the original dispersive hydrodynamics system (4), similar to the so-called generalized Riemann problems recently introduced in [50,51]. We shall sometimes refer to the problem (34), (36) as a “spectral Riemann problem” as it essentially describes the spatiotemporal evolution of the spectral components of the soliton gas.

The soliton gas shock-tube problem has been investigated for the KdV and focusing NLS two-component soliton gases ($n = 2$) in [16,17,47], and for n components in the context of generalized hydrodynamics [52–56]. Here we present the problem for the n -component bidirectional anisotropic soliton gases. An important difference of our consideration from the generalized hydrodynamics setting is that we are interested not only in the spectral characterization of soliton gases via solutions of the kinetic equations but also (and ultimately) in the description of the classical nonlinear wave fields associated with these solutions. The latter is achieved by the evaluation of the ensemble averages as described in Sec. III.

Due to the scaling invariance of the problem [the kinetic equation (34) and the initial condition (36) are both invariant with respect to the transformation $x \rightarrow Cx, t \rightarrow Ct$], the solution is a self-similar distribution $F(x/t)$. Because of the linear degeneracy of the quasilinear system (34) the only admissible solutions are constant separated by contact discontinuities (cf., for instance, [57]). Discontinuous, weak solutions are physically acceptable here since the kinetic equation describes the conservation of the number of solitons within any given spectral interval, and Rankine-Hugoniot type conditions can be imposed to ensure the conservation of the number of solitons across discontinuities. The solution of the Riemann problem is composed of $n + 1$ constant states, or plateaus, separated by n discontinuities (see, e.g., [58]):

$$F_i(x, t) = \begin{cases} F_i^1 = F_i^L, & x/t < Z_1 \\ \dots \\ F_i^j, & Z_{j-1} \leq x/t < Z_j \\ \dots \\ F_i^{n+1} = F_i^R, & Z_n \leq x/t, \end{cases} \quad (37)$$

where the index i indicates the i th component of the vector F , and the exponent j the index of the plateau. For clarity we labeled the superscripts $j = 1$ as “L” (left boundary condition) and $j = n + 1$ as “R” (right boundary condition). Additionally the index j of the plateau’s value F_i^j will be written as a Roman numeral in the examples considered later on. The contact discontinuities propagate at the characteristic velocities [58]:

$$Z_j = S_j(F_1^j, \dots, F_n^j) = S_j(F_1^{j+1}, \dots, F_n^{j+1}), \quad (38)$$

where the plateaus’ values F_i^j are given by Rankine-Hugoniot jump conditions:

$$-Z_j[F_i^{j+1} - F_i^j] + [S_i(F_1^{j+1}, \dots, F_n^{j+1})F_i^{j+1} - S_i(F_1^j, \dots, F_n^j)F_i^j] = 0, \quad (39)$$

where $i, j = 1 \dots n$. The Rankine-Hugoniot conditions with $i = j$ are trivially satisfied by the definition of contact discontinuity (38). Recalling the effective derivation of the equation of state in Sec. II B, the velocity of the contact discontinuity Z_j can be identified as the velocity of a trial soliton with parameter Λ_j propagating in a soliton gas of density $F = (F_1^j, \dots, F_n^j)$ or equivalently $F = (F_1^{j+1}, \dots, F_n^{j+1})$.

Note that, if the solitons were not interacting, the initial step distribution $F_i(x, 0)$ for the component $\lambda = \Lambda_i$ would have propagated at the free soliton velocity C_i :

$$F_i^{\text{free}}(x, t) = \begin{cases} F_i^L, & x/t < C_i \\ F_i^R, & C_i \leq x/t, \end{cases} \quad i = 1 \dots n, \quad (40)$$

which dramatically differs from the solution (37). In order to demonstrate the validity of the solution (37), (38), (39) the Riemann problem is investigated numerically for the DNLS and RNLS equations for two- and three-component soliton gases in the next sections.

1. Two-component soliton gas

We consider in this section the interaction between two components of soliton gas with respective parameters Λ_1 and Λ_2 (recall that $S_1 < S_2$). The solution of the equation of state (33) reads for $n = 2$:

$$S_1(F_1, F_2) = \frac{(1 - G_{21}F_1)C_1 - G_{12}F_2 C_2}{1 - G_{21}F_1 - G_{12}F_2},$$

$$S_2(F_1, F_2) = \frac{(1 - G_{12}F_2)C_2 - G_{21}F_1 C_1}{1 - G_{21}F_1 - G_{12}F_2}. \quad (41)$$

As noted in [17], the densities F_1 and F_2 must satisfy the inequality:

$$G_{21}F_1 + G_{12}F_2 < 1, \quad (42)$$

for the expressions (41) to remain valid; we suppose that this condition is always verified, constraining the DOS in the following. We suppose that $F_1^L = F_2^R = 0$ and $F_1^R = F_2^L = \zeta_0$: the region $x < 0$ is initially only populated with Λ_2 solitons and the region $x > 0$ of slower Λ_1 solitons. Since $S_1 < S_2$ the two “species” of soliton are interacting. Note that (42) implies $G_{12}\zeta_0, G_{21}\zeta_0 < 1$. The solution (37) has three plateaus:

$$F_i(x, t) = \begin{cases} F_i^I = \delta_{i,2}\zeta_0, & x/t < Z_1 \\ F_i^{II}, & Z_1 \leq x/t < Z_2 \\ F_i^{III} = \delta_{i,1}\zeta_0, & Z_2 \leq x/t, \end{cases} \quad (43)$$

where $i \in \{1, 2\}$, with the value at the intermediate plateau:

$$F_1^{II} = \frac{[1 - G_{12}\zeta_0]\zeta_0}{1 - G_{12}G_{21}\zeta_0^2}, \quad F_2^{II} = \frac{[1 - G_{21}\zeta_0]\zeta_0}{1 - G_{12}G_{21}\zeta_0^2}, \quad (44)$$

and the velocities of the discontinuities:

$$Z_1 = S_1(0, \zeta_0) = \frac{C_1 - G_{12}\zeta_0 C_2}{1 - G_{12}\zeta_0},$$

$$Z_2 = S_2(\zeta_0, 0) = \frac{C_2 - G_{21}\zeta_0 C_1}{1 - G_{21}\zeta_0}. \quad (45)$$

Both kinds of solitons propagate in the region delimited by $x = Z_1 t$ and $x = Z_2 t$ (since $F_1^{II} \neq 0, F_2^{II} \neq 0$), and we refer to this region as the interaction region in the following. The discontinuity’s velocity Z_i corresponds to the effective velocity of solitons Λ_i in this region. The total density of solitons

TABLE II. Initial conditions for the spectral Riemann problem (34), (36) considered in Sec. IV B. The constraint on the spectral parameters $|\Lambda_i| \leq 1.1$ in (i), (ii), and (iv) is due to the limits of the numerical scheme used to solve the RNLS equation (cf. Appendix B).

	Soliton parameter	Left boundary condition	Right boundary condition
(i)	$(\Lambda_1 = 1.05, \Lambda_2 \in [1.06, 1.10])$	$F^L = (0, 6.6) \times 10^{-2}$	$F^R = (6.6, 0) \times 10^{-2}$
(ii)	$(\Lambda_1 = -1.05, \Lambda_2 \in [1.06, 1.1])$	$F^L = (0, 6.6) \times 10^{-2}$	$F^R = (6.6, 0) \times 10^{-2}$
(iii)	$(\Lambda_1, \Lambda_2, \Lambda_3) = (-0.2, 0.1, 0.4)$	$F^L = (2.5, 0, 7.5) \times 10^{-2}$	$F^R = (5, 5, 0) \times 10^{-2}$
(iv)	$(\Lambda_1, \Lambda_2, \Lambda_3) = (-1.1, 1.05, 1.1)$	$F^L = (1.6, 0, 5) \times 10^{-2}$	$F^R = (3.3, 3.3, 0) \times 10^{-2}$

$\sum_i F_i$ in the interaction region is given by

$$F_1^{\text{II}} + F_2^{\text{II}} = \frac{2 - (G_{12} + G_{21})\zeta_0}{1 - G_{12}G_{21}\zeta_0^2} \zeta_0. \quad (46)$$

If $\text{sgn}(G_{12}) = \text{sgn}(G_{21}) > 0$ (< 0), then the total density $F_1^{\text{II}} + F_2^{\text{II}}$ is smaller (larger) than the sum of the initial soliton densities $2\zeta_0$, and $Z_1 < C_1 < C_2 < Z_2$ ($C_1 < Z_1 < Z_2 < C_2$) (cf., for instance, [17]).

The two-component shock-tube problem ($n = 2$) has been investigated numerically in [47] for KdV soliton gases. We have shown in Sec. II C that the kinetic dynamics of the KdV soliton and the isotropic DNLS soliton gas are both governed by Eqs. (1), (12) with $G_1(\lambda, \mu) > 0$. Thus solutions of the DNLS spectral Riemann problem and the KdV spectral Riemann problem are expected to describe very similar dynamics, and we rather focus on the anisotropic RNLS soliton gas exhibiting two distinct kinds of interaction. The solution of the RNLS spectral Riemann problem is given by (43), (44), (45) where $G_{ij} = G_2(\Lambda_i, \Lambda_j)$ with G_2 defined in (17).

To verify the validity of our spectral solutions in the context of the original nonlinear wave problem of the interaction of soliton gases, we solve numerically the RNLS equation (13) with initial conditions corresponding to the spectral Riemann data (36) for two different RNLS soliton gases with (i) overtaking collisions $G_{ij} > 0$ ($\Lambda_1 = 1.05, \Lambda_2 \in [1.06, 1.1]$), and (ii) head-on collisions $G_{ij} < 0$ ($\Lambda_1 = -1.05, \Lambda_2 \in [1.06, 1.1]$). The boundary values F^L and F^R for cases (i) and (ii) are indicated in Table II. Fifty initial conditions $\rho(x, 0), u(x, 0)$ are realized according to the initial step distribution (36) and evolved through a direct numerical simulation of the NLS equation (8) with $\sigma = -1$. The details of the numerical implementation of the initial condition (36) and the direct numerical resolution of (8) are given in Appendix B.

A typical RNLS soliton gas distribution $\rho(x, 0)$ and its corresponding numerical evolution $\rho(x, t)$ are displayed in Fig. 4 for the spectral Riemann problem (i); soliton gas realizations for the spectral Riemann problem (ii) have a similar variation with different velocities Z_1 and Z_2 . We emphasize that, although the soliton gas is initially prepared in a rarefied regime where solitons are spatially well separated (cf. Appendix B), the total density of solitons increases in the interaction region, and a dense soliton gas can be observed in Fig. 4 for which solitons exhibit significant overlap.

Spatiotemporal evolution of one soliton gas realization is displayed in Fig. 5, with overtaking collisions (i) and head-on collisions (ii). To enhance the discrepancy between free soliton velocities C_i and contact discontinuities velocity Z_i the

trajectories of the solitons are followed in the frames $(x - t, t)$ for overtaking collisions where $Z_i \sim C_i \sim 1$, and $(x \pm t, t)$ for head-on collisions where $Z_1 \sim C_1 \sim -1$ and $Z_2 \sim C_2 \sim 1$. One can notice that the interaction time between two solitons is very short for a head-on collision, which explains the weakness of head-on interactions compared to overtaking interactions.

The averaging of the 50 numerical solutions yields the statistical moments of the nonlinear wave fields of the RNLS dispersive hydrodynamics. Figure 6 displays the comparison between $\langle \rho(x, t) \rangle$ obtained numerically and the analytical solution (35), (43) for (i) and (ii). Note that the discontinuities in $\langle \rho(x, t) \rangle$ have a finite slope in Fig. 6, which is an artifact of the averaging procedure detailed in Appendix B. The comparison between the numerical values of $\langle \rho \rangle, Z_1, Z_2$ fitted from the nu-

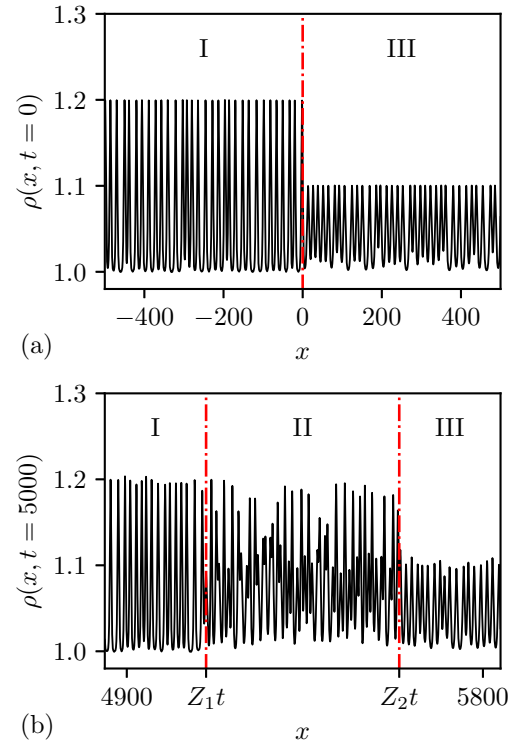


FIG. 4. Example of one realization of the soliton gas shock-tube problem (i) at $t = 0$ (a) and $t = 5000$ (b) with $(\Lambda_1, \Lambda_2) = (1.05, 1.10)$. The two regions I and III correspond, respectively, to the left and right boundary conditions prescribed in the initial condition [cf. (36)]. The variation of $\rho(x, t)$ clearly displays the formation of an intermediate interaction region, denoted region II, between the two positions $x = Z_1 t$ and $x = Z_2 t$, cf. (45), highlighted by vertical dash-dotted lines.

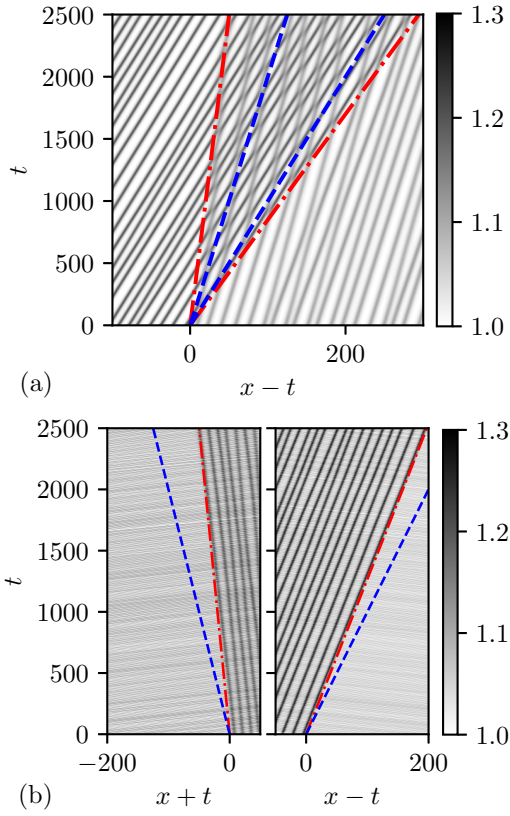


FIG. 5. Spatiotemporal plots of the field $\rho(x, t)$ for one realization of the soliton gas. Trajectories of the solitons appear in solid lines. Dash-dotted lines correspond to the trajectories of the contact discontinuities: $x = Z_1 t$, $x = Z_2 t$ [cf. (45)], and dashed lines to the free soliton trajectories: $x = C_1 t$, $x = C_2 t$. (a) Overtaking collisions $(\Lambda_1, \Lambda_2) = (1.05, 1.10)$ [cf. initial condition (i) in Table II]. (b) Head-on collisions $(\Lambda_1, \Lambda_2) = (-1.05, 1.10)$ [cf. initial condition (ii) in Table II].

merical solution $\langle \rho(x, t = 5000) \rangle$, and the analytical solutions (44), (45) for different values of Λ_2 is displayed in Fig. 7. The comparison shows good agreement between analytical and numerical solutions and highlights the contrasting effects of (i) overtaking and (ii) head-on collisions. As predicted $Z_1 < C_1 < C_2 < Z_2$ in case (i), whereas $C_1 < Z_1 < Z_2 < C_2$ in case (ii). In case (ii) $\langle \rho \rangle$ in the region of interaction is almost equal to the average value of ρ for a noninteracting soliton gas [cf. solution (40)]. This is due to the weakness of the head-on interaction, clearly displayed in the comparison between Δ_{+-} and Δ_{++} in Fig. 1.

The discrepancy between the analytical and numerical solutions can be associated to the numerical implementation and the time evolution of the soliton gas. The construction of the soliton gas at $t = 0$, detailed in Appendix B 1, is only valid if the overlap between solitons is negligible, which is not exactly the case for the parameters considered in Table II. Since $\sqrt{\Lambda_2^2 - 1}$ is the typical width of the Λ_2 soliton, the overlap between solitons becomes more important as Λ_2 decreases for a fixed initial density ζ_0 . Besides, the numerical scheme utilized to solve the RNLS equation is only valid for small

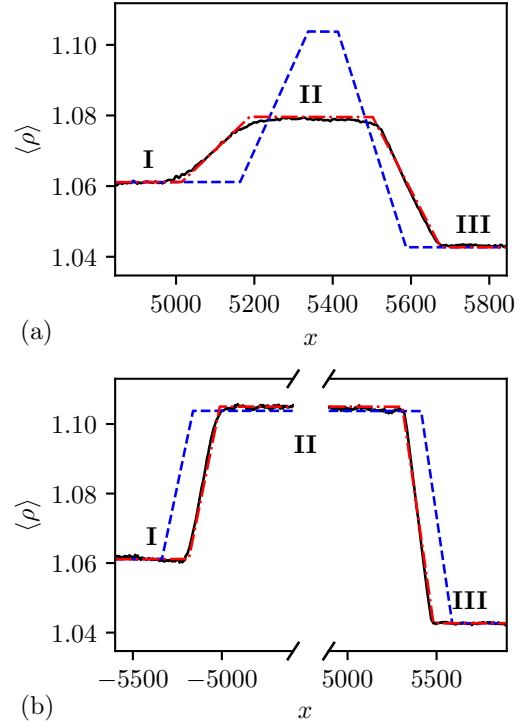


FIG. 6. Comparison between the ensemble average $\langle \rho(x, t = 5000) \rangle$ of 50 direct numerical solutions of the RNLS soliton gas shock-tube problem (solid line) and the analytical solution (35), (43) obtained via the spectral kinetic theory (dash-dotted line). The dashed lines correspond to the respective spectral solutions (35), (40) for a noninteracting soliton gas. (a) Overtaking collisions $(\Lambda_1, \Lambda_2) = (1.05, 1.10)$. (b) Head-on collisions $(\Lambda_1, \Lambda_2) = (-1.05, 1.10)$.

amplitude solitons (cf. Appendix B 2), and the discrepancy also increases as Λ_2 increases.

Additionally, we can compute the variation of the components $F_1(x, t)$ and $F_2(x, t)$ of the DOS using the expression (35):

$$\begin{pmatrix} F_1(x, t) \\ F_2(x, t) \end{pmatrix} = \begin{pmatrix} \bar{\eta}(\Lambda_1) & \bar{\eta}(\Lambda_2) \\ \bar{u}(\Lambda_1) & \bar{u}(\Lambda_2) \end{pmatrix}^{-1} \begin{pmatrix} \langle \rho(x, t) - 1 \rangle \\ \langle u(x, t) \rangle \end{pmatrix}, \quad (47)$$

providing that the determinant $\bar{\eta}(\Lambda_1)\bar{u}(\Lambda_2) - \bar{\eta}(\Lambda_2)\bar{u}(\Lambda_1)$ does not vanish. In particular, we can evaluate numerically the total density $F_1(x, t) + F_2(x, t)$ from the numerical solutions. Figure 8 displays the comparison of the total density corresponding to the examples presented in Fig. 6. Notice that, since $\langle \rho \rangle = \bar{\eta}(\Lambda_1)F_1 + \bar{\eta}(\Lambda_2)F_2$ with $\bar{\eta} > 0$, the variation of the moment $\langle \rho \rangle$ and the variation of the total density $F_1 + F_2$ are qualitatively similar. As expected the RNLS soliton gas rarefies when solitons interact with overtaking collisions ($F_1^{\text{II}} + F_2^{\text{II}} < 2\zeta_0$), and condenses with head-on collisions ($F_1^{\text{II}} + F_2^{\text{II}} > 2\zeta_0$). As pointed out previously, the total density in the example (ii) is very close to the total density of the noninteracting gas $2\zeta_0$ because of the weakness of the phase shift induced by head-on collisions.

2. Three-component gas

We consider now the case of three-component gases with one component belonging to the slow spectral branch and two

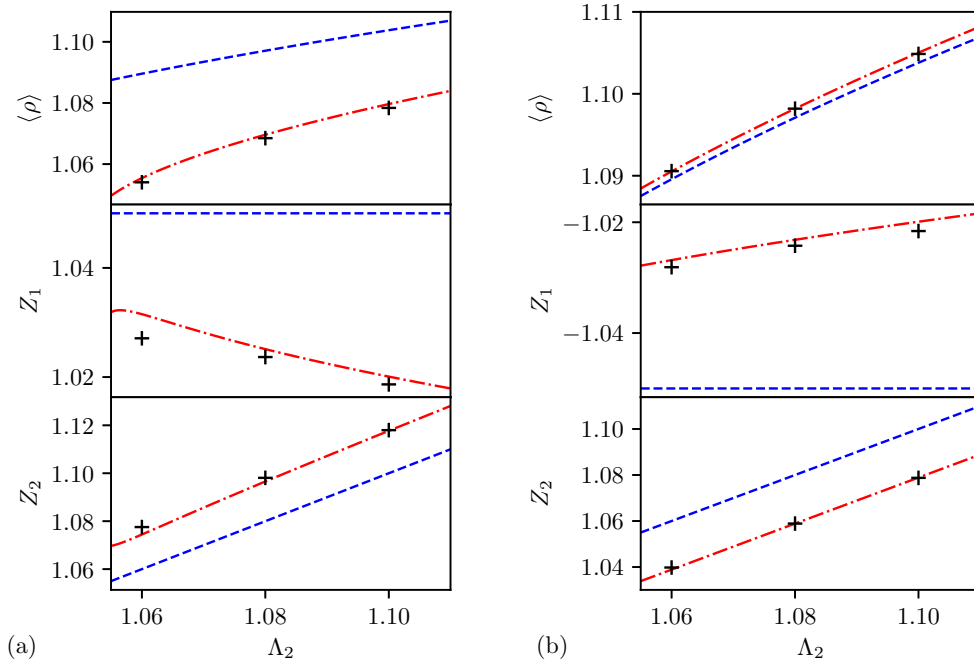


FIG. 7. Comparison between the parameters of the analytical solutions (35), (43) (dash-dotted line) and the corresponding fitted parameters of the numerical solution (crosses) with different spectral parameters Λ_2 ; numerical averages are obtained over 50 realizations. For comparison, the dashed lines correspond to the parameters of the noninteracting solitons solution (35), (40). $\langle \rho \rangle$ is evaluated in region II [cf. (35), (44)]. Z_1 is the velocity of the discontinuity separating regions I and II, and Z_2 the velocity of the discontinuity separating regions II and III [cf. (45)]. (a) Overtaking collisions $(\Lambda_1, \Lambda_2) = (1.05, 1.10)$. (b) Head-on collisions $(\Lambda_1, \Lambda_2) = (-1.05, 1.10)$.

components belonging to the fast branch for (iii) the DNLS equation and (iv) the RNLS equation. Note that in the latter case the anisotropic soliton gas features both overtaking collisions and head-on collisions. Although one can formally solve the equation of state (33) to obtain the expression of $S_i(\mathbf{F})$ and solve the Rankine-Hugoniot condition (39), the analytical expressions do not arise as easily as the expressions obtained in the two-component case. We choose here to solve (33), (39) numerically. The values \mathbf{F}^L and \mathbf{F}^R of the initial soliton densities considered numerically are indicated in Table II.

One-hundred initial conditions $\rho(x, 0)$, $u(x, 0)$ are realized according to the initial spectral step distribution (36) and evolved through a direct numerical simulation of the NLS equation (8). The statistics of the soliton gas is then obtained by computing the average $\langle \rho(x, t) \rangle$ from the evolution of the 100 realizations. Figure 9 displays the variation of the statistical moment $\langle \rho(x, t) \rangle$. As expected, the solution is composed of four plateaus, where regions II and III contain at least two distinct soliton components and are regions of interaction. The comparison in Fig. 9 shows good agreement between the analytical solution (35), (37) and the statistical averages of the numerical solutions.

V. CONCLUSIONS AND OUTLOOK

In this work we have developed the spectral kinetic theory of soliton gases in bidirectional integrable dispersive hydrodynamic systems. Previously, such theory had been developed for (effectively) unidirectional soliton gases, in which all pairwise soliton collisions are characterized by a single expression for the phase shift. Generally, however, the phase

shifts in the overtaking and head-on collisions of solitons are essentially different, which necessitates the extension of the existing theory to the bidirectional case. This extension is also motivated by the recent experimental results on the generation of bidirectional shallow-water soliton gases [31,32].

The definitive quantitative characteristics of an integrable soliton gas is the DOS, which is the density function $f(\lambda, x, t)$ in the spectral (IST) (x, λ) -phase space. The DOS evolution in a unidirectional nonuniform soliton gas is governed by the kinetic equation consisting of the continuity equation (1) complemented by the integral equation of state (2) relating the soliton gas velocity and the DOS. The presence of two distinct species of solitons corresponding to the slow and fast branches of the dispersion relation in bidirectional systems naturally calls for the introduction of two respective DOSs. As a result, one arrives at a system of two coupled kinetic equations, which is the subject of the present work.

We introduced the notion of isotropic and anisotropic bidirectional soliton gases based on the sign properties of the phase shifts in overtaking and head-on soliton collisions in a bidirectional gas. In the anisotropic case, where the distinction between overtaking and head-on soliton collisions is genuine, the kinetic of the gas is governed by two coupled equations (6), (7) which we obtained using an extension of the direct physical approach proposed in [17]. The approach of [17] combines the qualitative ideas of the original Zakharov paper [21] with the mathematical developments of [22] based on the spectral finite-gap theory. In the isotropic case, the coupled system (6), (7) reduces to a single kinetic equation (1), (2) making a bidirectional isotropic gas effectively equivalent to a unidirectional gas.

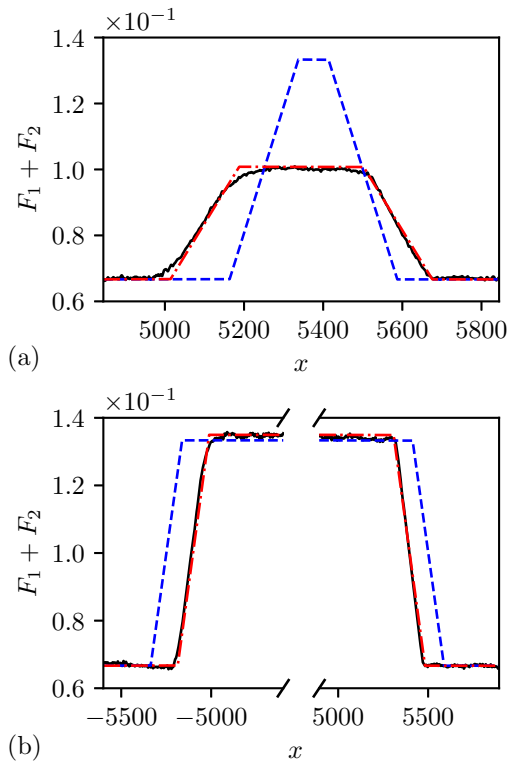


FIG. 8. Comparison between the total density of the soliton gas obtained by direct numerical solution of the RNLS soliton gas shock-tube problem (black solid line) and the corresponding spectral analytical solution $F_1(x, t) + F_2(x, t)$ where F_i is given by (43) (dash-dotted line); the total density in the region of interaction $F_1^{\text{II}} + F_2^{\text{II}}$ is given by (46). The dashed line corresponds to the total density $F_1^{\text{free}} + F_2^{\text{free}}$ [cf. (40)]. (a) Overtaking collisions $(\Lambda_1, \Lambda_2) = (1.05, 1.10)$. (b) Head-on collisions $(\Lambda_1, \Lambda_2) = (-1.05, 1.10)$.

To highlight the principal differences between isotropic and anisotropic soliton gases, we have considered two prototypical physically relevant examples: the (isotropic) soliton gas of the classical defocusing NLS (DNLS) equation (9) and the (anisotropic) soliton gas of the so-called resonant NLS (RNLS) equation (13) having applications in dispersive magnetohydrodynamics [35,40]. The results for the RNLS equation are also extended to the KB system (15) describing bidirectional shallow-water waves.

To provide a connection between the spectral kinetics of soliton gases and the dynamics of the physical parameters of the associated nonlinear wave fields, we have developed a general simple procedure enabling the evaluation of the basic ensemble averages of the soliton gas wave field in terms of the appropriate moments of the spectral DOS.

As an application of the developed kinetic theory we have considered the generalized Riemann (shock-tube) problem describing the collision of several monochromatic soliton beams, each consisting of solitons with nearly identical spectral parameters. The interaction dynamics of such beams is described by certain exact hydrodynamic reductions of the spectral kinetic equations. We constructed the weak solutions of these hydrodynamic reductions in the form of a system of constant states separated by propagating contact discontinu-

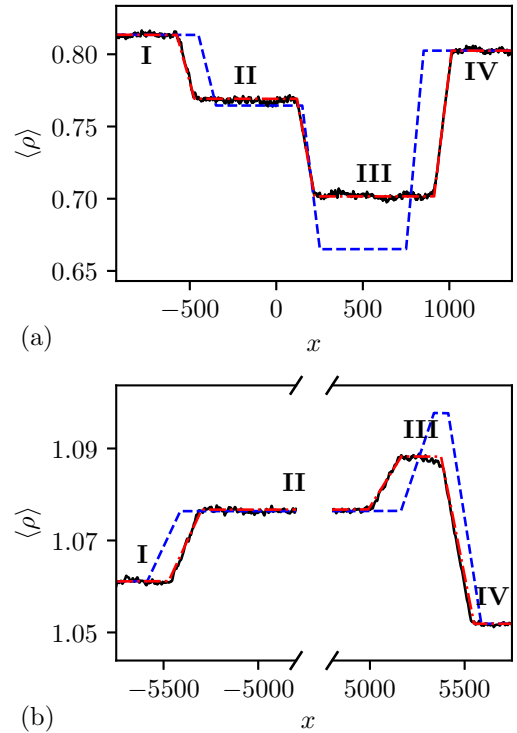


FIG. 9. Comparison between the ensemble average $\langle \rho(x, t) \rangle$ obtained by direct numerical solution of the soliton gas shock-tube problem (solid line) and the analytical solution (35), (37) (dash-dotted line). The dashed line corresponds to the average in the soliton gas composed of noninteracting solitons with the spectral distribution given by (35), (40). (a) DNLS soliton gas at $t = 2000$, case (iii). (b) RNLS soliton gas at $t = 5000$, case (iv).

ities satisfying appropriate Rankine-Hugoniot conditions. The obtained general solutions were then applied to the description of collisions of DNLS and RNLS soliton gases, and the comparison with direct numerical simulations of the DNLS and RNLS equation was made.

We stress that, although our derivation of the kinetic equation (6), (7) for a dense bidirectional soliton gas is based on the phenomenological method of [17], it can be formally justified using the thermodynamic limit of the modulation equations, that has been developed for the KdV and focusing NLS equations in [16,22] and can be readily generalized to other integrable systems supporting finite-gap solutions associated with hyperelliptic spectral Riemann surfaces. Such a mathematical justification will be the subject of a separate work. Meanwhile, the excellent agreement of the exact solutions of the Riemann problems for bidirectional kinetic equations with appropriate direct numerical simulations for the DNLS and RNLS equations provides a convincing confirmation of the validity of our results.

Despite the consideration of this work being formally reliant on the integrability of the nonlinear wave dynamics (4), the developed kinetic theory can be extended to non-integrable systems supporting solitary wave solutions that exhibit nearly elastic collisions. An experimentally accessible example of such physical system (albeit for a unidirectional case) is the so-called viscous fluid conduit equation describ-

ing the dynamics of the interface between two immiscible viscous fluids with high density and viscosity contrast ratios, the lighter fluid being buoyantly ascending through the heavier fluid forming a liquid “pipe,” a conduit [59]. This system supports solitary wave solutions that exhibit nearly elastic collisions as demonstrated numerically and confirmed experimentally [60]. Constructing kinetic theory of soliton gases for nonintegrable Eulerian dispersive hydrodynamic systems of this type represents a challenging open problem.

Another important direction of further research is the extension of the developed kinetic theory to perturbed integrable systems. In particular, kinetic theory of soliton gas for the perturbed DNLS equation could be used to describe soliton gas in a quasi-1D repulsive BEC in a trapping potential, which has been observed experimentally in [61]. The dynamics of the trapped condensate is governed by the celebrated Gross-Pitaevskii equation, which is the DNLS equation supplemented by an external potential term, which could be treated as a perturbation in certain configurations. Although some properties of a rarefied soliton gas in a trapped BEC have been studied in the previous works [37,38], the description of a dense gas is not available at present. The investigation of dense soliton gas dynamics in BECs can shed new light on turbulence in superfluids, or “quantum turbulence,” which has been the subject of intense research in recent decades (see, e.g., [62], and references therein).

The direct experimental verification of the developed theory could be made possible by the recent advances in the spectral synthesis of soliton gases with a prescribed DOS [18]. While the method of [18] was developed for deep water waves, its extension to other types of wave propagation well described by integrable or nearly integrable systems looks to be a very promising direction since the kinetic description of soliton gases is achieved essentially in spectral terms.

Concluding, we hope that our work will provide further motivation for the theoretical and experimental study of soliton gases.

ACKNOWLEDGMENTS

This work was partially supported by EPSRC Grant No. EP/R00515X/2 (T.C. and G.E.) and DSTL Grant No. DSTLX-1000116851 (G.E. and G.R.). The authors thank S. Randoux, P. Suret, and A. Tovbis for numerous stimulating discussions.

APPENDIX A: SOLITON SOLUTION OF THE KB SYSTEM

The soliton solution (16) of the RNLS equation reads after substitution in (14) as

$$\begin{aligned}\tilde{\rho}_s^\pm &= 1 + \lambda \tilde{u}_s - \frac{\tilde{u}_s^2}{2}, \\ \tilde{u}_s^\pm &= \frac{2(\lambda^2 - 1)[\lambda - \sqrt{\lambda^2 - 1} \tanh(\alpha/2)]}{2\lambda^2 - 1 + \cosh(\alpha)}, \\ \alpha &= \sqrt{3(\lambda^2 - 1)}(\tilde{x} - \lambda \tilde{t}),\end{aligned}\quad (\text{A1})$$

where $\lambda^2 > 1$. Note that the solution (A3) is not centered at $x = 0$ but $x = \phi(\lambda)$ with

$$\phi(\lambda) = \frac{\text{sgn}(\lambda)}{\sqrt{3(\lambda^2 - 1)}} \ln(|\lambda| - \sqrt{\lambda^2 - 1}). \quad (\text{A2})$$

The centered soliton solution reads

$$\begin{aligned}\tilde{\rho}_s^\pm[\tilde{x} + \phi(\lambda), \tilde{t}] &= 1 + \frac{2(\lambda^2 - 1)[1 + |\lambda| \cosh(\alpha)]}{[|\lambda| + \cosh(\alpha)]^2}, \\ \tilde{u}_s^\pm[\tilde{x} + \phi(\lambda), \tilde{t}] &= \frac{2 \text{sgn}(\lambda)(\lambda^2 - 1)}{|\lambda| + \cosh(\alpha)}, \\ \alpha &= \sqrt{3(\lambda^2 - 1)}(\tilde{x} - \lambda \tilde{t}),\end{aligned}\quad (\text{A3})$$

which coincides with the solution derived in [63].

APPENDIX B: NUMERICAL IMPLEMENTATION OF SOLITON GASES FOR THE NLS EQUATION

1. Implementation of the step distribution

We implement the soliton gas using the method developed in [47]. The initial step distribution of the spectral Riemann problem (36) with values given in Table II describes a rarefied gas where solitons do not overlap. Such a distribution is implemented by the superposition of solitons

$$\begin{aligned}\rho(x, t = 0) &= \sum_i \rho_s(x - \xi_i; \Lambda_i), \\ u(x, t = 0) &= \sum_i u_s(x - \xi_i; \Lambda_i),\end{aligned}\quad (\text{B1})$$

where the Λ_i 's are the spectral parameters of the solitons and the ξ_i 's their initial position. Although the particles' position ξ_i of an “ideal” soliton gas should be distributed according to a Poisson process [41], this cannot be implemented numerically since the solitons are not allowed to overlap. In our numerics, the distance between two solitons $\xi_{i+1} - \xi_i$ is uniformly distributed in the interval $[d_1, d_2]$ with $0 < d_1 < d_2$ such that the solitons do not overlap; the total density of solitons is given by $2/(d_1 + d_2)$. We choose $(d_1, d_2) = (10, 20)$ for the RNLS-Riemann problems (i), (ii), and (iv) and $(d_1, d_2) = (8, 12)$ for the DNLS-Riemann problem (cf. Sec. IV B).

2. Numerical scheme

The DNLS equation $i\psi_t + \frac{1}{2}\psi_{xx} - |\psi|^2\psi = 0$, $\psi = \sqrt{\rho} \exp(i \int u dx)$ is solved with periodic boundary conditions $\psi(x = L, t) = \psi(x = 0, t)$ using a Fourier spectral method. The linear part of the DNLS equation is resolved with an integrating factor and the problem is integrated in time using the fourth-order Runge-Kutta method.

Since the dispersive term in the RNLS equation (13) is a nonlinear term in ψ , the RNLS equation is first transformed into the KB equation (15) using the change of variables (14). The KB system is then solved with periodic boundary conditions $\psi(x = L, t) = \psi(x = 0, t)$ using a Fourier spectral method (with a fourth-order Runge-Kutta method for the time integration). Equation (15) displays a short-wavelength instability: the amplitude of modes $\tilde{\rho} - 1 \propto \tilde{u} \propto \cos(k_i \tilde{x})$ grows exponentially with time for $k_i > \sqrt{3}$. We thus filter out Fourier modes $k_i > \sqrt{3}$ after each time step. This imposes a constraint

on the type of solitons that can be implemented numerically. Indeed, large amplitude solitons $|\lambda| \gg 1$ populate the short-wavelength Fourier modes $k_i > \sqrt{3}$, which are not taken into account in the numerical scheme. We thus consider in the numerical simulations the solitons for which $|\lambda| \in (1, 1.1)$.

3. Spatial and ensemble averages

The statistical moment $\langle \rho \rangle$ determined numerically in Sec. IV B is obtained with (1) the average over ensembles of 50 or 100 realizations and (2) a local spatial average over the

mesoscopic space interval ℓ [cf. (29)]:

$$\ell = \frac{10}{\max [\sum_i F_i(x, t = 0)]}. \quad (\text{B2})$$

As pointed out in Sec. III, both averaging procedures are equivalent providing that the soliton gas is locally ergodic. The choice of the value for ℓ ensures that the space interval contains at least ten solitons. Note that the transitions of the numerically evaluated mean field $\langle \rho(x, t) \rangle$ corresponding to contact discontinuities in the analytical solution have a finite slope proportional to $1/\ell$ because of the spatial averaging.

-
- [1] G. Biondini, G. El, M. Hoefer, and P. Miller, Dispersive hydrodynamics: Preface, *Physica D (Amsterdam, Neth.)* **333**, 1 (2016).
- [2] M. D. Maiden, D. V. Anderson, N. A. Franco, G. A. El, and M. A. Hoefer, Solitonic Dispersive Hydrodynamics: Theory and Observation, *Phys. Rev. Lett.* **120**, 144101 (2018).
- [3] P. Sprenger, M. A. Hoefer, and G. A. El, Hydrodynamic optical soliton tunneling, *Phys. Rev. E* **97**, 032218 (2018).
- [4] G. A. El, M. A. Hoefer, and M. Shearer, Expansion shock waves in regularized shallow-water theory, *Proc. R. Soc. A* **472**, 20160141 (2016).
- [5] G. A. El and M. A. Hoefer, Dispersive shock waves and modulation theory, *Physica D (Amsterdam, Neth.)* **333**, 11 (2016).
- [6] V. E. Zakharov, Turbulence in integrable systems, *Stud. Appl. Math.* **122**, 219 (2009).
- [7] A. V. Gurevich, K. P. Zybkin, and G. A. Él, Development of stochastic oscillations in a one-dimensional dynamical system described by the Korteweg-de Vries equation, *J. Exp. Theor. Phys.* **88**, 182 (1999).
- [8] G. A. El, E. G. Khamis, and A. Tovbis, Dam break problem for the focusing nonlinear Schrödinger equation and the generation of rogue waves, *Nonlinearity* **29**, 2798 (2016).
- [9] P. Walczak, S. Randoux, and P. Suret, Optical Rogue Waves in Integrable Turbulence, *Phys. Rev. Lett.* **114**, 143903 (2015).
- [10] S. Randoux, P. Walczak, M. Onorato, and P. Suret, Nonlinear random optical waves: Integrable turbulence, rogue waves and intermittency, *Physica D (Amsterdam, Neth.)* **333**, 323 (2016).
- [11] A. A. Gelash and D. S. Agafontsev, Strongly interacting soliton gas and formation of rogue waves, *Phys. Rev. E* **98**, 042210 (2018).
- [12] A. Costa, A. R. Osborne, D. T. Resio, S. Alessio, E. Crivì, E. Saggese, K. Bellomo, and C. E. Long, Soliton Turbulence in Shallow Water Ocean Surface Waves, *Phys. Rev. Lett.* **113**, 108501 (2014).
- [13] S. Trillo, G. Deng, G. Biondini, M. Klein, G. F. Clauss, A. Chabchoub, and M. Onorato, Experimental Observation and Theoretical Description of Multisoliton Fission in Shallow Water, *Phys. Rev. Lett.* **117**, 144102 (2016).
- [14] S. Trillo, M. Klein, G. Clauss, and M. Onorato, Observation of dispersive shock waves developing from initial depressions in shallow water, *Physica D (Amsterdam, Neth.)* **333**, 276 (2016).
- [15] A. Gelash, D. Agafontsev, V. Zakharov, G. El, S. Randoux, and P. Suret, Bound State Soliton Gas Dynamics Underlying the Spontaneous Modulational Instability, *Phys. Rev. Lett.* **123**, 234102 (2019).
- [16] G. El and A. Tovbis, Spectral theory of soliton and breather gases for the focusing nonlinear Schrödinger equation, *Phys. Rev. E* **101**, 052207 (2020).
- [17] G. A. El and A. M. Kamchatnov, Kinetic Equation for a Dense Soliton Gas, *Phys. Rev. Lett.* **95**, 204101 (2005).
- [18] P. Suret, A. Tikan, F. Bonnefoy, F. Copie, G. Ducrozet, A. Gelash, G. Prabhudesai, G. Michel, A. Cazaubiel, E. Falcon, G. El, and S. Randoux, Nonlinear Spectral Synthesis of Soliton Gas in Deep-Water Surface Gravity Waves, *Phys. Rev. Lett.* **125**, 264101 (2020).
- [19] G. A. El, A. M. Kamchatnov, M. V. Pavlov, and S. A. Zykov, Kinetic equation for a soliton gas and its hydrodynamic reductions, *J. Nonlinear Sci.* **21**, 151 (2011).
- [20] M. J. Ablowitz and Y. Kodama, Note on asymptotic solutions of the Korteweg-de Vries equation with solitons, *Stud. Appl. Math.* **66**, 159 (1982).
- [21] V. E. Zakharov, Kinetic equation for solitons, *Sov. Phys. JETP* **33**, 538 (1971).
- [22] G. A. El, The thermodynamic limit of the Whitham equations, *Phys. Lett. A* **311**, 374 (2003).
- [23] G. A. El, Critical density of a soliton gas, *Chaos* **26**, 023105 (2016).
- [24] B. Doyon, T. Yoshimura, and J.-S. Caux, Soliton Gases and Generalized Hydrodynamics, *Phys. Rev. Lett.* **120**, 045301 (2018).
- [25] B. Doyon, H. Spohn, and T. Yoshimura, A geometric viewpoint on generalized hydrodynamics, *Nucl. Phys. B* **926**, 570 (2018).
- [26] D.-L. Vu and T. Yoshimura, Equations of state in generalized hydrodynamics, *SciPost Phys.* **6**, 23 (2019).
- [27] G. B. Whitham, *Linear and Nonlinear Waves* (Wiley, New York, 1999).
- [28] D. J. Kaup, A higher-order water-wave equation and the method for solving it, *Prog. Theor. Phys.* **54**, 396 (1975).
- [29] A. M. Kamchatnov, *Nonlinear Periodic Waves and their Modulations: An Introductory Course* (World Scientific, Singapore, 2000).
- [30] A. G. Abanov, E. Bettelheim, and P. Wiegmann, Integrable hydrodynamics of Calogero–Sutherland model: Bidirectional Benjamin–Ono equation, *J. Phys. A: Math. Theor.* **42**, 135201 (2009).
- [31] I. Redor, E. Barthélemy, H. Michallet, M. Onorato, and N. Mordant, Experimental Evidence of a Hydrodynamic Soliton Gas, *Phys. Rev. Lett.* **122**, 214502 (2019).

- [32] I. Redor, E. Barthélemy, N. Mordant, and H. Michallet, Analysis of soliton gas with large-scale video-based wave measurements, *Exp. Fluids* **61**, 216 (2020).
- [33] Y. Li and J. E. Zhang, Bidirectional soliton solutions of the classical Boussinesq system and AKNS system, *Chaos, Solitons Fractals* **16**, 271 (2003).
- [34] V. E. Zakharov and A. B. Shabat, Interaction between solitons in a stable medium, *Sov. Phys. JETP* **37**, 823 (1973).
- [35] J.-H. Lee, O. Pashaev, C. Rogers, and W. Schief, The resonant nonlinear Schrödinger equation in cold plasma physics. Application of Bäcklund-Darboux transformations and superposition principles, *J. Plasma Phys.* **73**, 257 (2007).
- [36] J. Yang, *Nonlinear Waves in Integrable and Nonintegrable Systems* (Society for Industrial and Applied Mathematics, Philadelphia, PA, 2010).
- [37] M. Schmidt, S. Erne, B. Nowak, D. Sexty, and T. Gasenzer, Non-thermal fixed points and solitons in a one-dimensional Bose gas, *New J. Phys.* **14**, 075005 (2012).
- [38] W. Wang and P. G. Kevrekidis, Transitions from order to disorder in multiple dark and multiple dark-bright soliton atomic clouds, *Phys. Rev. E* **91**, 032905 (2015).
- [39] J.-H. Lee and O. K. Pashaev, Solitons of the resonant nonlinear Schrödinger equation with nontrivial boundary conditions: Hirota bilinear method, *Theor. Math. Phys.* **152**, 991 (2007).
- [40] A. V. Gurevich and A. L. Krylov, The origin of a nondissipative shock wave, *Dokl. Akad. Nauk SSSR* **301**, 851 (1988); *Dokl. Math.* **33**, 603 (1988).
- [41] G. A. El, A. L. Krylov, S. Molchanov, and S. Venakides, Soliton turbulence as a thermodynamic limit of stochastic soliton lattices, *Physica D (Amsterdam, Neth.)* **152**, 653 (2001).
- [42] H. Flaschka, M. G. Forest, and D. W. McLaughlin, Multiphase averaging and the inverse spectral solution of the Korteweg–de Vries equation, *Commun. Pure Appl. Math.* **33**, 739 (1980).
- [43] J. Moser, *Integrable Hamiltonian Systems and Spectral Theory* (Scuola Normale Superiore, Pisa, 1981).
- [44] E. G. Shurgalina and E. N. Pelinovsky, Nonlinear dynamics of a soliton gas: Modified Korteweg–de Vries equation framework, *Phys. Lett. A* **380**, 2049 (2016).
- [45] D. Dutykh and E. Pelinovsky, Numerical simulation of a solitonic gas in KdV and KdV–BBM equations, *Phys. Lett. A* **378**, 3102 (2014).
- [46] M. V. Pavlov, V. B. Taranov, and G. A. El, Generalized hydrodynamic reductions of the kinetic equation for a soliton gas, *Theor. Math. Phys.* **171**, 675 (2012).
- [47] F. Carbone, D. Dutykh, and G. A. El, Macroscopic dynamics of incoherent soliton ensembles: Soliton gas kinetics and direct numerical modeling, *Europhys. Lett.* **113**, 30003 (2016).
- [48] E. Ferapontov, Integration of weakly nonlinear hydrodynamic systems in Riemann invariants, *Phys. Lett. A* **158**, 112 (1991).
- [49] S. P. Tsarëv, The geometry of Hamiltonian systems of hydrodynamic type. The generalized hodograph method, *Math. USSR-Izv.* **37**, 397 (1991).
- [50] P. Sprenger and M. A. Hoefer, Discontinuous shock solutions of the Whitham modulation equations as zero dispersion limits of traveling waves, *Nonlinearity* **33**, 3268 (2020).
- [51] S. Gavriluk, B. Nkonga, K.-M. Shyue, and L. Truskinovsky, Stationary shock-like transition fronts in dispersive systems, *Nonlinearity* **33**, 5477 (2020).
- [52] O. A. Castro-Alvaredo, B. Doyon, and T. Yoshimura, Emergent Hydrodynamics in Integrable Quantum Systems Out of Equilibrium, *Phys. Rev. X* **6**, 041065 (2016).
- [53] B. Bertini, M. Collura, J. De Nardis, and M. Fagotti, Transport in Out-of-Equilibrium XXZ Chains: Exact Profiles of Charges and Currents, *Phys. Rev. Lett.* **117**, 207201 (2016).
- [54] B. Doyon and H. Spohn, Dynamics of hard rods with initial domain wall state, *J. Stat. Mech.* (2017) 073210.
- [55] A. Kuniba, G. Misguich, and V. Pasquier, Generalized hydrodynamics in box-ball system, *J. Phys. A: Math. Theor.* **53**, 404001 (2020).
- [56] D. A. Croydon and M. Sasada, Generalized hydrodynamic limit for the box-ball system, *Commun. Math. Phys.* **383**, 427 (2021).
- [57] B. Rozhdzvenskii and N. Janenko, *Systems of Quasilinear Equations and Their Applications to Gas Dynamics* (American Mathematical Society, Providence, RI, 1983).
- [58] P. D. Lax, *Hyperbolic Systems of Conservation Laws and the Mathematical Theory of Shock Waves* (Society for Industrial and Applied Mathematics, Philadelphia, PA, 1973).
- [59] N. K. Lowman and M. A. Hoefer, Dispersive hydrodynamics in viscous fluid conduits, *Phys. Rev. E* **88**, 023016 (2013).
- [60] N. K. Lowman, M. A. Hoefer, and G. A. El, Interactions of large amplitude solitary waves in viscous fluid conduits, *J. Fluid Mech.* **750**, 372 (2014).
- [61] C. Hamner, Y. Zhang, J. J. Chang, C. Zhang, and P. Engels, Phase Winding a Two-Component Bose-Einstein Condensate in an Elongated Trap: Experimental Observation of Moving Magnetic Orders and Dark-Bright Solitons, *Phys. Rev. Lett.* **111**, 264101 (2013).
- [62] C. F. Barenghi, L. Skrbek, and K. R. Sreenivasan, Introduction to quantum turbulence, *Proc. Natl. Acad. Sci. USA* **111**, 4647 (2014).
- [63] J. E. Zhang and Y. Li, Bidirectional solitons on water, *Phys. Rev. E* **67**, 016306 (2003).

Chapter 5

Numerical synthesis of breather gas

5.1 Outline of the Problem

The work reviewed in this Chapter was motivated by the recent theoretical and experimental results in soliton gas theory. The kinetic spectral theory for soliton for the fNLSE has been recently developed by El and Tovbis in [53], and the controlled realisation of deep-water soliton gas in a water tank experiment has been reported in [52]. Moreover, it has been recently demonstrated numerically that the soliton gas dynamics of the fNLSE for the special case of the “bound state soliton condensate” gas provides a remarkably good description of the statistical properties of the nonlinear stage of MI [109].

The spectral kinetic theory [53] also covers breather gases, i.e. the random ensembles of interacting fNLSE solitons in the presence of finite background. Observation of deep water breather gas in the ocean have been reported in [123]. At the same time, numerical realisation of a breather gas for the fNLSE is a nontrivial task due to severe accuracy problems (this already proves a serious obstacle for the numerical construction of N -breather solution with $N \gtrsim 5$ [147, 148]). In fact a similar problem arises already at the level of numerical realisation of conventional soliton gases. An effective IST-based numerical algorithm to create N -soliton solution of the fNLSE with N large has been recently proposed in [149] by implementing high-precision arithmetics routines proposed. Here we take advantage of this algorithm to build random ensembles of $N \sim 50$ breathers via the Darboux transform recursive scheme.

The purpose of the work reported in this Chapter is twofold: (i) effective numerical realisation of a breather gas; (ii) verification of the spectral theory of breather gas developed in [53].

For clarity of the exposition we summarise here some of the results on breather gas spectral theory developed in [53] and discussed in Section 1.5.3.

As described in Section 1.5.3 the central concept of the soliton and breather gas (BG) theory is the density of state (DOS), or spectral distribution function, $f(\lambda, x, t)$. In the context of the fNLSE, where the spectral parameter is $\lambda = \xi + i\zeta \in \mathbb{C}$, the DOS $f(\lambda, x, t)$ is defined such that at any time t , $f d\xi d\zeta dx$ determines the number of soliton/breather states in the element $\lambda \in [\xi, \xi + d\xi] \times [\zeta, \zeta + d\zeta]$ of the spectral phase space and contained in a portion of the gas within $[x, x + dx]$. For the purpose of this work we assume the DOS to be a multicomponent (M -component) delta-function distribution:

$$f(\lambda, x, t) = \sum_{j=1}^M \omega_j(x, t) \delta(\lambda - \lambda_j) \quad (5.1)$$

where $\omega_j(x, t)$ are the components' weight and $\{\lambda_j\}_{j=1}^M \subset \Gamma$ ($\zeta_j \neq \zeta_k \iff j \neq k$) the discrete point of the spectrum. The breather gas is then characterised, in the spectral plane, by a vertical branch cut $\lambda \in [-iq, iq]$, $q > 0$ corresponding to the plane wave background of amplitude q and by the set of discrete spectral point λ_i , see Fig. 20. In this context, the breather gas can be viewed as an N -order breather solution of the fNLSE, i.e. the reflectionless soliton solutions on non-zero background. Physically it can be viewed as a random ensemble of interacting Tajiri-Watanabe (TW) breathers (see Section 1.1.7 for the description of a TW breather). Since the TW breather has three distinguished limits: the Akhmediev breather (AB), the Kuznetsov-Ma (KM) breather and the Peregrine soliton (PS) — the rogue wave prototypes, it is also natural to consider these limiting objects at the level of the respective “rogue wave gases”.

The analytical theory of spatially nonhomogeneous BGs was introduced and developed in [53]. This description consists of the kinetic equation formed by a transport equation for the slowly varying DOS $f(\lambda, x, t)$

$$f_t + (fs)_x = 0, \quad (5.2)$$

and the integral equation of state that describes the modification on a tracer or trial breather (gen-

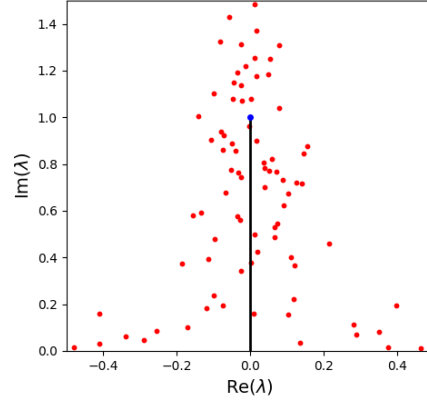


Figure 20: Spectral representation of a generic breather (TW) gas characterised by the branch cut (black vertical line) and a collection of points of discrete spectrum (red dots). The corresponding multicomponent DOS (5.1) has weights $\omega_j = 1 \forall j$.

erally a TW breather) velocity due to its interaction with the gas:

$$s(\lambda, x, t) = s_0(\lambda)\lambda + \iint_{\Gamma^+} \Delta(\lambda, \mu)[s(\lambda, x, t) - s(\mu, x, t)]f(\mu, x, t)d\xi d\zeta, \quad (5.3)$$

where $\mu = \xi + i\zeta$, Γ^+ is the two-dimensional compact support of the DOS in \mathbb{C}^+ , and s_0 is the velocity of a “free” TW breather given by

$$s_0(\lambda) = -2 \frac{\text{Im}[\lambda R_0(\lambda)]}{\text{Im}[R_0(\lambda)]}, \quad (5.4)$$

where $R_0(\lambda) = \sqrt{\lambda^2 - \delta_0^2}$ with $\delta_0 = iq$, the endpoint of the branch cut. The interaction kernel $\Delta(\lambda, \mu)$:

$$\Delta(\lambda, \mu) = \frac{1}{\text{Im}[R_0(\lambda)]} \left[\ln \left| \frac{\mu - \bar{\lambda}}{\mu - \lambda} \right| + \ln \left| \frac{R_0(\lambda)R_0(\mu) + \lambda\mu + q^2}{R_0(\bar{\lambda})R_0(\mu) + \bar{\lambda}\mu + q^2} \right| \right], \quad (5.5)$$

describes the position shift arising in a breather-breather interaction as reported in [53]. However, different forms of $\Delta(\lambda, \mu)$ have been derived in [131, 132]. The equivalence of the position shift (5.5) to the expressions obtained in [131, 132] is demonstrated in the Appendix A, where the detailed calculations are reported.

Considering a two-component breather gas with DOS:

$$f(\lambda) = \sum_{j=1}^2 w_j \delta(\lambda - \lambda_j), \quad (5.6)$$

an explicit solution of (5.3) can be obtained. As was explained in Section 1.5.3 a delta-function distribution function $\delta(\lambda - \lambda_j)$ is a mathematical idealisation of a physical spectral distribution concentrated in a narrow vicinity of λ_j .

Under the ansatz (5.6) the integral equation (5.6) reduces to a system of two algebraic equations for $s(\lambda_1)$, $s(\lambda_2)$ which are readily resolved to give

$$\begin{aligned} s(\lambda_1) &= s_0(\lambda_1) + \frac{\Delta_{1,2} w^{[2]} (s_0(\lambda_1) - s_0(\lambda_1))}{1 - (\Delta_{1,2} w^{[2]} + \Delta_{2,1} w^{[1]})}, \\ s(\lambda_2) &= s_0(\lambda_2) - \frac{\Delta_{2,1} w^{[1]} (s_0(\lambda_1) - s_0(\lambda_2))}{1 - (\Delta_{1,2} w^{[2]} + \Delta_{2,1} w^{[1]})}, \end{aligned} \quad (5.7)$$

where $\Delta_{j,k} = \Delta(\lambda_j, \lambda_k)$. In particular, we are interested in an even simpler setting, where a single ‘‘test’’ breather with parameter $\lambda = \lambda_1$ interacts with a one-component breather described by a DOS centred at $\lambda = \lambda_2$. Such a configuration is achieved by considering the limit $w_1 \rightarrow 0$ in (5.6), which that leads to

$$\begin{aligned} s(\lambda_1) &= \frac{s_0(\lambda_1) - \Delta_{1,2} w_2 s_0(\lambda_2)}{1 - \Delta_{1,2} w_2}, \\ s(\lambda_2) &= s_0(\lambda_2). \end{aligned} \quad (5.8)$$

The work presented in this Chapter aims to numerically verify the analytical result (5.8) for three different families of one-component breather gases: the Kuznetsov-Ma BG (KMBGs) characterised by $\lambda_2 = i\alpha$ with $\alpha > q$, the Akhmediev BG (ABGs) characterised by $\lambda_2 = i\alpha$ with $\alpha < q$, and the Peregrine BG (PBGs) characterised by $\lambda_2 = iq$ (without loss of generality the amplitude q of the plane wave background can be set equal to unity). The elementary components of the considered gases correspond, respectively, to KM, AB and PS breather solutions of the fNLSE.

The numerical verification of these results has required the implementation of a special algorithm to generate a random N -breather breather solution with N large. The algorithm employs the Darboux transform that has been extensively used as an effective method to generate high-order breather solutions of the fNLSE [28, 61, 147, 150, 151]. This method relies on a recursive scheme

where a known “seed solution” of the fNLSE is adopted as building block to generate higher-order solutions. The seeding solution for the generation of higher-order breather solutions is the plane wave with unitary amplitude, i.e. $u_0(x, t) = e^{2it}$. Then, given the set scattering data $\sigma_j = \{\lambda_j, c_j(x_j, t_j)\}$ with the norming constant c_j depending on the real t_j and x_j , the n -order solution $u_n(x, t)$ can be recursively generated using:

$$u_{n+1} = u_n + \frac{2(\lambda_n^* - \lambda_n)s_n r_n}{|r_n|^2 + |s_n|^2}, \quad (5.9)$$

where r_n and s_n are obtain by a recursive formula with $r_1(\sigma)$ and $s_1(\sigma)$ defined by the seed solution.

The practical numerical implementation of the Darboux algorithm can suffer from accuracy limitations. Standard computer simulations (double precision, 16 digit) fail to correctly generate higher-order ($N \gtrsim 5$) breather solution. To overcome this limitation we implemented a multiple precision library that allows to preform high-precision arithmetic. This strategy is analogous to the one implemented in [149] to realise strongly interacting soliton gas solution of the fNLSE. The implementation of this library enables the synthesis of N -breather solution up to order $N \sim 50$.

In practice, the spectral portrait used to generate the BGs consist of the branch cut and a set of $N = 50$ discrete spectral points randomly positioned in a small square area of width $\delta = 10^{-4}$ centred around λ_2 . The randomness of the gas is then achieved by uniformly distributing x_j in some in interval centred at x_0 . An additional spectral point $\lambda = \lambda_1$ corresponding to the test TW breather propagating through the gas is add to the spectral portrait. It is important to remark that the algorithm is adopted also to generate the time evolution of the breather gas. The solutions generated are unstable and the direct numerical solution of the fNLSE would lead to the development of the MI. For this reason, the spatio-temporal dynamics of the solution is obtained by generating the BG at different times t_j .

With this configuration, to verify the analytical predictions from the spectral theory (5.8), a series of numerical simulation have been performed for the different families of breather gases and different values of the spectral parameters λ_1 and λ_2 for the trial breather and the one-component breather gas respectively.

5.2 Summary of Results and Outlook

Employing a Darboux transform scheme we have implemented a numerical algorithm for the spectral synthesis of breather gas solution of the fNLSE. Adopting an high-precision library we overcome the limitations on the number of component of the gas reaching and we were able to generate higher-order breather solution with order up to $N \sim 50$. The numerical algorithm has been used to synthesise three different families of one-component breather gas and furthermore, to verify some of the analytical predictions of spectral kinetic theory [53].

In this work, using the algorithm developed, we investigate the propagation of a generic test TW breather through the different type of gases: AB, KM and PS. In particular, we test the theoretical prediction (5.8) for the effective velocity of the trial breather propagation through a BG. In all cases considered the results of the numerical simulations demonstrated an excellent agreement with the predicted effective mean velocity providing a convincing evidence of the efficacy of the spectral kinetic theory.

The quantitative verification of the spectral kinetic theory of breather gases realised in this work represents an important step in the effort to better understand properties of integrable turbulence.






The results of the project appear in:

- **G. Roberti**, G. El, A. Tovbis, F. Copie, P. Suret and S. Randoux “Numerical spectral synthesis of breather gas for the focusing nonlinear Schrödinger equation”, *Phys. Rev. E*, 103:042205, Apr 2021

Suggested by the results reported in this work we identify two major direction of future research:

- (i) Application of the numerical synthesis algorithm developed as a central tool for the controlled experimental generation of BGs. The possibility of this future development is suggested by the recently reported realisation of fNLSE soliton gas in the hydrodynamics setting [52].
- (ii) Verification of other results of the spectral theory of BGs and the study of the properties of localisation in space and time of fNLSE breather solutions of very high order.

Numerical spectral synthesis of breather gas for the focusing nonlinear Schrödinger equation

Giacomo Roberti ¹, Gennady El ¹, Alexander Tovbis,² François Copie ³, Pierre Suret ³, and Stéphane Randoux ^{3,*}

¹*Department of Mathematics, Physics and Electrical Engineering, Northumbria University, Newcastle upon Tyne NE1 8ST, United Kingdom*

²*Department of Mathematics, University of Central Florida, Orlando, Florida 32816, USA*

³*Univ. Lille, CNRS, UMR 8523 PhLAM Physique des Lasers Atomes et Molécules, F-59 000 Lille, France*



(Received 15 January 2021; accepted 16 March 2021; published 9 April 2021)

We numerically realize a breather gas for the focusing nonlinear Schrödinger equation. This is done by building a random ensemble of $N \sim 50$ breathers via the Darboux transform recursive scheme in high-precision arithmetics. Three types of breather gases are synthesized according to the three prototypical spectral configurations corresponding the Akhmediev, Kuznetsov-Ma, and Peregrine breathers as elementary quasiparticles of the respective gases. The interaction properties of the constructed breather gases are investigated by propagating through them a “trial” generic (Tajiri-Watanabe) breather and comparing the mean propagation velocity with the predictions of the recently developed spectral kinetic theory [El and Tovbis, *Phys. Rev. E* **101**, 052207 (2020)].

DOI: [10.1103/PhysRevE.103.042205](https://doi.org/10.1103/PhysRevE.103.042205)

I. INTRODUCTION

The study of nonlinear random waves in physical systems well described at leading order by the so-called integrable equations, such as the Korteweg–de Vries (KdV) or nonlinear Schrödinger (NLS) equations, has recently become the topic of intense research in several areas of nonlinear physics, notably in oceanography and nonlinear optics. This interest is motivated by the complexity of many natural or experimentally observed nonlinear wave phenomena often requiring a statistical description even though the underlying physical model is in principle amenable to the well-established mathematical techniques of integrable system theory such as the inverse scattering transform (IST) or finite-gap theory [1]. An intriguing interplay between integrability and randomness in such systems is nowadays associated with the concept of *integrable turbulence* introduced by Zakharov in [2]. The integrable turbulence framework is particularly pertinent to the description of modulationally unstable systems whose solutions, under the effect of random noise, can exhibit highly complex spatiotemporal dynamics that is adequately described in terms of turbulence theory concepts, such as the distribution functions, ensemble averages, and correlations.

Solitons and breathers are the elementary quasiparticles of nonlinear wave fields in integrable systems which can form ordered coherent structures such as modulated soliton trains and dispersive shock waves [3,4], superregular breathers [5,6], or breather molecules [7]. Furthermore, solitons and breathers can form *irregular* structures or statistical ensembles that can be viewed as soliton and breather gases. The nonlinear wave field in such integrable gases represents a particular case of integrable turbulence [2,8–13]. The observations of soliton and breather gases in the ocean have been reported in Refs. [14–17]. Recent laboratory experiments on

the generation of shallow-water and deep-water soliton gases were reported in Refs. [18,19], respectively. It has also been demonstrated that the soliton gas dynamics in the focusing NLS equation provides a remarkably good description of the statistical properties of the nonlinear stage of spontaneous modulational instability [20].

An analytical description of soliton gases was initiated by Zakharov in Ref. [21], where a spectral kinetic equation for KdV solitons was derived using an IST-based phenomenological procedure of computing an effective adjustment to a soliton’s velocity in a *rarefied* gas due to its collisions with other solitons, accompanied by appropriate phase shifts. Zakharov’s kinetic equation for KdV soliton has been generalized to the case of a *dense gas* in Ref. [22] using the spectral finite-gap theory. Within this theory, a uniform (equilibrium) soliton gas is modeled by a special infinite-phase thermodynamic-type limit of finite-gap KdV solutions. The kinetic description of the nonequilibrium soliton gas is then enabled by considering the same thermodynamic limit for the associated modulation (Whitham) equations. The resulting kinetic equation describes the evolution of the density of states defined as the density function in the spectral (IST) phase plane of soliton gas. The spectral construction of the KdV soliton gas in Ref. [22] was generalized to the soliton gas of the focusing NLS equation (NLSE) in Refs. [23,24]. The latter work [24] provides also the spectral kinetic description of a breather gas (BG), which is the main subject of the present work.

An isolated generic breather can be broadly viewed as a soliton on the plane-wave (or finite) background. The one-dimensional (1D) NLSE supports a large family of breather solutions that have attracted particular interest due to their explicit analytic nature and the potential for modeling the rogue wave events in the ocean and in nonlinear optical fibers [25–29]. Three types of breathers, namely, the Akhmediev breather (AB), the Kuznetsov-Ma (KM) breather, and the Peregrine soliton (PS) have aroused significant research

*stephane.randoux@univ-lille.fr

interest (see [30–35] and references therein). The AB, KM breather, and PS represent special cases of a generic breather called the Tajiri-Watanabe (TW) breather [36]. The simplest example of a breather gas can be viewed as an infinite random ensemble of TW breathers [24]. By manipulating the spectral parameters, the TW breather gas can be reduced to the AB, KM, and PS gases as well as to the fundamental soliton gas. The latter is achieved by vanishing the plane-wave background of the TW breather gas [24].

The present paper has two goals: (i) numerical realization of a breather gas and (ii) verification of the spectral theory of a breather gas developed in Ref. [24]. Numerical realization of a breather gas as a large ensemble of TW breathers with prescribed parameters represents a challenging problem. Numerical methods for the construction of breather solutions of the 1D NLSE suffer from accuracy problems that prevent the numerical synthesis of breathers of order $N \gtrsim 5$ [37,38]. In the context of soliton gases, this latter difficulty has been resolved recently by Gelash and Agafontsev [39] via the application of the so-called dressing method combined with high-precision numerical computations. In this paper we extend the algorithm of [39] to numerically realize various breather gases and verify some predictions of the spectral kinetic theory of [24]. In particular, we demonstrate that random ensembles of $N \sim 50$ breathers can be built via the Darboux transform recursive scheme in high-precision arithmetics. This represents an improvement of an order of magnitude compared to the results reported in previous numerical works. In addition, we show that the construction method can be used to provide evidence of the space-time evolution of the generated breather gases. This feature cannot be achieved by using direct numerical simulations of the 1D NLSE due to the inevitable presence of modulational instability that quickly disintegrates the plane-wave background.

The paper is organized as follows. In Sec. II we present the algorithm of the spectral synthesis of a breather gas using the Darboux transform. This algorithm is then realized numerically using the high-precision arithmetics. In Sec. III we numerically study the interactions in breather gases and compare the results of the numerical simulations with the theoretical predictions of the breather gas kinetic theory of Ref. [24]. Specifically, we consider the propagation of the “trial” breather through a homogeneous breather gas for three prototypical configurations: Akhmediev, Kuznetsov-Ma, and Peregrine gases. The study of interaction in the gas of Akhmediev breathers has revealed some special features that have required further development of the theory of Ref. [24]. The Appendix provides the identification of the interaction kernel in the breather gas with the position shift formula in two-breather collisions, obtained in earlier works.

II. NONLINEAR SPECTRAL SYNTHESIS OF BREATHER GASES

A. Overview of soliton and breather ensembles in the 1D NLSE

We consider the integrable 1D NLSE in the form

$$i\psi_t + \psi_{xx} + 2|\psi|^2\psi = 0, \quad (1)$$

where $\psi(x, t)$ represents the complex envelope of the wave field that evolves in space x and time t . In the IST method,

the 1D NLSE (1) is represented as a compatibility condition of two linear equations [1,40]

$$\Phi_x = \begin{pmatrix} -i\lambda & \psi \\ -\psi^* & i\lambda \end{pmatrix} \Phi, \quad (2)$$

$$\Phi_t = \begin{pmatrix} -2i\lambda^2 + i|\psi|^2 & i\psi_x + 2\lambda\psi \\ i\psi_x^* - 2\lambda\psi^* & 2i\lambda^2 - i|\psi|^2 \end{pmatrix} \Phi, \quad (3)$$

where λ is a (time-independent) complex spectral parameter and $\Phi(x, t, \lambda) = [r(x, t, \lambda), s(x, t, \lambda)]^T$ is a column vector. The spatial linear operator (2) and the temporal linear operator (3) form the Lax pair of Eq. (1). For a given potential $\psi(x, t)$ the problem of finding the scattering data $\sigma[\psi]$ (also sometimes called the IST spectrum) and the corresponding scattering solution Φ specified by the spatial equation (2) is called the Zakharov-Shabat (ZS) scattering problem [41]. The ZS scattering problem is formally analogous to calculating the Fourier coefficients in the Fourier theory of linear systems; hence the term nonlinear Fourier transform is often used in the context of telecommunication system research, particularly in the context of periodic boundary conditions [42–44].

For spatially localized potentials ψ such that $\psi(x, t) \rightarrow 0$ as $|x| \rightarrow \infty$, the complex eigenvalues λ are generally presented by a finite number of discrete points with $\text{Im}(\lambda) \neq 0$ (discrete spectrum) and the real line $\lambda \in \mathbb{R}$ (continuous spectrum). The scattering data $\sigma(\psi)$ consist of a set of N discrete eigenvalues λ_n ($n = 1, \dots, N$), a set of N norming constants C_n for each λ_n , and the so-called reflection coefficient $\rho(\xi)$,

$$\sigma(\psi) = \{\rho(\xi); \lambda_n, C_n\}, \quad (4)$$

where $\xi \in \mathbb{R}$ denotes the continuous spectrum component. In this setting where the wave field ψ exists on a zero background, the discrete part of the IST spectrum is related to the soliton content of the wave field whereas the continuous part of the IST spectrum is related to the nonlinear dispersive radiation [41].

A special class of (reflectionless) solutions of Eq. (1), the N -soliton solutions (NSSs), exhibits only a discrete spectrum [$\rho(\xi) = 0$] consisting of N complex-valued eigenvalues λ_n , $n = 1, \dots, N$, and N associated complex-valued norming constants. The IST formalism has been extensively applied to examine the processes of interaction, collision, and synchronization in NSSs (see, e.g., Refs. [41,45]). The numerical synthesis of NSSs can be achieved in standard computer simulations (double precision, 16 digits) up to $N \sim 10$ [39]. On the other hand, the numerical synthesis of NSSs with N large represents a challenging problem that has been resolved only recently [39]. Combining the so-called dressing method and numerical calculations made using high numerical precision (a 100-digit precision is typically necessary for the synthesis of NSSs with $N \sim 100$), the numerical synthesis of soliton gases (SGs), i.e., large ensembles of NSSs characterized by a given spectral distribution, has been demonstrated in Ref. [39]. The opportunity to synthesize numerically large soliton ensembles has opened the way to the experimental generation of strongly nonlinear wave fields with a pure solitonic content. In particular, recent experiments made in a one-dimensional water tank with deep-water surface gravity waves have revealed that the controlled synthesis of dense SGs can be achieved in hydrodynamics [19]. Moreover, it also

has been recently shown that the so-called bound-state SGs provide a model that describes well the nonlinear stage of the noise-induced modulation instability [20].

In addition to the soliton solutions existing on a zero background, the focusing NLS equation (1) admits a large variety of solutions existing on a nonzero (plane-wave) background. The IST theory for the focusing nonlinear Schrödinger equation with nonzero boundary conditions (NZBCs) at infinity has been reported in Refs. [46–48]. As in the IST with zero boundary conditions, the scattering data $\sigma[\psi]$ in the IST with NZBCs consist of a set of N discrete complex-valued eigenvalues λ_n , a set of N associated norming constants C_n , and the reflection coefficient $\rho(\lambda)$. In the IST with NZBCs, the continuous spectrum does not exist on the real axis \mathbb{R} but on $\mathbb{R} \cup [-iq_0, iq_0]$, where $q_0 > 0$ represents the amplitude of the plane-wave background [46,47].

The focusing NLS equation with NZBCs possesses a rich family of purely solitonic solutions [reflectionless potentials, $\rho(\lambda) = 0$] named breathers or sometimes solitons on a finite background. The generic “elementary” breather parametrized by one single complex-valued eigenvalue ($N = 1$) in the framework of the IST with NZBCs is the so-called Tajiri-Watanabe breather [36]. This elementary solution reduces under certain limits to the solutions found over the years by Kuznetsov [30], Ma [48], Peregrine [31], and Akhmediev [32]. Using the dressing method, Zakharov and Gelash constructed a class of two-soliton solutions on a finite background, termed superregular breathers and corresponding to small initial perturbations of a constant background [49]. This was generalized to several pairs of breathers in Refs. [5,50]. Note that most of these breather solutions of Eq. (1) have been experimentally realized in hydrodynamics and in optics [6,7,33,34,51–56] but also recently with matter waves [57].

B. Darboux transform-based synthesis of breather gases

The recent interest in studying the breather solutions of various kinds has been fueled by rogue-wave research (see, e.g., [58] and references therein). The prototypical rogue-wave solutions represent coherent structures of large amplitude, strongly localized in both space and time, on an otherwise quiescent background [25,27,38,59–65]. In this context the Darboux transform has been extensively used as a reliable method to generate higher-order breather solutions of Eq. (1), i.e., reflectionless solutions of the focusing 1D NLSE with NZBCs [37,66–69]. Note that the Darboux transform is now also used in the context of nonlinear eigenvalue communication to build ordered soliton ensembles used to carry out the transmission of information in fiber optic communication links [43,44,70].

The Darboux method is a recursive transformation scheme where a “seeding solution” of the focusing 1D NLSE is used as a building block for the construction of a higher-order solution through the addition of one discrete eigenvalue. Here we give a brief review of the Darboux transform method used for the generation of higher-order breathers. We largely follow the exposition given in Refs. [38,71], but other important references where this method is described and used are Refs. [37,66–69].

In the IST for the 1D NLSE with NZBCs, the seeding solution commonly used at the first step of the recursive process of constructing a higher-order breather solution is the plane-wave solution of Eq. (1) with unit amplitude, i.e., $\psi_0(x, t) = e^{2it}$. The first-order (Tajiri-Watanabe) breather $\psi_1(x, t)$ parametrized by the complex eigenvalue λ_1 is obtained by

$$\psi_1(x, t) = \psi_0(x, t) + \frac{2(\lambda_1^* - \lambda_1)s_{1,1}r_{1,1}^*}{|r_{1,1}|^2 + |s_{1,1}|^2}. \quad (5)$$

The functions $r_{1,1}(x, t)$ and $s_{1,1}(x, t)$ in Eq. (5) are obtained by setting $j = 1$ in the expressions

$$\begin{aligned} r_{1,j}(x, t) &= 2ie^{-it} \sin(A_j), \\ s_{1,j}(x, t) &= 2e^{it} \cos(B_j), \end{aligned} \quad (6)$$

where A_j and B_j are given by

$$\begin{aligned} A_j &= \frac{1}{2} \left[\arccos\left(\frac{\kappa_j}{2}\right) + (x - x_j)\kappa_j - \frac{\pi}{2} \right] + (t - t_j)\kappa_j\lambda_j, \\ B_j &= \frac{1}{2} \left[-\arccos\left(\frac{\kappa_j}{2}\right) + (x - x_j)\kappa_j - \frac{\pi}{2} \right] + (t - t_j)\kappa_j\lambda_j, \end{aligned} \quad (7)$$

with $\kappa_j = 2\sqrt{1 + \lambda_j^2}$. The parameters (x_j, t_j) are connected with the complex norming constants C_j in the IST with NZBCs [37]. The first-order breather $\psi_1(x, t)$ is parametrized by the complex eigenvalue λ_1 and by the two real parameters x_1 and t_1 . Once the first-order breather ψ_1 is constructed using Eqs. (5)–(7), breather solutions of order $n \geq 2$ can be recursively generated by using

$$\psi_n(x, t) = \psi_{n-1}(x, t) + \frac{2(\lambda_n^* - \lambda_n)s_{n,1}r_{n,1}^*}{|r_{n,1}|^2 + |s_{n,1}|^2}, \quad (8)$$

with

$$\begin{aligned} r_{n,p} &= [(\lambda_{n-1}^* - \lambda_{n-1})s_{n-1,1}^*r_{n-1,1}s_{n-1,p+1} \\ &\quad + (\lambda_{p+n-1} - \lambda_{n-1})|r_{n-1,1}|^2r_{n-1,p+1} \\ &\quad + (\lambda_{p+n-1} - \lambda_{n-1}^*)|s_{n-1,1}|^2r_{n-1,p+1}] \\ &\quad \times (|r_{n-1,1}|^2 + |s_{n-1,1}|^2)^{-1}, \end{aligned} \quad (9)$$

$$\begin{aligned} s_{n,p} &= [(\lambda_{n-1}^* - \lambda_{n-1})s_{n-1,1}r_{n-1,1}^*r_{n-1,p+1} \\ &\quad + (\lambda_{p+n-1} - \lambda_{n-1})|s_{n-1,1}|^2s_{n-1,p+1} \\ &\quad + (\lambda_{p+n-1} - \lambda_{n-1}^*)|r_{n-1,1}|^2s_{n-1,p+1}] \\ &\quad \times (|r_{n-1,1}|^2 + |s_{n-1,1}|^2)^{-1}. \end{aligned} \quad (10)$$

Despite the efficiency of the Darboux method for the construction of high-order breather solutions of Eq. (1), its practical implementation in numerics suffers from the same type of issues as those previously mentioned for the numerical construction of NSSs. As noted in Refs. [37,38], problems of numerical accuracy may prevent the numerical synthesis of breathers of order $N \gtrsim 5$. In this paper we show that this limit can be overcome by the implementation of the same strategy as the one used to build NSSs with N large [39]. Implementing the Darboux recursive scheme in high-precision arithmetics using the BOOST C++ multiple precision library, we show that breather solutions of Eq. (1)

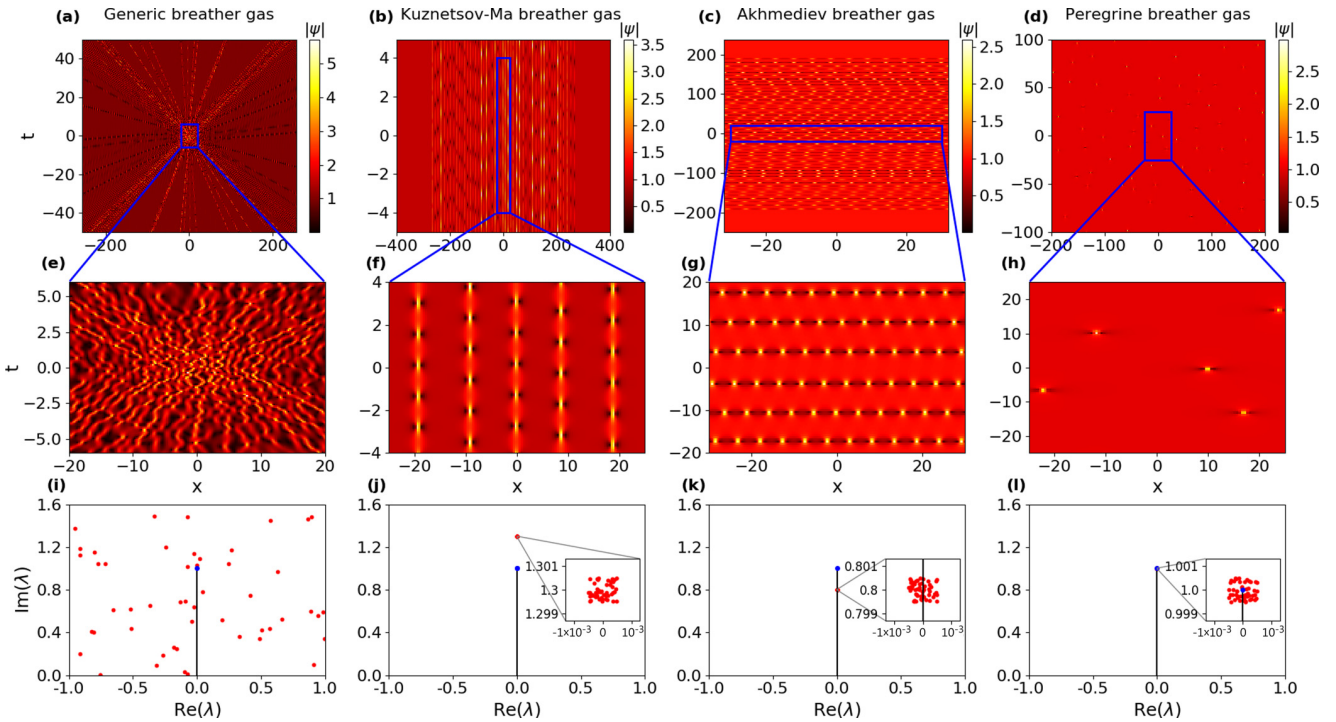


FIG. 1. Numerical synthesis of (a), (e), and (i) a generic BG (column 1) and of three single-component BGs (columns 2–4): (b), (f), and (j) a KMBG; (c), (g), and (k) an ABG; and (d), (h), and (l) a PS BG. The four BGs are parametrized by $N = 50$ complex eigenvalues λ_n [see (i)–(l)]. (a)–(d) Space-time evolution of the BGs. (e)–(h) Enlarged view of some restricted region of the (x, t) plane. (i)–(l) Spectral portraits of each BG with the vertical line between 0 and $+i$ being the branch cut associated with the plane-wave background. Each point in the upper complex plane in (i)–(l) represents a discrete eigenvalue in the IST problem with NZBCs. The eigenvalues parametrizing the single-component BGs are densely placed in a small square region which is centered around a point λ_0 of the imaginary vertical axis and which is greatly enlarged in the insets shown in (j)–(l). The x_j are uniformly distributed in the range $[-1, 1]$ for (a) the generic gas and (d) the Peregrine gas, while they are uniformly distributed in the range $[-32, 32]$ for (b) the KM gas and (c) the AB gas.

can be synthesized up to order $N \sim 50$. As will be shown in detail in Sec. III, this provides a numerical tool that enables one to verify the results of the spectral theory of breather gases recently developed in Ref. [24].

Figure 1(a) shows the space-time evolution of a generic BG, i.e., a breather solution of Eq. (1) of order $N = 50$ with random spectral characteristics. The amplitude of the plane-wave background is unity ($q_0 = |\psi_0| = 1$) and the 50 complex-valued eigenvalues λ_j ($j = 1-50$) parametrizing the BG are randomly distributed within some rectangular region of the upper complex plane [see Fig. 1(i)]. The parameters t_j are set equal to zero ($t_j = 0 \forall j$) and the randomness of the gas is achieved by uniformly distributing the x_j in some interval centered around $x_0 = 0$. Note that the vertical line between 0 and $+i$ in Fig. 1(i) represents the so-called branch cut associated with the plane-wave background in the IST formalism of the 1D NLSE with a nonzero background (see, e.g., [24,35,46,47]). Figure 1(a) reveals that the space-time dynamics of the generic BG synthesized in numerical simulations is highly complicated. In particular, breathers cannot be individualized due to their strong overlap and interaction. Note also that the maximum amplitude reached locally in space and time by the incoherent breather ensemble of Fig. 1(a) does not exceed ~ 5.5 , which demonstrates that the multiple breathers are far from a synchronization state that would eventually produce isolated rogue waves of large amplitude [72,73].

We emphasize that BGs shown in the space-time plots of Fig. 1 are not obtained from a numerical simulation of Eq. (1). Taking a BG generated at a given time t_0 using the Darboux method and using this wave field as the initial condition in a numerical simulation of Eq. (1), we observe that modulation instability quickly disintegrates the plane-wave background by amplifying the numerical noise inherent to any pseudospectral (split-step-like) method commonly used for the numerical integration of the 1D NLSE. On the other hand, space-time plots reported in Fig. 1 are obtained from a pure spectral (IST) construction based on the Darboux recursive method which has been implemented in computer simulations made with high numerical precision. Starting from an ensemble of N complex eigenvalues λ_j and N coordinates (x_j, t_j) , the BG is synthesized at time t using the Darboux machinery [Eqs. (5)–(10)]. A 100-digit precision is typically necessary to synthesize a BG parametrized by an ensemble of $N \sim 50$ eigenvalues. The space-time plots shown in Fig. 1 are obtained by reiterating the same synthesis at different values of time t . Our numerically synthesized solutions can be validated by computing the discrete Zakharov-Shabat spectrum (using, for instance, the Fourier collocation method [35,41]) at different moments of time to verify that the obtained discrete eigenvalues are indeed the same as the ones specified for the construction of the BG under consideration.

The central concept in the theory of SGs and BGs is the density of states (DOS) [74] which represents the distribution function $u(\lambda, x, t)$ in the spectral phase space. In the context of the 1D NLSE (1), the DOS $u(\lambda, x, t)$, where $\lambda = \beta + i\gamma$, is defined such that $ud\beta d\gamma dx$ is the number of breather states with complex spectral parameter $\lambda \in [\beta, \beta + d\beta] \times [\gamma, \gamma + d\gamma]$ contained in a portion of the BG within a spatial interval $[x, x + dx]$ at time t .

One-component BGs have been defined in Ref. [24] as being characterized by a DOS in the form of the Dirac δ distribution, i.e., $u(\lambda) = w\delta(\lambda - \lambda_0)$, where $w > 0$ represents the mass of the δ distribution which is centered around one specific point λ_0 in the complex spectral plane. Figures 1(b)–1(d) and 1(f)–1(h) display the space-time evolutions together with the spectral portraits [Figs. 1(j)–1(l)] typifying some one-component BGs of particular interest.

For the Kuznetsov-Ma BG (KMBG), the spectral portrait consists of the branch cut (associated with the plane-wave background of unity amplitude) and a dense set of $N = 50$ spectral points randomly placed in a small square region of width $\delta = 10^{-3}$ centered around $\lambda_0 = 1.3i$, as shown in Fig. 1(j). Figure 1(b) shows that the KMBG is a dense ensemble of individual KM breathers, all having a zero velocity in the (x, t) plane. In contrast to Fig. 1(a), each KM breather inside the BG can be individualized and the BG follows the same periodic time evolution where the time period is fully determined by $\text{Im}(\lambda_0)$. The randomness in the one-component KMBG can be seen from the random distance between individual KM breathers and their random initial phase [see Fig. 1(f)].

The Akhmediev BG (ABG) is characterized by the same distribution of the spectrum λ as the KMBG except that the point λ_0 around which the multiple discrete eigenvalues are accumulated is now placed inside the branch cut associated with the plane-wave background [see Fig. 1(k)], where $\lambda_0 = +0.8i$. As a result, the ABG is more naturally characterized by the *spectral flux density*, the temporal counterpart of the DOS. As shown in Fig. 1(c), the ABG consists of a random series of individual ABs having identical spatial period, which is fully determined by $\text{Im}(\lambda_0)$. Similarly to the KMBG, the randomness in the one-component ABG can be seen from the random time separation between individual Akhmediev breathers and their random relative phases [see Fig. 1(g)].

It must be mentioned that the density (spatial or temporal) of the AB or KM breather gases cannot be made arbitrarily large: There is a configuration termed breather condensate [24] corresponding to a critically dense breather gas, similar to a soliton condensate numerically realized in Ref. [20].

It is well known that the Peregrine breather can be obtained as the spatial and temporal infinite-period limits of Akhmediev and Kuznetsov-Ma breathers, respectively [68,71]. In the spectral (IST) domain, the Peregrine breather is obtained by placing the eigenvalue parametrizing a first-order breather solution of Eq. (1) exactly at the end point $+i$ of the branch cut associated with the plane-wave background of unit amplitude [35]. Following the same approach, the one-component Peregrine BG (PBG) is obtained by accumulating a large number of discrete eigenvalues in a small area surrounding the end point of the branch cut [see Fig. 1(l)]. As shown in Figs. 1(d) and 1(h), the PBG represents a collection of individual and

identical Peregrine breathers that are randomly positioned in space and time.

While the PG synthesized in our work represents a high-order breather solution of Eq. (1), this solution contrasts with the high-order breather solutions considered previously because it is intrinsically of a random nature. The localized breather solutions of high order that have been considered in previous works (see, e.g., Refs. [38,62,64,71]) have been arranged in regular patterns with well-organized geometrical shapes because they represented synchronized states having no degree of randomness. In contrast, in the construction plotted in Figs. 1(d) and 1(h), the parameters x_j are randomly and uniformly distributed over $[-1, +1]$, which implies that each individual Peregrine breather in the PG has a random position in the (x, t) plane. We also mention that the solitonic eigenvalues in our numerical construction are clustered (also randomly) in close proximity to the end points of the spectral branch cut, so the individual Peregrine solitons in the PG are realized in our synthesis approximately, with the accuracy determined by the closeness of the solitonic eigenvalues to the end points of the branch cut.

III. INTERACTIONS IN BREATHER GASES: COMPARISON BETWEEN NUMERICAL EXPERIMENTS AND SPECTRAL THEORY

The analytical theory of BGs was introduced and developed in Ref. [24]. It was shown that spatially nonhomogeneous BGs are described by a kinetic equation formed by a transport equation for the slowly varying DOS $u(\lambda, x, t)$ and the integral equation of state relating the gas velocity to the DOS. In this section we show that some predictions of the spectral theory of BGs can be verified in simulations involving BGs that have been numerically synthesized using the methodology described in Sec. II B. In Sec. III A we provide the key elements of spectral theory of BGs that are relevant for the comparison between theoretical and numerical results. In Sec. III B we examine the collision between one trial soliton and various single-component BGs.

A. Analytical results from the spectral theory of breather gases

The nonlinear spectral theory of SGs and BGs for the focusing 1D NLSE developed in Ref. [24] provides a full set of equations characterizing the macroscopic spectral dynamics in a spatially nonhomogeneous BG. An important result of the theory is the so-called equation of state which provides the mathematical expression of the modification of the mean velocity of a “tracer” breather due to its interaction with other breathers in the gas.

The group velocity [in the (x, t) plane] of a first-order (TW) breather parametrized by the complex eigenvalue $\lambda \equiv \eta$ (we will use in this section the latter notation for the spectral parameter to be consistent with notation of Ref. [24] and previous works on the spectral kinetic theory) is given by

$$s_0(\eta) = -2 \frac{\text{Im}[\eta R_0(\eta)]}{\text{Im}[R_0(\eta)]}, \quad (11)$$

where $R_0(z) = \sqrt{z^2 - \delta_0^2}$, with δ_0 the end point of the branch cut corresponding to the plane wave ($\delta_0 = i$ for the plane

wave of unit amplitude considered in all the numerical simulations reported in this paper). It is not difficult to see that, if $\eta \in i\mathbb{R} \setminus [-i, i]$ (KM breather), then $s_0(\eta) = 0$, while if $\eta \in (-i, i)$ (AB), then $s_0(\eta) = \pm\infty$ depending on the way the limit $\text{Re}(\eta) \rightarrow 0$ in Eq. (11) is taken (either from the left or right side of the branch cut).

As shown in Ref. [24], the equation of state of a BG reads

$$s(\eta) = s_0(\eta) + \int_{\Lambda^+} \Delta(\eta, \mu)[s(\eta) - s(\mu)]u(\mu)|d\mu|, \quad (12)$$

where Λ^+ is the two-dimensional compact support of the DOS $u(\eta)$ (defined earlier in Sec. II B) located in the upper half plane \mathbb{C}^+ of the complex spectral plane

$$\Delta(\eta, \mu) = \frac{1}{\text{Im}[R_0(\eta)]} \left[\ln \left| \frac{\mu - \bar{\eta}}{\mu - \eta} \right| + \ln \left| \frac{R_0(\eta)R_0(\mu) + \eta\mu - \delta_0^2}{R_0(\bar{\eta})R_0(\mu) + \bar{\eta}\mu - \delta_0^2} \right| \right]. \quad (13)$$

The integral term in Eq. (12) describes the modification of the tracer breather mean velocity in a gas due to its interaction with other breathers in the gas having a DOS specified by u . The spectral value η in Eq. (12) can be taken outside Λ^+ ; in that case formula (12) describes the mean velocity of a trial TW breather with the eigenvalue η propagating through a breather gas with the DOS supported Λ^+ .

The interaction kernel $\Delta(\eta, \mu)$ given by Eq. (13) describes the position shift arising in a two-breather interaction. We note that the two-breather interactions have been studied in Refs. [50,75] using the IST, where different forms of the expressions for the position shift were obtained. In the Appendix we demonstrate the equivalence of the kernel $\Delta(\eta, \mu)$ given by (13) to the position shift formula obtained for two-breather collisions in previous works.

For a two-component breather gas, the DOS is a superposition of two Dirac δ functions centered at the complex spectral points $\eta^{[j]}$ ($j = 1, 2$),

$$u(\eta) = \sum_{j=1}^2 w^{[j]} \delta(\eta - \eta^{[j]}), \quad (14)$$

where $w^{[j]}$ are the weights of the components. For the DOS specified by Eq. (14), Eq. (12) yields the linear system for the gas component velocities $s^{[j]} \equiv s(\eta^{[j]})$ ($j = 1, 2$),

$$\begin{aligned} s^{[1]} &= s_0^{[1]} + \frac{\Delta_{1,2} w^{[2]} (s_0^{[1]} - s_0^{[2]})}{1 - (\Delta_{1,2} w^{[2]} + \Delta_{2,1} w^{[1]})}, \\ s^{[2]} &= s_0^{[2]} - \frac{\Delta_{2,1} w^{[1]} (s_0^{[1]} - s_0^{[2]})}{1 - (\Delta_{1,2} w^{[2]} + \Delta_{2,1} w^{[1]})}, \end{aligned} \quad (15)$$

where $s_0^{[j]} \equiv s_0(\eta^{[j]})$ ($j = 1, 2$) and $\Delta_{j,k} = \Delta(\eta^{[j]}, \eta^{[k]})$.

In the numerical simulations presented in Sec. III B, we will consider an even simpler situation where a single trial breather parametrized by the eigenvalue $\eta^{[1]}$ interacts with a one-component breather gas having its spectral distribution centered in $\eta^{[2]}$. In such a limit $w^{[1]} \rightarrow 0$ and Eqs. (15) reduce

to

$$\begin{aligned} s^{[1]} &= \frac{s_0^{[1]} - \Delta_{1,2} w^{[2]} s_0^{[2]}}{1 - \Delta_{1,2} w^{[2]}}, \\ s^{[2]} &= s_0^{[2]}. \end{aligned} \quad (16)$$

The validity of Eqs. (16) in the context of the 1D NLSE dynamics (1) will be verified for the PBG, the KMBG, and the ABG in numerical simulations presented in Sec. III B. As a matter of fact, formula (16) can be obtained directly from Eq. (12) by setting $\eta = \eta^{[1]} \notin \Lambda^+$ (the trial breather eigenvalue), and using $u(\mu) = w^{[2]} \delta(\mu - \eta^{[2]})$, $s(\eta_2) = s_0^{[2]}$, where $\eta^{[2]} \in \Lambda^+$.

B. Interactions in one-component breather gases: Comparison between spectral theory and numerical simulations

In the numerical simulations presented in this section, a trial TW breather with the spectral parameter $\eta = \eta^{[1]}$ is propagated through various single-component BGs having their DOS defined by $u(\eta) = w^{[2]} \delta(\eta - \eta^{[2]})$. We define the spectral parameter $\eta^{[2]}$ as $\eta^{[2]} = \alpha i$, with $\alpha = 1$ for the PBG, $\alpha > 1$ for the KMBG, and $\alpha < 1$ for the ABG. Similar to Fig. 1, the spectral portrait of the considered BGs consists of the branch cut (associated with the plane-wave background of unity amplitude) and a cluster of $N = 50$ spectral points randomly placed in a small square region of width $\delta = 10^{-4}$ centered around $\eta^{[2]}$. The spectral parameter $\eta^{[1]}$ is chosen in such a way that $\text{Re}(\eta^{[1]}) > 0$, which implies that the free trial TW breather has a negative group velocity in the (x, t) plane [see Eq. (11)].

1. Interactions in the Peregrine breather gas

Figure 2 shows a trial Tajiri-Watanabe breather propagating through a PBG. We observe that the trial breather passes through the PBG without change in its group velocity. This confirms the theoretical result established in Ref. [24] that the propagation of a trial TW breather through a PBG is ballistic. This result can be understood at the qualitative level by the fact that the interaction cross section between the trial breather and the individual Peregrine breathers composing the gas is so weak that the propagation of the trial breather is unaffected by the PBG.

2. Interactions in the Kuznetsov-Ma breather gas

Figure 3 shows a trial TW breather propagating through a KMBG. In contrast to Fig. 2, the multiple interactions between the trial breather and the KM breathers composing the KMBG now significantly influence the propagation of the trial breather; see Figs. 3(a) and 3(b) for a comparison between the trajectory of the free Tajiri-Watanabe breather (white dashed lines) and the trajectory followed by the trial breather in the KMBG. As shown in Fig. 3(b), the trial breather acquires a significant space shift each time its trajectory intersects the trajectory of an individual KM breather composing the BG. At the macroscopic scale, this produces a velocity change of the trial breather inside the KMBG. This leads to a spatial shift ΔX in the position of the trial breather which is measurable when the trial breather emerges from the KMBG [see Fig. 3(a)].

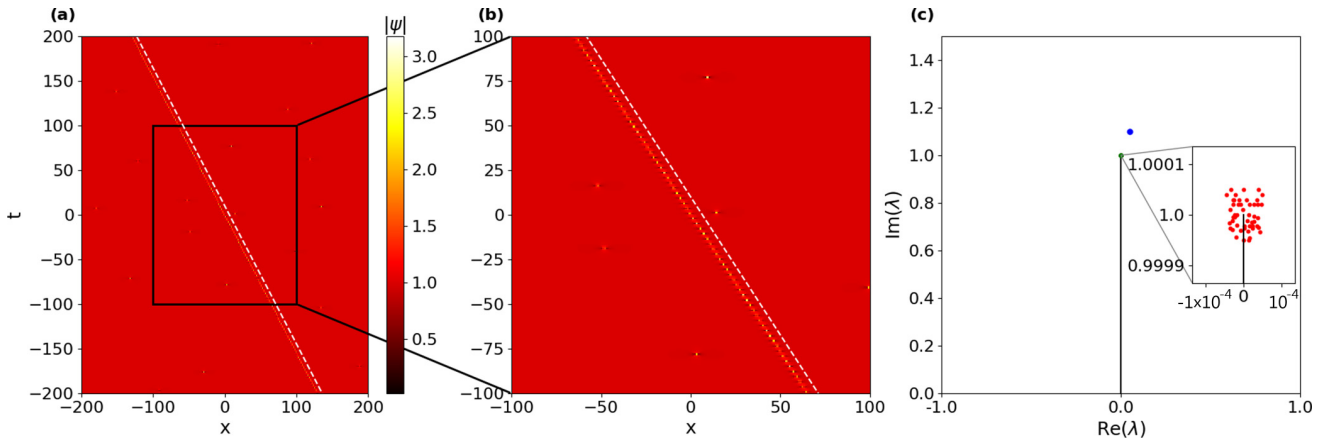


FIG. 2. (a) and (b) Propagation of a Tajiri-Watanabe breather with the spectral parameter $\eta^{[1]} = 0.05 + 1.1i$ inside a Peregrine BG. The space-time evolution shown in (b) represents an enlarged view of the one shown in (a). The white dashed line in (a) and (b) represents the trajectory of the “free” Tajiri-Watanabe breather propagating on a plane-wave background with a group velocity given by Eq. (11). (c) Spectral portrait associated with the numerical results shown in (a) and (b). The vertical line between 0 and $+i$ represents the branch cut associated with the plane-wave background and the blue point is the discrete eigenvalue $\eta^{[1]}$ associated with the Tajiri-Watanabe breather propagating in the PBG. The 50 spectral points characterizing the PBG are densely placed around $+i$ and they are shown in the inset plotted in (c).

For the KMBG, Eq. (16) simplifies to

$$s^{[1]} = \frac{s_0^{[1]}}{1 - \Delta_{1,2} w^{[2]}}, \quad (17)$$

given that $s_0^{[2]} = 0$. Equation (17) clearly shows that the group velocity of the trial Tajiri-Watanabe breather is increased by a factor $1/(1 - \Delta_{1,2} w^{[2]})$ due to the interaction with the KMBG.

Note that the space shift ΔX acquired by the trial breather as a result of propagation inside the KMBG simply represents the product of the number N of iterations (equivalently the number of breathers in the KMBG) and the elementary space shift $\Delta_{1,2}$ induced by each interaction: $\Delta X = N\Delta_{1,2}$. This provides an alternative and straightforward way to check the

validity of Eq. (17) which gives the group velocity of the trial breather inside the KMBG.

A set of numerical simulations with different values of the spectral parameters $\eta^{[1]}$ and $\eta^{[2]}$ has been made to check the validity of the spectral theory. Different realizations of the KMBG have been made and the value of $w^{[2]}$ is determined from numerical simulations as the ratio between the selected number N of breathers in the gas over the spatial extension L of the gas: $w^{[2]} = N/L$. As shown in Fig. 4, we observe full quantitative agreement between the numerical experiment and the predictions of the spectral theory.

3. Interactions in the Akhmediev breather gas

The case of the ABG is special and requires separate consideration, particularly because it was not considered in any

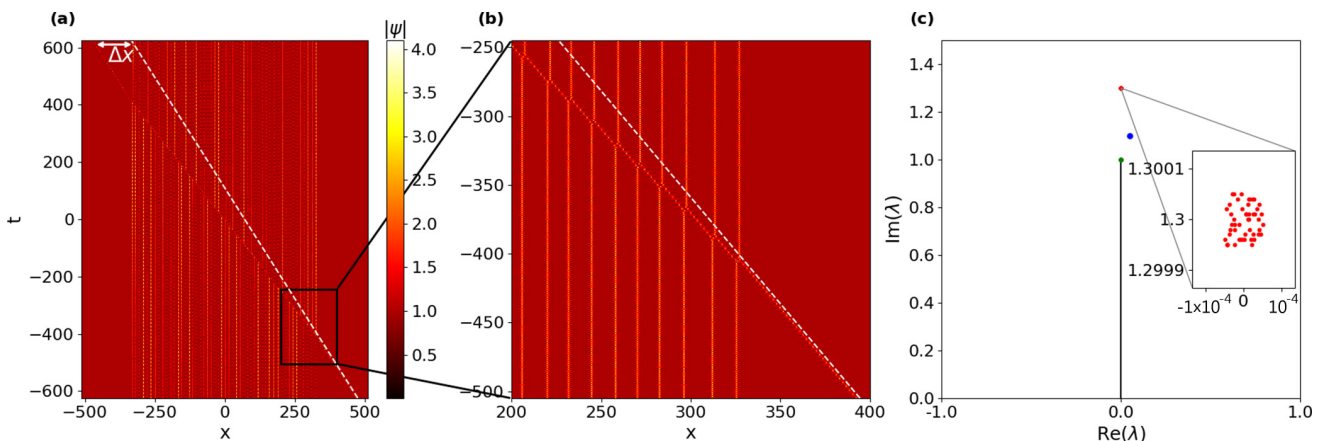


FIG. 3. (a) and (b) Propagation of a TW breather with the spectral parameter $\eta^{[1]} = 0.05 + 1.1i$ inside a Kuznetsov-Ma BG. The space-time evolution shown in (b) represents an enlarged view of the one shown in (a). The white dashed line in (a) and (b) represents the trajectory of the free TW breather propagating on a plane-wave background with a group velocity given by Eq. (11). (c) Spectral portrait associated with the numerical results shown in (a) and (b). The vertical line between 0 and $+i$ represents the branch cut associated with the plane-wave background and the blue point is the discrete eigenvalue $\eta^{[1]}$ associated with the TW breather propagating in the KMBG. The 50 spectral points characterizing the KMBG are densely placed around $\eta^{[2]} = 1.3i$ and they are shown in the inset plotted in (c).

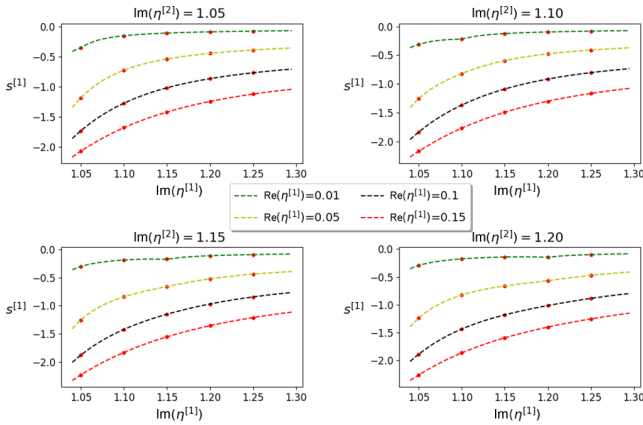


FIG. 4. Quantitative verification of the spectral theory of BGs introduced in Ref. [24]. A comparison is shown between numerics (red dots) and theory (dashed lines) for the effective velocity $s^{[1]}$ of a trial breather $\eta^{[1]}$ propagating in a KMBG $\eta^{[2]}$.

detail in Ref. [24]. The AB is a static object, not localized in space, so it is not immediately obvious how to identify the key quantities $u(\eta)$ and $s(\eta)$ for the ABG. A single AB is a limiting case of the TW breather where the soliton eigenvalue $\eta^{[2]}$ is placed within the branch cut $[0, i]$ in the upper half plane. The ABG is generally characterized by some distribution of soliton eigenvalues along the branch cut. Similar to the above consideration of the KMBG, we consider the ABG with soliton eigenvalues clustered around a given spectral point $\eta^{[2]}$ (and complex conjugate) to mimic a one-component gas.

As we have already mentioned in Sec. III A, the formula (11) for the group velocity of the TW breather implies $|s(\eta)| \rightarrow \infty$ as $\eta \rightarrow \eta^{[2]}$, which is consistent with the delocalized nature of the AB. On the other hand, it can be shown using the results of Ref. [24] that in the ABG limit the DOS

$u(\eta) \rightarrow 0$ while the spectral flux density function $v(\eta) = s(\eta)u(\eta) = O(1)$. This leads to the alternative form of the equation of state (12),

$$s(\eta) = s_0(\eta) + \int_{\Lambda^+} \Delta(\eta, \mu) \left[\frac{s(\eta)}{s(\mu)} - 1 \right] v(\mu) |d\mu|, \quad (18)$$

which is more suitable for the characterization of the ABG interactions. Equation (18) was obtained from (12) by substituting $u(\eta) = \frac{v(\eta)}{s(\eta)}$. Assuming Λ^+ to be a narrow region surrounding the branch cut $[0, i]$ and using $|s(\mu)| \gg 1$ for $\mu \in \Lambda^+$, Eq. (18) to leading order becomes

$$s(\eta) = s_0(\eta) - \int_{\Lambda^+} \Delta(\eta, \mu) v(\mu) |d\mu|. \quad (19)$$

Equation (19) describes the modification of the velocity of the TW breather with eigenvalue η propagating through the ABG characterized by the spectral flux density $v(\mu)$.

An important property of $\Delta(\eta, \mu)$ given by (13) is that

$$\Delta(\eta, \mu) + \Delta(\eta, -\bar{\mu}) = 0 \quad \text{when } \mu \in [0, i], \quad (20)$$

that is, when μ is on the branch cut $[0, i]$. The second variable η can take any value in the upper half plane. Equation (20) implies that $\Delta(\eta, \mu)$ takes opposite values on the opposite sides of the branch cut.

It can further be shown that in the case of a breather gas, whose spectral support Λ^+ is symmetric with respect to the branch cut $[0, i]$, the function $v(\eta)$ also takes opposite values on the opposite sides of $[0, i]$. Thus the speed of the ABG $s(\eta)$ from (18) *does not depend* on which side of the upper part of the branch cut $[0, i]$ the domain Λ^+ or its parts are situated.

Let us now consider a one-component ABG with the spectral flux density $v(\eta) = w^f \delta(\eta - \eta^{[2]})$, where $\eta^{[2]} \in [0, i]$ and w^f is a real constant weight. As a result, Eq. (19) assumes a simple form

$$s(\eta) = s_0(\eta) - w^f \Delta(\eta, \eta^{[2]}). \quad (21)$$

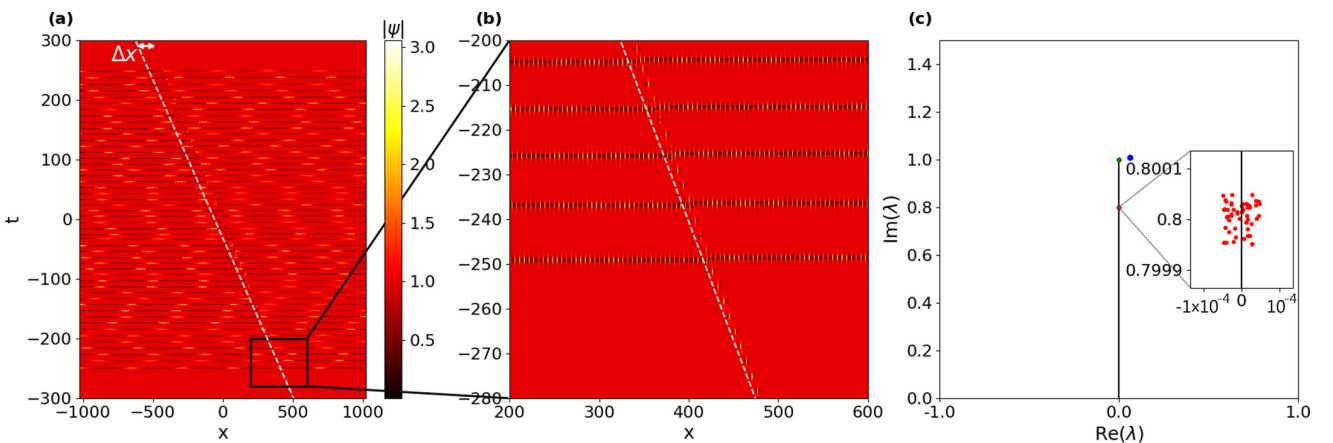


FIG. 5. (a) and (b) Propagation of a TW breather with the spectral parameter $\eta_1 = 0.06 + 1.01i$ inside an Akhmediev BG. The space-time evolution shown in (b) represents an enlarged view of the one shown in (a). The white dashed line in (a) and (b) represents the trajectory of the free TW breather propagating on a plane-wave background with a group velocity given by Eq. (11). (c) Spectral portrait associated with the numerical results shown in (a) and (b). The vertical line between 0 and $+i$ represents the branch cut associated with the plane-wave background and the blue point is the discrete eigenvalue η_1 associated with the TW breather propagating in the ABG. The 50 spectral points characterizing the KMBG are densely placed around $\eta^{[2]} = 0.8i$ and they are shown in the inset plotted in (c).

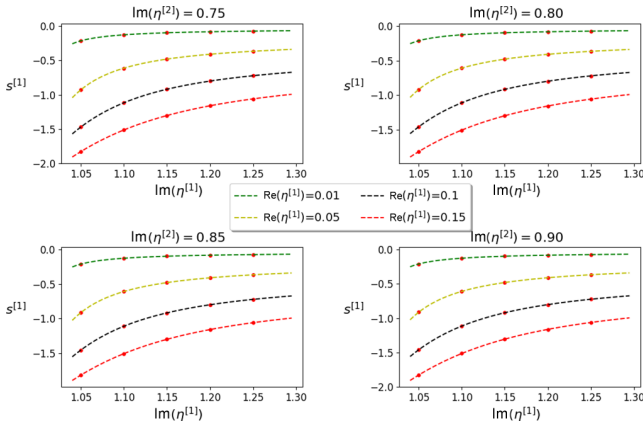


FIG. 6. Comparison between numerics (red dots) and theory (dashed lines) for the effective velocity $s^{[1]}$ of a trial TW breather $\eta^{[1]}$ propagating in an ABG $\eta^{[2]}$.

We note that the sign of w^t , as was explained above, depends on the side of $[0, i]$ but the sign of the product $w^t \Delta$ does not. Hence we have the general result $s(\eta) - s_0(\eta) < 0$ for the propagation of a trial breather through an ABG.

We note that formula (21) can be obtained directly from the basic result (16) by using $w^{[2]} \rightarrow 0$ and introducing $w^{[2],s_0^{[2]}} \equiv w^t$. This simple formal consideration, however, does not provide the important information about the sign of $w^t \Delta$.

Figure 5 shows a trial TW breather propagating through an ABG. Similar to Fig. 3, the propagation of the trial breather is significantly influenced by the multiple interactions with the ABs composing the ABG [see Figs. 5(a) and 5(b)]. One can see that, in contrast to the interaction of the trial TW breather with the KMBG, the group velocity of the trial TW breather is reduced in the interaction with the ABG, in agreement with Eq. (21). Indeed, the space shifts observed in Figs. 3(a) and 5(a) have opposite signs.

Similar to the KMBG interactions, a set of numerical simulations with different values of the spectral parameters $\eta^{[1]}$ and $\eta^{[2]}$ has been made to check the validity of Eq. (21). Different realizations of the ABG have been produced and the value of w^t was determined from numerical simulations as the ratio between the selected number N of ABs in the gas over the temporal extension T of the gas: $w^t = N/T$. As shown in Fig. 6, we observe full quantitative agreement between the numerical experiment and the predictions of the spectral theory.

IV. CONCLUSION

We have developed a numerical algorithm of the IST spectral synthesis of breather gases for the focusing 1D NLS equation. The algorithm is based on the recursive Darboux transform scheme realized in high-precision arithmetics. Using this algorithm, we have synthesized numerically three types of prototypical breather gases: the Akhmediev, Kuznetsov-Ma, and Peregrine gases.

Using the spectral algorithm developed, the interaction properties of breather gases, predicted by the kinetic theory of Ref. [24], have been tested by propagating through them a trial generic TW breather whose effective velocity is strongly

affected by the interaction with the gas. In all cases the theoretically predicted effective mean velocity of the trial breather propagating through a breather gas demonstrates excellent agreement with the results of the numerical simulations. The verification of the theory, despite the inevitable effects of modulational instability present in the 1D NLSE dynamics, has been made possible due to the whole numerical algorithm being based on the spectral construction rather than direct simulations of the 1D NLSE.

The quantitative verification of the kinetic theory of breather gases undertaken in this paper is an important step towards a better understanding of this type of turbulent motion in integrable systems. We also believe that the ability to synthesize numerically BGs represents an important step towards the controlled laboratory generation of BGs, possibly following an approach similar to the one recently reported for hydrodynamic SGs [19]. Finally, the possibility to generate numerically breather solutions of order $N \gtrsim 10$ paves the way for further works devoted to the investigation of the properties of localization in space and time of breather solutions of the 1D NLSE of very high order [38,50,73].

ACKNOWLEDGMENTS

This work was partially supported by the Agence Nationale de la Recherche through the I-SITE ULNE (Grant No. ANR-16-IDEX-0004), the LABEX CEMPI (Grant No. ANR-11-LABX-0007), and the Equipex Flux (Grant No. ANR-11-EQPX-0017), as well as by the Ministry of Higher Education and Research, Hauts de France Council and European Regional Development Fund through the CPER project Photonics for Society (P4S), EPSRC (UK) Grant No. EP/R00515X/2 (G.E.), US NSF Grant No. DMS 2009647 (A.T.), and Dstl (UK) Grant No. DSTLX-1000116851 (G.R., G.E., and S.R.). G.E., A.T., and G.R. thank the PhLAM laboratory at the University of Lille for hospitality and partial financial support.

APPENDIX: POSITION SHIFT IN TWO-BREATHER INTERACTIONS

Two-breather interactions have been studied in Refs. [50,75], where the expressions for the phase and position shifts in the interaction of two Tajiri-Watanabe breathers have been derived using the IST analysis. In Sec. III A the interaction kernel in the equation of state (12) for the breather gas was obtained in the form (13). The natural interpretation of this interaction kernel, consistent with the previously studied cases of KdV and NLS soliton gases, is the position shift in a two-breather collision. However, the equivalence between formula (13) and the expressions from [50,75] is far from obvious. Here we establish this equivalence, enabling one to extend the phenomenological interpretation of soliton gas kinetics [23] to breather gases.

We consider the position shift expression from [75],

$$\Delta \bar{\xi}_2 = -\ln(\xi_0)/c_{-,2} \cos \alpha_2 = \Delta(\lambda_2, \lambda_1), \quad (\text{A1})$$

where

$$\xi_0 = \frac{d_+ - 2[\cos(\alpha_1 - \alpha_2) + c_{-,1}c_{-,2}] \cos(\alpha_1 - \alpha_2)}{d_+ - 2[\cos(\alpha_1 + \alpha_2) - c_{-,1}c_{-,2}] \cos(\alpha_1 + \alpha_2)}, \quad (\text{A2})$$

with

$$\begin{aligned} c_{\pm,j} &= z_j \pm q_0^2/z_j, & \lambda_j &= (\zeta_j - q_0^2/\zeta_j)/2, \\ d_{\pm,j} &= z_j^2 \pm q_0^4/z_j^2, & q_0 &= -i\delta_0, \\ d_+ &= d_{+,1} + d_{+,2}, & R_0(\lambda_j) &= (\zeta_j + q_0^2/\zeta_j)/2, \\ \zeta_j &= R_0(\lambda_j) + \lambda_j = iz_j e^{i\alpha_j}. \end{aligned} \quad (\text{A3})$$

One can verify that substituting (A3) in Eq. (13) and invoking the identities

$$\begin{aligned} |\lambda_i|^2 &= (d_{+,i} + 2q_0^2 \cos \alpha_i)/4, \\ d_+ &= \left(z_1 z_2 + \frac{q_0^4}{z_1 z_2} \right) \left(\frac{z_1}{z_2} + \frac{z_2}{z_1} \right), \\ (\cos 2\alpha_1 + \cos 2\alpha_2)/2 &= \cos \alpha_1 + \alpha_2 \cos \alpha_1 - \alpha_2 \end{aligned} \quad (\text{A4})$$

yields the position shift expression (A1).

-
- [1] S. P. Novikov, S. V. Manakov, L. P. Pitaevskii, and V. E. Zakharov, *Theory of Solitons: The Inverse Scattering Method* (Springer Science + Business Media, New York, 1984).
- [2] V. E. Zakharov, Turbulence in integrable systems, *Stud. Appl. Math.* **122**, 219 (2009).
- [3] M. D. Maiden, D. V. Anderson, N. A. Franco, G. A. El, and M. A. Hofer, Solitonic Dispersive Hydrodynamics: Theory and Observation, *Phys. Rev. Lett.* **120**, 144101 (2018).
- [4] G. A. El and M. A. Hofer, Dispersive shock waves and modulation theory, *Physica D* **333**, 11 (2016).
- [5] A. A. Gelash and V. E. Zakharov, Superregular solitonic solutions: A novel scenario for the nonlinear stage of modulation instability, *Nonlinearity* **27**, R1 (2014).
- [6] B. Kibler, A. Chabchoub, A. Gelash, N. Akhmediev, and V. E. Zakharov, Superregular Breathers in Optics and Hydrodynamics: Omnipresent Modulation Instability Beyond Simple Periodicity, *Phys. Rev. X* **5**, 041026 (2015).
- [7] G. Xu, A. Gelash, A. Chabchoub, V. Zakharov, and B. Kibler, Breather Wave Molecules, *Phys. Rev. Lett.* **122**, 084101 (2019).
- [8] J. M. Soto-Crespo, N. Devine, and N. Akhmediev, Integrable Turbulence and Rogue Waves: Breathers or Solitons? *Phys. Rev. Lett.* **116**, 103901 (2016).
- [9] N. Akhmediev, J. M. Soto-Crespo, and N. Devine, Breather turbulence versus soliton turbulence: Rogue waves, probability density functions, and spectral features, *Phys. Rev. E* **94**, 022212 (2016).
- [10] S. Randoux, P. Walczak, M. Onorato, and P. Suret, Intermittency in Integrable Turbulence, *Phys. Rev. Lett.* **113**, 113902 (2014).
- [11] P. Walczak, S. Randoux, and P. Suret, Optical Rogue Waves in Integrable Turbulence, *Phys. Rev. Lett.* **114**, 143903 (2015).
- [12] P. Suret, R. El Koussaifi, A. Tikan, C. Evain, S. Randoux, C. Szewaj, and S. Bielawski, Single-shot observation of optical rogue waves in integrable turbulence using time microscopy, *Nat. Commun.* **7**, 13136 (2016).
- [13] G. Michel, F. Bonnefoy, G. Ducrozet, G. Prabhudesai, A. Cazaubiel, F. Copie, A. Tikan, P. Suret, S. Randoux, and E. Falcon, Emergence of peregrine solitons in integrable turbulence of deep water gravity waves, *Phys. Rev. Fluids* **5**, 082801(R) (2020).
- [14] A. Costa, A. R. Osborne, D. T. Resio, S. Alessio, E. Chirivì, E. Saggese, K. Bellomo, and C. E. Long, Soliton Turbulence in Shallow Water Ocean Surface Waves, *Phys. Rev. Lett.* **113**, 108501 (2014).
- [15] J. Wang, Q. W. Ma, S. Yan, and A. Chabchoub, Breather Rogue Waves in Random Seas, *Phys. Rev. Appl.* **9**, 014016 (2018).
- [16] A. R. Osborne, D. T. Resio, A. Costa, S. Ponce de León, and E. Chirivì, Highly nonlinear wind waves in Currituck Sound: Dense breather turbulence in random ocean waves, *Ocean Dyn.* **69**, 187 (2019).
- [17] A. R. Osborne, Breather turbulence: Exact spectral and stochastic solutions of the nonlinear Schrödinger equation, *Fluids* **4**, 72 (2019).
- [18] I. Redor, E. Barthélemy, H. Michallet, M. Onorato, and N. Mordant, Experimental Evidence of a Hydrodynamic Soliton Gas, *Phys. Rev. Lett.* **122**, 214502 (2019).
- [19] P. Suret, A. Tikan, F. Bonnefoy, F. Copie, G. Ducrozet, A. Gelash, G. Prabhudesai, G. Michel, A. Cazaubiel, E. Falcon, G. El, and S. Randoux, Nonlinear Spectral Synthesis of Soliton Gas in Deep-Water Surface Gravity Waves, *Phys. Rev. Lett.* **125**, 264101 (2020).
- [20] A. Gelash, D. Agafontsev, V. Zakharov, G. El, S. Randoux, and P. Suret, Bound State Soliton Gas Dynamics Underlying the Spontaneous Modulational Instability, *Phys. Rev. Lett.* **123**, 234102 (2019).
- [21] V. E. Zakharov, Kinetic equation for solitons, *Sov. Phys.—JETP* **33**, 538 (1971).
- [22] G. A. El, The thermodynamic limit of the Whitham equations, *Phys. Lett. A* **311**, 374 (2003).
- [23] G. A. El and A. M. Kamchatnov, Kinetic Equation for a Dense Soliton Gas, *Phys. Rev. Lett.* **95**, 204101 (2005).
- [24] G. El and A. Tovbis, Spectral theory of soliton and breather gases for the focusing nonlinear Schrödinger equation, *Phys. Rev. E* **101**, 052207 (2020).
- [25] N. Akhmediev, A. Ankiewicz, and J. M. Soto-Crespo, Rogue waves and rational solutions of the nonlinear Schrödinger equation, *Phys. Rev. E* **80**, 026601 (2009).
- [26] N. Akhmediev, A. Ankiewicz, and M. Taki, Waves that appear from nowhere and disappear without a trace, *Phys. Lett. A* **373**, 675 (2009).
- [27] D. J. Kedziora, A. Ankiewicz, and N. Akhmediev, Second-order nonlinear Schrödinger equation breather solutions in the degenerate and rogue wave limits, *Phys. Rev. E* **85**, 066601 (2012).
- [28] G. Genty, C. M. de Sterke, O. Bang, F. Dias, N. Akhmediev, and J. M. Dudley, Collisions and turbulence in optical rogue wave formation, *Phys. Lett. A* **374**, 989 (2010).
- [29] J. M. Dudley, G. Genty, A. Mussot, A. Chabchoub, and F. Dias, Rogue waves and analogies in optics and oceanography, *Nat. Rev. Phys.* **1**, 675 (2019).
- [30] E. A. Kuznetsov, On solitons in parametrically unstable plasma, *Akad. Nauk SSSR Dokl.* **236**, 575 (1977).
- [31] D. H. Peregrine, Water waves, nonlinear Schrödinger equations and their solutions, *J. Aust. Math. Soc. B* **25**, 16 (1983).

- [32] N. N. Akhmediev and V. I. Korneev, Modulation instability and periodic solutions of the nonlinear Schrödinger equation, *Theor. Math. Phys.* **69**, 1089 (1986).
- [33] B. Kibler, J. Fatome, C. Finot, G. Millot, F. Dias, G. Genty, N. Akhmediev, and J. M. Dudley, The Peregrine soliton in nonlinear fibre optics, *Nat. Phys.* **6**, 790 (2010).
- [34] A. Chabchoub, N. P. Hoffmann, and N. Akhmediev, Rogue Wave Observation in a Water Wave Tank, *Phys. Rev. Lett.* **106**, 204502 (2011).
- [35] S. Randoux, P. Suret, and G. El, Inverse scattering transform analysis of rogue waves using local periodization procedure, *Sci. Rep.* **6**, 29238 (2016).
- [36] M. Tajiri and Y. Watanabe, Breather solutions to the focusing nonlinear Schrödinger equation, *Phys. Rev. E* **57**, 3510 (1998).
- [37] N. N. Akhmediev, V. I. Korneev, and N. V. Mitskevich, N -modulation signals in a single-mode optical waveguide under nonlinear conditions, *Sov. Phys.—JETP* **67**, 89 (1988).
- [38] D. J. Kedziora, A. Ankiewicz, and N. Akhmediev, Classifying the hierarchy of nonlinear-Schrödinger-equation rogue-wave solutions, *Phys. Rev. E* **88**, 013207 (2013).
- [39] A. A. Gelash and D. S. Agafontsev, Strongly interacting soliton gas and formation of rogue waves, *Phys. Rev. E* **98**, 042210 (2018).
- [40] V. E. Zakharov and A. B. Shabat, Exact theory of two-dimensional self-focusing and one-dimensional self-modulation of waves in nonlinear media, *Sov. Phys.—JETP* **34**, 62 (1972).
- [41] J. Yang, *Nonlinear Waves in Integrable and Non-Integrable Systems* (Society for Industrial and Applied Mathematics, Philadelphia, PA, USA, 2010).
- [42] S. Wahls and H. V. Poor, Fast numerical nonlinear fourier transforms, *IEEE Trans. Inf. Theory* **61**, 6957 (2015).
- [43] S. T. Le, V. Aref, and H. Buelow, Nonlinear signal multiplexing for communication beyond the Kerr nonlinearity limit, *Nat. Photon.* **11**, 570 (2017).
- [44] S. K. Turitsyn, J. E. Prilepsky, S. T. Le, S. Wahls, L. L. Frumin, M. Kamalian, and S. A. Derevyanko, Nonlinear fourier transform for optical data processing and transmission: Advances and perspectives, *Optica* **4**, 307 (2017).
- [45] Y.-H. Sun, Soliton synchronization in the focusing nonlinear Schrödinger equation, *Phys. Rev. E* **93**, 052222 (2016).
- [46] G. Biondini and G. Kovačič, Inverse scattering transform for the focusing nonlinear Schrödinger equation with nonzero boundary conditions, *J. Math. Phys.* **55**, 031506 (2014).
- [47] G. Biondini and E. Fagerstrom, The integrable nature of modulational instability, *SIAM J. Appl. Math.* **75**, 136 (2015).
- [48] Y.-C. Ma, The perturbed plane-wave solutions of the cubic Schrödinger equation, *Stud. Appl. Math.* **60**, 43 (1979).
- [49] V. E. Zakharov and A. A. Gelash, Nonlinear Stage of Modulation Instability, *Phys. Rev. Lett.* **111**, 054101 (2013).
- [50] A. A. Gelash, Formation of rogue waves from a locally perturbed condensate, *Phys. Rev. E* **97**, 022208 (2018).
- [51] A. Chabchoub, N. Hoffmann, M. Onorato, and N. Akhmediev, Super Rogue Waves: Observation of a Higher-Order Breather in Water Waves, *Phys. Rev. X* **2**, 011015 (2012).
- [52] A. Chabchoub, N. Hoffmann, M. Onorato, A. Slunyaev, A. Sergeeva, E. Pelinovsky, and N. Akhmediev, Observation of a hierarchy of up to fifth-order rogue waves in a water tank, *Phys. Rev. E* **86**, 056601 (2012).
- [53] B. Frisquet, B. Kibler, and G. Millot, Collision of Akhmediev Breathers in Nonlinear Fiber Optics, *Phys. Rev. X* **3**, 041032 (2013).
- [54] B. Kibler, J. Fatome, C. Finot, G. Millot, G. Genty, B. Wetzel, N. Akhmediev, F. Dias, and J. M. Dudley, Observation of Kuznetsov-Ma soliton dynamics in optical fibre, *Sci. Rep.* **2**, 463 (2012).
- [55] J. M. Dudley, G. Genty, F. Dias, B. Kibler, and N. Akhmediev, Modulation instability, Akhmediev breathers and continuous wave supercontinuum generation, *Opt. Express* **17**, 21497 (2009).
- [56] J.-W. Goossens, H. Hafermann, and Y. Jaouën, Experimental realization of Fermi-Pasta-Ulam-Tsingou recurrence in a long-haul optical fiber transmission system, *Sci. Rep.* **9**, 18467 (2019).
- [57] D. Luo, Y. Jin, J. H. V. Nguyen, B. A. Malomed, O. V. Marchukov, V. A. Yurovsky, V. Dunjko, M. Olshani, and R. G. Hulet, Creation and Characterization of Matter-Wave Breathers, *Phys. Rev. Lett.* **125**, 183902 (2020).
- [58] G. Dematteis, T. Grafke, M. Onorato, and E. Vanden-Eijnden, Experimental Evidence of Hydrodynamic Instantons: The Universal Route to Rogue Waves, *Phys. Rev. X* **9**, 041057 (2019).
- [59] P. Dubard, P. Gaillard, C. Klein, and V. B. Matveev, On multi-rogue wave solutions of the NLS equation and positon solutions of the KdV equation, *Eur. Phys. J.: Spec. Top.* **185**, 247 (2010).
- [60] P. Dubard and V. B. Matveev, Multi-rogue waves solutions to the focusing NLS equation and the KP-I equation, *Nat. Hazards Earth Syst. Sci.* **11**, 667 (2011).
- [61] P. Gaillard, Families of quasi-rational solutions of the NLS equation and multi-rogue waves, *J. Phys. A: Math. Theor.* **44**, 435204 (2011).
- [62] A. Ankiewicz, D. J. Kedziora, and N. Akhmediev, Rogue wave triplets, *Phys. Lett. A* **375**, 2782 (2011).
- [63] Y. Ohta and J. Yang, General high-order rogue waves and their dynamics in the nonlinear Schrödinger equation, *Proc. R. Soc. A* **468**, 1716 (2012).
- [64] J. S. He, H. R. Zhang, L. H. Wang, K. Porsezian, and A. S. Fokas, Generating mechanism for higher-order rogue waves, *Phys. Rev. E* **87**, 052914 (2013).
- [65] W.-R. Sun, L. Liu, and P. G. Kevrekidis, Rogue waves of ultra-high peak amplitude: A mechanism for reaching up to thousand times the background level, *Proc. R. Soc. A* **477**, 20200842 (2021).
- [66] C. Gu, H. Hu, and Z. Zhou, *Darboux Transformations in Integrable Systems: Theory and their Applications to Geometry* (Springer Netherlands, Dordrecht, 2005), pp. 1–64.
- [67] N. N. Akhmediev and N. V. Mitskevich, Extremely high degree of N-soliton pulse compression in an optical fiber, *IEEE J. Quantum Electron.* **27**, 849 (1991).
- [68] N. Akhmediev, J. M. Soto-Crespo, and A. Ankiewicz, Extreme waves that appear from nowhere: On the nature of rogue waves, *Phys. Lett. A* **373**, 2137 (2009).
- [69] B. Guo, L. Ling, and Q. P. Liu, Nonlinear Schrödinger equation: Generalized Darboux transformation and rogue wave solutions, *Phys. Rev. E* **85**, 026607 (2012).

- [70] F. J. García-Gómez and V. Aref, Statistics of the nonlinear discrete spectrum of a noisy pulse, *J. Lightwave Technol.* **37**, 3563 (2019).
- [71] D. J. Kedziora, A. Ankiewicz, and N. Akhmediev, Circular rogue wave clusters, *Phys. Rev. E* **84**, 056611 (2011).
- [72] B. M. and A. Tovbis, Maximal amplitudes of finite-gap solutions for the focusing nonlinear Schrödinger equation, *Commun. Math. Phys.* **354**, 525 (2017).
- [73] B. Yang and J. Yang, Rogue wave patterns in the nonlinear Schrödinger equation, [arXiv:2101.00383](https://arxiv.org/abs/2101.00383).
- [74] I. M. Lifshits, S. A. Gredeskul, and L. A. Pastur, *Introduction to the Theory of Disordered Systems* (Wiley, New York, 1988).
- [75] S. Li and G. Biondini, Soliton interactions and degenerate soliton complexes for the focusing nonlinear Schrödinger equation with nonzero background, *Eur. Phys. J. Plus* **133**, 400 (2018).

Chapter 6

Extreme compression of optical pulses in highly nonlinear regimes

The material of this Chapter is motivated by the satellite project “Pulse compression in extremely nonlinear regimes” undertaken under the Research Contract with R&D company LumOptica Ltd, <https://lumoptica.com/> (PI Prof. G. El). While the LumOptica project was concerned with the applied aspects of the pulse compression within a specific range of input/output parameters, the scientific objective of this chapter is the theoretical study of the higher order effects (Raman scattering, third-order dispersion and self-steepening) on the pulse compression and the rogue wave formation within the semi-classical regime of propagation. We have already considered a similar issue in Chapter 3, where the effect of the higher order fNLSE corrections on the Bertola-Tovbis scenario of the Peregrine soliton (PS) emergence were considered in the physical context of deep-water waves. Here a counterpart problem will be considered for the nonlinear pulse compression in fibre optics described by the generalised NLS equation (gNLSE) (6.2) which is an appropriate model for the high intensity pulse propagation. The focus will be on the determination and manipulation of the rogue wave compression point along the fibre.

We stress that this Chapter does not aim at a comprehensive investigation of the optical pulse compression, which is a vast topic on its own, rather it considers the rogue wave emergence within the asymptotic setting of the semi-classical gNLSE as one of the physically relevant scenarios of the self-compression. Along with the theoretical/numerical results we present some realistic

characteristic physical parameters of the optical pulse compression corresponding to the employed mathematical approximations.

6.1 Introduction

Optical pulse compression is a long-standing and fundamental problem in laser physics motivated by various applications spanning from fusion plasma generation to supercontinuum generation and telecommunications (see e.g. [9, 18] and references therein). Generally pulse compression allows one to generate low power pulses of long duration (minimising damage problems), and subsequently compress optical pulses to achieve the short pulse duration and high peak powers required for a specific application. One can generally distinguish between two general types of optical pulse compression: linear and nonlinear.

- **Linear compression.**

When pulses are chirped, their duration can be reduced by reducing the chirp, i.e. by flattening the spectral phase. De-chirping can be achieved by sending the pulses through an optical element with a suitable amount of chromatic dispersion such as a pair of diffraction gratings, an optical fibre, a chirped mirror, etc. [9].

- **Nonlinear compression** can be achieved with different methods, techniques and configurations of optical elements. In particular, the process of nonlinear pulse self-compression has been widely investigated in the framework of supercontinuum generation [152]. It provides the access to ultra-short pulses having a broad spectrum and has been conventionally seen as a coherent nonlinear interaction of solitons constituting a wave packet, often called the higher-order soliton compression

While the higher-order soliton compression has been the dominating paradigm for the nonlinear self-compression for decades, the semi-classical analysis of Bertola and Tovbis [46] (see Section 1.4.4) has revealed some universal features of self-compression related to the PS emergence, suggesting a radical reconsideration of the widely-accepted concept of the solitonic nature of self-compression. In Chapter 3 we have already investigated the effect of the chirp on the pulse compression within the semi-classical fNLSE model modified by the higher order terms arising in

the deep-water wave theory (the Dysthe equation). Now we look at the nonlinear optics counterpart of this model which describes a very different physics that results in the different structure of the higher order corrections describing the Raman scattering, third order dispersion and self-steepening.

As was outlined in Section 1.4.4, within the semi-classical integrable fNLSE framework the nonlinear pulse compression process can be split into two qualitatively different stages: (i) the initial, nonlinearity dominated, stage of the geometric optics self-focusing, resulting in the formation of the gradient catastrophe; and (ii) the secondary, “rogue wave compression” stage of the dispersive regularisation of the gradient catastrophe via the generation of a narrow, large amplitude spike, locally approximated by the PS solution of the fNLSE.

We explore the effect of the higher order corrections on both stages of the pulse-compression.

The content of this Chapter has been adapted from the reports presented as part of the LumOptica project. Thus, the notation adopted slightly differs from the one used in the other parts of this Thesis.

6.2 Mathematical model

6.2.1 Model equations and characteristic parameters

In Section 1.1 the standard cubic nonlinear Schrödinger (NLS) equation has been derived as model to describe the light propagation through a fibre. However, this derivation relies on the specific approximations and assumptions considered. The high intensity light pulse propagation can be modelled, depending on the parameters of the pulse (the peak power and the pulse duration), by one of the three versions of the NLS equation presented below.

We will first present the NLS models in dimensional variables to elucidate the physical parameters and their typical values involved.

In the most general setting the pulse propagation along the fibre described by the non-local NLS

equation:

$$\begin{aligned} \frac{\partial A}{\partial z} + i\beta_2 \frac{1}{2} \frac{\partial^2 A}{\partial t^2} + \frac{\alpha}{2} A - \beta_3 \frac{1}{6} \frac{\partial^3 A}{\partial t^3} = \\ i\gamma \left(1 + \frac{i}{\omega_0} \frac{\partial}{\partial t} \right) \left(A \int_{-\infty}^{+\infty} R(t') |A(z, t - t')|^2 dt' \right), \end{aligned} \quad (6.1)$$

where z is the propagation distance along the fibre, t is time, $A(z, t)$ is the slowly varying electric field envelope, α is the dissipation coefficient, β_2 and β_3 are the second- and third-order dispersion coefficients, and $R(t)$ is the nonlinear response function (the Fourier transform of the nonlinear susceptibility of the fibre). See Section 1.1 for a more detailed description of the physics of the NLS equation. For soliton pulses longer than 100fs Eq. (6.1) can be approximated by the so-called generalised NLS equation:

$$\begin{aligned} \frac{\partial A}{\partial z} + i\beta_2 \frac{1}{2} \frac{\partial^2 A}{\partial t^2} - i\gamma |A|^2 A = \\ -\frac{\alpha}{2} A + \beta_3 \frac{1}{6} \frac{\partial^3 A}{\partial t^3} - 2 \frac{\gamma}{\omega_0} \frac{\partial(|A|^2 A)}{\partial t} - i\gamma T_R A \frac{\partial |A|^2}{\partial t}, \end{aligned} \quad (6.2)$$

where the left-hand part terms describe the leading-order, cubic fNLSE behaviour and the right-hand side contains perturbative terms: losses (α), third-order dispersion (β_3), self-steepening ($2\gamma/\omega_0$) and Raman scattering (γT_R).

If the width of the soliton pulse is indicatively larger than 5ps the governing equation can be even more simplified, and it is possible to neglect the terms related to self-steepening and Raman scattering. In this case, the contribution of the higher-order dispersion term can be neglected too and the standard cubic fNLSE is obtained,

$$\frac{\partial A}{\partial z} + i\beta_2 \frac{1}{2} \frac{\partial^2 A}{\partial t^2} - i\gamma |A|^2 A = 0. \quad (6.3)$$

We stress that equation (6.1) is the most general and includes the propagation regimes described by equations (6.2) and (6.3). At the same time, it is more complicated to analyse so it is desirable to use (6.2) and (6.3) when possible.

The typical values of the physical parameters in Equation (6.2) for $\lambda \approx 1.55\mu\text{m}$ (corresponding to the minimal losses in the anomalous dispersion regime for the standard telecommunications fibre) [9] are:

- $\omega_0 = 2\pi c/\lambda \approx 1.2 \times 10^{16} \text{s}^{-1}$,
- $\beta_2 \approx -20 \text{ps}^2/\text{km}$,
- $\beta_3 \approx 0.1 \text{ps}^3/\text{km}$,
- $\gamma \approx 1 \text{W}^{-1}/\text{km}$,
- $T_R = 3 \times 10^{-3} \text{ps}$ at $\lambda \approx 1.55 \mu\text{m}$ for pulses shorter than 1ps,
- $\alpha \approx 0.05 \text{km}^{-1}$ corresponding to 0.2dB/km.

The characteristic duration of a typical soliton pulse (the coherence length of the system) is given by

$$t_S = \left(\frac{\gamma P_0}{|\beta_2|} \right)^{-\frac{1}{2}}. \quad (6.4)$$

Given the above physical parameter values, we identify the characteristic value of the input power P_0 that would imply the gNLSE description (6.2) of the pulse compression. Using $t_S \sim 100$ fs we obtain from (6.4)

$$P_0 = \frac{|\beta_2|}{\gamma t_S^2} \approx 2 \text{kW}. \quad (6.5)$$

For the purposes of numerical simulations it is beneficial to non-dimensionalise the NLS equation (6.2) using the following rescaling:

$$\psi = \frac{A}{\sqrt{P_0}}, \quad T = t \sqrt{\frac{\gamma P_0}{|\beta_2|}}, \quad Z = z \gamma P_0. \quad (6.6)$$

Note that the duration of the input pulse rescales to $\tau_0 = t_0 \sqrt{\frac{\gamma P_0}{|\beta_2|}}$. Under these transformations, equation (6.2) takes the form of the (nondimensionalised) standard cubic NLS equation (6.3) modified by the higher order terms in the RHS:

$$\frac{\partial \psi}{\partial Z} - \frac{i}{2} \frac{\partial^2 \psi}{\partial T^2} - i|\psi|^2 \psi = -C_L \psi + C_{TOD} \frac{\partial^3 \psi}{\partial T^3} - C_S \frac{\partial(|\psi|^2 \psi)}{\partial T} - iC_R \psi \frac{\partial |\psi|^2}{\partial T}, \quad (6.7)$$

where for the suggested propagation parameters of $P_0 \approx 2 \text{kW}$:

- $C_L = \frac{\alpha}{2\gamma P_0} \approx 1.25 \times 10^{-5} \Rightarrow$ losses;
- $C_{TOD} = \frac{\beta_3}{6|\beta_2|} \sqrt{\frac{\gamma P_0}{|\beta_2|}} \approx 0.8 \times 10^{-2} \Rightarrow$ third-order dispersion;

- $C_S = \frac{2}{\omega_0} \sqrt{\frac{\gamma P_0}{|\beta_2|}} \approx 0.02 \Rightarrow$ self-steepening;
- $C_R = T_R \sqrt{\frac{\gamma P_0}{|\beta_2|}} \approx 0.03 \Rightarrow$ intrapulse Raman scattering.

The soliton width in the rescaled variable T is $\tau_s = 1$.

6.2.2 Chirped initial pulse

We are interested in the propagation of a chirped initial pulse. As described in [9] the chirping is achieved by propagating the pulse through a dispersive medium described by the *linear* Schrödinger equation, here in the non-dimensional form:

$$i \frac{\partial \psi(z, t)}{\partial z} - \frac{\beta'_2}{2} \frac{\partial^2 \psi(z, t)}{\partial t^2} = 0, \quad (6.8)$$

where we have introduced the notation β'_2 for the dispersion coefficient not to mix it with the coefficient β_2 in the NLS equation. To solve equation (6.8) we proceed in the Fourier space, writing the field $\psi(z, t)$ as inverse Fourier transform:

$$\psi(z, t) = \frac{1}{\sqrt{2\pi}} \int_{-\infty}^{+\infty} e^{i\omega t} \psi(z, \omega) d\omega. \quad (6.9)$$

Then we can rewrite Eq. (6.8) as:

$$\frac{\partial \psi(z, \omega)}{\partial z} - i \frac{\beta'_2}{2} \omega^2 \psi(z, \omega) = 0, \quad (6.10)$$

which can be readily solved to give

$$\psi(z, \omega) = \psi(0, \omega) e^{i \frac{\beta'_2}{2} \omega^2 z}. \quad (6.11)$$

Now, applying the inverse transform $\psi(z, \omega)$ we obtain the evolved field:

$$\psi(z, t) = \frac{1}{\sqrt{2\pi}} \int_{-\infty}^{+\infty} e^{i\omega t} e^{i \frac{\beta'_2}{2} \omega^2 z} \psi(\omega, 0) d\omega. \quad (6.12)$$

For a Gaussian initial pulse

$$\psi(0, t) = A e^{-\frac{t^2}{2\tau^2}}, \quad (6.13)$$

we obtain after the propagation in the linear medium [9]:

$$\psi(z, t) = \frac{A\tau}{\sqrt{\tau^2 - i\beta'_2 z}} e^{\frac{-t^2}{2(\tau^2 - i\beta'_2 z)}} = \frac{A\tau}{\sqrt{\tau^2 - i\beta'_2 z}} e^{\frac{-t^2(1+iC_1)}{2\tau_0^2}}, \quad (6.14)$$

where $C_1 = \frac{\beta'_2 z}{\tau^2}$ is the chirp parameter and $\tau_0^2 = \frac{\tau^4 + \beta'^2_2 z^2}{\tau^2}$. Depending on the sign of dispersion β'_2 one can have a positive chirp $C_1 > 0$ or a negative chirp $C_1 < 0$.

From Eq. (6.14) we can identify the chirp (the instantaneous frequency) u by isolating the phase ϕ of the field and differentiating it by t . After a simple manipulation we identify the phase:

$$\phi(z, t) = -\frac{\beta'_2 t^2 z}{2(\tau^4 + \beta'^2_2 z^2)} \Rightarrow u = \frac{\partial \phi}{\partial t} = -\frac{\beta'_2 z t}{\tau^4 + \beta'^2_2 z^2}. \quad (6.15)$$

After the propagation in the linear medium we can define a broadening (stretching) factor that relates the width of the initial pulse ($\tau_i = \tau$) and the final one ($\tau_0 = \sqrt{\frac{\tau^4 + \beta'^2_2 z^2}{\tau^2}}$):

$$\frac{\tau_0}{\tau_i} = \sqrt{1 + \left(\frac{\beta'_2 z}{\tau^2}\right)^2} = \sqrt{1 + C_1^2}. \quad (6.16)$$

Note that the chirp factor C_1 enters the stretching factor (6.16) as C_1^2 so that the same stretching can be achieved via both positive (focusing) and negative (defocusing) chirp. Importantly, the sign of the chirp has a strong effect on the subsequent propagation in a nonlinear fibre, see below. Note that for $|C_1| \gg 1$ one obtain $\frac{\tau_0}{\tau_i} \approx |C_1|$.

Thus, given the characteristic of the linear medium, one can design as initial condition of the NLS equation the chirped Gaussian profile [9]

$$\psi(0, T) = e^{-\frac{T^2}{2\tau_0^2}(1+iC_1)}. \quad (6.17)$$

We stress that the initial condition (6.17) is written in normalised variables; the physical pulse profile $A(z, t)$ is recovered by applying the inverse of the transformation (6.6).

6.2.3 Numerical method and computational resources

We employ a step-adaptive pseudo-spectral method to numerically determine the signal propagation along the fibre. While the time derivatives are evaluated using Fast Fourier Transform routines (FFTW, <http://www.fftw.org/>), the spatial evolution is performed with a numerical solver included in the code ('ROCK4' [153]); the code relies on a Runge-Kutta fourth-order method suitable for large stiff problems. Moreover, the solver adapts each propagation spatial step to minimise the numerical error and control the scheme stability.

The core of the code, first tested to solve the standard NLS equation (6.3), has been extended to include the extra terms of the extended NLS equation (6.7). The developed code has been tested against several known particular solutions of Eq.(6.7) available in the literature [9]. The testing has been performed by retaining the necessary term(s) in the NLS equation while “switching off” all other terms. The computations corresponding to a physically reasonable range of parameters have been performed on a cluster at Lille University, France.

The computations are quite resource consuming: e.g. the numerical simulation of the nondimensionalised gNLSE with initial data corresponding to the Gaussian pulse with $\tau_0 = 20$ (i.e. $P_0 = 2\text{kW}$, $t_0 = 2\text{ ps}$) and $C_1 \in [0, 60]$, discretised on a temporal grid of $N = 2^{16}$ points, takes about 15 hours of computer time on cluster. *This is why using an appropriate mathematical approximation is essential for the pulse compression modelling in strongly nonlinear propagation regimes.*

6.3 Semi-classical approximation

The semi-classical approximation is a powerful tool to investigate the system in exam when there exists a scale separation in the problem. The scale separation is determined by the small parameter $\varepsilon \ll 1$, defined by the ratio of the typical soliton pulse duration t_S to the typical input pulse duration t_0 . As we mentioned, direct numerical solution of the NLS equation with sufficiently small values of ε (i.e. $\tau_0 \gg 1$) requires significant computational resources. However, the semi-classical analysis enables one to predict some of the compression parameters analytically using a reduced, nonlinear geometric optics type model, which is valid for the initial compression stage

leading to gradient catastrophe.

6.3.1 Semi-classical generalised NLS model and the initial data

For the typical physical propagation parameters used in our modelling (see Section 6.2.1) the dimensionless duration of the initial pulse $\tau_0 \simeq 20$ is much greater than the typical soliton width $\tau_s = 1$. This suggests the possibility to introduce a small parameter

$$\varepsilon = \tau_s/\tau_0 = \frac{1}{t_0} \sqrt{\frac{|\beta_2|}{P_0\gamma}} \ll 1. \quad (6.18)$$

We re-normalise the independent Z - and T - variables as

$$T' = \varepsilon T, \quad Z' = \varepsilon Z. \quad (6.19)$$

Then, dropping primes for Z and T , we obtain the “semi-classical” form of the gNLSE Eq. (6.7):

$$\begin{aligned} \varepsilon \frac{\partial \psi}{\partial Z} - i \frac{\varepsilon^2}{2} \frac{\partial^2 \psi}{\partial T^2} - i |\psi|^2 \psi = \\ -C_L \psi + \varepsilon^3 C_{TOD} \frac{\partial^3 \psi}{\partial T^3} - \varepsilon C_S \frac{\partial(|\psi|^2 \psi)}{\partial T} - i \varepsilon C_R \psi \frac{\partial |\psi|^2}{\partial T}, \end{aligned} \quad (6.20)$$

which will be used for the analytical and numerical developments. The numerical values of the non-dimensional coefficients in (6.20) are the same as in Eq. (6.7).

In our analysis we consider two types of initial conditions for the semi-classical gNLSE (6.20). The first one, the chirped Gaussian pulse, is the most relevant in terms of the fibre optics propagation while the second one, the chirped “sech” profile enables explicit analytical results via the IST approach. Our strategy here will be to use the analytical insights from the “sech” pulse propagation and apply them to the Gaussian pulse propagation. The applicability of the “sech” profile results to the propagation of a Gaussian pulse will be verified numerically.

The chirped Gaussian pulse (6.17) yields the initial condition for the gNLSE (6.20):

$$\psi(T, 0) = \exp\left(-\frac{T^2}{2}\right) \exp\left(-\frac{iT^2\mu}{2\varepsilon}\right) \equiv \psi_1(T), \quad (6.21)$$

where μ is the normalised chirp factor. Indeed, it follows from (6.16) that for $C_1 \gg 1$ one has

$C_1 \sim \tau_0 = \varepsilon^{-1}$, and thus we have an important relation between the physical chirp factor C_1 and μ :

$$C_1 = \mu/\varepsilon. \quad (6.22)$$

Say, for the pulse with $t_0 = 2\text{ps}$, $P_0 = 2\text{kW}$, and $\mu = 1$ one has $C_1 = 20$.

The chirped “sech” initial pulse corresponds to the initial condition for (6.20):

$$\psi(T, 0) = \text{sech}(T) e^{i\phi/\varepsilon} \equiv \psi_2(T), \quad \phi = -\mu \log(\cosh(T)). \quad (6.23)$$

One can see from the comparison presented in Fig. 21 that the sech profile (6.23) provides a good approximation of a Gaussian pulse (6.21). Note that the chirp defined as $u = \partial\phi/\partial T$ for the sech pulse (6.23) has the form $u = -C_1 \tanh(T)$ providing, at the centre of the structure, a good approximation to the linear chirp of the Gaussian pulse, $u = -C_1 T$. We will further verify the

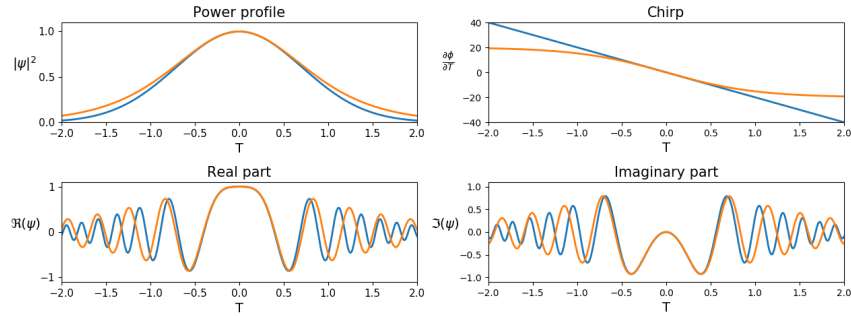


Figure 21: Comparison of the chirped Gaussian (blue) and “sech” (orange) initial profiles.

validity of the “sech-approximation” for the Gaussian pulse compression via comparison of some benchmark analytical results for the sech profile with numerical simulations of the Gaussian pulse self-compression.

Given the several transformations performed of the initial system, it is instructive to present the expressions for the physical (dimensional) variables A , z and t in terms of the non-dimensional variables ψ , Z and T of Eq. (6.20). Using (6.6), (6.19) we obtain

$$A = \sqrt{P_0} \psi, \quad z = \frac{t_0}{\sqrt{\gamma|\beta_2|P_0}} Z, \quad t = t_0 T. \quad (6.24)$$

Considering the small parameter ε define in Eq. (6.18) the physical chirp factor C_1 takes the form:

$$C_1 = \frac{\mu}{\varepsilon} = \mu t_0 \sqrt{\frac{\gamma P_0}{|\beta_2|}}. \quad (6.25)$$

6.3.2 Validity of semi-classical approximation

As already mentioned, in our modelling we assume that the chirped input pulse peak power $P_0 \simeq 2\text{kW}$, corresponding to a typical soliton duration of $t_S = 100\text{fs}$. We also assume a fixed duration of $t_0 = 2\text{ps}$ for the initial chirped pulse. Fixing the input chirped pulse duration t_0 rather than the initial (unchirped) pulse width t_i is essential for our semi-classical mathematical modelling, so that the small parameter $\varepsilon = \frac{1}{t_0} \sqrt{\frac{|\beta_2|}{P_0 \gamma}}$ is fully determined by the input peak power P_0 , while the normalised chirp factor μ is determined by t_i and P_0 via

$$\mu = C_1 \varepsilon = \frac{1}{t_i} \sqrt{\frac{|\beta_2|}{P_0 \gamma}}.$$

The characteristic value of ε involved is then found to be $\varepsilon \sim 10^{-2}$, which justifies the applicability of the semi-classical approach in the propagation regimes of our interest. The value of μ considered in the simulations is of $\mathcal{O}(1)$.

6.4 Gradient catastrophe analysis

As we have already discussed in Section 1.4.4, the availability of the small parameter ε in the semi-classical NLS model (6.20) enables one to split the evolution of a broad initial pulse along the fibre into two qualitatively and quantitatively different stages: (i) initial nonlinear compression leading to a *gradient catastrophe* (the nonlinear self-focusing point where the gradient of the intensity profile becomes infinite); (ii) dispersive regularisation of a gradient catastrophe via the emergence of a narrow high amplitude spike— the rogue wave. The first stage of the compression is characterised by the slow, large-scale, dynamics, while at the second stage the variations of the wave field are rapid.

6.4.1 The nonlinear geometric optics approximation

We take advantage of the small parameter ε in the gNLSE (6.20) to analyse the propagation of a broad pulse with high peak power. To this end we introduce the Madelung transformation for the wave field:

$$\psi = \sqrt{\rho} e^{\frac{i\phi}{\varepsilon}}, \quad \frac{\partial \phi}{\partial T} = u, \quad (6.26)$$

where $\rho(T, Z)$ is the (normalised) power and $u(T, Z)$ is the chirp. Substituting (6.26) in Eq. (6.20) and separating the real and imaginary parts we obtain:

$$\begin{cases} \rho_Z + (\rho u)_T = -2\frac{1}{\varepsilon} C_L \rho - 3C_S \rho \rho_T - 3C_{TOD} (u^2 \rho)_T \\ \quad + C_{TOD} \varepsilon^2 \left(\frac{3\rho_T^3}{4\rho^2} - \frac{3\rho_T}{2\rho} \rho_{TT} + \rho_{TTT} \right), \\ u_Z + uu_T - \rho_T - \frac{\varepsilon^2}{8} \left[\frac{\rho_{TT}}{\rho} + \left(\frac{\rho_T}{\rho} \right)_T \right]_T = -C_S (\rho u)_T - 3C_{TOD} u^2 u_T \\ \quad + \varepsilon C_R \rho_{TT} + C_{TOD} \varepsilon^2 \left[\frac{3}{4} \left[\frac{\rho_{TT}}{\rho} + \left(\frac{\rho_T}{\rho} \right)_T \right] u + \frac{3\rho_T}{2\rho} u_T + u_{TT} \right]_T. \end{cases} \quad (6.27)$$

Using the numerical values of the coefficients and typical values of ε for the pulse propagation of interest, one can see that the term $\sim C_L/\varepsilon \ll 1$, describing the fibre losses, can be neglected. Further, assuming finite values of all Z - and T -derivative for the initial condition, we can neglect the terms proportional to ε and ε^2 to obtain at leading order the following reduced, hydrodynamic type model:

$$\begin{cases} \rho_Z + (\rho u)_T = -3C_S \rho \rho_T - 3C_{TOD} (\rho u^2)_T, \\ u_Z + uu_T - \rho_T = -C_S (\rho u)_T - 3C_{TOD} u^2 u_T. \end{cases} \quad (6.28)$$

The system (6.28), describing the initial compression stage, represents the long-wave limit of the gNLSE (6.27). Traditionally such systems arise as a dispersionless limit of the full, dispersive equation. Note that the system (6.28) contains the terms coming from the third-order dispersive corrections in the gNLSE. It is interesting to note that system (6.28) contains the terms coming from the third-order dispersive corrections in the gNLSE.

The system (6.28) can be re-written in matrix form:

$$\begin{pmatrix} \rho \\ u \end{pmatrix}_Z + \begin{pmatrix} 3C_S \rho + u + 3C_{TOD} u^2 & \rho + 6C_{TOD} \rho u \\ C_S - 1 & C_S \rho + u + 3C_{TOD} u^2 \end{pmatrix} \begin{pmatrix} \rho \\ u \end{pmatrix}_T = 0. \quad (6.29)$$

The hydrodynamic model (6.28) has a number of important advantages, both analytical and computational, over the full gNLSE (6.20). We argue that it accurately describes the initial compression of the pulse and enables one to predict the point of the gradient catastrophe occurrence along the fibre (i.e. the point of the maximum nonlinear self-compression at the stage (i)). This point can then be manipulated by choosing an appropriate chirp profile.

To verify the validity of the modelling of the initial pulse compression with the hydrodynamic system (6.29) we compare the results of numerical simulations of the full gNLSE (6.20) with the simulations of the hydrodynamic system (6.29). This comparison is shown in Fig. 23. One can see that the hydrodynamic system (6.29) accurately captures the initial stage of the pulse compression up to the gradient catastrophe point.

Stability analysis

To analyse the linear stability of solutions to the dispersionless limit of the hydrodynamic system (6.29) we compute the eigenvalues of the coefficient matrix:

$$\lambda_{\pm} = u + 3C_{TOD}u^2 + 2C_S\rho \pm \sqrt{\Delta}, \quad (6.30)$$

where

$$\Delta = \rho [C_S^2\rho + (1 + 6C_{TOD}u)(C_Su - 1)]. \quad (6.31)$$

The sign of Δ defines the stability condition of the system, with $\Delta > 0$ corresponding to stable solutions and $\Delta < 0$ to unstable ones (hyperbolicity vs. ellipticity of the hydrodynamic type system (6.29)). This analysis is important as the condition $\Delta < 0$ ensures nonlinear self-focusing (self-compression) of the pulse. Note that for the standard case of the fNLSE (6.3), when $C_S = C_{TOD} = 0$, one has $\Delta = -\rho$, i.e. this case is always unstable and subject to self-focusing process. One can see that the general propagation regime is more complicated, with the higher order effects capable, in principle, of suppressing the pulse self-focusing.

To identify the possible transition between stable (defocusing) and unstable (focusing) propagation regimes we evaluate the roots of $\Delta = 0$. Given convexity of the function $\Delta(\rho)$, the solution will

be unstable for ρ lying between the two roots of $\Delta(\rho) = 0$ given by

$$\rho_1 = 0, \quad \rho_2 = \frac{1}{C_S^2} (1 + 6C_{TOD}u) (1 - C_S u) . \quad (6.32)$$

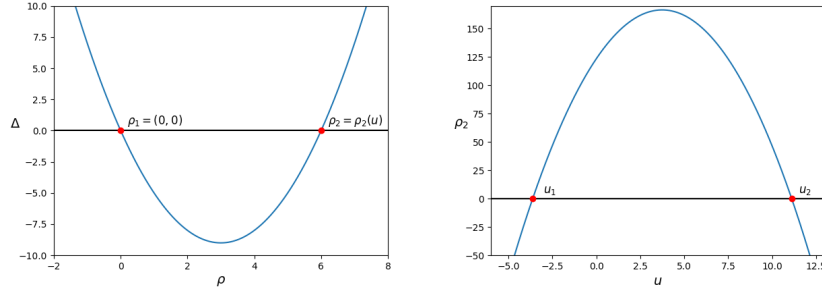


Figure 22: Schematic for the stability criterion $\Delta < 0$. Left: Δ as function of ρ ; Right: The root ρ_2 as function of the chirp u

Thus for the self-compression regime the pulse intensity ρ should be less than the second root ρ_2 . The value of ρ_2 can be manipulated by choosing a suitable chirp u . The reduced model (6.28), which essentially represents the nonlinear geometric optics approximation, is much simpler than the original gNLSE (6.20), while providing an accurate description of the initial stage of nonlinear self-compression of a broad pulse. The comparison between the numerical solutions of the full gNLSE (6.20) with $\varepsilon = 0.05$ and the reduced model (6.28) for the propagation of an unchirped Gaussian pulse is shown in Fig. 23. One can see excellent agreement, confirming the efficacy of the reduced hydrodynamic model (6.28).

It follows from (6.28) that at the initial stage of self-compression the second-order dispersive effects are less important, and the nonlinear evolution is dominated by Kerr nonlinearity (self-phase modulation), self-steepening and, somewhat paradoxically, the third-order dispersion. It also turns out that, for the propagation regimes of our interest, the intrapulse Raman scattering can also be neglected at this compression stage.

The instability growth rate, $\sqrt{-\Delta}$, along with the initial chirp, determines the propagation length Z^* at which the gradient catastrophe occurs. We note that, in the absence of the higher order effects, i.e. when $C_S = C_{TOD} = 0$ one has $\Delta = -\rho$, which is consistent with the known results for the cubic fNLSE (6.3). Furthermore, given the typical propagation regimes used in our modelling one can verify that the condition $\Delta < 0$ is always valid, i.e. the higher order effects do

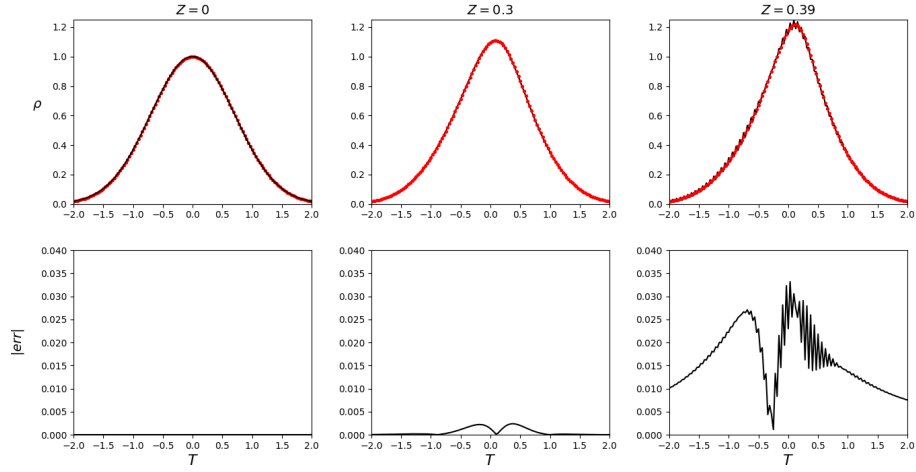


Figure 23: Comparison between the numerical solutions of the gNLSE (6.20) with $\varepsilon = 0.05$ (red dots) and of the reduced model (6.28) (solid line) at $Z = 0$, $Z = 0.3$ and $Z = 0.39$. The initial pulse is $\psi(T, 0) = \exp(-T^2/2)$. Upper row: the evolution of the intensity (power) $\rho = |\psi|^2$ profile. The error (the absolute value of the difference between the two solutions) is shown in the bottom row.

not change the self-focusing character of the initial pulse propagation.

6.4.2 Gradient catastrophe and rogue wave compression distance

In the vicinity of the gradient catastrophe point $Z = Z_c$, the reduced model fails to describe the evolution of the system and the full gNLSE (6.20) has to be considered. The dispersive effects (possibly modified by the higher order effects) lead to the regularisation of the gradient catastrophe via the local emergence of a coherent structure. Here we focus on two features of the regularisation process: (i) the propagation distance $Z = Z^*$ along the fibre, where the maximum compression occurs via the emergence of a rogue wave; and (ii) the characterisation of the rogue wave in terms of its local background value, the peak power, the width, the waveform etc.

To determine the gradient catastrophe position Z_c and the rogue wave compression distance Z^* for the gNLSE case we first invoke the available results for the integrable, cubic fNLSE.

For the chirped initial “sech” pulse (6.23) the analysis of the dispersionless limit of the fNLSE (the reduced system (6.28) with $C_S = C_{TOD} = 0$) yields the exact result for the gradient catastrophe distance [154]

$$Z_c = \frac{1}{\mu + 2}, \quad (6.33)$$

where μ , we recall, is the normalised chirp factor. A more refined analysis for $Z > Z_c$, using the semi-classical limit of the IST and the Riemann-Hilbert problem approach [46], yields the correction to (6.33) due to finite value of ε :

$$Z^* \approx \frac{1}{2 + \mu} + \varepsilon^{4/5} h \left(\frac{2}{3} \frac{1}{(\mu + 2)^6} \right)^{1/5}, \quad (6.34)$$

where $h \approx 2.38$. Formula (6.34) for the (non-dimensional) distance of the rogue wave compression translates into the physical distance (metres) along the fibre as

$$z^* \approx \frac{t_0}{(2 + \mu) \sqrt{\gamma |\beta_2| P_0}} + \frac{h}{\gamma P_0} \left(t_0 \sqrt{\frac{\gamma P_0}{|\beta_2|}} \frac{2}{3} \frac{1}{(\mu + 2)^6} \right)^{1/5}. \quad (6.35)$$

We recall that the normalised chirp factor μ is related to the physical chirp C_1 by the formula (6.25).

It is remarkable that the formula (6.34) obtained in [46] by a rigorous asymptotic analysis for $\varepsilon \ll 1$ exhibits a very good agreement with the numerical simulations performed for rather moderate values of ε . Moreover, as we will see, it gives a very reasonable approximation of the rogue wave compression distance for chirped Gaussian pulses and is even quite robust with respect to small perturbations due to the higher order terms included in the gNLSE (6.20). This is an important result in the context of fibre optics applications as it provides, with the manipulation of the chirp, the practical tool to control the distance of maximum compression of the rogue wave. We have already discussed this effect in Chapter 3 in the framework of the deep-water wave system.

A number of numerical simulations of the unperturbed fNLSE (6.41) was first performed to compare the analytical result (6.34) with the values of the rogue wave compression distance obtained numerically for the chirped sech (6.23) and chirped Gaussian (6.21) pulses. As shown in Fig. 24 the agreement with the theoretical prediction is excellent for the ‘‘sech’’ pulse as expected. For chirped Gaussian pulses, the introduction of an extra delay, obtained numerically (Fig. 24, right panel) is required to obtain an accurate estimation of the maximum compression distance. It is expected that the delay would decrease with the increase of the peak power P_0 so formula (6.34) should be quite accurate for Gaussian pulses in the high power propagation regime.

The next step was to see whether the analytical formula (6.34) derived by neglecting the higher

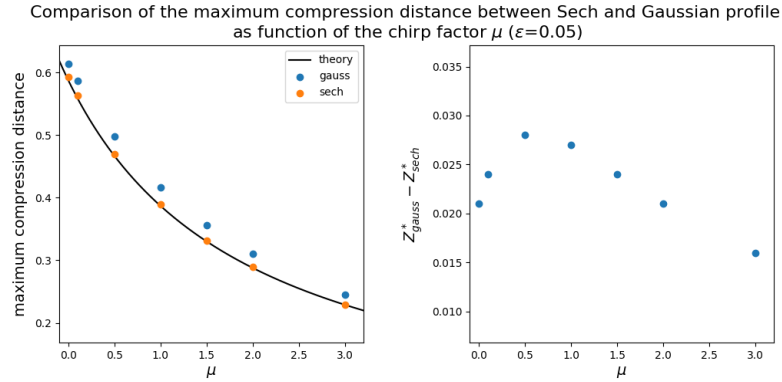


Figure 24: **Left:** the rogue wave compression distance Z^* . Solid line: formula (6.34). Orange dots: numerical simulations of the fNLSE (6.41) for “sech” pulses; blue dots: numerical simulations for Gaussian pulses. **Right:** the Gaussian pulse delay function (the difference between the rogue wave compression distances for the Gaussian and sech pulses)

order terms in the gNLSE (6.20) is still valid in practical terms when the higher order terms in (6.20) are taken into account. Our numerical simulations of the gNLSE for moderate to high powers P_0 showed that the effect of the higher order terms *on the rogue wave compression distance* is insignificant, which is the evidence of practical applicability of the approximate formula (6.34) to the gNLSE.

6.5 Rogue wave compression

Having discussed the validity of equation (6.34) to estimate the rogue wave compression for a Gaussian profile, here we focus on the rogue wave formation in terms of its peak power, width, local background etc.

6.5.1 Primary rogue wave compression: peak power

As discussed in Section 1.4.4, one of the fundamental result found in [46] and experimentally confirmed in [4] is the *local* formation of the PS (cf. Eq. (6.36)) as regularisation process of the gradient catastrophe in the fNLSE (6.41). This result has been exploited in Chapter 3 in the analysis of deep water rogue wave emergence. Here this analysis is developed in the nonlinear

optics context. The profile of the PS in terms of the “optical” variables takes the form

$$|\psi_{PS}(T, Z^*)| \approx a_0 \left[1 - \frac{4}{1 + 4a_0^2 (T/\varepsilon)^2} \right], \quad (6.36)$$

where $a_0(\mu)$ is the *local rogue wave background* determined by the value of $|\psi|$ at the gradient catastrophe point $T = 0, Z = 1/(\mu + 2)$ while the rogue wave distance Z^* is given by (6.34). As shown in [154] the local rogue wave background a_0 correspond to the filed amplitude $|\psi|$ at the gradient catastrophe point. For the chirped sech initial profile (6.23) it can be determined analytically:

$$a_0 = \sqrt{2 + \mu}. \quad (6.37)$$

The numerical simulations of the Gaussian pulse propagation show that formula (6.37) provides a good approximation of the rogue wave background, see Fig 25.

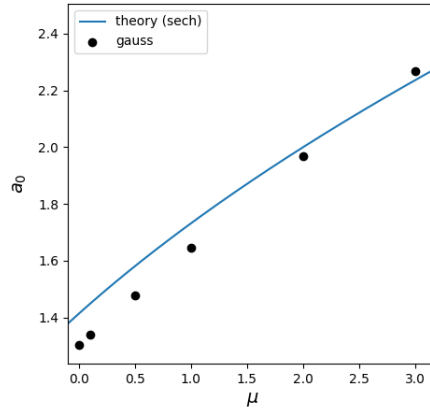


Figure 25: The local rogue wave background a_0 as function of the normalised chirp factor μ . The curve is given by the analytical expression $a_0 = \sqrt{2 + \mu}$ obtained for sech pulses; the dots show $a_0(\mu)$ obtained numerically for Gaussian pulses.

Assuming (6.37) the peak power in the PS (6.36) is given by the formula

$$P_{\max} = 9(\mu + 2) P_0 \quad [\text{W}], \quad (6.38)$$

where μ is the normalised chirp factor (6.25) of the input pulse. Moreover, the temporal width of

the PS (the duration between the two points where $|\psi_{PS}| = 0$) is given by

$$\Delta_{PS} = \sqrt{\frac{3}{(\mu + 2)}} \sqrt{\frac{|\beta_2|}{\gamma P_0}} \quad [\text{s}]. \quad (6.39)$$

Combining (6.38), and (6.39) a *universal relation* describing the rogue wave pulse compression is derived:

$$P_{\max} \Delta_{PS}^2 = 18 \frac{|\beta_2|}{\gamma}. \quad (6.40)$$

6.5.2 Secondary rogue wave compression at high propagation powers

The importance and the qualitative effects of the higher order corrections (particularly Raman scattering) in the rogue wave compression process can be observed at the relatively modest input power $P_0 = 2\text{kW}$. Numerical results showing the comparison of a Gaussian pulse compression in the standard NLS propagation and the gNLSE propagation at $P_0 = 2\text{ kW}$, and $t_0 = 2\text{ps}$ are shown in Figs. 26-28.

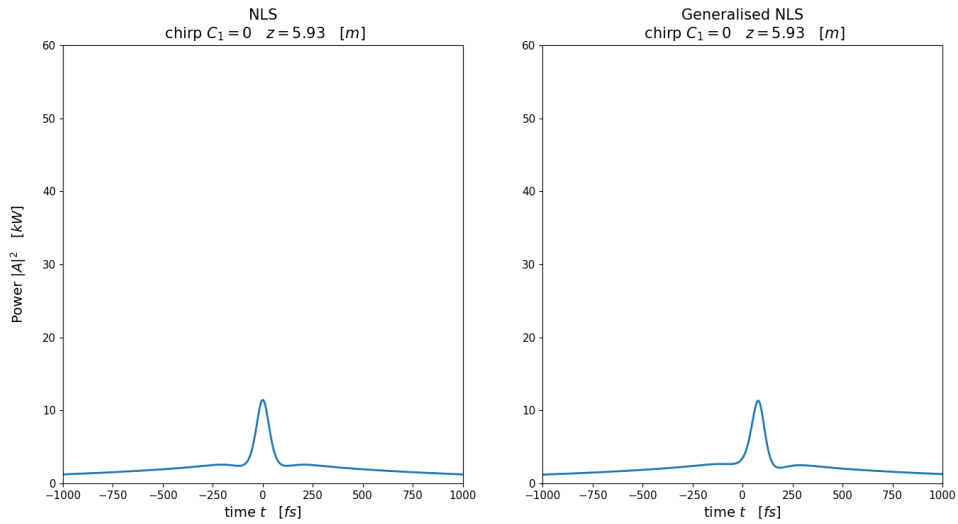


Figure 26: Gradient catastrophe in the Gaussian pulse compression. Left: fNLSE propagation; Right: gNLSE

Note that the pulse compression within fNLSE and the gNLSE models is very similar up to the point of the gradient catastrophe (Fig. 26). As expected, the distance of the first rogue wave compression is virtually the same for the cubic NLS and gNLSE although the peak powers of the

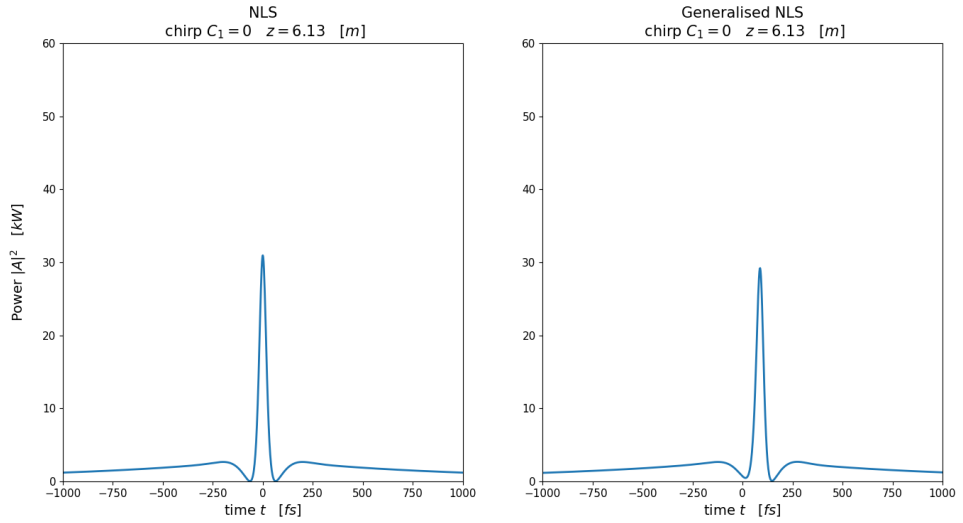


Figure 27: Primary rogue compression due to the PS emergence. Left: fNLSE propagation; Right: gNLSE

rogue wave slightly differ (Fig. 27) (one may expect a more significant peak power difference at higher input powers). However, one can see the drastic difference between the two evolutions at a later stage (Fig.28) when the gNLSE exhibits the secondary rogue wave compression, which is completely absent in the “pure” cubic fNLSE equation. Our analysis shows that the secondary rogue wave compression is mainly due to the Raman scattering.

6.5.3 Energy analysis of the rogue wave pulse compression

In the last step of our analysis we investigate the energy re-distribution during the rogue wave compression process. Specifically, we evaluate the proportion of energy of the initial pulse that is transferred into the rogue wave.

First, we consider the energy transfer in the case of the cubic fNLSE, here in the semi-classical formulation:

$$\varepsilon \frac{\partial \psi}{\partial Z} - i \frac{\varepsilon^2}{2} \frac{\partial^2 \psi}{\partial T^2} - i |\psi|^2 \psi = 0, \quad (6.41)$$

where the explicit relation between the non-dimensional variables in (6.41) and the physical quan-

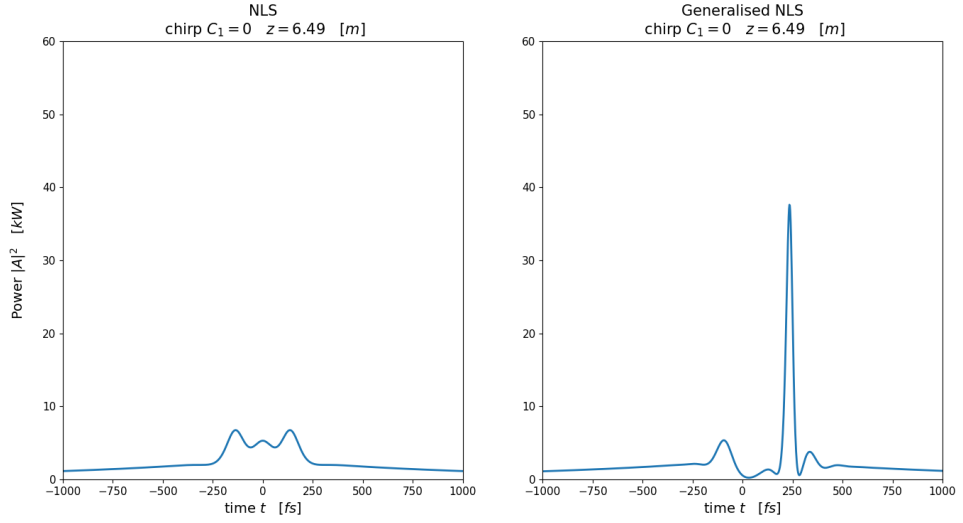


Figure 28: Secondary compression in the propagation of a Gaussian pulse. Left: cubic fNLSE (no secondary compression); Right: gNLSE—secondary compression due to the Raman effect.

ities A, z, t by (cf. Eqs. (6.24)) are

$$\psi = \frac{A}{\sqrt{P_0}}, \quad T = t \sqrt{\frac{\gamma P_0}{|\beta_2|}} \varepsilon, \quad Z = z \gamma P_0 \varepsilon, \quad \varepsilon = \frac{1}{t_0} \sqrt{\frac{|\beta_2|}{P_0 \gamma}}, \quad (6.42)$$

with P_0 input peak power, t_0 input pulse width, and $t_S = \sqrt{|\beta_2|/(P_0 \gamma)}$ the characteristic size of the soliton in the system.

As discussed in Section 6.3.1, the study of Eq. (6.41) with the “sech” initial profile:

$$\psi(T, 0) = \text{sech}(T) e^{i\phi/\varepsilon} \equiv \psi_2(T), \quad \phi = -\mu \log(\cosh(T)),$$

has a number of advantages due to the availability of explicit analytical results [46, 154], giving at the same time a good approximation of the evolution of a less treatable analytically Gaussian pulse evolution.

Considering the PS (6.36), the non-dimensional energy “stored” in the rogue wave at the maximum compression point is given by the integral

$$\tilde{E}_{PS} = \int_{T_z^-}^{T_z^+} |\psi_{PS}(T, Z^*)|^2 dT = 3\sqrt{3} a_0(\mu) \varepsilon, \quad (6.43)$$

where $|\psi_{PS}|^2$ is the power profile of the PS and $T_z^\pm = \pm \frac{\varepsilon\sqrt{3}}{2a_0}$ are the points where $|\psi_{PS}| = 0$, see Fig. 29. Rescaling to dimensional units the PS energy (6.43), the energy confined in the core part of the rogue wave results

$$E_{PS} = \sqrt{3(\mu + 2)} \sqrt{\frac{P_0|\beta_2|}{\gamma}}. \quad [\text{J}] \quad (6.44)$$

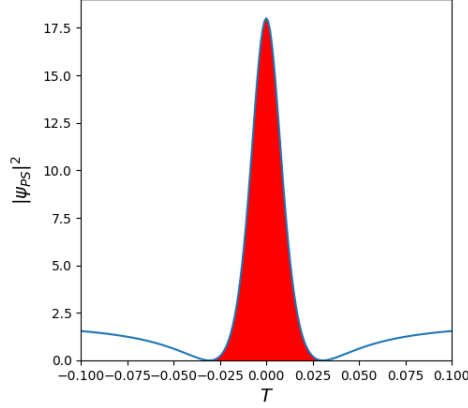


Figure 29: Schematic of the energy “stored” in the Peregrine soliton

The relative amount of the energy transferred to the rogue wave from the initial pulse (6.23) with total energy $\tilde{E}_0 = \int_{-\infty}^{+\infty} \text{sech}^2(T) dT = 2$ is

$$\alpha = \frac{\tilde{E}_{PS}}{\tilde{E}_0} = \frac{3\sqrt{3}}{2} a_0(\mu)\varepsilon \approx \frac{3\sqrt{3(2+\mu)}}{2t_0} \sqrt{\frac{|\beta_2|}{P_0\gamma}}. \quad (6.45)$$

From equation (6.45) one can note that by tweaking the chirp μ one can increase/decrease the energy transfer rate to the rogue wave.

Using (6.39) for the PS duration and (6.44) for the energy stored in the PS we obtain the *universal energy relation* for the rogue wave compression:

$$E_{PS}\Delta_{PS} = 3\sqrt{6} \frac{|\beta_2|}{\gamma}, \quad (6.46)$$

which complements the universal rogue wave power relation (6.40).

We note that the universal relations (6.40) and (6.46), actually represent general properties of the PS solution (6.36). The novelty here is the application to the rogue wave compression by taking advantage of the fundamental nature of the PS as universal regularising process of gradient

catastrophe. Importantly, these relations *do not depend on the input pulse parameters* (provided ε is sufficiently small to guarantee the Bertola-Tovbis scenario).

6.6 Summary

The main findings of this Chapter can be summarised as follows.

- The compression of broad light pulses in optical fibres in highly nonlinear propagation regimes is a complex multi-scale problem with two distinct stages of the evolution: (i) the initial “slow” compression leading to the formation of the gradient catastrophe, a point with infinite derivative at the pulse centre; followed by (ii) the “fast” rogue wave compression accompanied by the generation of a narrow high-amplitude peak.
- We have identified the semi-classical NLS approximation as an appropriate mathematical framework to model the evolution of light pulses in highly nonlinear propagation regimes. Within this modelling, the rogue wave compression has previously been shown to be universally described by the so-called Peregrine Soliton solution of the fNLSE.
- The higher order effects (the intrapulse Raman scattering, the third order dispersion and the self-steepening) are accounted for by using the generalised and non-local NLS equations. These effects, in particular, lead to the secondary rogue wave compression, which can exceed in the peak power the primary rogue wave.
- The semi-classical analysis yields an accurate formula (6.35) for the distance at which the rogue wave compression occurs along the fibre; it also gives an accurate prediction for the rogue wave peak power (6.38). These results are numerically verified to hold well for Gaussian pulses in the highly nonlinear regimes of propagation governed by the gNLSE. The rogue wave compression distance, as well as the peak power, can be manipulated by varying the chirp of the input pulse.

Appendix 1 : Numerical Code Testing

To verify quantitative validity and accuracy of our numerical code for the pulse propagation, we have performed a number of tests by applying the code to several reduced versions of the gNLSE for which particular analytical solutions are known and can be found in the literature [9]. The testing has been performed by retaining the necessary term(s) in the gNLSE while “switching off” all other terms. Some results are presented in Fig. 1.

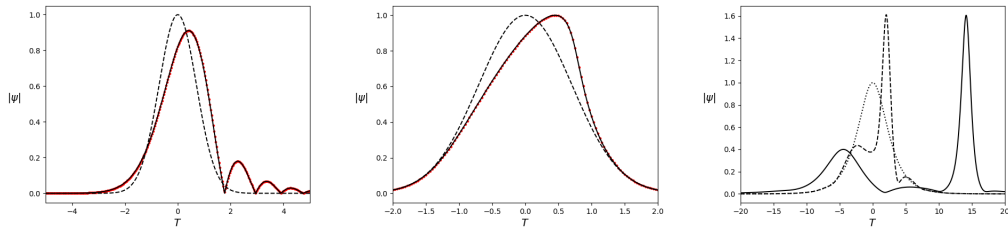


Figure 30: Comparison of numerical solutions of the gNLSE (6.7) with known particular solutions [9] for pulse propagation. **Left:** Third-order dispersion: (dashed) Gaussian shape initial pulse with $T_0^2 = 1/2$, (red dots) output of the numerical simulation for the third dispersion coefficient $\beta_3' = 0.01$ and the propagation length $Z = 10$, (solid line) analytical expression of the evolved signal. **Middle:** Self-steepening: (dashed) Gaussian shape initial condition, (red dots) output of the numerical simulation for $C_s = 0.01$ (self-steepening coefficient) and $Z = 15$, (solid line) analytical expression of the signal at $Z = 15$. **Right:** Intrapulse Raman scattering: soliton fission of the two-soliton initial condition (dotted line). The evolution is shown at $Z = 6$ (dashed line) and $Z = 16$ (solid line). The results fully agree with those available in [9].

Chapter 7

Conclusion and Outlook

7.1 Conclusions

In this PhD project we have investigated several problems related to the emergence, control and manipulation of rogue waves (RWs)—large-amplitude localised coherent structures spontaneously generated in the evolution of nonlinear random wave fields. The original motivation for the project comes from the fibre optics applications, where RWs represent high-power fluctuations of an incoherent optical wave field that can, in principle, lead to a damage of the fibre. In a different context, RWs can have a detrimental effect on the signal propagation in optical telecommunication systems. The basic model for the optical signal propagation through a fibre is the nonlinear Schrödinger (NLS) equation, which is an integrable equation amenable to exact analytical methods such as the Inverse Scattering Transform and Finite-Gap Integration. RWs occur in the self-focusing regime of propagation, corresponding to the anomalous dispersion case in the fibre optics context and described by the version of NLS called the focusing NLS equation (fNLSE), which is also a standard model for propagation of quasi-monochromatic weakly nonlinear wave packets on deep water.

The particular emphasis in the Thesis has been on the study of RWs emerging in the propagation of the so-called partially coherent waves that can be viewed as random infinite sequences of broad pulses. The natural scale separation between the coherence scale of the system (the typical width/duration of a soliton) and the typical scale/duration of the input pulses suggests the use

of asymptotic methods such as semi-classical analysis or modulation theory. The fundamental proposition of the Thesis is that the RW emergence in the evolution of partially coherent waves in optical fibres and in deep-water gravity waves (e.g. in a 1D water tank) can be effectively described within the framework of the semi-classical fNLSE. The study of random wave solution to the fNLSE falls into the general area of integrable turbulence, and it has been shown in the Thesis that the semi-classical approximation in integrable turbulence enables explicit analytical results in the problems that, until recently, had only been amenable to numerical methods.

The study of the RW formation in this project has also prompted the analytical and numerical investigation of soliton and breather gases representing particular, yet very important, classes of integrable turbulence that can be realised in nonlinear optics and water wave systems. The main contributions of the Thesis in this direction are the construction of analytical kinetic theory of soliton gases in bidirectional systems (e.g. dispersive shallow water equations) and the numerical synthesis of breather gases for the focusing NLS equation.

The results reported in this Thesis have been obtained in collaboration with my supervisors, Prof. Gennady El (Northumbria University) and Prof. Stéphane Randoux (Lille University, France) and members of their research teams. The water tank experiment has been performed at École Centrale de Nantes in collaboration with several research teams from France and USA. The part of the project related to the RW compression of optical pulses in highly nonlinear regimes of propagation has been performed under the Research Contract with LumOptica Ltd.

The main results of the project can be summarised as follows

(i) The short-time evolution of partially coherent waves within the mathematical framework of the semi-classical NLS equation in the focusing and defocusing regimes of propagation has been studied. It has been shown that the initial stage of evolution of partially coherent waves is described by the dispersionless (nonlinear geometric optics) approximation of the NLS equation and derived a simple analytic formula for the normalised fourth moment κ_4 (the kurtosis) of the corresponding random wave field. This approximate formula, applied to the problem of the NLS evolution of random waves initially having Gaussian statistics, has been shown to describe the formation of heavy tails of the probability density function of the random field amplitude in the focusing case and the formation of low tails in the defocusing case. The analytical results have been shown

to be in excellent agreement with direct numerical simulations of the partially coherent wave propagation in the full dispersive NLS dynamics.

(ii) We have realised the mathematically predicted universal mechanism of the local emergence of a Peregrine Soliton (PS) in the semi-classical fNLSE dynamics (Bertola and Tovbis [46]) in a water tank experiment. By employing the inverse scattering transform (ISTs) for the synthesis of the initial data, we have produced a localised wave packet with a prescribed solitonic content. In accordance with the theory, the local PS emergence was observed irrespectively of the amount of discrete spectrum in the input signal, the latter only affected the position of the PS emergence following the gradient catastrophe. This has enabled us to manipulate the RW generation by adjusting the inverse scattering spectrum of the input pulse. The proposed method of *nonlinear spectral engineering* was found to be robust to higher-order nonlinear effects inevitable in realistic wave propagation conditions.

(iii) The spectral kinetic theory theory of soliton gases in bidirectional integrable Eulerian systems has been developed. We identified two qualitatively different types of bidirectional soliton gases: isotropic gases, in which the position shifts accompanying the head-on and overtaking soliton collisions have the same sign, and anisotropic gases, in which the position shifts for head-on and overtaking collisions have opposite signs. Kinetic equations describing the evolution of the spectral distribution function for both types of bidirectional soliton gases have been constructed. The Riemann (shock tube) problem for the collision “monochromatic” soliton beams has been solved. Concrete examples of bidirectional Eulerian soliton gases for the defocusing NLS equation and the resonant NLS equation have been considered and the Riemann problem solutions have been shown to be in excellent agreement with direct numerical simulations.

(iv) An effective numerical algorithm of the ISTs spectral synthesis of breather gases (BGs) for the fNLSE has been developed. The algorithm is based on the recursive Darboux transform scheme realised in high-precision arithmetics. Using this algorithm, we have synthesised numerically three types of BGs consisting of standard breathers: the gases of Akhmediev breathers, Kuznetsov-Ma breathers, and Peregrine solitons. The propagation of a generic (Tajiri-Watanabe) breather through the three model BGs has been considered and the results of the numerical simulations have been compared with the analytical predictions following from the spectral theory of breather

gases recently developed in [53]. The comparison showed an excellent agreement confirming the validity of the spectral theory of BGs. As a by-product of this research the new expression for the position shift in two-breather collisions obtained in [53] has been identified with the expressions derived in previous works [131, 132].

(v) Rogue Wave compression of broad optical pulses in fibres has been studied for the highly nonlinear regimes of propagation when the “nonintegrable” corrections to the fNLSE describing the effects of intrapulse Raman scattering, self-steepening and the third order dispersion become important. By applying the semi-classical approximation to the generalised fNLSE we have studied the process of the gradient catastrophe formation and have shown numerically that, while the higher order effects significantly modify the parameters of the RWs emerging after gradient catastrophe, the point of their emergence can be rather accurately estimated using the Bertola-Tovbis results for the “core” integrable fNLSE dynamics. This, in particular, enables the application of the methods of nonlinear spectral engineering developed in Chapter 3 for the effective manipulation of RWs in strongly nonlinear regimes of propagation in optical fibres.

7.2 Future research

The research presented in this Thesis suggests a number of interesting and important problems for future research. Some of these problems are already under active investigation.

One of the major problems inspired by this project is a comprehensive analytical description of the “semi-classical” integrable turbulence. In the context of fNLSE this would include the determination of the evolution of the kurtosis $\kappa_4(t)$ for partially coherent waves. In this Thesis we have only produced the asymptotic formula for $\kappa_4(t)$ for $t \ll 1$. At the same time, the numerical results of [6] strongly suggest that the fNLSE evolution of partially coherent waves with initially Gaussian statistics with $\kappa_4(0) = 2$ exhibits the following properties: (i) $\kappa_4(t) = 4$ as $t \rightarrow \infty$; (ii) the position in time of the overshoot in the graph of κ_4 (see Fig. 16) correlates with the time interval of the most probable emergence of the Peregrine Solitons due to the Bertola-Tovbis scenario [46]. The analytical interpretation of these properties would require incorporating the deterministic Bertola-Tovbis semi-classical results into the statistical setting of integrable turbulence. The

understanding of the kurtosis evolution in the course of the random wave propagation will enable the analytical description of the heavy tail effect, which is the well-established statistical signature of the RW presence in the nonlinear wave field.

The nonlinear spectral engineering method for the prediction and manipulation of the RW emergence developed in this Thesis the context of deep-water waves can be applied to fibre optics pulse compression. The next step in the development of the method would involve its application to partially coherent waves. One can expect that this would allow one to control the RW overshoot in the kurtosis curve $\kappa_4(t)$ by applying an appropriately chosen chirp to an input signal. This research, in fact, was one of the original objectives of the project but the planned fibre optics experiments in Lille have been interrupted by the Covid pandemic. It is expected that these experiments will resume in 2021/22

The kinetic theory for bidirectional soliton gases constructed in the Thesis is based on the soliton collision rate ansatz proposed in [49]. A rigorous justification of the developed theory via the thermodynamic limit of multiphase Whitham equations [48, 53] represents an outstanding problem. Another direction of research suggested by the developed kinetic theory is the experimental realisation of soliton gases in bidirectional systems (e.g. shallow water waves) and comparison of the experimental results with the theoretical predictions, particularly for the Riemann problems.

The numerical algorithm for the spectral synthesis of breather gases developed in the Thesis for the fNLSE can be applied to other integrable equations exhibiting breather solutions, in particular, the focusing modified KdV equation and vector NLS equation.

Appendix A

Position shift in two breather interactions

In the literature, the position shift characterising the two-breather interaction has been studied and derived with different techniques [53, 131, 132]. However, the equivalence between the expressions derived in these works is far from obvious. Here we want to demonstrate the equivalence between the formula derived in [53], and used in Chapter 5:

$$\Delta(\lambda, \mu) = \frac{1}{\underbrace{2\text{Im}[R_0(\lambda)]}_{T1}} \left[\ln \underbrace{\left| \frac{\mu - \bar{\lambda}}{\mu - \lambda} \right|^2}_{T2} + \ln \underbrace{\left| \frac{R_0(\lambda)R_0(\mu) + \lambda\mu - \delta_0^2}{R_0(\bar{\lambda})R_0(\mu) + \bar{\lambda}\mu - \delta_0^2} \right|^2}_{T3} \right], \quad (\text{A.1})$$

where $R_0(z) = \sqrt{z^2 - \delta_0^2}$ ($\delta_0 = iq_0$ being the endpoint of the branch cut corresponding to the plane wave), and the expression obtained in [131]:

$$\Delta\bar{\xi}_2 = -\ln(\xi_0)/(c_{-,2} \cos \alpha_2), \quad (\text{A.2})$$

where

$$\xi_0 = \frac{d_+ - 2(\cos(\alpha_1 - \alpha_2) + c_{-,1}c_{-,2}) \cos(\alpha_1 - \alpha_2)}{d_+ - 2(\cos(\alpha_1 + \alpha_2) - c_{-,1}c_{-,2}) \cos(\alpha_1 + \alpha_2)}, \quad (\text{A.3})$$

with

$$\begin{aligned}
 c_{\pm,j} &= z_j \pm q_0^2/z_j, & \lambda_j &= (\zeta_j - q_0^2/\zeta_j)/2, \\
 d_{\pm,j} &= z_j^2 \pm q_0^4/z_j^2, & d_+ &= d_{+,1} + d_{+,2}, \\
 R_0(\lambda_j) &= (\zeta_j + q_0^2/\zeta_j)/2, & \zeta_j &= R_0(\lambda_j) + \lambda_j = iz_j e^{i\alpha_j}.
 \end{aligned} \tag{A.4}$$

Note that $\lambda(k)$ in [131] corresponds to $R_0(k)$ in our notation, whereas in this thesis λ has been chosen to represent the points of the IST discrete spectrum. To map expression (A.1) into (A.2)-(A.4) (i.e to verify the identity $\Delta\bar{\xi}_2 = \Delta(\lambda_2, \lambda_1)$), one can substitute (A.4) in (A.1) and invoke the identities:

- $|\lambda_i|^2 = (|\zeta_i|^2 + q_0^4/|\zeta_i|^2 - q_0^2\zeta_i/\zeta_i^* - q_0^2\zeta_i^*/\zeta_i)/4 = (d_{+,i} + 2q_0^2 \cos \alpha_i)/4,$
- $(\cos 2\alpha_1 + \cos 2\alpha_2)/2 = \cos(\alpha_1 + \alpha_2) \cos(\alpha_1 - \alpha_2),$
- $d_+ = z_1^2 + z_2^2 + \frac{q_0^4}{z_1^2} + \frac{q_0^4}{z_2^2} = \left(z_1 z_2 + \frac{q_0^4}{z_1 z_2}\right) \left(\frac{z_1}{z_2} + \frac{z_2}{z_1}\right).$

To better handle the computation we consider separately the three different terms T1, T2 and T3 from (A.1).

First we consider the term T1 in (A.1)

$$\begin{aligned}
 \text{T1 : } \quad 2\text{Im}[R_0(\lambda_2)] &= -i[(\zeta_2 + q_0^2/\zeta_2)/2] - [(\zeta_2 + q_0^2/\zeta_2)/2]^* \\
 &= -i(\zeta_2 - \zeta_2^* + q_0^2/\zeta_2 - q_0^2/\zeta_2^*) \\
 &= -i(i z_2 \cos \alpha_2 - q_0^2 i/z_2 \cos \alpha_2) \\
 &= (z_2 - q_0^2/z_2) \cos \alpha_2 = c_{-,2} \cos \alpha_2.
 \end{aligned} \tag{A.5}$$

Then, computing the term T2, we obtain:

$$\begin{aligned}
 \text{T2 : } \quad & \left| \frac{\lambda_1 - \lambda_2^*}{\lambda_1 - \lambda_2} \right|^2 = \frac{|\lambda_1|^2 + |\lambda_2|^2 - \lambda_1 \lambda_2 - \lambda_1^* \lambda_2^*}{|\lambda_1|^2 + |\lambda_2|^2 - \lambda_1 \lambda_2^* - \lambda_1^* \lambda_2} \\
 &= \frac{d_+ + 2q_0^2(\cos \alpha_1 + \cos \alpha_2) - \left(\zeta_1 - \frac{q_0^2}{\zeta_1}\right) \left(\zeta_2 - \frac{q_0^2}{\zeta_2}\right) - \left(\zeta_1^* - \frac{q_0^2}{\zeta_1^*}\right) \left(\zeta_2^* - \frac{q_0^2}{\zeta_2^*}\right)}{d_+ + 2q_0^2(\cos \alpha_1 + \cos \alpha_2) - \left(\zeta_1 - \frac{q_0^2}{\zeta_1}\right) \left(\zeta_2^* - \frac{q_0^2}{\zeta_2^*}\right) - \left(\zeta_1^* - \frac{q_0^2}{\zeta_1^*}\right) \left(\zeta_2 - \frac{q_0^2}{\zeta_2}\right)} \\
 &= \frac{d_+ + 4q_0^2 \cos(\alpha_1 + \alpha_2) \cos(\alpha_1 - \alpha_2) + 2 \left(z_1 z_2 + \frac{q_0^4}{z_1 z_2}\right) \cos(\alpha_1 + \alpha_2) + 2q_0^2 \left(\frac{z_1}{z_2} + \frac{z_2}{z_1}\right) \cos(\alpha_1 - \alpha_2)}{d_+ + 4q_0^2 \cos(\alpha_1 + \alpha_2) \cos(\alpha_1 - \alpha_2) - 2 \left(z_1 z_2 + \frac{q_0^4}{z_1 z_2}\right) \cos(\alpha_1 - \alpha_2) - 2q_0^2 \left(\frac{z_1}{z_2} + \frac{z_2}{z_1}\right) \cos(\alpha_1 + \alpha_2)} \\
 &= \left[\frac{\left(\frac{z_1}{z_2} + \frac{z_2}{z_1}\right) + 2 \cos(\alpha_1 + \alpha_2)}{\left(\frac{z_1}{z_2} + \frac{z_2}{z_1}\right) - 2 \cos(\alpha_1 - \alpha_2)} \right] \left[\frac{\left(z_1 z_2 + \frac{q_0^4}{z_1 z_2}\right) + 2q_0^2 \cos(\alpha_1 - \alpha_2)}{\left(z_1 z_2 + \frac{q_0^4}{z_1 z_2}\right) - 2q_0^2 \cos(\alpha_1 + \alpha_2)} \right].
 \end{aligned}$$

(A.6)

And lastly we compute the term T3:

$$\begin{aligned}
 \text{T3} &: \left| \frac{R_0(\lambda_2)R_0(\lambda_1) + \lambda_2\lambda_1 + q_0^2}{R_0(\lambda_2^*)R_0(\lambda_1) + \lambda_2^*\lambda_1 + q_0^2} \right|^2 \\
 &= \left| \frac{(\zeta_2 + q_0^2/\zeta_2)(\zeta_1 + q_0^2/\zeta_1) + (\zeta_2 - q_0^2/\zeta_2)(\zeta_1 - q_0^2/\zeta_1) + 4q_0^2}{(\zeta_2^* + q_0^2/\zeta_2^*)(\zeta_1 + q_0^2/\zeta_1) + (\zeta_2^* - q_0^2/\zeta_2^*)(\zeta_1 - q_0^2/\zeta_1) + 4q_0^2} \right|^2 \\
 &= \left| \frac{2\left(\zeta_2\zeta_1 + \frac{q_0^4}{\zeta_2\zeta_1}\right) + 4q_0^2}{2\left(\zeta_2^*\zeta_1 + \frac{q_0^4}{\zeta_2^*\zeta_1}\right) + 4q_0^2} \right|^2 = \left| \frac{-2\left[z_2z_1e^{i(\alpha_1+\alpha_2)} + \frac{q_0^4}{z_2z_1}e^{-i(\alpha_1+\alpha_2)}\right] + 4q_0^2}{2\left[z_2z_1e^{i(\alpha_1-\alpha_2)} + \frac{q_0^4}{z_2z_1}e^{-i(\alpha_1-\alpha_2)}\right] + 4q_0^2} \right|^2 \\
 &= \left| \frac{-2\left[z_2z_1e^{i(\alpha_1+\alpha_2)} + \frac{q_0^4}{z_2z_1}e^{-i(\alpha_1+\alpha_2)}\right] + 4q_0^2}{2\left[z_2z_1e^{i(\alpha_1-\alpha_2)} + \frac{q_0^4}{z_2z_1}e^{-i(\alpha_1-\alpha_2)}\right] + 4q_0^2} \right|^2 \tag{A.7} \\
 &= \frac{16q_0^4 - 16q_0^2\left(z_1z_2 + \frac{q_0^4}{z_1z_2}\right)\cos(\alpha_1 + \alpha_2) + 4\left(z_1^2z_2^2 + \frac{q_0^8}{z_1^2z_2^2}\right) + 8q_0^4\cos(2(\alpha_1 + \alpha_2))}{16q_0^4 + 16q_0^2\left(z_1z_2 + \frac{q_0^4}{z_1z_2}\right)\cos(\alpha_1 - \alpha_2) + 4\left(z_1^2z_2^2 + \frac{q_0^8}{z_1^2z_2^2}\right) + 8q_0^4\cos(2(\alpha_1 - \alpha_2))} \\
 &= \frac{-16q_0^2\left(z_1z_2 + \frac{q_0^4}{z_1z_2}\right)\cos(\alpha_1 + \alpha_2) + 4\left(z_1z_2 + \frac{q_0^4}{z_1z_2}\right)^2 + 16q_0^4\cos^2(\alpha_1 + \alpha_2)}{16q_0^2\left(z_1z_2 + \frac{q_0^4}{z_1z_2}\right)\cos(\alpha_1 - \alpha_2) + 4\left(z_1z_2 + \frac{q_0^4}{z_1z_2}\right)^2 + 16q_0^4\cos^2(\alpha_1 - \alpha_2)} \\
 &= \frac{\left[\left(z_1z_2 + \frac{q_0^4}{z_1z_2}\right) - 2q_0^2\cos(\alpha_1 + \alpha_2)\right]^2}{\left[\left(z_1z_2 + \frac{q_0^4}{z_1z_2}\right) + 2q_0^2\cos(\alpha_1 - \alpha_2)\right]^2}.
 \end{aligned}$$

Combining the terms T2 and T3 to obtain the argument of the logarithm in (A.1), we can write:

$$\begin{aligned}
 \text{T2} \times \text{T3} &: \left| \frac{\lambda_1 - \lambda_2^*}{\lambda_1 - \lambda_2} \right|^2 \left| \frac{R_0(\lambda_2)R_0(\lambda_1) + \lambda_2\lambda_1 + q_0^2}{R_0(\lambda_2^*)R_0(\lambda_1) + \lambda_2^*\lambda_1 + q_0^2} \right|^2 = \left[\frac{\left(\frac{z_1}{z_2} + \frac{z_2}{z_1}\right) + 2\cos(\alpha_1 + \alpha_2)}{\left(\frac{z_1}{z_2} + \frac{z_2}{z_1}\right) - 2\cos(\alpha_1 - \alpha_2)} \right] \\
 &\times \left[\frac{\left(z_1z_2 + \frac{q_0^4}{z_1z_2}\right) + 2q_0^2\cos(\alpha_1 - \alpha_2)}{\left(z_1z_2 + \frac{q_0^4}{z_1z_2}\right) - 2q_0^2\cos(\alpha_1 + \alpha_2)} \right] \left[\frac{\left(z_1z_2 + \frac{q_0^4}{z_1z_2}\right) - 2q_0^2\cos(\alpha_1 + \alpha_2)}{\left(z_1z_2 + \frac{q_0^4}{z_1z_2}\right) + 2q_0^2\cos(\alpha_1 - \alpha_2)} \right]^2 \\
 &= \frac{\left[\left(\frac{z_1}{z_2} + \frac{z_2}{z_1}\right) + 2\cos(\alpha_1 + \alpha_2)\right] \left[\left(z_1z_2 + \frac{q_0^4}{z_1z_2}\right) - 2q_0^2\cos(\alpha_1 + \alpha_2)\right]}{\left[\left(\frac{z_1}{z_2} + \frac{z_2}{z_1}\right) - 2\cos(\alpha_1 - \alpha_2)\right] \left[\left(z_1z_2 + \frac{q_0^4}{z_1z_2}\right) + 2q_0^2\cos(\alpha_1 - \alpha_2)\right]} \\
 &= \frac{\left(z_1z_2 + \frac{q_0^4}{z_1z_2}\right)\left(\frac{z_1}{z_2} + \frac{z_2}{z_1}\right) - 2q_0^2\cos(\alpha_1 + \alpha_2)\left[2\cos(\alpha_1 + \alpha_2) + \left(\frac{z_1}{z_2} + \frac{z_2}{z_1}\right) - \left(z_1z_2 + \frac{q_0^4}{z_1z_2}\right)\right]}{\left(z_1z_2 + \frac{q_0^4}{z_1z_2}\right)\left(\frac{z_1}{z_2} + \frac{z_2}{z_1}\right) - 2q_0^2\cos(\alpha_1 - \alpha_2)\left[2\cos(\alpha_1 - \alpha_2) - \left(\frac{z_1}{z_2} + \frac{z_2}{z_1}\right) + \left(z_1z_2 + \frac{q_0^4}{z_1z_2}\right)\right]} \\
 &= \frac{d_+ - 2q_0^2\cos(\alpha_1 + \alpha_2)[2\cos(\alpha_1 + \alpha_2) - c_{-,1}c_{-,2}]}{d_+ - 2q_0^2\cos(\alpha_1 - \alpha_2)[2\cos(\alpha_1 - \alpha_2) + c_{-,1}c_{-,2}]} = \xi_0^{-1}.
 \end{aligned}$$

(A.8)

Finally combining all the terms from equation (A.1), we obtain:

$$\Delta(\lambda_2, \lambda_1) = \ln(\xi_0^{-1})/(c_{-,2} \cos \alpha_2) = -1 \ln(\xi_0)/(c_{-,2} \cos \alpha_2) \equiv \Delta \bar{\xi}_2, \quad (\text{A.9})$$

i.e. we verify the equivalence of the expression (A.2) with the expression (A.1).

Acronyms

AB	Akhmediev breather
ABG	Akhmediev Breather Gas
BG	Breather Gas
dNLSE	Defocusing Nonlinear Schrödinger Equation
DOS	Density of States
DSW	Dispersive Shock Waves
FGT	Finite Gap Theory
fNLSE	Focusing Nonlinear Schrödinger Equation
gNLSE	Generalised Nonlinear Schrödinger Equation
IST	Inverse Scattering Transform
KB	Kaup-Boussinesq
KdV	Korteweg-de Vries
KM	Kuznetsov-Ma breather
KMBG	Kuznetsov-Ma Breather Gas
MI	Modulational Instability

Acronyms

NLS	Nonlinear Schrödinger
PBG	Peregrine Breather Gas
PCW	Partially Coherent Waves
PDE	Partially Differential Equation
PDF	Probability Density Function
PS	Peregrine soliton
rNLSE	Resonant Nonlinear Schrödinger Equation
RW	Rogue Wave
SFB	Soliton on a Finite Background
TOD	Third-Order-Dispersion
TW	Tajiri-Watanabe

References

- [1] M. Ding, D. Fan, W. Wang, Y. Luo, and G.-D. Peng. *Basics of Optical Fiber Measurements*, pages 1–39. Springer Singapore, Singapore, 2018.
- [2] M. Onorato, A. R. Osborne, M. Serio, L. Cavaleri, C. Brandini, and C. T. Stansberg. Observation of strongly non-gaussian statistics for random sea surface gravity waves in wave flume experiments. *Phys. Rev. E*, 70:067302, Dec 2004.
- [3] M. Bertola, G. A. El, and A. Tovbis. Rogue waves in multiphase solutions of the focusing nonlinear Schrödinger equation. *Proc. Math. Phys. Eng. Sci.*, 472(2194):20160340, October 2016.
- [4] A. Tikan, C. Billet, G. El, A. Tovbis, M. Bertola, T. Sylvestre, F. Gustave, S. Randoux, G. Genty, P. Suret, and J. M. Dudley. Universality of the peregrine soliton in the focusing dynamics of the cubic nonlinear schrödinger equation. *Phys. Rev. Lett.*, 119:033901, Jul 2017.
- [5] A. E. Kraych, D. Agafontsev, S. Randoux, and P. Suret. Statistical Properties of the Non-linear Stage of Modulation Instability in Fiber Optics. *Phys. Rev. Lett.*, 123(9), August 2019.
- [6] A. Tikan. Effect of local peregrine soliton emergence on statistics of random waves in the one-dimensional focusing nonlinear schrödinger equation. *Phys. Rev. E*, 101(1):012209, 2020.
- [7] F. Carbone, D. Dutykh, and G. El. Macroscopic dynamics of incoherent soliton ensembles: Soliton gas kinetics and direct numerical modelling. *EPL*, 113(3):30003, 2016.

REFERENCES

- [8] S. Randoux, P. Suret, and G. El. Inverse scattering transform analysis of rogue waves using local periodization procedure. *Sci. Rep.*, 6:29238, July 2016.
- [9] G. P. Agrawal. Nonlinear fiber optics. In *Nonlinear Science at the Dawn of the 21st Century*, pages 195–211. Springer, 2000.
- [10] N. J. Zabusky and M. D. Kruskal. Interaction of "Solitons" in a Collisionless Plasma and the Recurrence of Initial States. *Phys. Rev. Lett.*, 15(6):240, 1965.
- [11] C. S. Gardner, J. M. Greene, M. D. Kruskal, and R. M. Miura. Method for Solving the Korteweg-deVries Equation. *Phys. Rev. Lett.*, 19(19):1095–1097, November 1967.
- [12] G. B. Whitham. *Linear and Nonlinear Waves*. John Wiley & Sons, Inc., Jun 1999.
- [13] A. Osborne and T. Burch. Internal solitons in the andaman sea. *Science*, 208(4443):451–460, 1980.
- [14] L. Ostrovsky and Y. A. Stepanyants. Do internal solitons exist in the ocean? *Reviews of Geophysics*, 27(3):293–310, 1989.
- [15] R. H. Grimshaw, L. Ostrovsky, V. Shrira, and Y. A. Stepanyants. Long nonlinear surface and internal gravity waves in a rotating ocean. *Surveys in Geophysics*, 19(4):289–338, 1998.
- [16] Y. Kivshar and G. Agrawal. *Optical Solitons: From Fibers to Photonic Crystals*. Elsevier sci., 2003.
- [17] A. Hasegawa. Optical solitons in fibers. In *Optical solitons in fibers*, pages 1–74. Springer, 1989.
- [18] J. R. Taylor. *Optical Solitons: Theory and Experiment*. Cambridge University Press, April 1992. Google-Books-ID: nZRffsTBnYoC.
- [19] V. E. Zakharov. Stability of periodic waves of finite amplitude on the surface of a deep fluid. *J. Appl. Mech. Tech. Phys.*, 9(2):190–194, 1968.
- [20] D. J. Benney and A. C. Newell. The propagation of nonlinear wave envelopes. *Journal of mathematics and Physics*, 46(1-4):133–139, 1967.

REFERENCES

- [21] V. Talanov. Self focusing of wave beams in nonlinear media. *ZhETF Pisma Redaktsiiu*, 2:218, 1965.
- [22] P. Kelley. Self-focusing of optical beams. *Physical Review Letters*, 15(26):1005, 1965.
- [23] V. E. Zakharov and A. B. Shabat. Exact theory of two-dimensional self-focusing and one-dimensional self-modulation of waves in nonlinear media. *J. Exp. Theor. Phys.*, 34:62–69, 1972.
- [24] V. E. Zakharov and A. B. Shabat. Interaction between solitons in a stable medium. *Sov. Phys. JETP*, 37(5):823–828, 1973.
- [25] E. D. Belokolos, A. I. Bobenko, V. Z. Enolski, A. R. Its, and V. B. Matveev. *Algebro-geometric approach to nonlinear integrable equations*. Springer, New York, 1994.
- [26] A. Osborne. *Nonlinear Ocean Waves and the Inverse Scattering Transform*, volume 97. Academic Press, 2010.
- [27] D. H. Peregrine. Water waves, nonlinear schrödinger equations and their solutions. *ANZIAM J.*, 25(1):16–43, 1983.
- [28] N. Akhmediev, J. Soto-Crespo, and A. Ankiewicz. Extreme waves that appear from nowhere: On the nature of rogue waves. *Phys. Lett. A*, 373(25):2137–2145, 2009.
- [29] M. Onorato, A. R. Osborne, M. Serio, and S. Bertone. Freak waves in random oceanic sea states. *Physical review letters*, 86(25):5831, 2001.
- [30] P. K. D. R. Solli, C. Ropers and B. Jalali. Optical rogue waves. *Nature*, 450:1054–1057, Dec 2007.
- [31] M. Onorato, S. Residori, U. Bortolozzo, A. Montina, and F. Arecchi. Rogue waves and their generating mechanisms in different physical contexts. *Phys. Rep.*, 528(2):47–89, 2013. Rogue waves and their generating mechanisms in different physical contexts.
- [32] S. Nazarenko. *Wave Turbulence*. Lecture Notes in Physics. Springer-Verlag Berlin Heidelberg, 1 edition, 2011.

REFERENCES

- [33] M. Onorato, D. Proment, G. El, S. Randoux, and P. Suret. On the origin of heavy-tail statistics in equations of the nonlinear schrödinger type. *Phys. Lett. A*, 380(39):3173–3177, 2016.
- [34] R. El Koussaifi, A. Tikan, A. Toffoli, S. Randoux, P. Suret, and M. Onorato. Spontaneous emergence of rogue waves in partially coherent waves: A quantitative experimental comparison between hydrodynamics and optics. *Phys. Rev. E*, 97(1):012208, 2018.
- [35] S. Randoux, P. Walczak, M. Onorato, and P. Suret. Nonlinear random optical waves: Integrable turbulence, rogue waves and intermittency. *Physica D*, 333:323–335, 2016.
- [36] D. Agafontsev, S. Randoux, and P. Suret. Extreme rogue wave generation from narrowband partially coherent waves. *Physical Review E*, 103(3):032209, 2021.
- [37] V. E. Zakharov. Turbulence in integrable systems. *Stud Appl Math*, 122(3):219–234, 2009.
- [38] A. Monin and A. Yaglom. *Statistical Fluid Mechanics Mechanics of Turbulence V.1,2*. Dover Publications, 1 edition, 2013.
- [39] V. E. Zakharov, V. S. L'vov, and G. Falkovich. *Kolmogorov spectra of turbulence I: Wave turbulence*. Springer Science & Business Media, 2012.
- [40] P. Walczak, S. Randoux, and P. Suret. Optical rogue waves in integrable turbulence. *Phys. Rev. Lett.*, 114:143903, Apr 2015.
- [41] D. S. Agafontsev and V. E. Zakharov. Integrable turbulence and formation of rogue waves. *Nonlinearity*, 28(8):2791, 2015.
- [42] M. Onorato, D. Proment, G. Clauss, and M. Klein. Rogue waves: from nonlinear schrödinger breather solutions to sea-keeping test. *PloS one*, 8(2):e54629, 2013.
- [43] T. B. Benjamin. Instability of periodic wavetrains in nonlinear dispersive systems. *Proc. Math. Phys. Eng. Sci.*, 299(1456):59–76, 1967.
- [44] B. Kibler, J. Fatome, C. Finot, G. Millot, F. Dias, G. Genty, N. Akhmediev, and J. M. Dudley. The peregrine soliton in nonlinear fibre optics. *Nat. Phys.*, 6(10):790–795, 2010.
- [45] A. Chabchoub, N. P. Hoffmann, and N. Akhmediev. Rogue wave observation in a water wave tank. *Phys. Rev. Lett.*, 106:204502, May 2011.

REFERENCES

- [46] M. Bertola and A. Tovbis. Universality for the focusing nonlinear Schrödinger equation at the gradient catastrophe point: rational breathers and poles of the tritronquée solution to Painlevé I. *Commun Pure Appl Math*, 66(5):678–752, 2013.
- [47] V. Zakharov. Kinetic equation for solitons. *Sov. Phys. JETP*, 33:538–541, 1971.
- [48] G. El. The thermodynamic limit of the Whitham equations. *Phys. Lett. A*, 311(4-5):374–383, May 2003.
- [49] G. A. El and A. M. Kamchatnov. Kinetic equation for a dense soliton gas. *Phys. Rev. Lett.*, 95:204101, Nov 2005.
- [50] A. Costa, A. R. Osborne, D. T. Resio, S. Alessio, E. Chrivì, E. Saggese, K. Bellomo, and C. E. Long. Soliton turbulence in shallow water ocean surface waves. *Phys. Rev. Lett.*, 113(10):108501, 2014.
- [51] I. Redor, E. Barthélemy, H. Michallet, M. Onorato, and N. Mordant. Experimental Evidence of a Hydrodynamic Soliton Gas. *Phys. Rev. Lett.*, 122(21):214502, 2019.
- [52] P. Suret, A. Tikan, F. Bonnefoy, F. Copie, G. Ducrozet, A. Gelash, G. Prabhudesai, G. Michel, A. Cazaubiel, E. Falcon, et al. Nonlinear spectral synthesis of soliton gas in deep-water surface gravity waves. *Phys. Rev. Lett.*, 125(26):264101, 2020.
- [53] G. El and A. Tovbis. Spectral theory of soliton and breather gases for the focusing nonlinear Schrödinger equation. *Phys. Rev. E*, 101(5):052207, May 2020.
- [54] M. J. Ablowitz. *Nonlinear dispersive waves: asymptotic analysis and solitons*, volume 47. Cambridge University Press, 2011.
- [55] W. Bao. The nonlinear schrödinger equation and applications in bose-einstein condensation and plasma physics. *Dynamics in models of coarsening, coagulation, condensation and quantization*, 9:141–239, 2007.
- [56] M. J. Ablowitz and H. Segur. *Solitons and the inverse scattering transform*. SIAM, 1981.
- [57] E. A. Kuznetsov. Solitons in a parametrically unstable plasma. In *Akademiia Nauk SSSR Doklady*, volume 236, pages 575–577, 1977.

REFERENCES

- [58] Y.-C. Ma. The perturbed plane-wave solutions of the cubic schrödinger equation. *Stud Appl Math*, 60(1):43–58, 1979.
- [59] N. Akhmediev and V. Korneev. Modulation instability and periodic solutions of the nonlinear schrödinger equation. *Theor. Math. Phys.*, 69(2):1089–1093, 1986.
- [60] M. Tajiri and Y. Watanabe. Breather solutions to the focusing nonlinear schrödinger equation. *Phys. Rev. E*, 57(3):3510, 1998.
- [61] N. N. Akhmediev and N. V. Mitzkevich. Extremely high degree of n-soliton pulse compression in an optical fiber. *IEEE J. Quantum Electron.*, 27(3):849–857, 1991.
- [62] T. B. Benjamin and J. E. Feir. The disintegration of wave trains on deep water part 1. theory. *J. Fluid Mech.*, 27(3):417–430, 1967.
- [63] V. E. Zakharov and L. A. Ostrovsky. Modulation instability: the beginning. *Physica D*, 238(5):540–548, 2009.
- [64] T. Taniuti and H. Washimi. Self-trapping and instability of hydromagnetic waves along the magnetic field in a cold plasma. *Phys. Rev. Lett.*, 21(4):209, 1968.
- [65] K. E. Strecker, G. B. Partridge, A. G. Truscott, and R. G. Hulet. Formation and propagation of matter-wave soliton trains. *Nature*, 417(6885):150–153, 2002.
- [66] P. Grinevich and P. Santini. The finite gap method and the analytic description of the exact rogue wave recurrence in the periodic nls cauchy problem. 1. *Nonlinearity*, 31(11):5258, 2018.
- [67] M. Conforti, S. Li, G. Biondini, and S. Trillo. Auto-modulation versus breathers in the nonlinear stage of modulational instability. *Opt. Lett*, 43(21):5291–5294, 2018.
- [68] G. Biondini, S. Li, and D. Mantzavinos. Oscillation structure of localized perturbations in modulationally unstable media. *Phys. Rev. E*, 94(6):060201, 2016.
- [69] G. Biondini, S. Li, D. Mantzavinos, and S. Trillo. Universal behavior of modulationally unstable media. *SIAM Review*, 60(4):888–908, 2018.

REFERENCES

- [70] A. Gurevich, V. Khodorovskii, A. Krylov, et al. Modulational instability and formation of a nonlinear oscillatory structure in a “focusing” medium. *Phys. Lett. A*, 177(4-5):357–361, 1993.
- [71] V. E. Zakharov and A. Gelash. Nonlinear stage of modulation instability. *Phys. Rev. Lett.*, 111(5):054101, 2013.
- [72] A. Gelash and V. E. Zakharov. Superregular solitonic solutions: a novel scenario for the nonlinear stage of modulation instability. *Nonlinearity*, 27(4):R1, 2014.
- [73] B. Kibler, A. Chabchoub, A. Gelash, N. Akhmediev, and V. Zakharov. Superregular breathers in optics and hydrodynamics: omnipresent modulation instability beyond simple periodicity. *Phys. Rev. X*, 5(4):041026, 2015.
- [74] S. Haver. A possible freak wave event measured at the draupner jacket january 1 1995. In *Rogue waves*, volume 2004, pages 1–8, 2004.
- [75] G. F. Clauss. Dramas of the sea: episodic waves and their impact on offshore structures. *Applied Ocean Research*, 24(3):147–161, 2002.
- [76] M. S. Longuet-Higgins. On the statistical distribution of the heights of sea waves. *J. Mar. Res.*, 11(3):245–266, 1952.
- [77] A. Slunyaev, I. Didenkulova, and E. Pelinovsky. Rogue waters. *Contemp. Phys.*, 52(6):571–590, 2011.
- [78] J. M. Dudley, G. Genty, and B. J. Eggleton. Harnessing and control of optical rogue waves in supercontinuum generation. *Opt. Express*, 16(6):3644–3651, 2008.
- [79] A. Ganshin, V. Efimov, G. Kolmakov, L. Mezhev-Deglin, and P. V. McClintock. Observation of an inverse energy cascade in developed acoustic turbulence in superfluid helium. *Phys. Rev. Lett.*, 101(6):065303, 2008.
- [80] A. Montana, U. Bortolozzo, S. Residori, and F. Arecchi. Non-gaussian statistics and extreme waves in a nonlinear optical cavity. *Phys. Rev. Lett.*, 103(17):173901, 2009.
- [81] R. Höhmann, U. Kuhl, H.-J. Stöckmann, L. Kaplan, and E. Heller. Freak waves in the linear regime: A microwave study. *Phys. Rev. Lett.*, 104(9):093901, 2010.

REFERENCES

- [82] V. Shrira and V. Geogjaev. What makes the peregrine soliton so special as a prototype of freak waves? *J. Eng. Math.*, 67(1-2):11–22, 2010.
- [83] N. Akhmediev, A. Ankiewicz, and M. Taki. Waves that appear from nowhere and disappear without a trace. *Phys. Lett. A*, 373(6):675–678, 2009.
- [84] S. Randoux, P. Suret, A. Chabchoub, B. Kibler, and G. El. Nonlinear spectral analysis of peregrine solitons observed in optics and in hydrodynamic experiments. *Phys. Rev. E*, 98:022219, Aug 2018.
- [85] D. Agafontsev, S. Randoux, and P. Suret. Integrable turbulence developing from strongly nonlinear partially coherent waves. *arXiv preprint arXiv:2003.03218*, 2020.
- [86] P. Lax. Integrals of nonlinear equations of evolution and solitary waves. *Comm. Pur. Appl. Math.*, 21:467–490, 1968.
- [87] V. A. Marchenko. On reconstruction of the potential energy from phases of the scattered waves. In *Dokl. Akad. Nauk SSSR*, volume 104, pages 695–698, 1955.
- [88] E. D. Belokolos, A. I. Bobenko, V. Z. Enolski, A. R. Its, and V. B. Matveev. *Algebro-geometric approach to nonlinear integrable equations*. Springer, New York, 1994.
- [89] S. Novikov, S. V. Manakov, L. Pitaevskii, and V. E. Zakharov. *Theory of solitons: the inverse scattering method*. Springer Science & Business Media, 1984.
- [90] A. R. Its and V. P. Kotlyarov. Explicit formulas for solutions of the nonlinear Schrödinger equation. *Doklady Akad. Nauk Ukrainian SSR, ser.A*, 10:965–968, 1976.
- [91] Y. Ma and M. Ablowitz. The periodic cubic nonlinear Schrödinger equation. *Stud.Appl.Math.*, 65:113–158, 1981.
- [92] E. R. Tracy and H. H. Chen. Nonlinear self-modulation: An exactly solvable model. *Phys. Rev. A*, 37(3):815, 1988.
- [93] M. Kamalian, J. E. Prilepsy, S. T. Le, and S. K. Turitsyn. Periodic nonlinear Fourier transform for fiber-optic communications, Part I: theory and numerical methods. *Opt. Express*, 24(16):18353, August 2016.

REFERENCES

- [94] M. Kamalian, A. Vasylichenkova, D. Shepelsky, J. E. Prilepsky, and S. K. Turitsyn. Signal Modulation and Processing in Nonlinear Fibre Channels by Employing the Riemann–Hilbert Problem. *J. Light. Technol.*, 36(24):5714–5727, December 2018.
- [95] M. G. Forest and J.-E. Lee. Geometry and modulation theory for the periodic nonlinear schrodinger equation. In *Oscillation Theory, Computation, and Methods of Compensated Compactness*, pages 35–69. Springer, 1986.
- [96] M. Bertola and A. Tovbis. Maximal amplitudes of finite-gap solutions for the focusing Nonlinear Schrödinger Equation. *Communications in Mathematical Physics*, 354(2):525–547, September 2017.
- [97] E. Madelung. Quantentheorie in hydrodynamischer Form. *Z. Physik*, 40(3-4):322–326, 1927.
- [98] G. El and M. Hoefer. Dispersive shock waves and modulation theory. *Physica D*, 333:11–65, Oct 2016.
- [99] Y. Kodama and S. Wabnitz. Analytical theory of guiding-center nonreturn-to-zero and return-to-zero signal transmission in normally dispersive nonlinear optical fibers. *Opt. Lett.*, 20(22):2291–2293, 1995.
- [100] S. Randoux, F. Gustave, P. Suret, and G. El. Optical random riemann waves in integrable turbulence. *Phys. Rev. Lett.*, 118:233901, Jun 2017.
- [101] B. Dubrovin. On universality of critical behaviour in Hamiltonian PDEs. *arXiv preprint arXiv:0804.3790*, 2008.
- [102] A. Tovbis and S. Venakides. The eigenvalue problem for the focusing nonlinear schrödinger equation: new solvable cases. *Physica D*, 146(1):150–164, 2000.
- [103] A. Tikan, S. Randoux, G. El, A. Tovbis, F. Copie, and P. Suret. Local emergence of peregrine solitons: Experiments and theory. *Front. Phys.*, 8:561, 2021.
- [104] A. Tikan, F. Bonnefoy, G. Roberti, G. El, A. Tovbis, G. Ducrozet, A. Cazaubiel, G. Prabhudesai, G. Michel, F. Copie, et al. Prediction and manipulation of hydrodynamic rogue waves via nonlinear spectral engineering. *arXiv preprint arXiv:2108.02698*, 2021.

REFERENCES

- [105] U. Frisch and A. N. Kolmogorov. *Turbulence: the legacy of AN Kolmogorov*. Cambridge university press, 1995.
- [106] P. Suret, R. El Koussaifi, A. Tikan, C. Evain, S. Randoux, C. Sz waj, and S. Bielawski. Single-shot observation of optical rogue waves in integrable turbulence using time microscopy. *Nat. Commun.*, 7(1):1–8, 2016.
- [107] P. Suret, G. El, M. Onorato, and S. Randoux. Rogue waves in integrable turbulence: semi-classical theory and fast measurements. *Nonlinear Guided Wave Optics*, pages 2053–2563, 2017.
- [108] A. Tikan, S. Bielawski, C. Sz waj, S. Randoux, and P. Suret. Single-shot measurement of phase and amplitude by using a heterodyne time-lens system and ultrafast digital time-holography. *Nat. Photonics*, 12(4):228–234, 2018.
- [109] A. Gelash, D. Agafontsev, V. Zakharov, G. El, S. Randoux, and P. Suret. Bound state soliton gas dynamics underlying the spontaneous modulational instability. *Phys. Rev. Lett.*, 123(23):234102, Dec 2019.
- [110] A. Picozzi, J. Garnier, T. Hansson, P. Suret, S. Randoux, G. Millot, and D. N. Christodoulides. Optical wave turbulence: Towards a unified nonequilibrium thermodynamic formulation of statistical nonlinear optics. *Phys. Rep.*, 542(1):1–132, 2014.
- [111] E. Fermi, P. Pasta, S. Ulam, and M. Tsingou. Studies of the nonlinear problems: Los alamos scientific lab. *N. Mex*, 1955.
- [112] A. Mussot, C. Naveau, M. Conforti, A. Kudlinski, F. Copie, P. Szriftgiser, and S. Trillo. Fibre multi-wave mixing combs reveal the broken symmetry of fermi–pasta–ulam recurrence. *Nat. Photonics*, 12(5):303–308, 2018.
- [113] D. Pierangeli, M. Flammini, L. Zhang, G. Marcucci, A. Agranat, P. Grinevich, P. Santini, C. Conti, and E. DelRe. Observation of fermi-pasta-ulam-tsingou recurrence and its exact dynamics. *Phys. Rev. X*, 8(4):041017, 2018.
- [114] G. Berman and F. Izrailev. The fermi–pasta–ulam problem: fifty years of progress. *Chaos*, 15(1):015104, 2005.

REFERENCES

- [115] S. Randoux, P. Walczak, M. Onorato, and P. Suret. Intermittency in Integrable Turbulence. *Phys. Rev. Lett.*, 113(11):113902, September 2014.
- [116] P. Suret, A. Picozzi, and S. Randoux. Wave turbulence in integrable systems: nonlinear propagation of incoherent optical waves in single-mode fibers. *Opt. Express*, 19(18):17852–17863, 2011.
- [117] J. W. Goodman. *Statistical optics*. John Wiley & Sons, 2015.
- [118] Y. Bromberg, Y. Lahini, E. Small, and Y. Silberberg. Hanbury brown and twiss interferometry with interacting photons. *Nat. Photonics*, 4(10):721–726, 2010.
- [119] S. Derevyanko and E. Small. Nonlinear propagation of an optical speckle field. *Phys. Rev. A*, 85(5):053816, 2012.
- [120] G. Biondini, G. El, M. Hoefer, and P. Miller. Dispersive hydrodynamics: preface, 2016.
- [121] Y. Pomeau, M. Le Berre, P. Guyenne, and S. Grilli. Wave-breaking and generic singularities of nonlinear hyperbolic equations. *Nonlinearity*, 21(5):T61, 2008.
- [122] B. Dubrovin, T. Grava, and C. Klein. On universality of critical behavior in the focusing nonlinear schrödinger equation, elliptic umbilic catastrophe and the tritronquée solution to the painlevé-i equation. *J Nonlinear Sci .*, 19(1):57–94, 2009.
- [123] A. R. Osborne, D. T. Resio, A. Costa, S. P. de León, and E. Chirivì. Highly nonlinear wind waves in currituck sound: dense breather turbulence in random ocean waves. *Ocean Dyn.*, 69(2):187–219, 2019.
- [124] G. A. El. Soliton gas in integrable dispersive hydrodynamics. *J. Stat. Mech. Theory Exp.*, 2021(11):114001, nov 2021.
- [125] E. Pelinovsky, E. Shurgalina, A. Sergeeva, T. Talipova, G. El, and R. Grimshaw. Two-soliton interaction as an elementary act of soliton turbulence in integrable systems. *Phys. Lett. A*, 377(3-4):272–275, January 2013.
- [126] P. G. Drazin and R. S. Johnson. *Solitons: an introduction*, volume 2. Cambridge university press, 1989.

REFERENCES

- [127] G. A. El, A. M. Kamchatnov, M. V. Pavlov, and S. A. Zykov. Kinetic Equation for a Soliton Gas and Its Hydrodynamic Reductions. *J Nonlinear Sci*, 21(2):151–191, April 2011.
- [128] P. D. Lax. *Hyperbolic systems of conservation laws and the mathematical theory of shock waves*. SIAM, 1973.
- [129] S. P. Tsarev. Poisson brackets and one-dimensional Hamiltonian systems of hydrodynamic type. *Sov. math. Dokl.*, 31:488–491, 1985.
- [130] B. Rozhdestvenskii and N. Janenko. *Systems of quasilinear equations and their applications to gas dynamics*. RI: American Mathematical Society, Providence, 1983.
- [131] S. Li and G. Biondini. Soliton interactions and degenerate soliton complexes for the focusing nonlinear schrödinger equation with nonzero background. *Eur. Phys. J. Plus*, 133(10):400, 2018.
- [132] A. Gelash. Formation of rogue waves from a locally perturbed condensate. *Phys. Rev. E*, 97(2):022208, 2018.
- [133] J. P. Boyd. *Chebyshev and Fourier spectral methods*. Courier Corporation, 2001.
- [134] J. Yang. *Nonlinear waves in integrable and nonintegrable systems*. SIAM, 2010.
- [135] G. Boffetta and A. R. Osborne. Computation of the direct scattering transform for the nonlinear schrödinger equation. *J. Comput. Phys.*, 102(2):252–264, 1992.
- [136] J. M. Dudley, F. Dias, M. Erkintalo, and G. Genty. Instabilities, breathers and rogue waves in optics. *Nat. Photonics*, 8:755, Sep 2014.
- [137] S. Toenger, T. Godin, C. Billet, F. Dias, M. Erkintalo, G. Genty, and J. M. Dudley. Emergent rogue wave structures and statistics in spontaneous modulation instability. *Sci. Rep.*, 5, 2015.
- [138] A. Goulet and W. Choi. A numerical and experimental study on the nonlinear evolution of long-crested irregular waves. *Phys. Fluids*, 23(1):016601, 2011.
- [139] P. Ryczkowski, M. Närhi, C. Billet, J.-M. Merolla, G. Genty, and J. M. Dudley. Real-time full-field characterization of transient dissipative soliton dynamics in a mode-locked laser. *Nat. Photonics*, 12(4):221–227, 2018.

REFERENCES

- [140] I. Chekhovskoy, O. V. Shtyrina, M. P. Fedoruk, S. B. Medvedev, and S. K. Turitsyn. Non-linear fourier transform for analysis of coherent structures in dissipative systems. *Phys. Rev. Lett.*, 122(15):153901, 2019.
- [141] S. Sugavanam, M. K. Kopae, J. Peng, J. E. Prilepsky, and S. K. Turitsyn. Analysis of laser radiation using the nonlinear fourier transform. *Nat. Commun.*, 10(1):1–10, 2019.
- [142] S. K. Turitsyn, I. S. Chekhovskoy, and M. P. Fedoruk. Nonlinear fourier transform for characterization of the coherent structures in optical microresonators. *Opt. Lett.*, 45(11):3059–3062, 2020.
- [143] I. Redor, E. Barthélemy, N. Mordant, and H. Michallet. Analysis of soliton gas with large-scale video-based wave measurements. *Exp. Fluids*, 61(10):216, Sep 2020.
- [144] D. Kaup. A higher-order water-wave equation and the method for solving it. *Prog. Theor. Phys.*, 54(2):396–408, 1975.
- [145] J.-H. Lee, O. Pashaev, C. Rogers, and W. Schief. The resonant nonlinear Schrödinger equation in cold plasma physics. application of Bäcklund–Darboux transformations and superposition principles. *J. Plasma Phys.*, 73(2):257–272, Apr 2007.
- [146] N. K. Lowman, M. A. Hoefler, and G. A. El. Interactions of large amplitude solitary waves in viscous fluid conduits. *J. Fluid Mech.*, 750:372–384, 2014.
- [147] N. Akhmediev, V. Korneev, and N. Mitskevich. N-modulation signals in a single-mode optical fiber with allowance for nonlinearity. *Zhurnal Eksperimentalnoi i Teoreticheskoi Fiziki*, 94:159–170, 1988.
- [148] D. J. Kedziora, A. Ankiewicz, and N. Akhmediev. Classifying the hierarchy of nonlinear-schrödinger-equation rogue-wave solutions. *Phys. Rev. E*, 88(1):013207, 2013.
- [149] A. Gelash and D. Agafontsev. Strongly interacting soliton gas and formation of rogue waves. *Phys. Rev. E*, 98(4):042210, 2018.
- [150] C. Gu, H. Hu, A. Hu, and Z. Zhou. *Darboux transformations in integrable systems: theory and their applications to geometry*. Springer Science & Business Media, 2004.

REFERENCES

- [151] B. Guo, L. Ling, and Q. Liu. Nonlinear schrödinger equation: generalized darboux transformation and rogue wave solutions. *Phys. Rev. E*, 85(2):026607, 2012.
- [152] J. M. Dudley, G. Genty, and S. Coen. Supercontinuum generation in photonic crystal fiber. *Rev. Mod. Phys.*, 78(4):1135, 2006.
- [153] A. Abdulle. Fourth order chebyshev methods with recurrence relation. *SIAM Journal on Scientific Computing*, 23(6):2041–2054, 2002.
- [154] A. Tovbis, S. Venakides, and X. Zhou. On semiclassical (zero dispersion limit) solutions of the focusing nonlinear Schrödinger equation. *Commun Pure Appl Math*, 57(7):877–985, 2004.